

MICROREACTORS FOR GAS/LIQUID REACTIONS: THE ROLE OF SURFACE PROPERTIES

zur Erlangung des akademischen Grades eines
DOKTORS DER INGENIEURWISSENSCHAFTEN (Dr.-Ing.)

der Fakultät für Chemieingenieurwesen und Verfahrenstechnik des
Karlsruher Instituts für Technologie (KIT)

genehmigte
DISSERTATION

von
M.Sc. Kristin Hecht
aus Powell, Wyoming, USA

Referent: Prof. Dr. Bettina Kraushaar-Czarnetzki

Korreferent: Prof. Dr. David W. Agar

Tag der mündlichen Prüfung: 4 Oktober 2013

CONTENTS

LIST OF FIGURES	V
LIST OF TABLES	IX
ABSTRACT	X
NOMENCLATURE	XI
ACKNOWLEDGMENTS	XIV
1 INTRODUCTION	1
2 PREVIOUS WORK AND THEORY	3
2.1 CONCEPTS FOR GAS/LIQUID MICROREACTORS	3
2.1.1 <i>Microchannels</i>	3
2.1.2 <i>Microstructured Falling Film Reactors</i>	6
2.2 REACTIONS STUDIED IN GAS/LIQUID MICROREACTORS	7
2.3 CHARACTERIZATION STUDIES OF GAS/LIQUID REACTORS	14
2.3.1 <i>Microstructured Falling Film Reactors</i>	14
2.3.2 <i>Microchannels/Capillaries</i>	16
2.3.3 <i>Conventional Gas/Liquid Reactors</i>	21
2.4 TWO FILM THEORY	24
2.4.1 <i>Transport in the Gas Film</i>	25
2.4.2 <i>Henry's Law</i>	25
2.4.3 <i>Transport in the Liquid Film</i>	25
2.4.4 <i>Reaction in the Liquid Bulk</i>	25
2.4.5 <i>Reaction in the Liquid Film</i>	25
3 SCOPE	28
4 METHODS	30
4.1 MATERIAL PROPERTIES CHARACTERIZATION	30
4.1.1 <i>Atomic Force Microscopy</i>	31
4.1.2 <i>Scanning Electron Microscopy</i>	31
4.1.3 <i>Contact Angle Measurement</i>	31
4.1.4 <i>Surface Tension Measurement</i>	32
4.2 INVESTIGATION OF GAS/LIQUID FLOW AND REACTION.....	32
4.2.1 <i>Test Apparatus for the Investigation of Gas/Liquid Flow and Reaction</i>	32
4.2.2 <i>Commercial Capillary Reactors</i>	34
4.2.3 <i>Microstructured Falling Film Reactor</i>	35
4.2.4 <i>Reaction of Carbon Dioxide with Aqueous Sodium Hydroxide</i>	38
5 RESULTS AND DISCUSSION	41
5.1 INVESTIGATIONS OF MATERIAL PROPERTIES	42
5.1.1 <i>Effect of Milling, Polishing, and Grinding on the Surface Roughness of Various Materials</i>	42
5.1.2 <i>Commercial Capillaries</i>	50
5.1.3 <i>Gas/Liquid/Solid Contact Angle</i>	52
5.1.3.1 <i>Effect of Pressure on the Contact Angle</i>	52
5.1.3.2 <i>Effect of Drop Size on the Contact Angle</i>	55

5.1.3.3	Effect of Surface Tension on the Contact Angle.....	59
5.1.3.4	Effect of Gas Composition on the Contact Angle.....	64
5.1.3.5	Effect of Surface Roughness on the Contact Angle.....	64
5.1.3.6	Effect of Solid Material on the Contact Angle.....	66
5.1.3.7	Effect of Reaction on the Contact Angle	67
5.1.3.8	Statistical Significance of the Investigated Parameters.....	68
5.2	DEPENDENCE OF GAS/LIQUID FLOW REGIMES ON MATERIAL PROPERTIES.....	70
5.2.1	<i>Reaction Conversion</i>	75
5.2.2	<i>Interfacial Area</i>	79
5.2.3	<i>Pressure Drop</i>	87
5.2.3.1	Lockhart-Martinelli Correlation for Gas/Liquid Flows	88
5.2.3.2	Single Phase Pressure Drops: Liquid	89
5.2.3.3	Single Phase Pressure Drops: Gas.....	92
5.3	THERMOGRAPHIC INVESTIGATION OF A MICROSTRUCTURED FALLING FILM REACTOR	94
5.3.1	<i>Interfacial Area</i>	95
5.3.2	<i>Conversion and Concentration Profiles</i>	96
5.3.3	<i>Reaction Rate</i>	98
5.3.4	<i>Liquid Mass Transport Coefficient, Enhancement Factor, and Hatta Number</i> ...	99
5.4	MEASUREMENTS OF SLUG FLOW IN 1.6 MM GLASS CAPILLARIES OF DIFFERENT LENGTHS.	103
5.4.1	<i>Description of T-Junction</i>	104
5.4.2	<i>Determination of Interfacial Area and Mass Transport Coefficient with Danckwerts Plot</i>	106
5.4.3	<i>Determination of Interfacial Area with Analytical Solution</i>	113
5.4.4	<i>Model Description of Capillary: A Simplified Film Model</i>	114
5.4.4.1	Simplified Film Model Results	116
5.4.4.2	Validity of Simplified Film Model.....	121
5.4.5	<i>Comparison of Methods Used to Obtain Values of Interfacial Area and Mass Transport Coefficient</i>	128
6	SUMMARY AND CONCLUSIONS	130
7	REFERENCES	133
8	SUPPLEMENTARY MATERIAL	144
8.1	ANALYTICAL METHODS	144
8.2	CONTACT ANGLE AND SURFACE TENSION MEASUREMENTS	144
8.3	AFM MEASUREMENTS	144
8.4	VIDEOS OF TWO-PHASE FLOW IN CAPILLARIES.....	144
8.5	CALCULATIONS OF CONVERSION, INTERFACIAL AREA, AND LIQUID MASS TRANSPORT COEFFICIENTS FROM CAPILLARY MEASUREMENTS	144
8.6	CALCULATION OF LIQUID MASS TRANSPORT COEFFICIENT FOR FALLING FILM REACTOR INVESTIGATIONS.....	144
8.7	MEASUREMENTS OF DIFFERENT LENGTHS OF GLASS CAPILLARY AND DISCRETIZED REACTOR MODELS (SIMPLIFIED FILM MODEL & FILM MODEL).....	144

LIST OF FIGURES

Figure 1: Wide variety of flow regimes observed by Serizawa et al. in a 100 μm quartz capillary.....	4
Figure 2: A flow map for the flow of air and water in a 1.097 mm pyrex glass capillary from Triplett et al. compared to flow regime transitions observed by Taitel et al., Taitel and Dukler, Suo and Griffith, and Barnea et al.....	4
Figure 3: IMVT falling film microreactor: water flow on an unstructured plate and on a plate structured with microchannels	6
Figure 4: Round-bottom etched channel	15
Figure 5: Values of interfacial area determined by Yue et al. for gas/liquid flow in a 500 μm x 1000 μm rectangular microchannel.....	19
Figure 6: Liquid mass transport coefficient determined by Yue et al. for gas/liquid flow in a 500 μm x 1000 μm rectangular microchannel	19
Figure 7: The film model describes a gas/liquid reaction as occurring between two uniform phases with mass transport through diffusion in stagnant films at the interface.....	24
Figure 8: The enhancement factor as a function of Hatta number as predicted by van Krevelen and Hoftijzer.....	27
Figure 9: Contact angle measurement apparatus; syringe and drop; software identified drop contours and contact angle	32
Figure 10: Schematic of the experimental setup	33
Figure 11: Disassembled falling film microreactor: heat exchange module; reaction module, cover.....	36
Figure 12: Microstructured falling film foil.....	36
Figure 13: Assembled falling film microreactor for thermographic investigations and thermographic image during operation	37
Figure 14: Relationship between electrical conductivity and conversion of NaOH for the reaction of CO_2 with aqueous solutions of NaOH for concentrations between 0.1 M and 5 M	39
Figure 15: Relationship between pH and conversion of NaOH for the reaction of CO_2 with aqueous NaOH for concentrations of 0.1 M and 1 M	40
Figure 16: SEM and AFM measurements of milled stainless steel surface.....	43
Figure 17: SEM and AFM measurements of polished stainless steel surface	43
Figure 18: SEM and AFM measurements of milled PTFE surface	43
Figure 19: SEM and AFM measurements of polished PTFE surface	44
Figure 20: SEM and AFM measurements of ground PTFE surface	44
Figure 21: 3D Renderings of polished, machined, and ground PTFE and stainless steel surfaces from AFM data.....	46
Figure 22: Surface roughness dependence on material hardness	48
Figure 23: Surface roughness dependence on material density	48
Figure 24: Surface roughness dependence on tensile strength.....	48
Figure 25: Relationship between R_q and R_a	49
Figure 26: Relationship between R_{max} and R_a	49
Figure 27: Relationship between Surface Area Difference and R_a	49
Figure 28: SEM photos of 250 μm fused silica capillary: capillary interior—resin in which the capillary was embedded and abraded walls from grinding can be seen at the top and bottom; magnification of the capillary wall—fragments broken off during grinding can also be seen; cross-section—diameter was measured to be 237 μm	50

Figure 29: SEM photos of 250 μm PEEK capillary: capillary interior —abraded walls can be seen at the top and bottom; magnification of the capillary wall, visible striations along the length; cross-section—diameter was measured to be 243 μm	51
Figure 30: SEM photos of 250 μm PTFE capillary: abraded walls can be seen at the top and bottom, the entire capillary interior can be seen; magnification of the capillary wall—capillary wall contains ridges perpendicular to the length; cross-section—diameter was measured to be 249 μm	51
Figure 31: SEM photos of 250 μm FEP capillary: abraded walls from grinding can be seen at the top and bottom, the entire capillary interior can be seen; magnification of the capillary wall—capillary wall appears smooth; cross-section—diameter was measured to be 299 μm	51
Figure 32: Contact angle formed at a gas/liquid/solid boundary	52
Figure 33: Contact angle variation with changing pressure for drops of water on polished stainless steel in CO_2	53
Figure 34: Contact angle variation with pressure for drops of water on polished stainless steel, colored according to radius of drop base in mm	54
Figure 35: Contact angle variation with drop size for water in N_2 and CO_2 on polished stainless steel	56
Figure 36: Langmuir linear regression on the relationship between contact angle and drop size (the radius of the drop base	58
Figure 37: Values of gas/liquid surface tension measured for mixtures of ethanol and water compared to data from Belda et al.	59
Figure 38: Relationship between the contact angle of a drop of liquid on a glass slide and the liquid/vapor surface tension for various liquids: (a) as predicted by the Young Equation; (b) the Zisman plot; (c) simple direct relationship.....	61
Figure 39: Relationship between the contact angle of a drop of liquid on a polished stainless steel surface and the liquid/vapor surface tension for various liquids: (a) as predicted by the Young Equation; (b) the Zisman plot; (c) simple direct relationship	62
Figure 40: Relationship between the contact angle of a drop of liquid on a polished PTFE surface and liquid/vapor surface tension for various liquids: (a) as predicted by the Young equation; (b) the Zisman plot; (c) simple direct relationship	63
Figure 41: Effect of surface roughness for contact angles measured on PEEK.....	64
Figure 42: Effect of surface roughness for contact angles measured on PTFE	64
Figure 43: Effect of surface roughness on the observed contact angle according to the relations of Wenzel and Cassie-Baxter	66
Figure 44: Difference in the contact angle of a drop of liquid on polished stainless steel between reactant (NaOH) and product (Na_2CO_3) for the reaction of CO_2 with aqueous NaOH	68
Figure 45: Experimentally measured values of contact angle shown against model.....	69
Figure 46: High speed photographs of gas/liquid flow in a 1.6 mm ID glass capillary shown against where they occur on a flow map	70
Figure 47: High speed photographs of gas/liquid flow in a 1.5mm ID FEP capillary shown against where they occur on a flow map	70
Figure 48: High speed photographs of gas/liquid flow in a 250 μm ID fused silica capillary	72
Figure 49: High speed photographs of gas/liquid flow in a 250 μm ID FEP capillary.....	72
Figure 50: Gas/liquid flow patterns observed in 1.6 mm glass and 250 μm fused silica capillaries	73
Figure 51: Gas/liquid flow patterns observed in 1.5 mm and 250 μm FEP capillaries	74
Figure 52: Conversion of OH^- measured for reaction of CO_2 with 2M NaOH in a 10 cm long, 250 μm ID PEEK capillary, $j_L = 0.05\text{--}0.07$ m/s	75

Figure 53: Conversion of OH ⁻ measured for reaction of CO ₂ (y _{CO₂,0}) with 2M NaOH in a 10 cm long, 250 μm ID PEEK capillary, j _L = 0.11 m/s	75
Figure 54: Conversion of OH ⁻ measured for reaction of CO ₂ (y _{CO₂,0}) with 2M NaOH in a 10 cm long, 250 μm ID PEEK capillary, j _L = 0.20 m/s	76
Figure 55: Conversion of 2M NaOH measured for reaction with different liquid flow rates in a 10 cm long, 250 μm ID PEEK capillary, y _{CO₂,0} = 0.05	77
Figure 56: Conversion of 2M NaOH measured for reaction with different liquid flow rates in a 10 cm long, 250 μm ID PEEK capillary, y _{CO₂,0} = 0.18–0.34	77
Figure 57: Conversion of 2M NaOH measured for reaction with different liquid flow rates in a 10 cm long, 250 μm ID PEEK capillary, y _{CO₂,0} = 0.54–0.62	77
Figure 58: Conversion in fused silica, PEEK, and FEP capillaries, j _L = 0.11 m/s, y _{CO₂,0} = 0.33–0.34.....	78
Figure 59: Conversion in fused silica, PEEK, and FEP capillaries, j _L = 0.20 m/s, y _{CO₂,0} = 0.58–0.61.....	79
Figure 60: Enhancement factor versus Hatta number for the reaction of CO ₂ with aqueous NaOH	80
Figure 61: A Hatta number between 3 and E _i (shown for 0.5 bar and 1 bar) fulfills the criteria for a pseudo-1st-order reaction. The Hatta number depends on k _L	81
Figure 62: Interfacial areas calculated from measurements in a 250 μm ID PEEK capillary .	83
Figure 63: Interfacial areas calculated from measurements in a 250 μm ID fused silica capillary.....	84
Figure 64: Interfacial areas calculated from measurements in a 250 μm ID FEP capillary	84
Figure 65: Pressure drop in fused silica, PEEK, and FEP capillaries for the reactive flow of 2M NaOH and CO ₂ , j _L = 0.11 m/s, y _{CO₂,0} = 0.18–0.34	87
Figure 66: Pressure drop in fused silica, PEEK, and FEP capillaries for the reactive flow of 2M NaOH and CO ₂ , j _L = 0.20 m/s, y _{CO₂,0} = 0.54–0.61	88
Figure 67: Pressure drops for the flow of water in PEEK, stainless steel, fused silica, and PTFE capillaries of 250 μm diameter	90
Figure 68: Pressure drops for the flow of isooctane in PEEK, stainless steel, and PTFE capillaries of 250 μm inner diameter	91
Figure 69: Pressure drop for the flow of gas in PEEK, stainless steel, and PTFE capillaries of 250 μm inner diameter	92
Figure 70: Correlations for pressure drop of gas in capillaries	93
Figure 71: Temperature profiles extracted from thermographic images of falling film reactor for dry and humid experiments (Q _L = 30 mL/min, X _{OH⁻} = 0.78, 0.76) and for complete conversion case (Q _L = 5.2 mL/min, X _{OH⁻} = 1)	94
Figure 72: Profiles of conversion and concentration derived from falling film reactor temperature profiles for dry and humid experiments	97
Figure 73: Profiles of conversion and concentration derived from falling film reactor temperature profiles for complete conversion experiment.....	97
Figure 74: Reaction rate calculated along the reactor length from thermographic temperature measurements of the reaction of 2M NaOH with dry CO ₂ , prehumidified CO ₂ , and at a low flow rate where complete conversion is achieved in the middle of the reactor	98
Figure 75: Liquid transport coefficient, enhancement factor, and Hatta number derived along reactor profile for dry and humid experiments.....	101
Figure 76: Liquid transport coefficient, enhancement factor, and Hatta number derived along reactor profile for high conversion experiment.....	101
Figure 77: Conversion of OH ⁻ as a function of capillary length for the reaction of pure CO ₂ with NaOH (j _G = 10 m/s, j _L = 0.1 m/s) in a 1.6 mm ID glass capillary: C _{OH⁻,0} from 2 M to 5 M (z = 2)	103

Figure 78: Conversion of OH^- as a function of capillary length for the reaction of pure CO_2 with NaOH ($j_G = 10$ m/s, $j_L = 0.1$ m/s) in a 1.6 mm ID glass capillary: $C_{\text{OH}^-,0}$ from 0.1 M to 1 M ($z = 1$).....	104
Figure 79: Diagram of T-junction where gas and liquid phases are combined (Swagelok tee union)	105
Figure 80: Reaction conversion occurring in T-junction	105
Figure 81: Empirical relation of $\Phi/C_{\text{CO}_2,i}$ and $D_{\text{CO}_2}k_{\text{OH}^-}C_{\text{OH}^-}$ describing T-junction	106
Figure 82: Enhancement factor as a function of Hatta number for 0.1 M NaOH, 2 M NaOH, and 5 M NaOH compared to the approximations $E = Ha$ and $E = \sqrt{1 + Ha^2}$ and the exact solution $E = Ha/\tanh(Ha)$	109
Figure 83: Danckwerts plot (Equation 75) used to determine a and k_L	110
Figure 84: Danckwerts plot modified with $C_{\text{CO}_2,i}$ (Equation 76)	111
Figure 85: E/Ha-style graph (Equation 79)	112
Figure 86: Reactor segment of a gas/liquid capillary.....	114
Figure 87: Comparison of model using $a = 1000$ m^2/m^3 , $k_L = 70 \times 10^{-4}$ m/s to experimental measurements	117
Figure 88: Comparison of model using $a = 3000$ m^2/m^3 , $k_L = 20 \times 10^{-4}$ m/s to experimental measurements	117
Figure 89: Reaction rate compared between measurements and model	118
Figure 90: Profiles of C_{NaOH} , $C_{\text{Na}_2\text{CO}_3}$, Φ , E , and Ha calculated with simplified film model along capillary length for 2 M ($a = 3000$ m^2/m^3 , $k_L = 20 \times 10^{-4}$ m/s)	119
Figure 91: Profiles of C_{NaOH} , $C_{\text{Na}_2\text{CO}_3}$, Φ , E , and Ha calculated with simplified film model along capillary length for 3 M ($a = 3000$ m^2/m^3 , $k_L = 20 \times 10^{-4}$ m/s)	119
Figure 92: Sum of square errors between experiments and predictions of simplified film model.....	121
Figure 93: Comparison of liquid bulk concentrations C_{NaOH} and C_{CO_2} along the capillary length calculated with the (a) simplified film model and (b) 2D film model for conditions of the experiments of the reaction of CO_2 with 3 M NaOH ($T = 21$ °C, $P = 1$ bar)	124
Figure 94: Comparison of profiles of C_{NaOH} and C_{CO_2} within the liquid film calculated with the 2D film model for the (a) capillary entrance (b) capillary exit using the starting conditions of the experiments of the reaction of CO_2 with 3 M NaOH ($T = 21$ °C, $P = 1$ bar)	125
Figure 95: Comparison of liquid bulk concentrations C_{NaOH} and C_{CO_2} along the capillary length (a) simplified film model and (b) 2D film model for conditions of the experiments of the reaction of CO_2 with 1 M NaOH ($T = 21$ °C, $P = 1$ bar)	126
Figure 96: Comparison of profiles of C_{NaOH} and C_{CO_2} within the liquid film calculated with the 2D film model for the (a) capillary entrance (b) capillary exit using the starting conditions of the experiments of the reaction of CO_2 with 1 M NaOH ($T = 21$ °C, $P = 1$ bar)	127

LIST OF TABLES

Table 1: Reactions studied in microreactors	8
Table 2: Characteristics determined for microstructured falling film reactors	14
Table 3: Microstructured falling film reactor plates investigated by Claudel et al.....	15
Table 4: Characteristics determined for microchannel gas/liquid contactors	17
Table 5: Characteristics of conventional gas/liquid contactors.....	22
Table 6: Gas mass flow controllers	34
Table 7: Liquid mass flow controllers.....	34
Table 8: Specifications of investigated capillaries	35
Table 9: Surface roughness determined with AFM	45
Table 10: Contact angles measured for some liquid/solid systems.....	67
Table 11: Significance of investigated parameters on contact angle determined from a multiple linear regression analysis	68
Table 12: Comparison of gas/liquid flows in 1.6 mm ID glass and 1.5 mm FEP capillaries at similar gas and liquid flow rates	71
Table 13: Comparison of gas/liquid flows in 250 μm ID glass and FEP capillaries at similar gas and liquid flow rates.....	72
Table 14: Constants at 20 $^{\circ}\text{C}$ used for calculating interfacial area and transport coefficients .	84
Table 15: Ion contributions for the calculation of the Henry constant for CO_2 in solutions of electrolytes	99
Table 16: Average values for the Enhancement factor for an instantaneous reaction, actual calculated enhancement factor, liquid transport coefficient, and Hatta number calculated by assuming a constant reaction rate for the entire reactor volume	101
Table 17: Values of concentration, temperature, and pressure from the presented measurements and values of the physical properties corresponding to these conditions.....	107
Table 18: Values of a and k_L determined with Danckwerts plot (Equation 75).....	110
Table 19: Values of a and k_L determined from pseudo-1 st -order measurements (Equation 79)	112
Table 20: Values of interfacial area determined from analytical solution for a pseudo-1 st -order reaction (Equation 48).....	114
Table 21: Effect of temperature and pressure profiles on Φ calculated with simplified film model for $C_{\text{OH}^-,0} = 3 \text{ M}$ ($a = 3000 \text{ m}^{-1}$, $k_L = 20 \times 10^{-4} \text{ m/s}$)	120
Table 22: Values of interfacial area and mass transport coefficient determined using various methods	128

ABSTRACT

The widespread adoption of microreactors has been hindered by a lack of knowledge regarding rules and parameters needed for their design. This dissertation deals with the investigation of interfacial area and liquid mass transport in microreactors for gas/liquid reactions. Observations of a reduction in conversion occurring when changing from a glass laboratory device to a stainless steel process device motivated investigations into the effect of material and surface properties on the gas/liquid flow and reaction. This work takes a look inside the machined microstructures produced at the Institute for Micro Process Engineering of the Karlsruhe Institute of Technology and investigates the nature of the solid surfaces resulting from the machining process—the surface roughness and the contact angle of the resulting surface. The effect of wettability on gas/liquid flow in microreactors has been investigated in capillaries of various materials. The absorption of carbon dioxide into aqueous solutions of sodium hydroxide has been used to investigate gas/liquid flow and reaction in capillaries and in a microstructured falling film reactor. Under certain limiting assumptions depending upon the exact rates of reaction and transport, values of the interfacial area and liquid mass transport coefficient can be derived from measurements of reaction. This dissertation contributes a small step towards a better understanding of how measurements of the interfacial area and mass transfer coefficient can be performed, demonstrates why the effect of material wettability cannot be ignored, and provides a stronger basis for further work in the development of general correlations describing microstructured gas/liquid reactors.

ZUSAMMENFASSUNG

Mikrostrukturierte Reaktoren zeigen gegenüber konventionellen Apparaten viele Vorteile; auch für Gas-Flüssig-Reaktionen. Mit einem besseren Verständnis für die Auslegungsregeln mikrostrukturierter Reaktoren wird auch deren Akzeptanz in der verfahrenstechnischen Praxis steigen. Die vorliegende Dissertationsschrift beschreibt die Untersuchung von Grenzflächen und Flüssig-Transportkoeffizienten in Mikrostrukturen für Gas-Flüssig-Reaktionen. Die Beobachtung, dass beim Wechsel von Glasapparaten (typisches Labormaterial) zu Edelstahlapparaten (typisches Material der industriellen Praxis) geringere Umsatzgrade beobachtet wurden motivierten Untersuchungen des Einflusses des Reaktormaterials und der Oberflächeneigenschaften auf Gas-Flüssig-Strömungen und auf chemische Reaktionen. In dieser Arbeit werden Untersuchungen der inneren Oberflächen von mikrostrukturierten Apparaten beschrieben, die am Institut für Mikroverfahrenstechnik des Karlsruher Instituts für Technologie hergestellt wurden. Die wichtigsten Parameter, die sich aus dem Bearbeitungsprozess ergeben sind die Oberflächenrauigkeit und der Gas-Flüssig-Fest-Kontaktwinkel. Der Effekt der Benetzbarkeit auf Gas-Flüssig-Strömungen wurde in Kapillaren aus verschiedenen Werkstoffen untersucht. Die Absorption von Kohlenstoffdioxid in wässrige Lösungen von Natriumhydroxid wurde als chemische Testreaktion zur Charakterisierung verschiedener Kapillaren und eines mikrostrukturierten Fallfilmreaktors verwendet. Unter vereinfachten Bedingungen, die vom jeweiligen Betriebszustand abhängen können aus der Testreaktion Werte für die Grenzfläche und die Flüssigtransportkoeffizienten abgeleitet werden. Diese Dissertationsschrift ist ein Beitrag zum besseren Verständnis der experimentellen Bestimmung von Grenzflächen und Flüssigtransportkoeffizienten. Sie zeigt, warum der Effekt der Benetzbarkeit nicht vernachlässigt werden kann und legt die Basis für künftige Entwicklungen einer verallgemeinerten Beschreibung mikrostrukturierter Gas-Flüssig-Reaktoren.

NOMENCLATURE

ACRONYMS

AFM	atomic force microscope
FEP	fluorinated ethylene propylene
HSS	high speed steel
ID	inner diameter
IMM	Institut für Mikrotechnik Mainz
IMVT	Institut für Mikroverfahrenstechnik
KIT	Karlsruhe Institute of Technology
LTF	Little Things Factory GmbH
PEEK	polyetheretherketone
PMMA	poly(methyl methacrylate)
PTFE	polytetrafluoroethylene
SATP	standard atmospheric temperature and pressure (25°C, 1 bar)
SE	secondary electron
SEM	scanning electron microscope
SSE	sum of square errors

SYMBOLS

A	gaseous reactant	
a	specific interfacial area	m ² surface/m ³ reactor
B	liquid reactant	
b	(1) channel width	m
	(2) intercept of a linear regression	
b'	length of gas/liquid interface across channel	m
C	Chisholm equation constant	
C _A	concentration of dissolved species A	mol/L
C _{A,i}	concentration of dissolved A at the interface	mol/L
C _{A,bulk}	concentration of dissolved A in the liquid bulk	mol/L
C _B	concentration of dissolved species B	mol/L
C _{B,0}	initial concentration of dissolved species B	mol/L
C _{CO2}	concentration of dissolved CO ₂	mol/L
C _{CO2,bulk}	concentration of dissolved CO ₂ in the liquid bulk	mol/L
C _{CO2,i}	concentration of dissolved CO ₂ at the interface	mol/L
C _{CO3}	concentration of dissolved species CO ₃ ²⁻	mol/L
C _{NaOH}	concentration of NaOH, equivalent to C _{OH⁻}	mol/L
C _{OH⁻}	concentration of OH ⁻	mol/L
C _{OH⁻,0}	initial concentration of OH ⁻	mol/L
C _{OH⁻,bulk}	concentration of OH ⁻ in the liquid bulk	mol/L
C _{OH⁻,L}	concentration of OH ⁻ at length L	mol/L
D, D _h	diameter, hydraulic diameter	m
D _A	diffusion coefficient of species A in the liquid	m ² /s
D _B	diffusion coefficient of species B in the liquid	m ² /s
D _{CO2}	diffusion coefficient of CO ₂ in the liquid	m ² /s
D _{CO2,0}	diffusion coefficient of CO ₂ in the liquid at the initial conditions	m ² /s
D _{CO2,L}	diffusion coefficient of CO ₂ in the liquid at the conditions of the outlet	m ² /s

D_{OH^-}	diffusion coefficient of OH^- in the liquid	m^2/s
E	liquid film enhancement factor	
E_i	enhancement factor for an instantaneous reaction	
f	fraction	
f	Darcy friction factor	
G	mass flux	$kg/m^2 \cdot s$
g	gravitational acceleration	m^2/s
H_A	Henry constant of species A	$L \cdot Pa/mol$
H_{CO_2}	Henry constant of CO_2	$L \cdot Pa/mol$
$H_{CO_2,0}$	Henry constant of CO_2 at the initial conditions	$L \cdot Pa/mol$
$H_{CO_2,L}$	Henry constant of CO_2 at the outlet conditions	$L \cdot Pa/mol$
$H_{CO_2}^\infty$	Henry constant of CO_2 in pure water	$L/mol \cdot s$
h	(1) height	m
	(2) contribution factor for calculating the effect of dissolved species on the Henry constant	
Ha	Hatta number	
I	ionic strength	mol/L
j	velocity	m/s
j_G	gas superficial velocity	m/s
$j_{G,0}$	initial gas superficial velocity	m/s
j_L	liquid superficial velocity	m/s
k_2	reaction rate constant for a second-order reaction	$L/mol \cdot s$
k_G	gas film mass transport coefficient	m/s
k_L	liquid film mass transport coefficient	m/s
k_{OH^-}	reaction rate constant for the reaction of CO_2 with NaOH	$L/mol \cdot s$
$k_{OH^-,0}$	reaction rate constant for the reaction of CO_2 with NaOH at the initial conditions	$L/mol \cdot s$
$k_{OH^-,L}$	reaction rate constant for the reaction of CO_2 with NaOH at the outlet conditions	$L/mol \cdot s$
$k_{OH^-}^\infty$	reaction rate constant for the reaction of CO_2 with NaOH at infinite dilution	$L/mol \cdot s$
L	length	m
m	slope of a linear regression	
M_w	molecular weight	kg/mol
N	number of measurements, points, elements, etc.	
\dot{N}_G	molar flow rate of gas	mol/s
$\dot{N}_{G,0}$	initial molar flow rate of gas	mol/s
\dot{N}_{inert}	molar flow rate of inert gas	mol/s
\dot{N}_{OH^-}	molar flow rate of OH^-	mol/s
$\dot{N}_{OH^-,0}$	initial molar flow rate of OH^-	mol/s
P	pressure, relative unless otherwise noted	Pa
P_0	initial pressure	Pa
$p_{A,i}$	partial pressure of A at the interface	Pa
$p_{A,bulk}$	partial pressure of A in the gas bulk	Pa
p_{CO_2}	partial pressure of CO_2	Pa
$p_{CO_2,i}$	partial pressure of CO_2 at the interface	Pa

P_{inside}	pressure on the inside of a drop or bubble	Pa
P_L	pressure at length L	Pa
P_{outside}	pressure on the outside of a drop or bubble	Pa
Q_L	liquid volumetric flow rate	m^3/s
r	radius	m
r_A	rate of reaction	$\text{mol}/\text{m}^3 \cdot \text{s}$
R_a	average roughness	m
r_{CO_2}	rate of reaction of CO_2	$\text{mol}/\text{m}^3 \cdot \text{s}$
Re	Reynolds number ($\rho_L D/\mu$)	
R_g	ideal gas constant	$\text{J}/\text{K} \cdot \text{mol}$
R_{max}	difference between highest and lowest point	m
R_q	root mean square roughness	m
Sc	Schmidt number ($\mu_L/\rho_L D_{\text{CO}_2}$)	
Sh	Sherwood number ($k_L D_h/D_{\text{CO}_2}$)	
T	temperature	K
T_0	initial temperature	K
T_0	outlet temperature	K
V	volume	m^3
V_{bulk}	volume of liquid in the liquid bulk	m^3
V_{film}	volume of liquid in the liquid film	m^3
V_{mixer}	volume of T-junction prior to capillary	m^3
V_R	reactor volume	m^3
X_{OH^-}	conversion of OH^-	
x	position within liquid film or along reactor length	m
y_{CO_2}	mole fraction of CO_2 in the gas phase	
$y_{\text{CO}_2,0}$	initial mole fraction of CO_2 in the gas phase	
X_M	Martinelli parameter	
z	stoichiometric coefficient	mole $\text{OH}^-/\text{mole CO}_2$

GREEK SYMBOLS

δ_L	liquid film thickness	m
δ_r	distance within liquid film to position where instantaneous reaction occurs	m
ε_L	liquid volume fraction	$\text{m}^3 \text{ liquid}/\text{m}^3 \text{ reactor}$
ϕ	local rate of gas absorption	$\text{mol}/\text{m}^3 \cdot \text{s}$
Φ	average rate of gas absorption	$\text{mol}/\text{m}^3 \cdot \text{s}$
ϕ_G	gas multiplication factor in Lockhart-Martinelli correlation	
ϕ_L	liquid multiplication factor in Lockhart-Martinelli correlation	
σ_{LV}	surface tension of liquid/vapor interface	J/m^2
σ_{SL}	surface tension of solid/liquid interface	J/m^2
σ_{SV}	surface tension of solid/vapor interface	J/m^2
μ	viscosity	$\text{Pa} \cdot \text{s}$
θ	contact angle	$^\circ$
θ^*	apparent contact angle	$^\circ$
ρ	density	kg/m^3

ACKNOWLEDGMENTS

I would like first and foremost to thank those who supervised this work, my advisors Dr. Peter Pfeifer and Prof. Bettina Kraushaar-Czarnetzki, for their time and support.

Luck played a large role in my coming to Germany and receiving the opportunity to conduct this research at the Institute for Micro Process Engineering at the Karlsruhe Institute of Technology for which I am indebted to the support of the former director of the institute, Dr. Klaus Schubert, and the current director, Prof. Roland Dittmeyer. Only through the help of our adept technicians, Martin Jäger, Frank Pfeffer, and Conrad Grehl, as well as Dr. Peter Pfeifer, was it possible to establish the experimental setup used in this work. Very few of my colleagues did not influence this work. Each of the colleagues in the workshop played an important role in the manufacture and design of the microstructured devices used in this work, particularly the efforts of Lothar Bohn, Matthias Schöffler, Heinz Lambach, and Manuel Schmidt.

Also from the workshop, Cornelia Schorle was particularly important in assembling the reactors and taking the photos contained in this thesis. Not to be forgotten is Robin Dürrschnabel from the design group, who had the frustrating task of turning wishes and ideas in physically realizable devices. During my work I also benefitted from the efforts of masters student Georg Fröhlich and the assistance of Stephan Kohl and Ron Zscherpe. Regarding the surfaces and their preparation and characterizations, I must acknowledge the efforts of Florian Messerschmidt, who carefully prepared the samples for measurement, Volker Toth, who made the perthometer measurements, Manfred Zürker, who conducted the SEM measurements, and Dr. Hendrik Hölscher from the IMT for AFM measurements. Especially helpful with the high speed camera measurements and FTIR was the group of Dr. Jürgen Brandner and specifically Stefan Maikowske. And last but not least among my colleagues, I would like to thank Manfred Kraut and Dr. Andreas Kölbl for the engaging discussions and encouragement that were necessary for the completion of this work and development of its themes and ideas. Sincerely, I would like finally to thank my parents, Scott and Janice Hecht, who have supported me through my long years of studying and also their company, Wyoming Completion Technologies, which contributed the samples for the contact angle measurements in a plethora of materials.

1 INTRODUCTION

A microreactor revolution is currently underway. Technologies enabling the economic structuring of hair-fine surfaces and structures in glass, plastics, and metal have spurred interest in the possible uses of these structures. Since the late 1990s intensive research has been conducted examining the properties and potential for these devices. Numerous advantages have been identified.

These advantages include not only incremental improvements but even order of magnitude differences in heat and mass transfer rates and interfacial areas. For analytical applications the advantages of miniaturization have long been obvious: small sample volumes, faster response times, smaller equipment. For chemical production there are also advantages. Microscale typically refers to typical length scales ranging from a millimeter (1000 μm) down to a single micrometer (1 μm). This scale is larger than the molecular scale, and continuum physics still provide an accurate depiction of phenomena at ambient pressure. This scale is smaller than the macro scale. Turbulence is rare; laminar flow is typical, and viscous and diffusive forces are dominant. Microstructured elements can achieve process conditions not possible in conventional equipment, such as completely isothermal conditions or quick changes in temperature, extremely fast mixing rates leading to uniform compositions, and high interfacial areas, which are beneficial to most multiphase and heterogeneously catalyzed processes. Since reactors for large throughputs are typically composed of microstructured elements but may be large devices themselves, they are sometimes referred to as microstructured reactors instead of microreactors. In this thesis the terms are used interchangeably.

As compelling as their many advantages are, microreactors have only slowly crept into industrial use, and even then, only for processes which are otherwise not possible. There are several reasons for the slow adoption. One may be that there is not a simple off the shelf microreactor solution. Microstructured reactors require special expertise to design and fabricate, which is not without cost. Another difficulty is the unit operations approach to process and plant design. Equipment is typically specified to perform a single unit operation function such as mixing, heat transfer, or reaction. Although a large advantage of microreactors is the easy integration of multiple unit operations to create synergetic energy savings, it requires rethinking the process, not just buying a new heat exchanger or mixer. There is always the technological gap, the time lag from when new and better technologies mature and the time that old, existing production plants are taken off line. Other obstacles to microreactor adoption could be the unexpected problems experienced when trying out microreactors for the first time such as clogging or high pressure drops. Microreactors are surely not a panacea to all chemical process problems, and they must be intelligently used to provide benefit.

How can a microreactor revolution be occurring when the adoption of microstructured technology in chemical processes is only crawling along? The revolution is occurring at the moment in the way chemical processes are investigated and developed. One cogent advantage of microreactors is that parallel systems can be numbered up instead of conventional equipment which is typically scaled up with an inherent decrease in performance and efficiency. As an instrument in the chemist's toolbox, microreactors allow chemists designing processes to research and optimize continuous processes while wasting minimal amounts of reagents. Previously, most chemists worked only with batch processes, and scale up was a major issue. Continuous processes are much preferred in a chemical plant since they are easier to control and can be optimized to produce a higher quality product through statistical control methods. There is likely no chemical company that operates today without statistical control

and continuous production of their most important products and with microreactors in the hands of chemists and engineers adapting lab results into continuous processes. The revolution lies not only in the advantages of the microscale, but also in the shifting paradigm of how processes and unit operations are integrated into a process or plant. As the process design paradigm evolves, microreactor technology will surely be more frequently employed over the next decades so that the principles of choosing the appropriate scale for reactions can improve the efficiencies of chemical processes.

One major hindrance to the widespread adoption of microreactors in the actual chemical production is still simply a lack of knowledge. This is partially a result of microreactors representing a radical departure from conventional process design and not just an incremental improvement. The potential of microreactors has thus far been examined in some detail, but many of the design rules and parameters are either not available or not applicable to microscale technologies. For example, microreactors are well suited for fast reactions, but what exactly is a fast reaction? For some reactions, reaction kinetics have been exactly determined, but many reactions are “fast” because the chemistry in a beaker is completed on the order of minutes. However, for the design of a microreactor system, it is necessary to know just how fast the reaction is. Does the reaction take place in seconds or milliseconds?

This thesis specifically deals with the investigation of interfacial area and liquid mass transport in microreactors for gas/liquid reactions. Compared to conventional devices, microstructured gas/liquid reactors offer many advantages in terms of magnitudes of order larger interfacial areas, large mass transport coefficients, and the good temperature control or heat transfer capabilities. However, gas/liquid reactor design parameters such as the specific interfacial area and gas and liquid mass transport coefficients are not widely available for microstructured devices. They cannot be found in tables given in engineers’ reference books. Although there are a handful of papers where these properties have been measured that provide valuable insights into the advantages of microreactors and an idea of possible values, there are frequent and large discrepancies among these values.

The geometry of the reactor system including such small details as the shape of the gas and liquid feed inlets prior to their contacting can influence the reactor hydrodynamics. Another aspect, which was first identified as being of major significance in 1993, is the microchannel material. It may seem obvious to the reader that a gas/liquid flow would behave differently in glass and PTFE microchannels, but what about metal versus glass? In this case the decrease in performance from the glass laboratory apparatus to the stainless steel process apparatus was unexpected and motivated this work.

Previous work has demonstrated that the wettability of the solid material influences the hydrodynamics of gas/liquid flow in a manner that would presumably influence the interfacial area of the phases. Wettability is typically characterized through the contact angle, the angle formed at the three-phase boundary of a liquid drop lying on a solid surface. This work takes a look inside the machined microstructures typically produced at the Institute for Micro Process Engineering at the Karlsruhe Institute of Technology and investigates the nature of the solid surfaces resulting from the machining process—the surface roughness and the contact angle of the resulting surface. The topic of how to characterize microreactors is discussed in depth since characterization of these devices presents its own novel challenges. The results of this work are by no means a complete description of multiphase flow in all microreactors, but they do explain and reveal some interesting phenomena that can be used to improve models, understanding, and eventually designs for gas/liquid microreactors.

2 PREVIOUS WORK AND THEORY

Gas/liquid reactions have been studied with the use of microreactors by many groups [1-7]. These studies have generally shown that the exceptional interfacial areas, fast mass transport, and good temperature control can improve reaction conversion and selectivity compared to current state of the art processes. Somewhat less attention has been paid to the reactors themselves. There are only a handful of studies that have measured the exact values of interfacial area and transport coefficients in the reactors, parameters important to engineers for designing gas/liquid reactors. These studies have revealed a wide range of possible values depending strongly on material properties and different flow regimes that occur in microreactors.

2.1 CONCEPTS FOR GAS/LIQUID MICROREACTORS

A microchannel is the most prevalent form of microreactor, but microstructures can be used for gas/liquid reactors in many variations. Concepts incorporating microchannel grooves to improve liquid distribution in falling film reactors have also been presented.

2.1.1 Microchannels

A closed channel with a characteristic inner diameter on the scale of several to several hundred micrometers is the most simple and ubiquitous form of microreactor. Microchannels can also be packed, e.g. with catalyst [2]. For industrially relevant throughputs arrays of multiple microchannels are needed [1]. The equal distribution of gas and liquid phases among arrays of channels can be especially challenging [3,7].

The flow within a microchannel can take different forms depending on the gas and liquid flow rates and material properties such as the contact angle. Figure 1 shows pictures of different gas/liquid flow patterns observed by Serizawa et al. [4] for air/water flows in a 100 μm quartz capillary. The nomenclature and conditions at which different flow regimes occur varies among different literature sources. The definitions of plug, slug, and annular flow from Serizawa et al. [4] are used in this work. A number of parameters, including the channel shape and size, capillary material, densities and viscosities of the fluids, interfacial tension, velocities, and relative volumes of gas and liquid, influence the flow pattern. The flow regimes are most strongly associated with the gas and liquid superficial velocities (j_G, j_L), and their occurrence is typically reported in a flow map, as shown in the example from Triplett et al.[6] in Figure 2 for the flow of air and water in a horizontal glass tube of 1.097 mm inner diameter.

The flow pattern itself is a visual reflection of the hydrodynamics and mass transport occurring in a particular gas/liquid flow. Identifying the conditions under which each flow pattern occurs is a major topic of a large number of investigations [4,6,8-11].

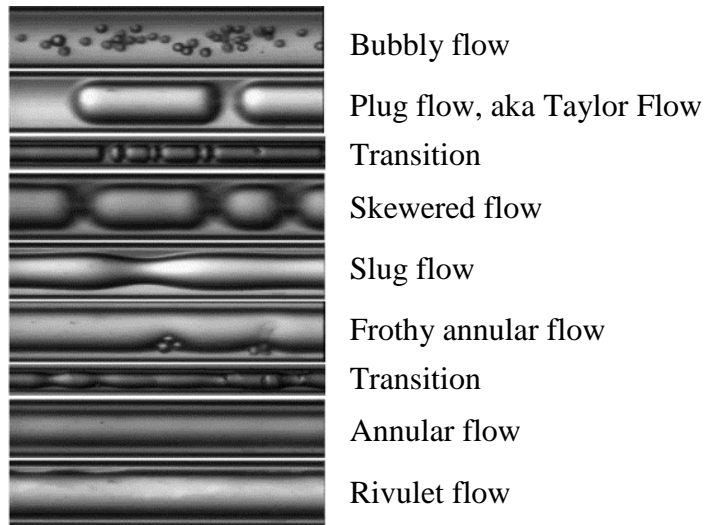


Figure 1: Wide variety of flow regimes observed by Serizawa et al. [4] in a 100 μm quartz capillary

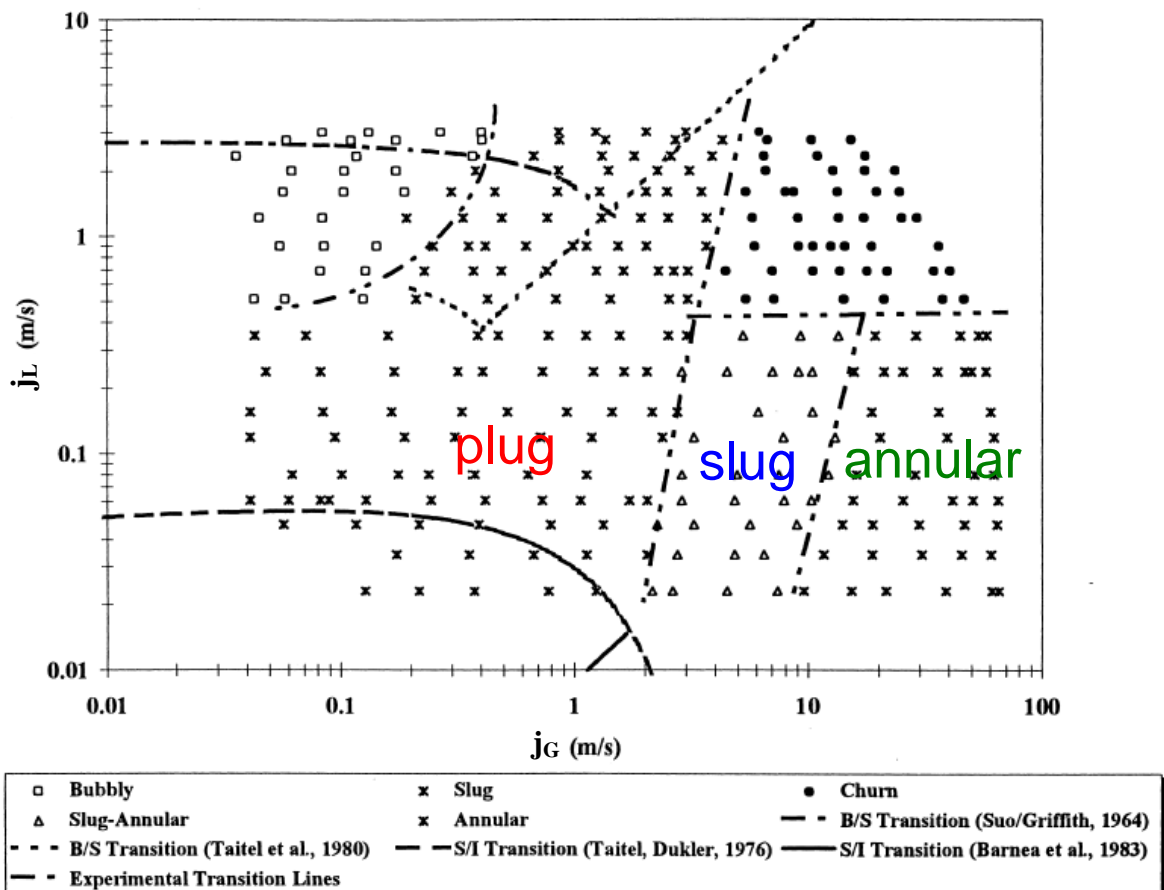


Figure 2: A flow map for the flow of air and water in a 1.097 mm pyrex glass capillary from Triplett et al. [6] compared to flow regime transitions observed by Taitel et al. [5], Taitel and Dukler [12], Suo and Griffith [13], and Barnea et al. [14]

At high liquid superficial velocities, bubble flow occurs at lower gas superficial velocities, and churn flow occurs at higher gas flow rates. At low liquid superficial velocities, plug flow occurs when the relative volume of gas to liquid is close to equal. This flow is also frequently called Taylor flow [15], after the first of two classic papers on the topic published in the 1961 *Journal of Fluid Mechanics* by Taylor [16] of Cavendish Laboratories and by Bretherton [17] of Trinity College, both located in Cambridge, England. As the gas superficial velocity increases, the lengths of the gas plugs become longer. Further increases in the gas flow rate result in plug flow, where the small liquid amounts are able or nearly able to form liquid plugs only to be rapidly accelerated as periodic swells of liquid. A liquid film is typically continuously present on the walls for slug flow in glass capillaries. With further increases in the gas flow rate, the liquid slugs become less frequent and then nonexistent, with the liquid being transported as a film along the walls and the gas flowing through the center. This flow regime is referred to as annular flow. The liquid film often contains ripples and is not necessarily smooth. Plug, slug, and annular flow regimes have been investigated in this dissertation.

The occurrence of each flow regime and the location of the transitions to other flow regimes are not well defined and depend on the material properties and geometry. The influence of the wettability of the three phase system, characterized by the observed contact angle, was first reported by Barajas and Panton [8]. They observed flow patterns for the flow of air and water through 1.6 mm tubes of pyrex glass ($\theta = 34^\circ$), polyethylene ($\theta = 61^\circ$), and FEP ($\theta = 106^\circ$). They demonstrated that the wettability influences the location of the transitions between the flow regimes as well as the flow regimes that occur. For instance, in hydrophobic materials such as fluorinated ethylene propylene (FEP), annular flow was replaced by rivulet flow. Plug and slug flow, however, were reported in every material, and the transition between plug and slug flow occurred at nearly the same flow rates.

Lee and Lee [9] further developed the understanding of the role of wettability in gas/liquid flows. They studied air and water or methanol flows in glass, "Teflon," and polyurethane tubes between 1.46 and 2 mm inner diameters. They were able to create general flow maps adequately describing their data and that from Barajas and Panton [8] by correcting j_L according to the contact angle. A very interesting aspect of their work is their observation of differences between what they called wet or dry plug, slug, or annular flow. From high resolution photographs of the flows, Lee and Lee were able to approximately ascertain whether or not a continuous liquid film was present at the edge of the gas bubble. Despite the apparent equivalence of all situations called plug flow, or slug flow or annular flow, the characteristics of transport and especially interfacial area can actually be drastically different depending on the presence or absence of this film.

Although glass is a convenient material for laboratory investigations, less brittle materials possessing greater strength are often preferred for industrial applications, e.g. steel or stainless steel. Since the change from glass to metal is accompanied by changes in the surface wettability, it is important to understand the effect of surface properties in gas/liquid flows. Early investigations into gas/liquid reactions at the Institute for Micro Process Engineering (IMVT) encountered a surprising decrease in conversion when changing from glass capillaries used for preliminary laboratory tests to stainless steel microchannel modules intended for industrial use. This work is intended to further elucidate the reason and rules according to which material interactions alter the hydrodynamics and interfacial area in microchannel gas/liquid flow, which could influence conversion and selectivity, especially for fast reactions.

2.1.2 Microstructured Falling Film Reactors

Falling film microreactors are available from the Institut für Mikroverfahrenstechnik (IMVT) of the Karlsruhe Institute of Technology (KIT), the Institut für Mikrotechnik in Mainz (IMM), Little Things Factory GmbH (LTF), Mikroglas Chemtech GmbH, and Ehrfeld Mikrotechnik BTS, among others. These reactors consist of a solid surface over which a thin liquid film flows in contact with a gas. A microstructured plate is the most common configuration for this reactor, but the IMM also produces a symmetrical, cylindrical geometry [18]. The falling film microreactor from the IMVT is described in Section 4.2.3. The reactor can house different surfaces over which the liquid flows. A flat stainless steel surface and a surface containing microchannels are shown in Figure 3. The IMVT reactor has been used for the sulfation of fatty acids in the framework of the EU FP6 IMPULSE Project (2005–2009). Fatty acids have a small contact angle with stainless steel, resulting in a wetted-wall on the unstructured metal foil. Water has a substantially higher contact angle and creates liquid rivulets on the unstructured foil, but the microchannels disperse it to create a uniform film as seen in Figure 3.

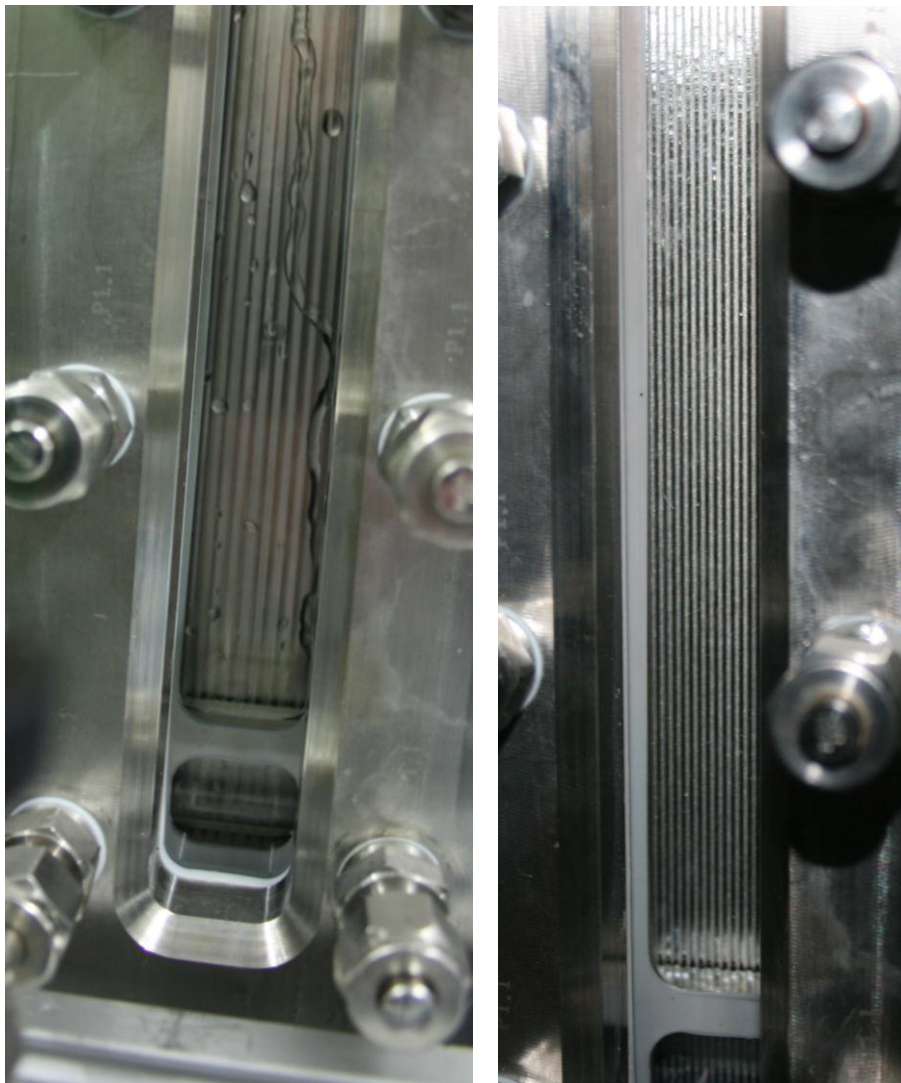


Figure 3: IMVT falling film microreactor: water flow on an unstructured plate (left) and on a plate structured with microchannels (right)

2.2 REACTIONS STUDIED IN GAS/LIQUID MICROREACTORS

Reactions that have been previously studied in microreactors are listed in Table 1. The most notable success of these efforts has been the development of direct fluorination processes, which were not previously utilized due to the large energy releases and hazards of that route [19-21]. Ozonolysis, halogenation, oxidation, hydrogenation, sulfonation, and nitration have been studied. Absorption of gases (CO_2 , SO_2 , NH_3) have also been studied; these simple reactions can be useful as test reactions for device characterization when the reactions are already well understood.

Table 1: Reactions studied in microreactors

Gas Reactant	Liquid Reactant	Microreactor Studies
F₂	toluene	Löwe et al. 1998 [22] Hessel et al. 1999 [23] Jähnisch et al. 2000 [24] de Mas et al. 2001 [25] de Mas 2002 [26] de Mas et al. 2003 [27] de Mas 2004 [28] de Mas et al. 2009 [29]
	sulfur pentafluoride derivatives, dicarbonyl and aromatic compounds, perfluorination, 4-nitrotoluene	Chambers and Spink 1999 [30] Chambers et al. 2001 [31]
	cyclohexanol	Chambers et al. 2003 [32]
	1,2-cyclohexanediol	
	1,4-cyclohexanediol	
	cyclohexanone	
	2-acetylcyclohexanone	Chambers and Sandford 2004 [33]
	2,4-dinitrotoluene	
	trifluoro(3-nitrophenyl)-sulfur	
	2,5-bis(1,1,2,3,3,3-hexafluoropropyl)tetrahydro-furan	
	Acetylacetic acid ethyl ester	
	2-oxocyclohexanecarboxylic acid ethyl ester	
	malonic acid	
	1-acetoxycyclohexene	
	ethyl acetoacetate	Chambers 2005 [34]
	ethylene carbonate	Lang et al. 2012 [35]
	diethyl malonate, Meldrum's acid	Chambers et al. 2005 [36]
	1,3-ketoesters, 1,3-diketones	Chambers et al. 2005 [1]
	1,3- 1,4- and 1,3,4-substituted aromatic rings	Chambers et al. 2007 [37]

Table 1 continued

Gas Reactant	Liquid Reactant	Microreactor Studies
Cl₂	toluene-2,4-diisocyanate (photochemical)	Ehrich et al. 2002 [38] Morgenschweis et al. 2004 [39]
	cyclohexane (photochemical) acetic acid	Matsubara et al. 2011 [40] Wehle et al. 2002 [41]
CO	copper ammonia formate	TeGrotenhuis et al. 1999 [42]
	Halogenated alkenes (palladium acetate) 3-methylphenyl iodide 3-methoxyphenyl iodide 4-nitrophenyl iodide 4-(Trifluoromethyl)phenyl iodide 2-Acetylphenyl iodide 3-Chlorophenyl iodide 2-Bromophenyl iodide 3-Iodobenzylamine 2-Thienyl iodide 4-Iodo-1-methylpyrazole 2-Pyridyl iodide 1-tert-Butoxycarbonyl-3-iodo-1H-indole (E)-1-Octenyl iodide 4-Nitrophenyl bromide	Koos et al. 2011 [43]
CO + H₂ Hydrogenations with homogeneous chiral catalysts	Z-acetamido cinnamic methyl ester	de Bellefon et al. 2000 [44] de Bellefon et al. 2001 [45]
	methyl cinnamate	de Bellefon et al. 2003 [46] Abdallah et al. 2004 [47]
	methylacetamidocinnamate, methylacetamidoacrylate, dimethylitaconate, methone, α -pinene acrylate esters	de Bellefon et al. 2005 [48] Leclerc et al. 2008 [49]

Table 1 continued

Gas Reactant	Liquid Reactant	Microreactor Studies
H₂ Hydrogenation with homogeneous chiral catalysts	Alkenes (Crabtree's catalyst) ethyl cinnamate cinnamyl alcohol α -methylcinnamic alcohol (E)-stilbene 4-methylbenzalacetone 1-nonadecene anisole chalcone	O'Brien et al. 2011 [50]
	Alkenes (Wilkinson's catalyst) chalcone cinnamic acid 1-dodecene anethole eugenol (allyloxy)benzene dihydrocarvone diethylfumarate p-chlorostyrene 5-ethenyl-1,3-benzodioxole	Mercadante et al. 2012 [51]
VOCs Tetrachloroethylene (Cl ₂ C=CCl ₂)	di(2-ethylhexyl)adipate	Mhiri et al. 2011 [52]
SO₃	toluene	Müller et al. 2004 [53] Müller et al. 2005 [54] Jähnsich et al. 2005 [55]
SO₂	NaOH	Commenge et al. 2003 [56]
NH₃	H ₂ SO ₄	Shaw et al. 1998 [57]
H₂S	methyldiethanolamine	Su et al. 2010 [58]

Table 1 continued

Gas Reactant	Liquid Reactant	Microreactor Studies
CO ₂	<p>Bases NaOH</p> <p>NaOH/NaClO/Na₂CO₃ NaHCO₃/ Na₂CO₃</p> <p>KHCO₃/ K₂CO₃/NaClO</p>	<p>Wille 2002 [59] Hessel et al. 2000 [60] Claudel et al. 2005 [61] Zanfir and Gavriilidis 2005 [62] Hecht and Kraut 2010 [63] Sobieszuk et al. 2010 [64] Su et al. 2010 [58] Ziegenbalg et al. 2010 [65] Claudel et al. 2005 [61] Yue et al. 2007 [66] Hou et al. 2011 [67] Sobieszuk et al. 2011 [68]</p>
	<p>Amines diethanolamine monoethanolamine ethylbutylamine dipropylamine methyl diethanolamine</p>	<p>TeGrotenhuis et al. 1999 [42] Sobieszuk et al. 2010 [64] Li et al. 2011 [69]</p>
	<p>Magnesium halide Grignard reagents chloro(3,5-dimethoxyphenyl)-magnesium chloro(2-phenylethyl)-magnesium chloro-2-naphthalenyl-magnesium bromo(3-fluoro-4-methylphenyl)-magnesium bromo(4-methoxy-2-methylphenyl)-magnesium bromo[2-(4-methoxyphenyl)ethyl]-magnesium bromo(2,4,6-trimethylphenyl)-magnesium chloro-2-thienyl-magnesium bromo(2-phenylethynyl)-magnesium 4-biphenylmagnesium bromide</p>	<p>Polyzos et al. 2011 [70]</p>

Table 1 continued

O₂	butyraldehyde	Haverkamp et al. 2001 [71] Haverkamp 2002 [72]
	cyclohexane	Leclerc et al. 2008 [49] Fischer et al. 2010 [73]
	octanal (manganese acetate)	Rebrov et al. 2012 [74]
	sulfite	Hessel et al. 2000 [60] Haverkamp et al. 2001 [71] Haverkamp 2002 [72]
	not given	Woerz 2001 [75]
	α -terpinene	Wootton et al. 2002 [76]
	cyclopentadiene	Jähnisch and Baerns 2004 [77]
	citronellol	Levesque and Seeberger 2011 [78]
	trimethylethylene	
	α -pinene	
p-cymene		
furan		
2-(ethylthio)ethanol		
Singlet O₂	Photochemical reactions with activator, e.g. rose bengal	

Table 1 continued

Gas Reactant	Liquid Reactant	Microreactor Studies
O₃	Alkenes and alkynes (ozonolysis)	
	decene	Wada et al. 2003 [79] Wada et al. 2006 [80] Steinfeldt et al. 2010 [81] Royhouse et al. 2011 [82] Steinfeldt et al. 2007 [83] Irfan et al. 2011 [84]
	acetic acid 1-vinyl-hexyl ester	
	β-pinene	
	propynol	
	α-(2-methyl-2-phenylpropyl)styrene	
	p-fluoro-α-methylstyrene	
	p-nitrostyrene	
	anethole	
	2-methyl-4-(adamantane-2'-spiro)-oxazolin-5-one	Battilocchio et al. 2012 [85]
	Thioethers (ozonolysis)	
	thioanisole	Irfan et al. 2011 [84]
	Esters (oxidation)	
	triethyl phosphate	Wada et al. 2003 [79] Wada et al. 2006 [80]
	Amines (oxidation)	
	nonylamine	Wada et al. 2003 [79]
	octylamine	Wada et al. 2006 [80]
	octan-1-amine	Irfan et al. 2011 [84]

2.3 CHARACTERIZATION STUDIES OF GAS/LIQUID REACTORS

This work concerns itself particularly with the quantitative determination of values of interfacial area and mass transport coefficients in microstructured reactors. The hydrodynamics of plug flow, a.k.a. Taylor flow, have been intensively studied, especially within the context of upflow through vertical monoliths, and many phenomena are understood regarding the bubble and liquid plug lengths and velocities, film thickness, and recirculation of the liquid phase [15]. However, there are no expressions or values for the interfacial area (a) or the liquid mass transport coefficient (k_L) that can generally be applied to microreactors. Sobieszuk et al. [86] and Yue et al. [10] have found poor agreement between measurements of $k_L a$ in microchannels and correlations developed for flow in vertical monoliths, e.g. developed by Bercic and Pintar [87], Vandu et al. [88], and van Baten and Krishna [89].

For fast reactions such as the absorption of carbon dioxide into aqueous solutions of sodium hydroxide which is studied in this work, reaction occurs completely or to a significant extent within the liquid film. To calculate reaction in the film, separate values for a and k_L are required. Although no generally applicable rules are available, some authors have measured these parameters for certain reactors and hydrodynamic situations. Previous work determining exact values of a and k_L are summarized in Section 2.3.1 for microstructured falling film reactors and in Section 2.3.2 for gas/liquid flow in microchannels and capillaries. Characteristics of conventional gas/liquid reactors have been summarized and compared to microstructured devices in Section 2.3.3.

2.3.1 Microstructured Falling Film Reactors

Table 2 lists values of interfacial area and mass transport coefficients determined for microstructured falling film reactors. Falling film reactors are operated with much larger gas volumes compared to the volume of liquid. The interfacial area is often approximated as equal to the area occupied by the microstructured channels or features in which the liquid flows. The values of interfacial area given for microstructured falling film reactors are given with respect to the reactor volumes. The reactor volume is the sum of the volume of the reactor occupied by the liquid, i.e. the microchannels, and the volume of the reactor occupied by the gas. Since the falling film reactors are operated with very low relative volumes of liquid (ϵ_L), the given values of interfacial area appear to be low. Dividing a by ϵ_L gives the interfacial area per volume of liquid gives interfacial order values on the order of 10^3 m^{-1} .

Table 2: Characteristics determined for microstructured falling film reactors

Contactor	Flow Pattern	a (m^2/m^3 reactor)	ϵ_L (%)	k_L (m/s) $\times 10^4$	k_G ($\text{mol}/\text{m}^2 \cdot \text{Pa} \cdot \text{s}$) $\times 10^5$
Falling Film Claudel et al. [61]	cocurrent	169–189	2–6*	4.81–10.8	1.32
Falling Film Zhang et al. [90]	cocurrent	300– 900*	9–27*	0.58–1.34	

*estimated from flow rates and reactor geometry

Claudel et al. (2005) [61] investigated a falling film microreactor produced by the IMM. Round-bottomed microchannels as sketched in Figure 4 were etched into stainless steel plates. Claudel et al. investigated three different microstructured plates, where the size and number of the channels were varied such that the structured area of the liquid plate was approximately constant. Channel widths of 328 μm (64 channels), 645 μm (32 channels), and 1200 μm (16

channels) were investigated; the channel depth also varied: 97 μm for the 328 μm channels, 226 μm for the 645 μm channels, and 400 μm for the 1200 μm channels. The geometries of the investigated plates and results of the investigations are summarized in Table 3.

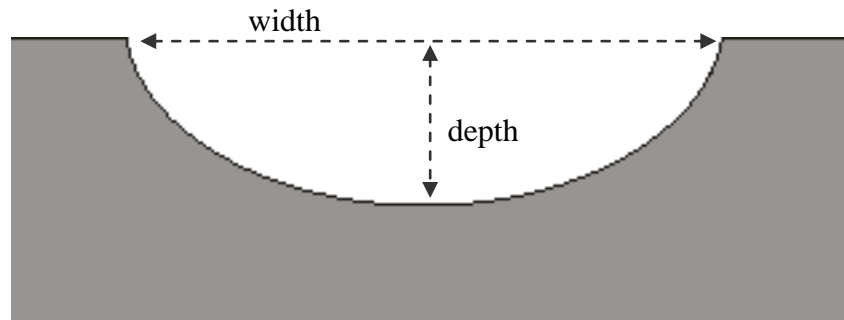


Figure 4: Round-bottom etched channel

Table 3: Microstructured falling film reactor plates investigated by Claudel et al. [61]

Plate	Number of channels	Channel width (μm)	Channel depth (μm)	Liquid Flowrate (L/hr)	a (m^2/m^3 reactor)	k_L (m/s) $\times 10^4$	k_G ($\text{mol}/\text{m}^2 \cdot \text{s} \cdot \text{Pa}$) $\times 10^5$
A	64	328	97	0.05			
B	32	645	226	0.2	183	4.81	
				0.4	189	4.78	1.32
C	16	1200	400	0.5	188	8.29	
				1	187	10.8	
				1.5	169	7.04	

Claudel et al. [61] characterized a , k_L , and k_G using pseudo-1st-order reactions and the Danckwerts plot (This method is employed and described in Section 5.4.2.). A pseudo-1st-order reaction is presumed to occur for values of the Hatta number between 3 and $E_i/2$ [91]. The absorption of 10% CO_2 into 0.5 M Na_2CO_3 catalyzed by NaClO was used to determine a and k_L ; the absorption of 10% CO_2 into NaOH (0.79 M–1.85 M) was used to determine a and k_G . The values determined from these investigations are given in Table 3. For the absorption of CO_2 into NaOH , the Hatta number ranged between 5.65 and 10.53, and E_i was between 180 and 623, meeting the conditions for a pseudo-1st-order reaction. For the NaClO catalyzed absorption of CO_2 into Na_2CO_3 , the Hatta number ranged between 0.34 and 1.11, and E_i was between 57 and 98. The Hatta numbers for this reaction are slightly lower than those suggested for use with characterization through pseudo-1st-order reaction. The Hatta numbers are lower than commonly encountered for a fast reaction. This occurs, interestingly, because the measured k_L values are very high (see Figure 8).

From the reactor geometry and reaction rates given in the paper, moderate liquid reactant conversions of 0.2 to 0.5 can be back calculated. Claudel et al. also attempted to characterize Plate A but were unable to do so because as they write, “For each plate, higher is the flow rate, lower is residence time and the conversion and higher is uncertainty on the CO_2 flux determination.” Presumably, the conversion on Plate A was very high due to the low flow rate, and it was not possible to draw meaningful results when the reaction reached completion within the reactor. Attempts to characterize the reaction using the physical absorption of CO_2 by water were also unsuccessful due to the small amount of CO_2 transferred. Physical absorption measurements can only be analyzed insofar as the gas/liquid system does not reach equilibrium.

Zhang et al. (2009) [90] studied the hydrodynamics and mass transport and the effects of viscosity, surface tension, and contact angle in a transparent falling film microreactor constructed of poly(methyl methacrylate) (PMMA). Their reactor looks very similar to the IMM reactor studied by Claudel et al. [61]. They reported some problems associated with the liquid distribution in the reactor such as poorly filled channels or liquid flowing outside of the microchannels. The startup procedure for their reactor involved flooding the entire reactor with liquid then draining the liquid and starting the gas flow. Mass transport experiments were conducted using the physical absorption of CO₂ into water.

Zhang et al. [90] measured k_L values between 0.58×10^{-4} and 1.34×10^{-4} m/s. The k_L value increased with increasing liquid flow rate and was negligibly increased by increasing gas velocity. The influence of surface tension was investigated by comparing absorption experiments conducted with water and 50 and 100 ppm solutions of sodium lauryl sulfate. The surface tension of water is 72 mN/m. The surface tensions of the sodium lauryl sulfate solutions were 69.8 mN/m and 66.1 mN/m, respectively. No effect due to these changes in the surface tension was observed. The effect of viscosity was examined by comparing experiments with 5.2 wt% and 12 wt% ethylene glycol with water. The viscosity of water is 8.97×10^{-7} m²/s. The viscosities of the ethylene glycol solutions were 9.4×10^{-7} m²/s and 11.04×10^{-7} m²/s, respectively. The surface tensions of the two ethylene glycol solutions were comparable to those of the sodium lauryl sulfate solutions. The mass transport coefficient decreased with increasing viscosity, and the effect was more pronounced at higher Reynolds numbers ($Re = \rho_j L D / \mu$). Zhang et al. fit their measurements to an empirical correlation:

$$Sh = 0.0145 Re^{0.69} Sc^{0.57} \quad [1]$$

Sh is the Sherwood number ($k_L D_h / D_A$) and Sc the Schmidt number ($\mu_L / \rho_L D_A$).

Zhang et al. found that the wettability of the solid material affected the interfacial area. They coated one microstructured plate with an aluminum hydroxide sol gel preparation. The contact angle of this material with water is very small, i.e. the wetting is very good. The contact angle of water with PMMA is around 75°. Zhang et al. noticed a substantial increase in the rate of CO₂ absorption on the coated plate. From these observations they proposed a correlation for the interfacial area as a function of the contact angle and the channel width:

$$b' = \frac{b \pi}{\cos \theta} \frac{90^\circ - \theta}{180^\circ} \quad [2]$$

In this equation b is the width of the channel, b' is the length of the gas/liquid interface, and θ is the contact angle.

2.3.2 Microchannels/Capillaries

As described in Section 2.1.1, the flow of gases and liquids together in microchannels can take many forms. “Plug flow” and “slug flow” as defined in that section have been investigated by several groups. The interfacial areas and mass transport coefficients determined for gas/liquid flows in microchannels are summarized in Table 4. The values of a are given with respect to the volume of the reactor, i.e. the volume of the microchannel. Both measured interfacial areas and the surface area to volume ratio of the reactor wall are compared in Table 4; for gas/liquid flows in microchannels the interfacial area can differ substantially from the intrinsic surface area to volume ratio.

Table 4: Characteristics determined for microchannel gas/liquid contactors

Microchannel Characteristics	Flow Pattern	j_G (m/s)	j_L (m/s)	ϵ_L (%)	a^{**} (m^2/m^3 reactor)	k_L (m/s) $\times 10^4$	k_G (m/s)	Reaction
500 μm x 1000 μm PMMA Yue et al. [66]	plug flow, slug flow	0.7–10	0.8–1	2–20*	3000–9000 (6000)	4–13		CO ₂ /NaOH (a) CO ₂ /Na ₂ CO ₃ / NaHCO ₃ (k _{L,a})
2 mm x 2 mm PMMA Roudet et al. [92]	plug flow	0.02–0.4	0.07–0.2	16–87*	100–1500 (2000)	1– 4.5		Physical absorption of oxygen/air into water
D = 1mm Stainless steel Su et al. [58]	plug flow, slug flow	1–8	0.01–1	0.1–4.8*	4500–10 000 (4000)		0.007– 0.02	CO ₂ /NaOH (a) H ₂ S/MDEA (k _{Ga})
D = 0.4 mm glass Sobieszuk et al. [68]	plug flow	0.5–0.8	0.05–0.5	7–45*	5500–12 000 (10 000)	2–6		CO ₂ / K ₂ CO ₃ / KHCO ₃ /NaOCl
Characteristic dimensions ~1 mm Hou et al. [67]		50–200*	10–50*	6–47*	1400–12 000 (~ 4000)	2–14		CO ₂ /NaOH (a) CO ₂ /Na ₂ CO ₃ / NaHCO ₃ (k _{L,a})

* estimated from flow rates and reactor geometry

** top range is from measurements; second entry in parentheses is the surface area to volume ratio of the microchannel wall

Yue et al. (2007) [66] measured values of a and k_L for gas/liquid slug and plug flows in a horizontal, rectangular microchannel 500 μm wide and 1000 μm deep. The microchannel was constructed in PMMA with adhesive tape on the top side. They measured $k_L a$ values using the physical absorption of CO_2 into water and using the absorption of CO_2 into 0.3 M NaHCO_3 /0.3 M Na_2CO_3 solutions, a slow reaction that can be analyzed the same as physical absorption ($k_L a \gg \varepsilon_L k_2 C_{B,0}$). They measured interfacial area values using the absorption of CO_2 into 1 M NaOH (assuming pseudo-1st-order reaction behavior). Separate values of a and k_L could then be obtained from the complementary measurements, assuming that the differences of viscosity, surface tension, and contact angle among the aqueous solutions were negligible and the hydrodynamic situations comparable.

A 4 mm tube was used as the reactor outlet. For the experiments with physical absorption, a phase separator at the reactor outlet was employed, but for the chemical absorption, the gas was dissipated into the atmosphere, and the liquid sample was collected. Experiments were conducted using a 4.8 cm long microchannel and also using the setup without microchannel. End effects were accounted for by calculating $k_L a$ values from the experiments without the microchannel and using these values to account for the exit channel and mathematically determine the concentration at the microchannel exit itself.

The values of a and k_L measured by Yue et al. are shown in Figure 5 and Figure 6. The values in the graphs have been determined according to the data reported in their publication. The transition from plug to slug flow was observed to occur at a superficial gas velocity between 2 and 3 m/s. The interfacial area initially increased with increasing gas velocity and reached a constant value nearly equal to the geometric surface area to volume ratio of the microchannel. The measurements with a liquid superficial velocity of 0.5 m/s differed from the other measurements, and Yue et al. reported a flow regime other than plug or slug flow for those measurements. The measured data were fitted via regression to empirical correlations [93-96] for plug flow:

$$Sh \cdot a \cdot D_h = 0.084 Re_G^{0.213} Re_L^{0.937} Sc^{0.5} \quad [3]$$

and for slug flow:

$$Sh \cdot a \cdot D_h = 0.058 Re_G^{0.344} Re_L^{0.912} Sc^{0.5} \quad [4]$$

Sh is the Sherwood number ($k_L D_h / D_{\text{CO}_2}$) and Sc the Schmidt number ($\mu_L / \rho_L D_{\text{CO}_2}$). The Reynolds numbers for the respective fluids are based on their superficial velocities, i.e. as if they were flowing alone in the channel.

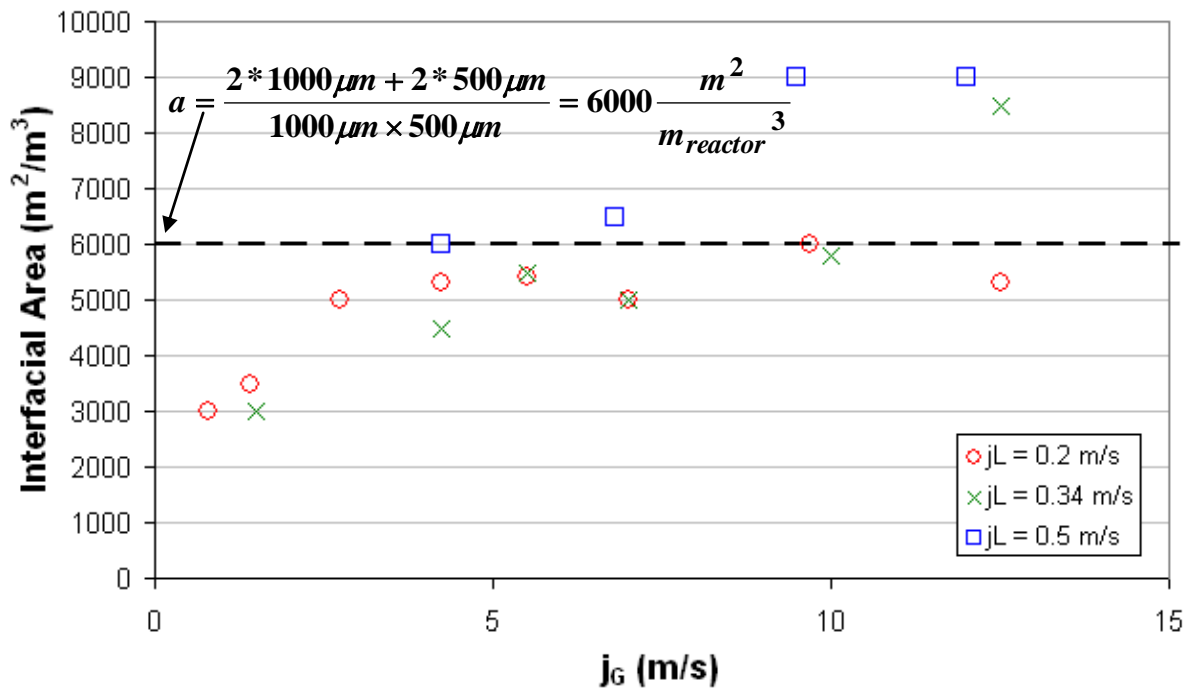


Figure 5: Values of interfacial area determined by Yue et al. [66] for gas/liquid flow in a 500 μm x 1000 μm rectangular microchannel

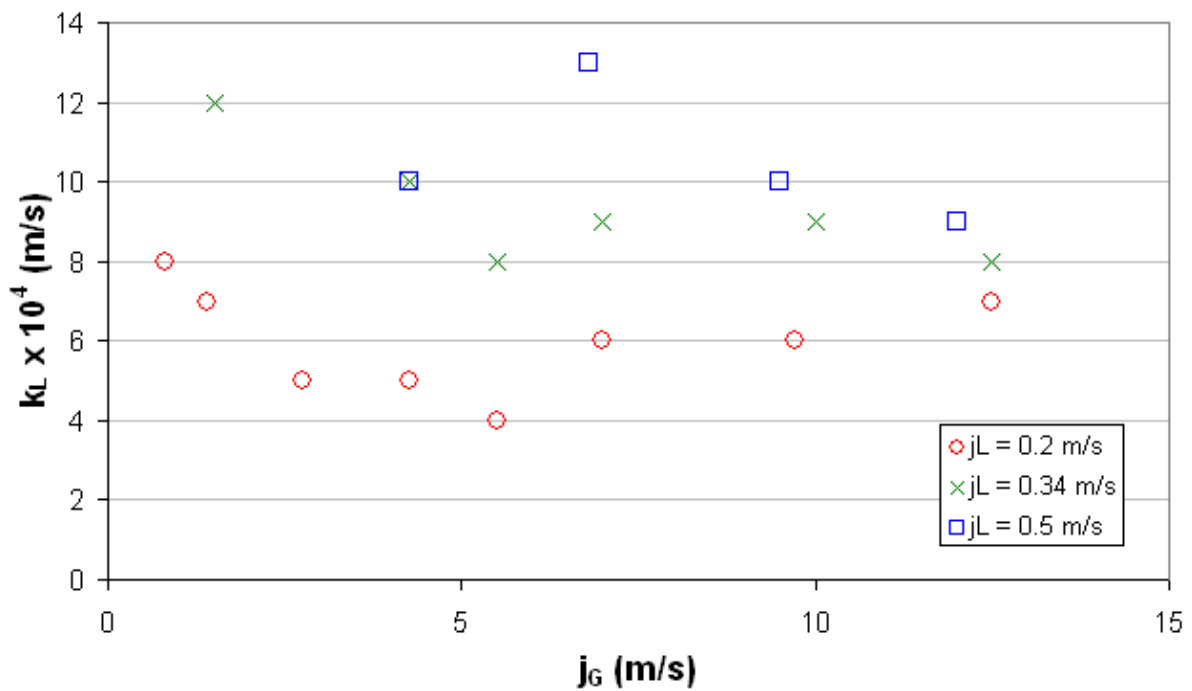


Figure 6: Liquid mass transport coefficient determined by Yue et al. [66] for gas/liquid flow in a 500 μm x 1000 μm rectangular microchannel

Su et al. (2010) [58] determined the interfacial area for gas/liquid flows in a horizontal 1 mm inner diameter (ID) stainless steel capillary using the absorption of CO₂ ($y_{\text{CO}_2} = 0.118$) into 1 M NaOH assuming negligible gas transport resistance and pseudo-1st-order reaction. They further derived values of k_{Ga} from measurements of the absorption of H₂S (1200 ppm) into an aqueous solution of methyldiethanolamine (40 wt%) assuming transport through the gas film to be the rate controlling step. Values of k_{G} from 0.007–0.02 m/s were obtained by dividing measurements for k_{Ga} at similar gas and liquid flow rates by the corresponding values of a determined using the absorption of CO₂ into NaOH. The derived values of k_{G} most strongly depending on the liquid flow rate with higher liquid flow rates corresponding to higher values of k_{G} . Derived values of a were also higher for higher liquid flow rates. Values of a initially increased with increasing gas flow rates before reaching relatively constant values at gas superficial velocities of 2–4 m/s, depending on the liquid flow rate. These gas superficial velocities correspond to approximately the transition from plug flow to slug flow (compare Figure 2) although no optical observations could be made of the flow. Although Su et al. noted the need to separate entrance and exit effects from the flow in the channel, they concluded that these effects were negligible. The separation of gas and liquid was assumed to be negligible due to the small interfacial area in the separator despite that the volume of the gas/liquid separator was two orders of magnitude larger than that of the investigated microchannel.

Roudet et al. (2011) [92] used the absorption of oxygen from air into water to examine horizontal, straight, and meandering channels with square 2 mm x 2 mm cross sections. Using multiple gas inlets along the channels, Roudet et al. were able to conduct measurements using different channel lengths. Roudet et al. observed that the reaction occurring during bubble formation caused the initial concentration of dissolved oxygen at a channel length of 0 to be greater than zero, and based their calculation on the slope, i.e. increase of dissolved oxygen along the channel length. Thus, Roudet et al. were able to directly exclude the effects of bubble formation and the gas/liquid separation at the exit from the measurements of flow in the channel. Assuming negligible mass transport resistance in the gas film, values of k_{La} could be derived from the absorption measurements. For plug flow Roudet et al. assumed the interfacial area to be the sum of the length of the bubble plus spherical caps on the ends, yielding interfacial areas between 100 and 1500 m²/m³ reactor. Higher gas flow rates, and to a lesser extent lower liquid flow rates, corresponded to higher interfacial areas. Dividing the values of k_{La} determined from the oxygen absorption by the interfacial areas determined from the bubble lengths and channel dimensions yielded k_{L} values of 1–4.5 x 10⁻⁴ m/s.

Sobieszuk et al. (2011) [68] investigated plug flow in a 400 μm ID glass microchannel. They used the absorption of CO₂ in nitrogen ($y_{\text{CO}_2,0} \approx 0.4$) into buffer solutions of 0.3 M K₂CO₃/0.3 M KHCO₃ using concentrations of NaOCl catalyst between 5.18 and 100 mol/m³ to adjust the rate of reaction. By adjusting the rate of reaction via the catalyst, Sobieszuk et al. were able to determine interfacial areas using a Danckwerts plot (see Section 5.4.2). The values of interfacial area determined from the absorption measurements were comparable to values of the interfacial area determined from photographs with a maximum variation of about ± 45%. Using the measurements at multiple concentrations, separate values of k_{L} for the bubble caps and the thin wall film could be derived. However, the values of k_{L} for the different zones were nearly the same. The values of k_{L} determined for the different zones varied between 2 and 6 x 10⁻⁴ m/s. Sobieszuk et al. also noted the need to account for entrance and exit effects individually. They performed measurements using the y-mixer and gas/liquid separator with and without microchannel to exclude exit effects.

Hou et al. (2011) [67] investigated gas/liquid flow in several variations of parallel nozzles or T-junctions. Due to the short length of the microchannels, their investigations provide insights into the effect of the gas/liquid mixers at the microchannel entrances. Values of $k_L a$ were derived from measurements of the absorption of CO_2 into aqueous solutions of 0.3 M Na_2CO_3 / 0.3 M NaHCO_3 . Hou et al. assumed that the slow reaction could be evaluated as physical absorption. Values of a were derived from measurements of the absorption of CO_2 into aqueous solutions of 1 M NaOH using a pseudo-1st-order reaction assumption. Values of a between 1400 and 12000 m^2/m^3 reactor were derived, and k_L values of $2\text{--}14 \times 10^{-4}$ m/s were calculated. Values of a and k_L increased both with increasing gas and liquid flow rates. The T-junction mixer was observed to generally produce higher values of a than the nozzles.

2.3.3 Conventional Gas/Liquid Reactors

Table 5 lists values of interfacial area, liquid volume fraction, and liquid mass transport coefficient measured for conventional gas/liquid reactors. The values are not a perfect estimation since the values often depend on a number of factors such as gas and liquid flow rates, temperature, pressure, dosing methods, agitation. The values are often not constant along the length of the reactor; e.g., coalescence can reduce the interfacial area along the length [97]. Material effects have also been observed in conventional reactors; e.g. the interfacial area of packed columns also depends on the wettability of the packing [98,99].

Comparing characteristics determined for microstructured falling film reactors (Table 2) and gas/liquid flow in microchannels (Table 4) with the characteristics of conventional gas/liquid reactors listed in Table 5, microchannels can be seen to offer some advantages over conventional gas/liquid reactors. Microchannels potentially offer up to an order of magnitude larger interfacial area than the best conventional reactor; interfacial areas in microchannels of up to 12 000 m^2/m^3 reactor have been reported. Larger interfacial areas allow for more gas to be absorbed in the liquid, which could increase the rate of reaction or efficiency of the reactor for reactions that are limited by mass transport in either the gas or liquid phase. The large surface to volume ratio of the microstructured reactors also allows for better temperature control and more efficient heat exchange.

Table 5: Characteristics of conventional gas/liquid contactors

Contactors	Comments/ Operation Mode	a (m²/m³)	ε_L (%)	k_L x 10⁴ (m/s)	References
Bubble Column	Countercurrent or cocurrent	50-500	60-99.9	0.5-5	Yoshida & Akita 1965 [100] Dillon & Harris 1966 [101] Mashelkar & Sharma 1970 [102] Akita & Yoshida 1973 [103] Akita & Yoshida 1974 [104] Shah et al. 1982 (review) [105] Chaumat et al. 2005 [106]
Packed Column	Countercurrent	30-600	40-85	0.3-3	Onda et al. 1959 [107] Yoshida & Miura 1963 [108] Richards et al. 1964 [109] Danckwerts & Gillham 1966 [110] Danckwerts & Sharma 1966 [111] De Waal & Beek 1967 [112] Carleton et al. 1967 [113] Mashelkar & Sharma 1970 [102] Chen & Vallabh 1970 [114] Danckwerts & Rizvi 1971 [115] Sahay & Sharma 1973 [98]
	Cocurrent	50-1400	20-99.9	0.8-8	Reiss 1967 [116] Voyer & Miller 1968 [117] Mashelkar & Sharma 1970 [102] Gianetto et al 1973 [118] Shende & Sharma 1974 [119] Snider & Perona 1974 [120] Sharma et al. 1969 [121]
Plate Column	Bubble cap Sieve plate	100-250 100-2040	20-45	0.1-50	Calderbank 1959 [122] Calderbank & Moo-Young 1960 [123]

						Barrett 1966 [124] Pohorecki 1968 [125] Sharma et al. 1969 [121]
Mechanically Agitated Tank		113-3179	60-99	0.4-10		Hatta 1928/1929 [126] Calderbank 1959 [122] Westerterp et al. 1963 [127] Danckwerts & Gillham 1966 [110] Mehta & Sharma 1971 [128] Robinson & Wilke 1974 [97] Joshi & Sharma 1977 [129] Hassan & Robinson 1977 [130] Farritor & Hughmark 1980 [131]

2.4 TWO FILM THEORY

In the characterization of both the microstructured gas/liquid reactors and the conventional devices, physical absorption of a gas or absorption of a gas accompanied by chemical reaction occurring in the liquid phase have been used to derive information about the characteristics of the gas/liquid reactor. The analysis of the gas absorption in the previous work as well as in this work is conducted according to a specific model, which describes the gas/liquid reactor as a combination of perfectly mixed gas and liquid phases and gas and liquid films, where mass transport occurs only through diffusion, on each side of the gas/liquid interface.

A gas/liquid system is depicted in Figure 7. In the “gas bulk” are numerous gas molecules (A) at a specific partial pressure. In the “liquid bulk” are numerous dissolved molecules (B), which can react with species A to form a product (C). Between the gas and liquid phases is an interface. Equilibrium is assumed at the interface, where the concentration of dissolved species A is a function of its partial pressure in the gas as described by Henry’s law. Species B cannot cross the interface and remains in the liquid phase. As species A dissolves in the liquid, its concentration in the gas region immediately next to the interface decreases, resulting in a concentration gradient of species A across the “gas film.” Similarly, the concentration of dissolved species A next to the interface is greater than that in the bulk of the liquid. This description of gas/liquid contacting is called the “two film theory” [132,133].

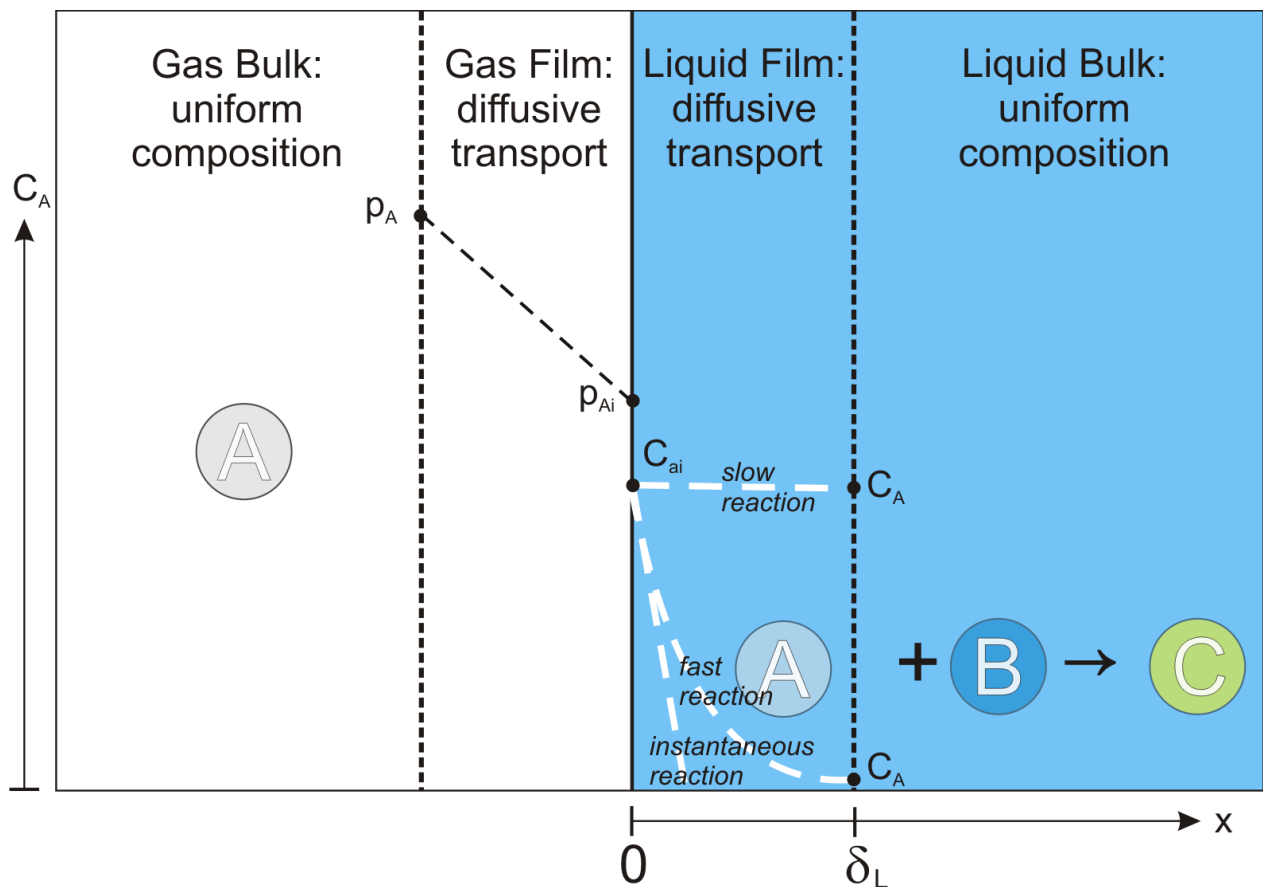


Figure 7: The film model describes a gas/liquid reaction as occurring between two uniform phases with mass transport through diffusion in stagnant films at the interface

2.4.1 Transport in the Gas Film

The rate of diffusion for a species A in the gas film can be described as molecular diffusion of an ideal gas according to Fick's law:

$$\phi = k_G \cdot a \cdot \left(\frac{p_{A,bulk} - p_{A,i}}{R_g \cdot T} \right) \quad [5]$$

where ϕ is the rate of transport in moles per second per unit of reactor volume; k_G in this case is the diffusion coefficient of the gas divided by the thickness of the gas film and is commonly called the gas transport coefficient; a is the interfacial area; $p_{A,bulk}$ is the partial pressure of A in the bulk and $p_{A,i}$ at the interface.

2.4.2 Henry's Law

Equilibrium is assumed at the phase interface. For ideal-dilute solutions, the amount of gas dissolved in the liquid is proportional to the partial pressure of the gas at the interface and can be approximated according to Henry's law [134]:

$$p_{A,i} = H_A \cdot C_{A,i} \quad [6]$$

where H_A is the Henry's constant with units of L·Pa/mol; $C_{A,i}$ is the concentration of species A at the interface.

2.4.3 Transport in the Liquid Film

The movement of a dissolved molecule of A without reaction through the stagnant "liquid film" can accordingly be considered to be accomplished purely through molecular motion and described according to Fick's law:

$$\phi = k_L \cdot a \cdot (C_{A,i} - C_{A,bulk}) \quad [7]$$

where k_L is the liquid transport coefficient; and $C_{A,bulk}$ is the concentration of species A in mol/L in the liquid bulk.

2.4.4 Reaction in the Liquid Bulk

If reaction occurs between species A and species B, the local reaction rate with respect to species A may be described:

$$-r_A = k_2 \cdot C_A \cdot C_B \quad [8]$$

where r_A is the rate of consumption of A due to reaction, and k_2 is the reaction rate constant. The reaction rate given in Equation 8 indicates a second order reaction. Other reaction orders may also occur, but for the purposes of this work, a second order reaction rate has been used (see Section 4.2.4).

2.4.5 Reaction in the Liquid Film

For rapid reaction, reaction occurs in the liquid film. When reaction occurs in the film, the rate gas uptake into the liquid film may be enhanced. An enhancement factor 'E' is inserted

into the equation describing transport through the liquid film to account for the effect of reaction.

$$\phi = k_L \cdot a \cdot E \cdot (C_{A,i} - C_{A,bulk}) \quad [9]$$

The enhancement factor of Equation 9 is the ratio between the rate of transport of species A through the liquid film under actual conditions (with reaction) and the rate of transport for pure physical absorption of species A (no reaction) given in Equation 7. The exact value of E lies between the limiting cases of no reaction ($E = 1$) and an infinitely fast reaction ($E = E_i$), assumed to proceed instantaneously and limited only by the rate of diffusion of the reactants. The value of E can be determined from E_i and the Hatta number, Ha.

An enhancement factor for an instantaneous reaction, E_i , can be derived by assuming that the reaction reaches completion at a plane within the liquid film. The concentration of both species is 0 at this plane, and the reaction rate is determined by the rates of diffusion for each species:

$$\phi = z \cdot a \cdot D_A \cdot \frac{(C_{A,i} - 0)}{\delta_r} = a \cdot D_B \cdot \frac{(C_{B,bulk} - 0)}{\delta_L - \delta_r} \quad [10]$$

where z is a stoichiometric factor (moles gas per mole liquid); D_A and D_B are the diffusion coefficients of the respective species; $C_{B,bulk}$ is the concentration of B in the liquid bulk; δ_L is the thickness of the liquid film; and δ_r is the distance from the gas/liquid interface to the reaction plane.

Solving for δ_r

$$\delta_r = \frac{\delta_L}{\left(1 + \frac{D_B \cdot C_{B,bulk}}{z \cdot D_A \cdot C_{A,i}}\right)} \quad [11]$$

therefore

$$\phi = z \cdot a \cdot \frac{D_A}{\delta_L} \cdot (C_{A,i} - 0) \cdot \left(1 + \frac{D_B \cdot C_{B,bulk}}{z \cdot D_A \cdot C_{A,i}}\right) \quad [12]$$

In the film model k_L is equal to D_A over δ_L . k_L is proportional to the square root of D_A in the Danckwerts and Higbie models, which is in line with experimental observations, but these models include additional empirical factors. The enhancement factor for an instantaneous reaction is thus defined:

$$\phi = z \cdot a \cdot k_L \cdot E_i \cdot (C_{A,i} - 0) \quad [13]$$

$$E_i = \left(1 + \frac{D_B \cdot C_{B,bulk}}{z \cdot D_A \cdot C_{A,i}}\right) \quad [14]$$

The Hatta number is defined as the ratio between the maximum conversion that can be achieved in the liquid film and the maximum amount of gas solute that can be transported through the liquid film via diffusion. For a second order reaction rate given in Equation 8, Ha is defined:

$$Ha^2 = \frac{k \cdot C_{A,i} \cdot C_{B,bulk} \cdot \delta_L}{\frac{D_A}{\delta_L} C_{A,i}} = \frac{k_2 \cdot C_{B,bulk} \cdot D_A}{\left(\frac{D_A}{\delta_L}\right)^2} = \frac{k_2 \cdot C_{B,bulk} \cdot D_A}{k_L^2} \quad [15]$$

Exact solutions for E are possible only for the limiting cases [135] of instantaneous reaction ($E \rightarrow E_i$) and pseudo-1st-order reaction ($E \rightarrow Ha / \tanh Ha$), but numerical solutions have been obtained for all cases [136]. The approximate numeric solution developed by van Krevelen and Hoftijzer [137] relates E to Ha and E_i :

$$E = \frac{\sqrt{Ha^2 \frac{E_i - E}{E_i - 1}}}{\tanh \sqrt{Ha^2 \frac{E_i - E}{E_i - 1}}} \quad [16]$$

The values of E calculated according to Equation 16 are shown in Figure 8 with respect to Ha.

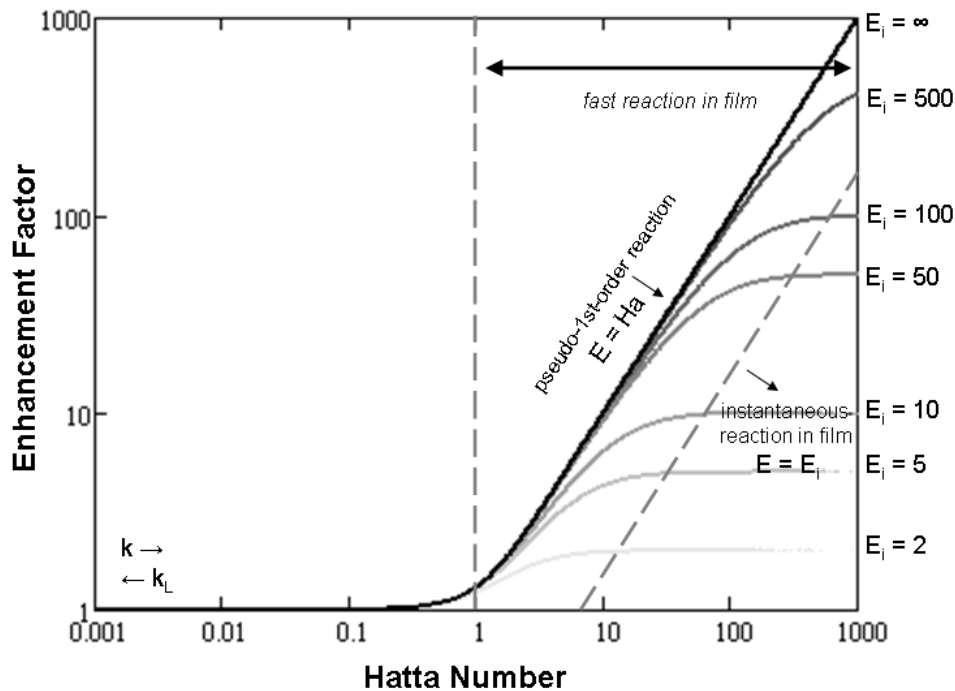


Figure 8: The enhancement factor as a function of Hatta number as predicted by van Krevelen and Hoftijzer [137]

Thus, in order to derive values of a or k_L from measurements of reaction, measurements must necessarily be undertaken under conditions at which reasonable assumptions can be made to estimate the value of E.

3 SCOPE

This work uses the absorption of carbon dioxide into aqueous solutions of sodium hydroxide to investigate the interfacial area and liquid mass transport coefficients in microstructured gas/liquid reactors. This reaction is presumed to fall in the pseudo-1st-order regime shown in Figure 8, where the limiting assumption can be made that the enhancement factor is equal to the Hatta number. This reaction has been used to investigate gas/liquid flow and reaction in both capillaries and in a microstructured falling film reactor. The reactors, reaction, and analytical methods employed are discussed in *Section 4: Methods*. The results and examination thereof are presented in *Section 5: Results and Discussion*.

Section 5.1: Material Properties Characterization investigates the effect of wettability on gas/liquid boundary conditions. The static contact angle was measured for different materials prepared by polishing, grinding, or milling, resulting in different surface roughnesses. The surfaces used in this work are practical surfaces; they are not perfectly smooth or dry but rather represent the conditions that might be found in actual microchannels. A quantitative value of the wettability provides basis for interpreting the effect of the material on gas/liquid flow and reaction.

In *Section 5.2: Dependence of Gas/Liquid Flow Regimes on Material Properties*, videos were collected of non-reacting gas/liquid flows in wettable glass or fused silica capillaries of 1.6 mm and 250 μm ID and in hydrophobic FEP capillaries of 1.5 mm and 250 μm ID. Flow maps, relating the flow pattern to the gas and liquid superficial velocities, were constructed so that the effect of the material on the observed flow pattern could be compared. The reaction of CO_2 with aqueous solutions of 2.0 M NaOH was carried out in 10 cm lengths of 250 μm ID capillaries of fused silica, PEEK, and FEP. The capillary materials differ according to wettability. If a pseudo-1st-order reaction is assumed, then the average interfacial areas can be determined from the measurements of chemical reaction. These experiments probe the influence of wettability on the hydrodynamics of gas/liquid flow and thus the reaction.

Section 5.3: Thermographic Investigation of a Microstructured Falling Film Reactor uses infrared photographs collected while performing the absorption of CO_2 with aqueous solutions of 2.0 M NaOH, an exothermic reaction, in a microstructured falling film reactor to derive local rates of reaction along the reactor length. At a low liquid flow rate, the reaction reaches completion well before the end of the reactor. At a higher flow rate where the conversion is less than complete, changes in the reaction rate along the length and their effect on the final results can be compared. Since measurements of reaction are necessarily completed at the end of the reactor, these investigations examine whether average values determined for entire reactors may be compared to local values occurring within the reactor.

In *Section 5.4: Measurements of Slug Flow in 1.6 mm glass capillaries* of different length, the absorption of CO_2 with aqueous solutions of different concentrations of NaOH is carried out for different lengths of capillaries. The selected reactor and reaction conditions demonstrate a low pressure drop along the reactor length and by using a high gas flow rate so that the gas flow rate does not change along the length, provide a flow pattern that remains the same along the reactor length even for capillaries as long as 40 cm. These investigations allow for a thorough analysis of the selected flow conditions. By varying the reactant concentration, values of both a and k_L can be determined, and the effect of various reaction parameters and constants can be examined. Two models based on two film theory are investigated for use in modeling the results. This section examines the variability and error associated with the

derivation of values of a and k_L from measurements of reaction and evaluates the use of the film model for modeling gas/liquid reactions in microstructured reactors.

This work does not fulfill the gaps of knowledge identified in the introduction. Lastly, a correlation to describe a and k_L for all possible materials and flow rates is needed to provide engineering handbooks with the design tools to accurately integrate microstructured gas/liquid reactors into existing processes. This dissertation hopefully contributes a small step towards a better understanding of how measurements supporting these correlations should be performed, explains why the effect of material wettability cannot be ignored, and provides a stronger basis for further work in providing this information.

4 METHODS

The experimental methods employed include techniques related to the characterization of material properties (Section 4.1), and the observation of gas/liquid flows with and without chemical reaction in different microstructured reactors (Sections 4.2.2 and 4.2.3).

To determine the influence of solid surface properties on gas/liquid flows, glass, stainless steel, polytetrafluoroethylene (PTFE), polyethyletherketone (PEEK), and polystyrene samples were structured by grinding, polishing, and machining (Section 4.1). The surface roughness of the samples was investigated with atomic force microscopy (AFM) (Section 4.1.1). Scanning electron microscope (SEM) images of the samples were collected (Section 4.1.2). The contact angle was measured on the prepared samples for various solid/liquid/gas systems (Section 4.1.3). The surface tension of the liquids used for the contact angle measurements was measured using the pendant drop method (Section 4.1.4).

Gas/liquid flow and reaction were studied in various experiments (Section 4.2). The test apparatus constructed for these experiments provided means of controlling gas and liquid flow rates and temperature as well as, depending on the particular experiment, a high-speed video camera or infrared camera for observation (Section 4.2.1). Gas/liquid flows were examined in single capillaries (Section 4.2.2) and in a falling film reactor with microstructured plate (Section 4.2.3). The reaction of CO₂ with aqueous solutions of NaOH (Section 4.2.4) was used in this work as a model system for which the reaction rate constant and physical properties of the system can be found in literature.

4.1 MATERIAL PROPERTIES CHARACTERIZATION

The effect of solid surface characteristics on the contact angle was investigated for the following materials:

- glass (Menzel-Gläser microscope slides; Germany)

Metals:

- 8620 alloy steel (nickel-chromium-molybdenum alloy; ASTM A322 ASTM A304 steel; Magellan; China)
- aluminum (Alloy 6081; Alaskan Copper & Brass Company; USA)
- bronze (660 bearing bronze; K. P. Bronze; Canada)
- cast iron (G2 gray iron; Dura-bar Metal Services; Illinois, USA)
- stainless steel (T-304/304-L; Viraj Impoexpo; India)

Plastics:

- nylon (Nylatron GS rod; Quadrant EPP USA, Inc.; Pennsylvania, USA)
- PEEK (polyether ether ketone; Ensinger Tecapeek; Germany)
- PMMA (acrylic/poly(methyl methacrylate); Alro Plastics; USA)
- polystyrene (Goodfellow ST313200; Germany)
- PTFE (polytetrafluoroethylene; Interstate Plastics; California, USA)
- UHMW PE (ultra high molecular weight polyethylene; Tivar; Quadrant EPP USA, Inc.; Pennsylvania, USA)

Samples from each of the various materials were prepared by polishing, milling, and grinding. Ground samples were prepared by grinding samples with 320 grit silicon carbide paper at 120 revolutions per minute on an ATM Saphir 550. Polished samples were consecutively ground

with 320, 600, and 1200 grit grinding papers and then polished with a 3 micrometer silicon carbide polishing disc at 100 revolutions per minute. The machined samples were milled (EMCO FB-3, dry, without cooling) with a high speed steel (HSS) shell end mill (35 mm diameter, 160/min, 150 mm/min). The PEEK machined samples were milled at a slightly higher speed (245/min).

4.1.1 Atomic Force Microscopy

Atomic Force Microscopy (AFM) measurements of the surfaces of the samples prepared for contact angle measurements were performed with a Veeco AFM. A cantilever (Nanosensors Pointprobe Plus PPP-LFMR; Budget Sensors AIO) was used to scan the surface in contact mode or tapping mode. The collected data was analyzed with Veeco NanoScope Analysis 1.10. PEEK and PTFE surfaces were sputtered with a 10 nanometer thick layer of platinum to prevent the surface from collecting a static charge that would interfere with the measurement.

The roughness is reported in several forms: the root mean square roughness (R_q) (Equation 17); the average roughness (R_a) (Equation 18); the maximum height variation between the lowest point and the highest point (R_{max}); the surface area difference, which is the ratio of the surface area of the three-dimensional surface divided by the two-dimensional measurement area.

$$R_q = \sqrt{\frac{\sum h_i^2}{N}} \quad [17]$$

$$R_a = \frac{1}{N} \sum_{i=1}^N |h_i| \quad [18]$$

In the definitions of R_q and R_a in Equation 17 and Equation 18, h_i denotes the measured height of a given point (i), and N is the total number of measured points on the surface.

4.1.2 Scanning Electron Microscopy

Secondary electron (SE) images were collected of the capillaries and from several contact angle surface samples using a Scanning Electron Microscope (SEM) (Jeol JSM-6300). Nonconductive surfaces were sputtered with 10 nanometer thick layers of platinum prior to measurement.

4.1.3 Contact Angle Measurement

The contact angle measurement apparatus [138,139] is shown in Figure 9. It measures contact angles on a flat surface using the sessile drop method [140].

The apparatus consisted of an optical cell (SITEC AG, Maur/Zürich, 740.2086) with sapphire windows for observation of the droplet, gas introduction with pressure regulation (Rotarex/SMT, Genlis, France, SL225-16), and liquid dosing through means of a hand-operated pump (SITEC AG, Maur/Zürich, 750.1400). An Imaging Source C3516-M(KP) (35mm focal length) lens with 5 mm and 10 mm extension rings was used with a SONY AVC-D5CE CCD camera. A light (HLV-24SW-NR-3W, CCS Inc., Japan) was passed through a series of lenses to create a parallel beam.

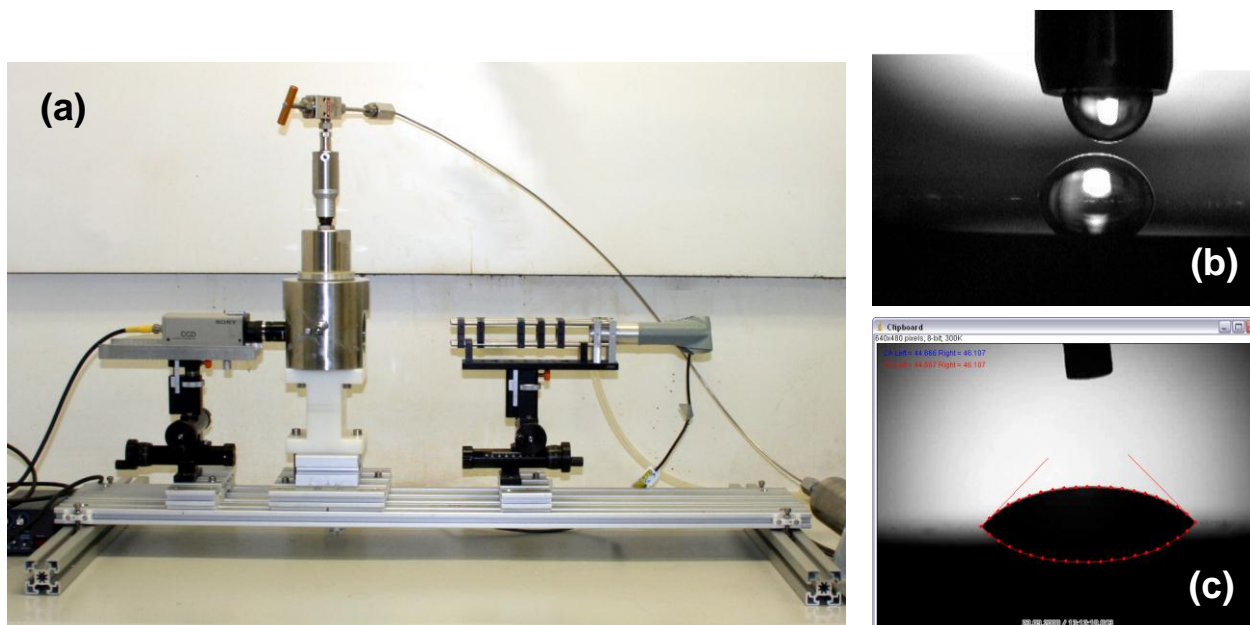


Figure 9: Contact angle measurement apparatus (a); syringe and drop (b); software identified drop contours and contact angle (c)

All solid samples were cleaned with water and isopropanol and air dried before being placed in the optical cell. Prior to measurement the accuracy of the setup was checked with a standard (Appendix 8.2). The chamber was filled with gas and brought to the desired pressure. Video images were collected of the initial transfer of the drops from the syringe to the surface and lying on the surface. On a clean surface, the drop quickly reaches a stable shape. On unclean surfaces, the drop spreads out over time [141]. Video frames collected from the apparatus were analyzed with the DropSnake plugin for Image J [142-144] and with SCA20 from Dataphysics.

4.1.4 Surface Tension Measurement

Surface tension was measured using the pendant drop method [140] with the same apparatus as the contact angle measurements. Drops large enough to be deformed by gravity were freely suspended from the syringe tip. The liquid surface tension was calculated from axisymmetric drop analysis using SCA20 from Dataphysics.

4.2 INVESTIGATION OF GAS/LIQUID FLOW AND REACTION

Gas/liquid flow patterns were observed in transparent glass and fluorinated ethylene propylene (FEP) capillaries for capillaries of 250 μm and 1.5 mm inner diameter (ID). The reaction of CO_2 with aqueous solutions of NaOH was performed in 10 cm lengths of 250 μm capillaries of fused silica, PEEK, and FEP and in differing lengths of 1.5 mm ID glass capillary. Temperature profiles along the channels of a falling film microreactor were collected with an infrared camera for the absorption of CO_2 into aqueous NaOH.

4.2.1 Test Apparatus for the Investigation of Gas/Liquid Flow and Reaction

A schematic of the experimental setup is shown in Figure 10. The apparatus for the investigation of gas/liquid flow and reaction consisted of a gas flow system shown in blue, a liquid flow system shown in red, a temperature control system shown in green, and additional components such as a camera and analytical equipment. The separation of gas and liquid at the exit of the reactor was accomplished by allowing the gas to dissipate in the atmosphere and collecting the remaining liquid.

The gas flow system could deliver argon, nitrogen, and carbon dioxide gases at flow rates between 2 mL/min and 20 L/min. All volumetric gas flow rates are given at SATP (standard ambient temperature and pressure; 25°C, 1 bar). The flows of gases from compressed gas cylinders (Air Liquide Argon N50, 99.999%; Air Liquide Nitrogen N50, 99.999%; Basi Carbon Dioxide, 99.995%) were controlled by mass flow controllers. The details of the gas mass flow controllers are listed in Table 6. In the optical observations of the gas/liquid flow patterns, several points requiring gas flow rates of less than 2 mL/min were measured by feeding air from a syringe pump (Harvard PHD Ultra) equipped with 1 to 4 100 mL syringes (BD Plastipak). In one experiment, the gas was prehumidified by first bubbling the gas stream through a gas washing bottle containing water at a temperature of 60 to 80°C and then passing the gas through a condenser at 15°C.

Liquids were delivered through a pulsation-free, pressure-driven system across liquid mass flow controllers. The details of the liquid mass flow controllers are listed in Table 7. For liquid flow rates less than 0.25 mL/min, a syringe pump (Harvard PHD Ultra) equipped with 1 to 4 100 mL syringes (BD Plastipak) was used.

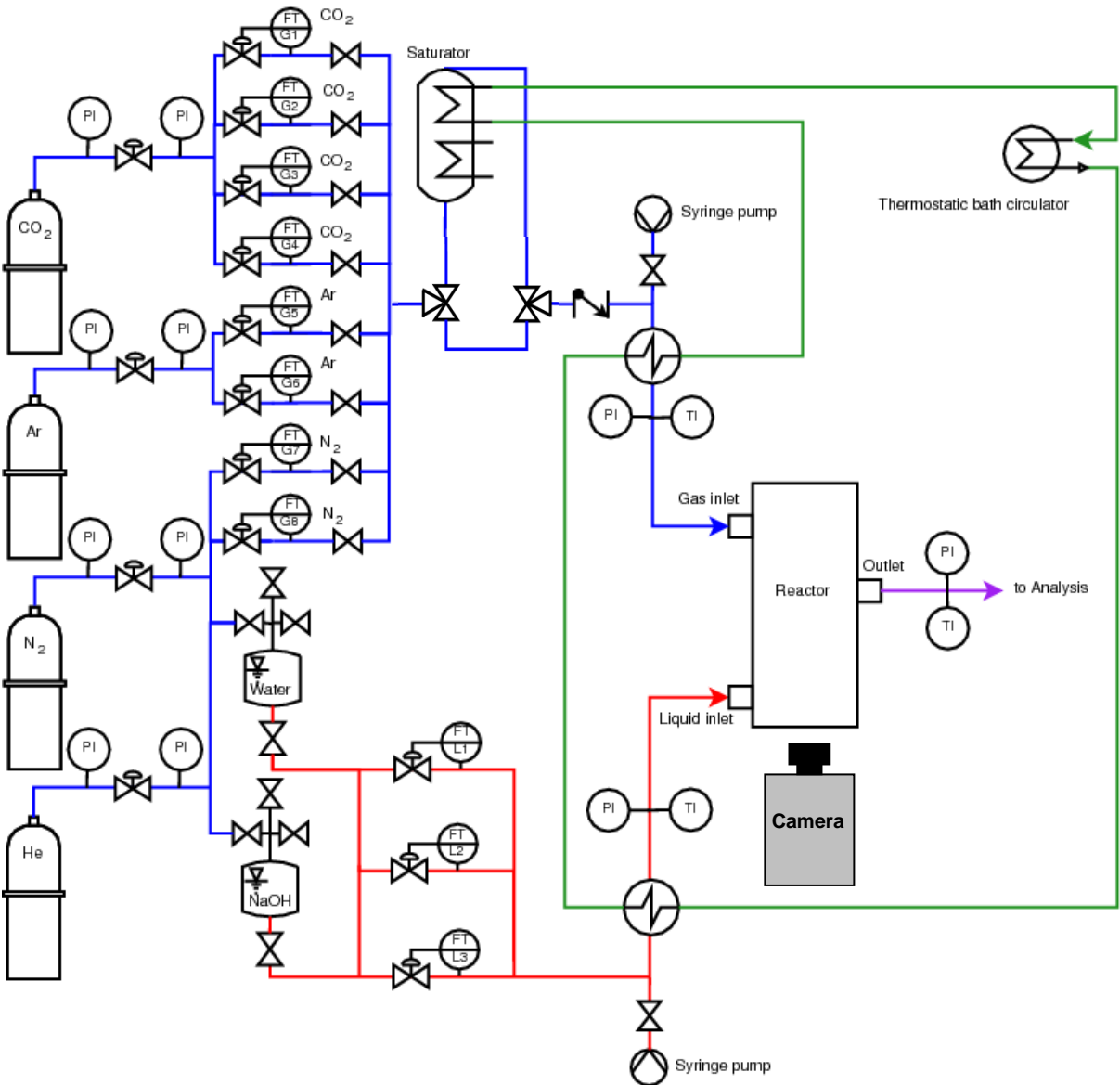


Figure 10: Schematic of the experimental setup

Table 6: Gas mass flow controllers

G1	Brooks 5850/BC1HA1EC2BA1B1 Serial T11971/002 Argon 0–50 mL/min	G5	Brooks 5850/BC1HC1EC2BA1B1 Serial T77997/004 Carbon Dioxide 0–200 mL/min
G2	Brooks 5850/BC1HC1EC2BA1B1 Serial T77997/003 Nitrogen 0–200 mL/min	G6	Brooks 5850/BC1HA1EC2BA1B1 Serial T117500/001 Argon 0–10 mL/min
G3	Brooks 5850/BC1HC1EC2BA1B1 Serial T77997/004 Nitrogen 0–2 L/min	G7	Brooks 5850 Serial T98521/006 Carbon Dioxide 0–20 mL/min
G4	Brooks 5850/BC1HC1EC2BA1B1 Serial T77997/002 Carbon Dioxide 0–2 L/min	G8	Brooks 5850 Serial T98296/001 Carbon Dioxide 0–20 L/min

Table 7: Liquid mass flow controllers

L1	Brooks Flomega 5882/D1A1A4A001 T97825/001 Water 0–1 kg/hr
L2	Brooks Flomega 5882/D1A1A4A001 T97825/002 Water 0–1 kg/hr
L3	Brooks Flomega 5882/D1A1A4A001 T97825/003 Water 4–200 gm/hr

The pressure of the gas and liquid feeds were measured with pressure transducers (WIKA S-10, 0–10 bar), and the system outlet pressure was assumed to be atmospheric when the reactor outlet was directly exposed to the atmosphere. The temperatures of the gas and liquid feed streams as well as the liquid sample at the outlet were measured with type-K thermocouples.

For visualization of the flow, image sequences were collected with a VDS Vosskühler HCC-1000 camera at a rate of 1825 frames per second. For the thermographic investigations, infrared images were collected with a VarioCAM HR HEAD camera (InfraTec) at a resolution of 19 pixels per cm of reactor and analyzed with IRBIS3 software.

The reactor in Figure 10 represents either a commercially-available T-junction and an attached capillary (Section 4.2.2) or a microstructured falling film reactor constructed at the IMVT (Section 4.2.3).

4.2.2 Commercial Capillary Reactors

For experiments with capillaries, commercially available capillaries were connected to standard T-junctions.

For the experiments exploring the effect of the material properties on the flow patterns and reaction, round capillaries of 250 μm inner diameter and 10 cm length were connected to 1/16 inch Swagelok T-junctions. The gas and liquid feeds were thus initially contacted in a stainless steel Swagelok T-junction prior to entering the capillary. Specifications of the 250

μm ID capillaries are given in Table 8. Capillaries were attached using Swagelok 1/16 inch ferrules and nuts, except for the glass capillary, which was attached with a graphite ferrule (Agilent 5080-8853).

Gas/liquid flow patterns were also imaged in 1.6 mm inner diameter glass and 1.5 mm ID FEP capillaries, which were attached to 3 mm Swagelok T-junctions using 3 mm Swagelok nuts and ferrules. The specifications of these capillaries are also given in Table 8.

Table 8: Specifications of investigated capillaries

Material	ID	OD	Manufacturer	Part Number
<i>PEEK</i>	250 μm	1/16 inch	Agilent	0890-1762
<i>Fused Silica</i>	250 μm		Agilent	160-2250-5
<i>PTFE</i>	250 μm	1/16 inch	VICI	JR-T-4011-M3
<i>FEP</i>	250 μm	1/16 inch	VICI	JR-T-6812-M3
<i>Stainless Steel</i>	250 μm	1/16 inch	Agilent	5065-9930
<i>Glass</i>	1.6 mm	3 mm	VWR	201-1003
<i>FEP</i>	1.5 mm	1/8 inch	Agilent	5062-2483

Measurements of the absorption of carbon dioxide into sodium hydroxide for different lengths of capillary were made in 2, 5, 10, 15, 20, 30, and either 38.4 or 46.2 cm lengths of 1.6 mm ID glass capillaries. Pure CO_2 was dosed at 1.2 L/min. The liquid solutions were stored in tank pressurized by helium at 4 bar, and a flow rate of 12.06 mL/min was controlled with a mass flow controller. The gas and liquid feed tubes were jacketed, and a thermostatic bath with circulating water was used to control the gas and liquid feed temperatures. The pressures on the gas and liquid feed sides were measured with pressure transducers. The temperatures of the gas and liquid feeds and of the liquid sample were measured with thermocouples. A beaker was placed below the end of the capillary to collect the liquid sample.

4.2.3 Microstructured Falling Film Reactor

The microstructured falling film reactor used in these studies was developed at the IMVT. Photographs of the reactor and microstructured plate are shown in Figure 11 and Figure 12. The reactor was constructed modularly with a removable heat exchange module and interchangeable liquid plates.

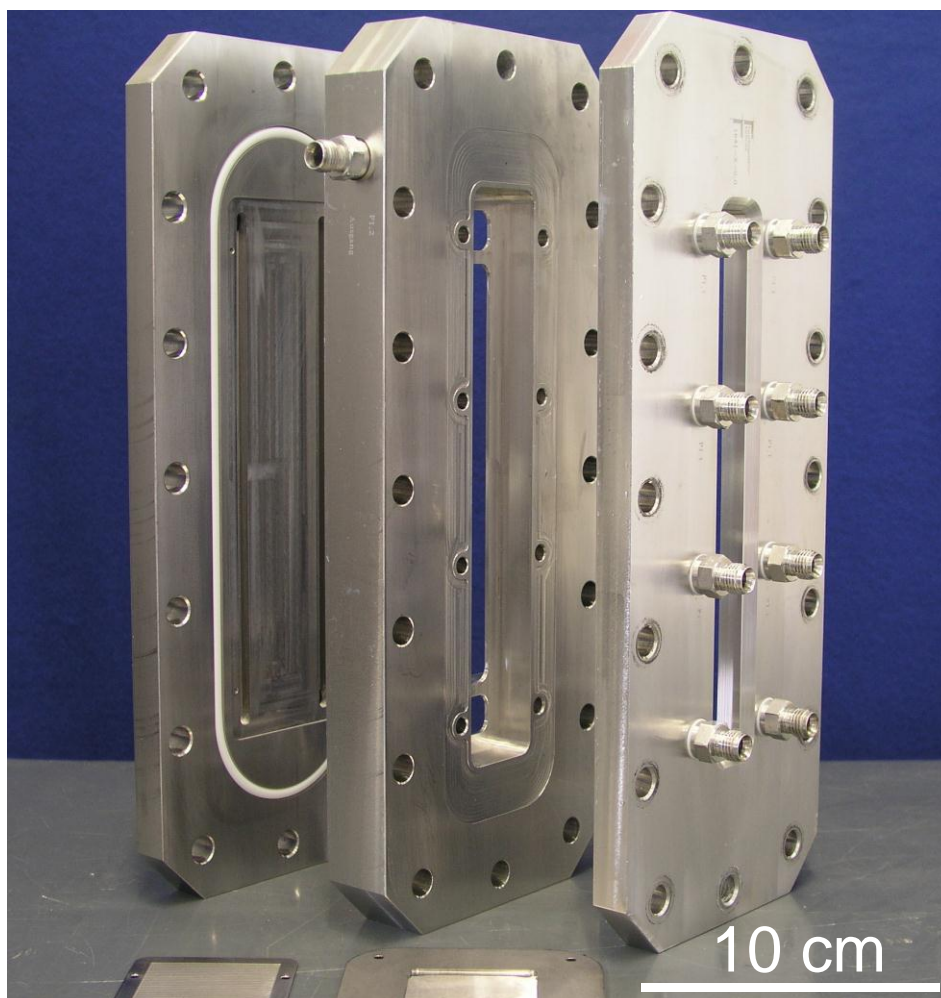


Figure 11: Disassembled falling film microreactor: heat exchange module (left); reaction module (middle), cover (right)

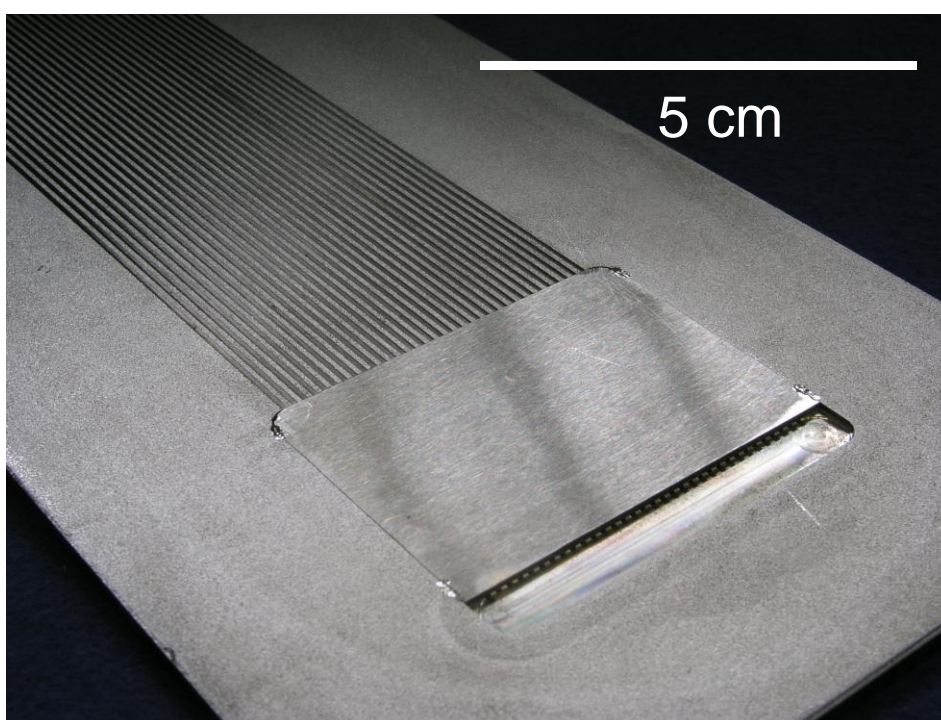


Figure 12: Microstructured falling film foil

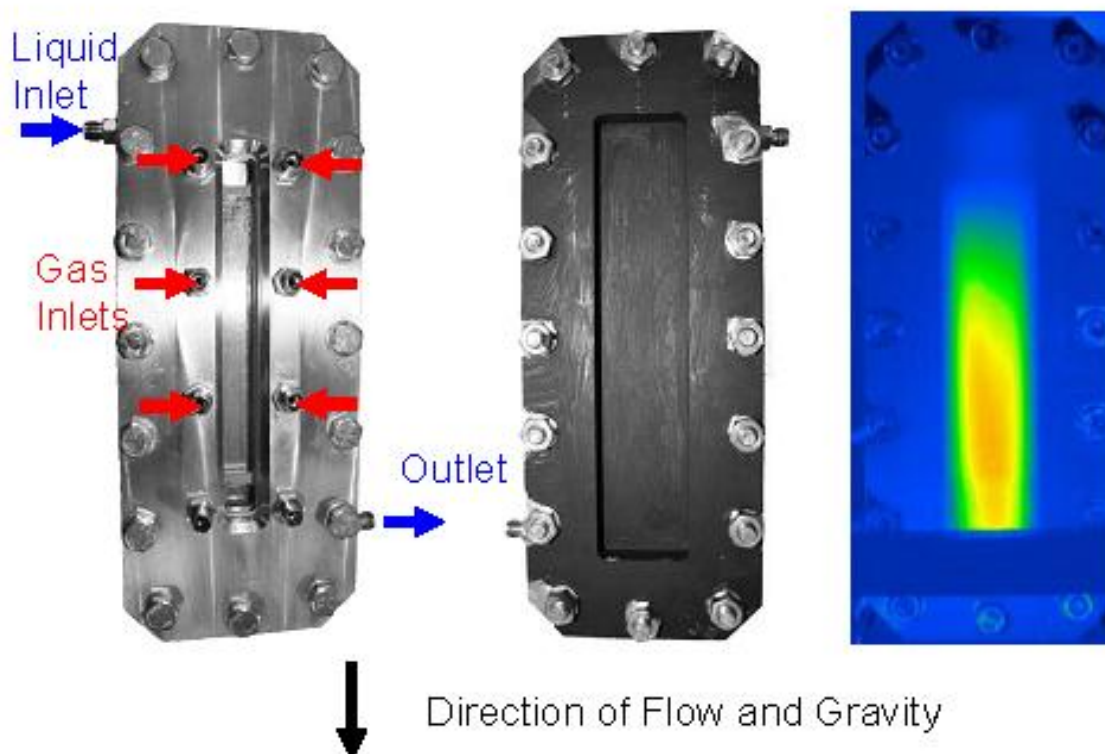


Figure 13: Assembled falling film microreactor for thermographic investigations and thermographic image during operation

At the heart of the reactor was the liquid plate with a length exposed to the gas chamber of 197.5 mm. The 2 mm-thick, stainless steel plate was structured with 33 machined channels each 0.6 mm wide, 1 mm deep, and spaced 0.6 mm apart. A picture of the microstructured plate is shown in Figure 12. The liquid entrance consisted of closed microchannels, which forced the liquid into the microchannels and provided a good distribution of the liquid. The channels were separated by 10 mm from the glass window by the gas chamber.

The front of the reactor contained six ports for the gas feeds. The first pair of gas entries was located above the point at which the microchannels are open to the gas chamber. The other entries would allow for staging of the gas feed but were not used in this work. The area of the gas cross section was 622 mm².

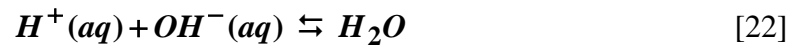
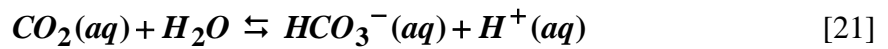
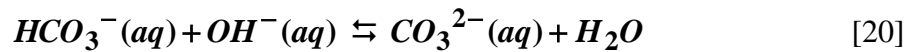
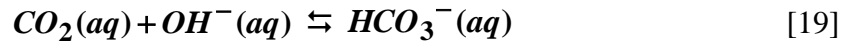
It is possible to place a heat exchange module in direct contact with the reverse side of the microstructured foil; however, for the thermographic investigations, the heat exchange module was removed and thermographic measurements were collected directly on the reverse side of the microstructured foil. The foil was painted black in order to provide a homogeneous heat emitting surface. The two phase flow exited through a single outlet port located at the bottom right side of the reactor. The assembled reactor and an image of the reactor taken during operation with the infrared camera are shown in Figure 13.

The gas was fed symmetrically through the top two gas entries and the gas/liquid flow exited together through the bottom exit. A 1 L/min flow of carbon dioxide gas and 2.0 M NaOH were used.

4.2.4 Reaction of Carbon Dioxide with Aqueous Sodium Hydroxide

The absorption of gaseous carbon dioxide into aqueous solutions of sodium hydroxide (NaOH) was used as a standard reaction for examining reactor characteristics. This reaction can be considered to be very fast, second order reaction with values for the kinetic rate constant available in the scientific literature [145].

The reaction of carbon dioxide with sodium hydroxide can be described by Equations 19 to 22 [146]:



The extent of each equilibrium reaction and thus the type of carbonate species is dependent upon the pH [147]. For high pH values ($pH > 7$), only Equations 19 and 20 occur to any significant extent.

For pH exceeding 10.5, nearly all of the dissolved CO_2 exists in solution as CO_3^{2-} . Thus, two moles of NaOH react for each mole of CO_2 , and the stoichiometric coefficient is 2 ($z = 2$). The overall reaction stoichiometry for $pH > 10.5$ be simplified to Equation 23.



For pH less than 10, nearly all of the dissolved CO_2 reacts to HCO_3^- . The overall reaction stoichiometry can be simplified to Equation 24, and the stoichiometric coefficient is 1 ($z = 1$).



For the relevant pH values examined in this work (i.e. basic solutions of NaOH), Reaction 20 is the rate determining step, and the kinetic rate expression for the reaction has been determined by Pohorecki and Moniuk [145] as a function of temperature (T) and ionic strength (I). The second order reaction rate constant for the reaction is k_{OH^-} , and $k_{OH^-}^\infty$ is the reaction rate constant determined at infinite dilution.

$$\log \left(\frac{k_{OH^-}}{k_{OH^-}^\infty} \right) = 0.221 \frac{I}{L} - 0.016 \frac{I^2}{L} \quad [25]$$

$$k_{OH^-}^\infty = 10^{11.895 - \frac{2382K}{T}} \frac{m^3}{kmol \cdot s} \quad [26]$$

The reaction rate between carbon dioxide and aqueous NaOH can thus be expressed as a second order reaction:

$$-r_{CO_2} = k_{OH^-} \cdot C_{CO_2} \cdot C_{OH^-} \quad [27]$$

where r_{CO_2} is the rate at which CO_2 is consumed by the reaction, C_{CO_2} and C_{OH^-} are local concentrations of the dissolved species, and k_{OH^-} is the reaction rate constant given in Equation 25.

The extent of reaction for the absorption of CO_2 into aqueous solutions of NaOH was determined from liquid samples collected at the reactor exit. The conversion of NaOH (X_{OH^-}) was defined as the fraction of OH^- consumed in the reaction, i.e. the normalized difference between the inlet and outlet concentrations of OH^- :

$$X_{OH^-} = \frac{C_{OH^-,0} - C_{OH^-}}{C_{OH^-,0}} \quad [28]$$

X_{OH^-} was determined from probe-based measurements of pH (Inlab Expert Pro; Mettler Toledo SevenMulti) and electrical conductivity (Inlab 730; Mettler Toledo SevenMulti). The relationship between the conversion of NaOH and electrical conductivity and pH are shown in Figure 14 and Figure 15, respectively, for calibration mixtures created by dissolving in deionized water solid NaOH and Na_2CO_3 for concentrations of 2M and higher and combinations of NaOH and $NaHCO_3$ for concentrations of 1M and less.

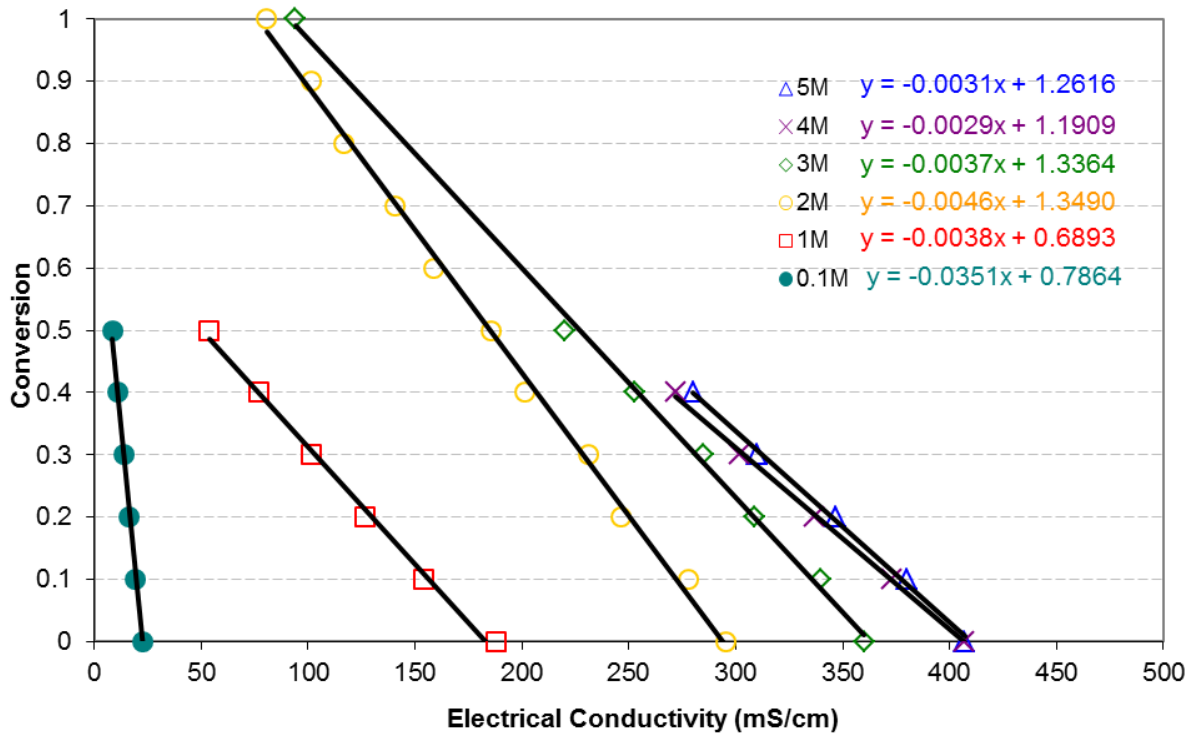


Figure 14: Relationship between electrical conductivity and conversion of NaOH for the reaction of CO_2 with aqueous solutions of NaOH for concentrations between 0.1 M and 5 M

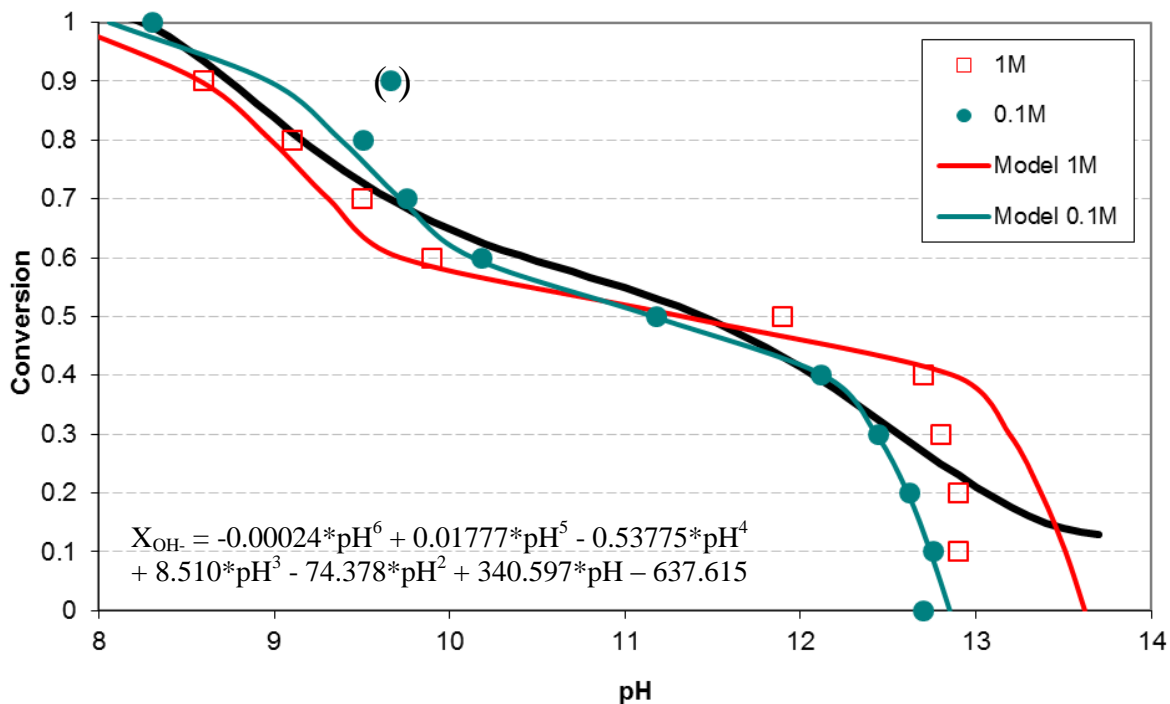


Figure 15: Relationship between pH and conversion of NaOH for the reaction of CO₂ with aqueous NaOH for concentrations of 0.1 M and 1 M

Values of pH predicted by Chembuddy BATE pH calculator using calculations including the effect of ionic strength on pH are shown in Figure 15 along with measurements of the prepared mixtures of NaOH and NaHCO₃ and the fitted function that was used to correlate pH and conversion. Deviations of the 1M measurements from the model predictions at high pH are likely due to miscalibration of the pH meter, which is challenging to calibrate at very high pH values. However, the agreement between the fitted function and the measured and expected values in the region of interest (conversion > 0.5) is acceptable even if measurements at higher pH are not perfectly calibrated.

Electrical conductivity measurements were used for concentrations of 2 M to 5M NaOH. For experiments with 0.1 M to 1 M NaOH, both measurements were collected; electrical conductivity measurements were used for conversions of up to 0.5, and pH measurements were used for conversions between 0.5 and 1. The probe based methods for determining conversion were compared to titration as well as alternative methods including acidic evolution and density measurements. Further details regarding the analytical methods and a comparison of their accuracy can be found in Appendix 8.1.

5 RESULTS AND DISCUSSION

The results of the experimental investigations are presented and analyzed in this chapter.

Section 5.1: Investigations of Material Properties investigates material properties, i.e. surface roughness and wettability. Material wettability is quantified in a parameter called the contact angle, the angle which forms at a gas/liquid/solid boundary. The contact angle is an important boundary condition for gas/liquid flows. The contact angle depends on a large number of variables. The variables of pressure, drop size, surface tension, gas composition, surface roughness, solid material, and reaction have been investigated.

Section 5.2: Dependence of Gas/Liquid Flow Regimes on Material Properties examines gas/liquid flow patterns and reactions in capillaries of FEP, PEEK, and fused silica. The contact angle at the gas/liquid/solid boundary differs drastically among these materials as discussed in Section 5.1. The impact of the differing boundary conditions occurring as a result of the wettability of each material impacts the flow and rate of gas absorption. Estimations of the Hatta number indicate a pseudo-1st-order reaction, which allows for a calculation of the average interfacial area based on film theory. Better wettability corresponds to higher interfacial areas, which reflects the visual observations of the flow pattern.

Section 5.3: Thermographic Investigation of a Microstructured Falling Film Reactor uses thermographic measurements of temperature rise along the length of a microstructured falling film reactor to determine the local rate of reaction. Since the interfacial area of a falling film reactor can be estimated, values of the liquid mass transport coefficient could be derived along the reactor length using film theory. The values of the Hatta number, enhancement factor, and liquid mass transport coefficient along the reactor length were compared to integral values calculated for the reactor as a whole (as is done with the capillaries in Section 4.2). The average values of the interfacial area and the liquid mass transport coefficient determined for the complete reactor are comparable to those determined along the reactor length unless the reaction proceeds to completion before the end of the reactor.

Section 5.4: Measurements of Slug Flow in 1.6 mm glass capillaries of different lengths uses measurements for a system where the hydrodynamics of the gas/liquid flow are constant along the length of the reactor to examine if the values of the interfacial area and liquid mass transport coefficient are also constant along the length. The characterization of the interfacial area and liquid mass transport coefficient according to film theory is scrutinized to estimate the error for the derived values of the interfacial area and liquid mass transport coefficient depending on constants and methods used to derive them. A discretized model based on the film theory is compared to the experimental measurements. The assumptions of the model and the film theory itself are rigorously evaluated for their applicability to the gas/liquid flow pattern examined.

5.1 INVESTIGATIONS OF MATERIAL PROPERTIES

The surface roughness was examined in SEM photos and AFM profiles of surfaces structured through different machining processes. This section examines the effect of different machining processes—milling, polishing, and grinding—on the surface roughness of different types of metal and plastic. The same machining process can produce a wide range of surface roughnesses depending on the material being machined. The surface roughness was further investigated as a variable influencing the contact angle at a gas/liquid solid boundary. The variables of pressure, drop size, surface tension, gas composition, solid material, and reaction were also investigated. The result is a correlation that can predict the contact angle $\pm 50\%$ using only the surface tension, surface roughness, and drop size. Excerpts of Section 5.1 have been published in [148].

5.1.1 Effect of Milling, Polishing, and Grinding on the Surface Roughness of Various Materials

SEM photos of stainless steel and PTFE samples are shown in Figure 16 through Figure 20. Despite the materials being prepared in the same manner, it can be seen that the resulting surfaces may differ. The polished stainless steel sample appears to be flatter than the polished PTFE surface. The machined grooves on the PTFE surface appear wider than those of the milled stainless steel sample. Such pictures provide an impression of the nature of the surfaces studied.

To obtain values for the roughness of the surface, a profile or surface contour map is needed. AFM measurements of surfaces were collected as described in Section 4.1.1. AFM images were flattened to adjust for tilt in the sample. The result of the AFM height sensor and profiles of slices of the contour map are shown for stainless steel and PTFE surfaces in Figure 16 through Figure 20. The roughness values determined for selected surfaces are presented in Table 9. Results of measurements for all surfaces investigated are found in Appendix 8.3.

The AFM scans covered as large of a scan area as possible, typically slightly less than $100\ \mu\text{m} \times 100\ \mu\text{m}$. The SEM photos already reveal that the materials seem to respond differently to the same preparation processes. The polished PTFE surface contains grooves over the entire surface, while the polished stainless steel surface appears nearly perfectly flat except for several scratches; also, the textures of the ground surfaces appear to differ. These differences can be further examined in Figure 21, which shows three-dimensional renderings of the surfaces from the AFM data.

In general the stainless steel samples are much smoother than the corresponding PTFE surfaces. Additionally, the general nature of the surface also differs. The machined stainless steel surface contains a number of parallel grooves, but the machined PTFE sample appears more amorphous. Harder materials are capable of being polished to higher degree than soft materials.

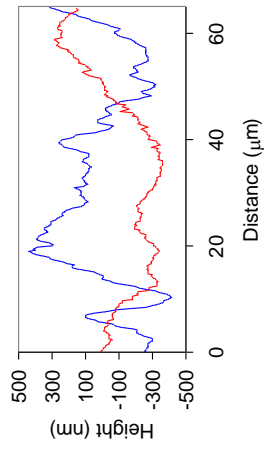
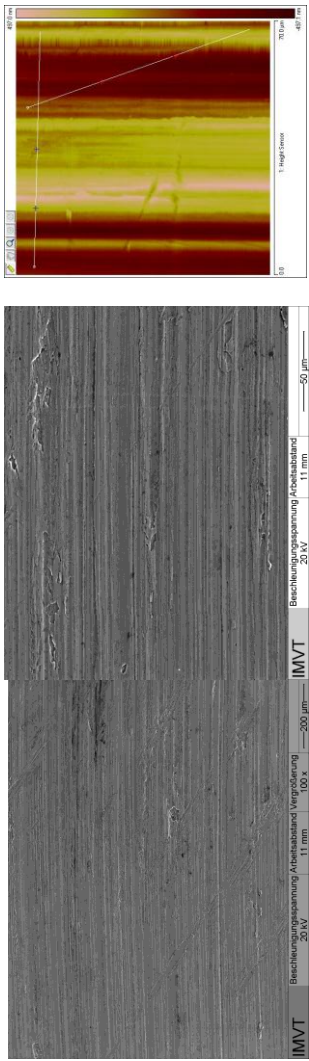


Figure 16: SEM and AFM measurements of milled stainless steel surface

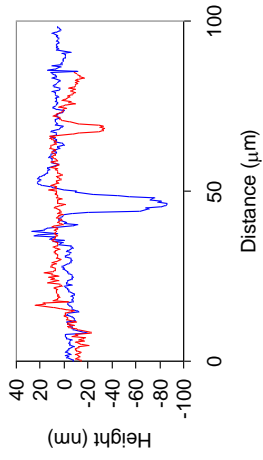
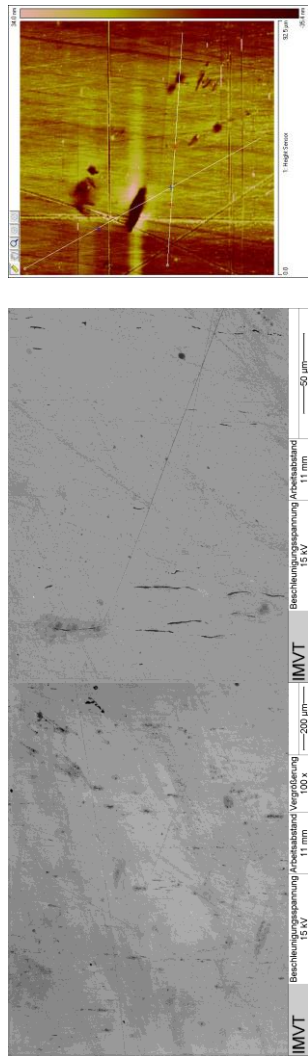


Figure 17: SEM and AFM measurements of polished stainless steel surface

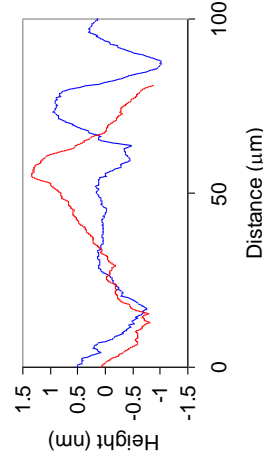
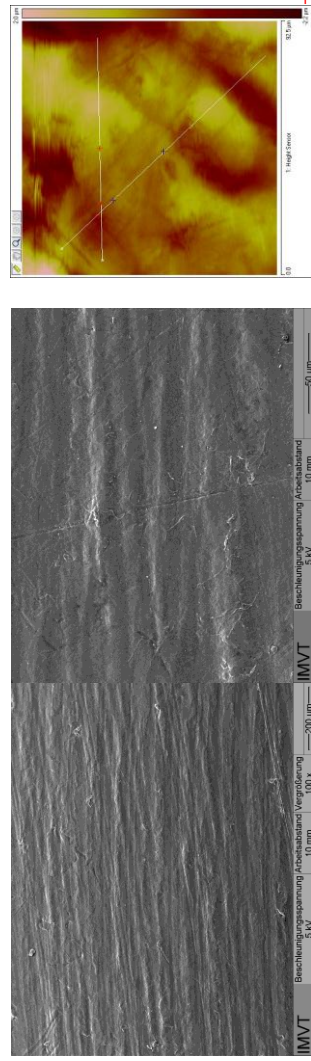


Figure 18: SEM and AFM measurements of milled PTFE surface

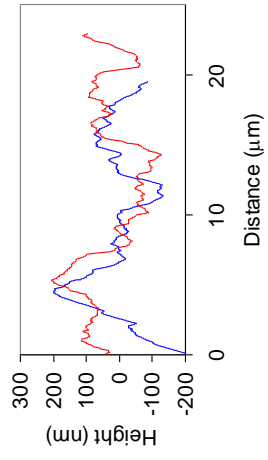
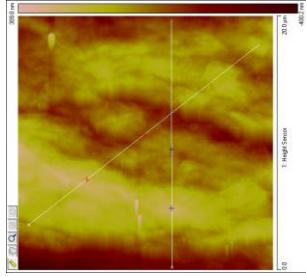
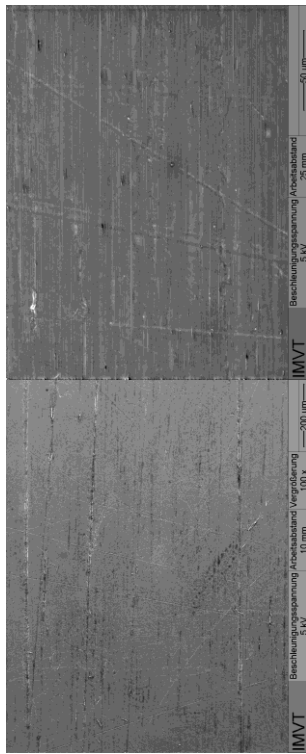


Figure 19: SEM and AFM measurements of polished PTFE surface

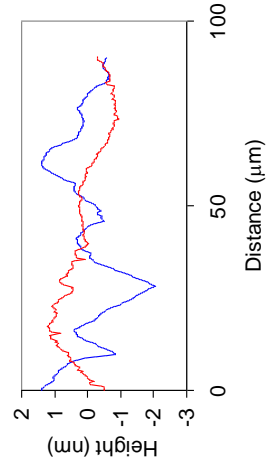
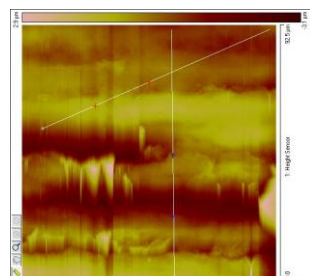
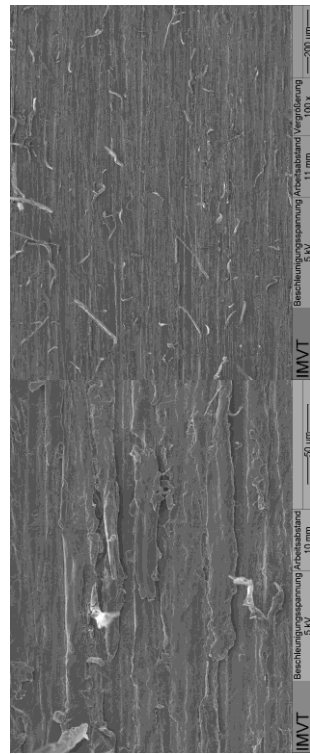


Figure 20: SEM and AFM measurements of ground PTFE surface

Table 9: Surface roughness (as defined in Section 4.1.1) determined with AFM

Material	polished				ground				milled				Density (gm/cm ³)	Brinell Hardness	Tensile Strength (MPa)	
	R _q (nm)	R _a (nm)	R _{max} (nm)	Surface Area Difference (%)	R _q (nm)	R _a (nm)	R _{max} (nm)	Surface Area Difference (%)	R _q (nm)	R _a (nm)	R _{max} (nm)	Surface Area Difference (%)				
Metal	8620	8	106	0.0647	142	109	926	0.95	too rough to measure	too rough to measure	too rough to measure	too rough to measure	7.8	201	97,000	
	Aluminum	14	86	0.997		not available			212	180	1076	1.79	2.7	23	40,000	
	Bronze	14	11	97	0.139	314	258	1608	2.38	162	135	697	0.693	8.4	65	35,000
	Cast Iron	20	12	623	0.188	215	175	1070	1.92					7.06	230	57,000
	L80	4	3	29	0.118	141	111	854	1.07					2.69	60	80,000
	Stainless Steel	13	9	234	0.0184	111	85.7	666	0.688	230	200	920	0.583	7.48	171	860,000
	Nylon	86	64	989	0.805		not available			655	519	2877	1.52	2.15	12	75,000
	PEEK	25	16	459	0.0906	343	262	1788	4.47	776	642	3486	1.43	1.32	99	90,000
	PMMA	44	34	452	0.724	685	548	4094	15	703	455	4921	8.81	1.18	20	55,000
	Polystyrene	20	16	129	0.0191	1353	979	8211	20.9	731	625	3135	7.53	1.05	25	40,000
Plastic	PTFE	102	79	747	1.01	887	686	6043	8.47	1054	829	7406	4.83	2.2	1	27,000
	UHMW PE	284	229	1453	2.18	559	447	3125	5.24	1076	867	9807	14.4	0.99	64	46,000
	Glass slide	1.3	0.79	50	0.04											

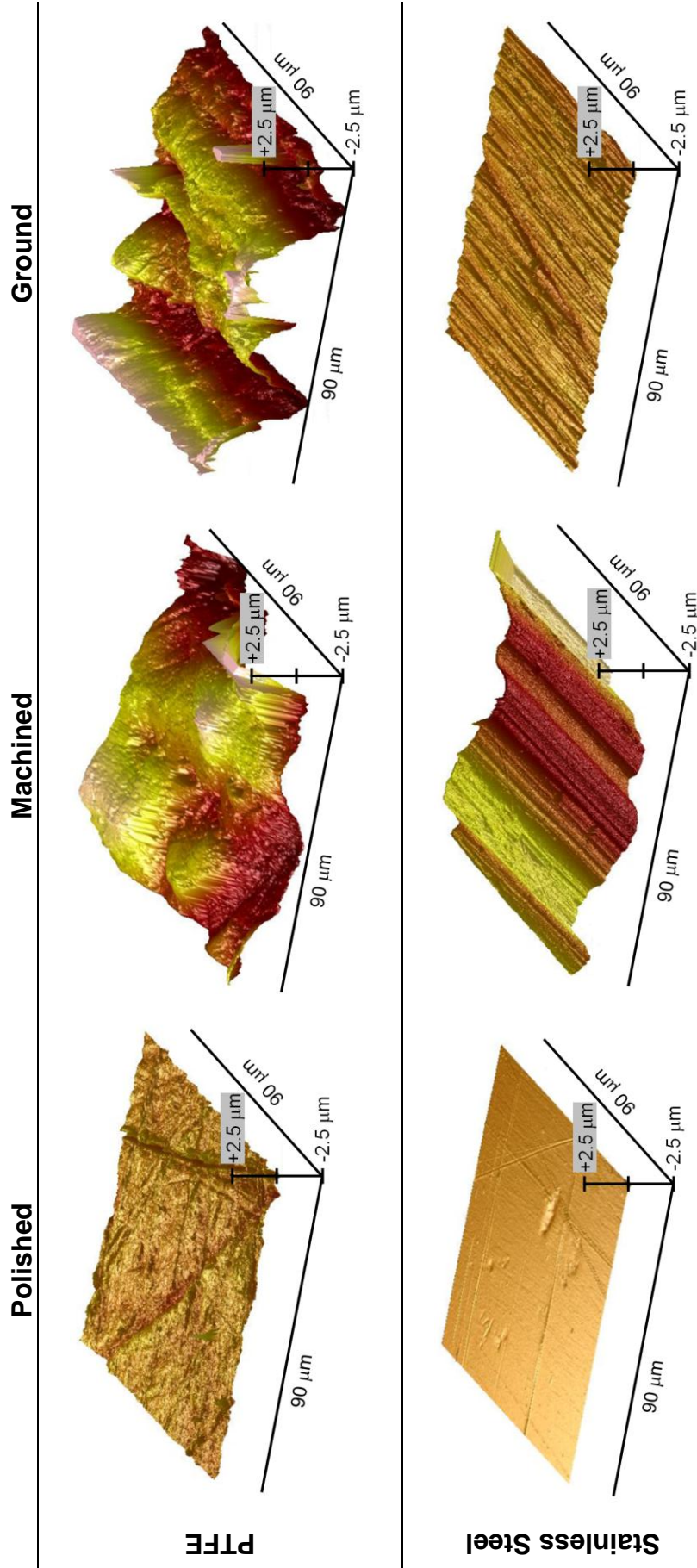


Figure 21: 3D Renderings of polished, machined, and ground PTFE and stainless steel surfaces from AFM data

The average roughness (R_a) for the polished, milled, and ground surfaces is plotted against the Brinell material hardness in Figure 22, material density in Figure 23, and material tensile strength in Figure 24. Generally, the resulting roughness is inversely proportional to each of these material properties; however, there is a large variation in the resulting roughness for materials with low values in each of these properties. For every material the roughness of the polished surface is substantially less than the roughness resulting from milling or grinding; the roughnesses of the polished surfaces have been plotted against a secondary axis with a smaller scale in the graphs. Surprisingly, although the roughnesses achieved for a particular material through grinding and milling are typically different, neither of the methods consistently produced a smoother surface than the other. For hard metals ground surfaces were smoother than milled surfaces; in some cases, the milled surfaces of hard metals were too rough to be measured with AFM. However, this trend cannot be generalized for softer materials such as plastics. In these investigations the same parameters were used for the milling of each surface. However, the surface roughness could be reduced by optimizing the milling parameters for the specific surface, for example by using cooling, adjusting the velocity and rotational speed of the tool, and using different end mills.

The different forms of roughness—the root mean square roughness (R_q) (Equation 17), the average roughness (R_a) (Equation 18), the maximum height variation between the lowest point and the highest point (R_{max}), and the surface area difference—have been compared in Figure 25 through Figure 27. From these graphs it can be seen that R_q , R_a , and R_{max} are all nearly equivalent measures of roughness. The surface area difference percentage differs somewhat from these other values because it depends on the shape of the surface roughness and not only the height difference between peaks and valleys.

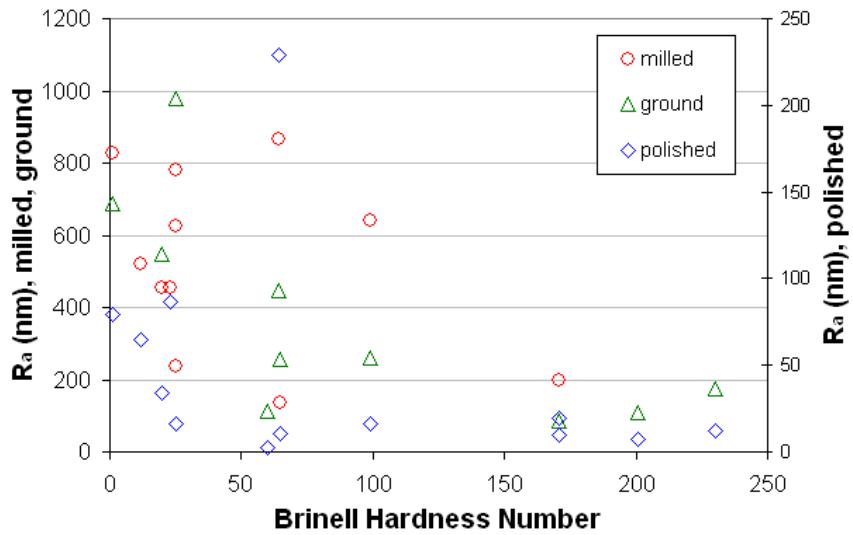


Figure 22: Surface roughness dependence on material hardness

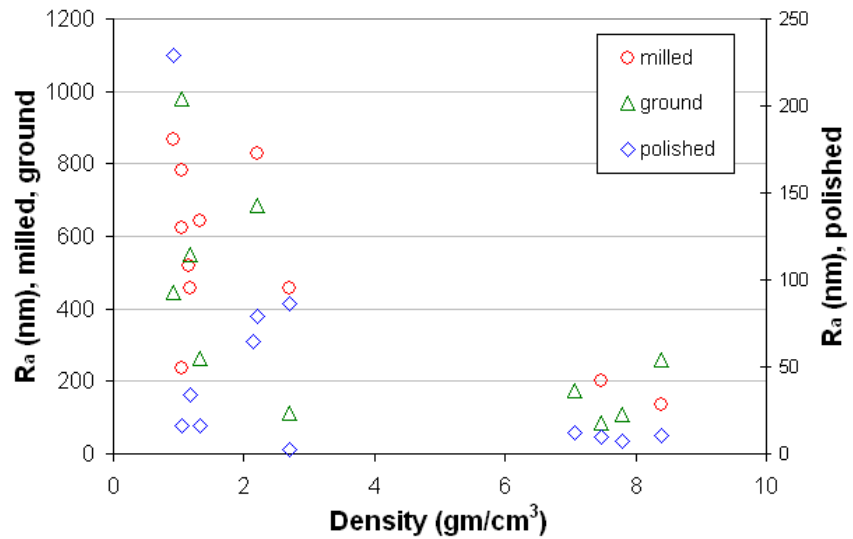


Figure 23: Surface roughness dependence on material density

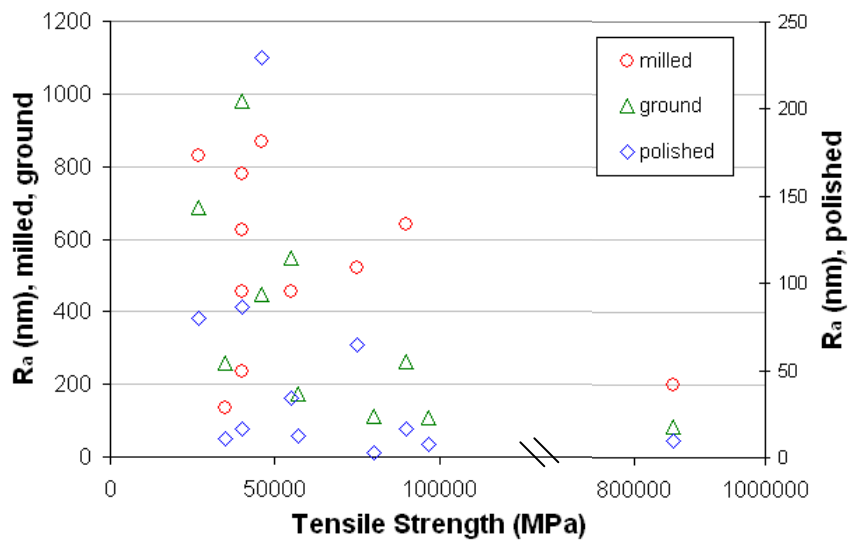


Figure 24: Surface roughness dependence on tensile strength

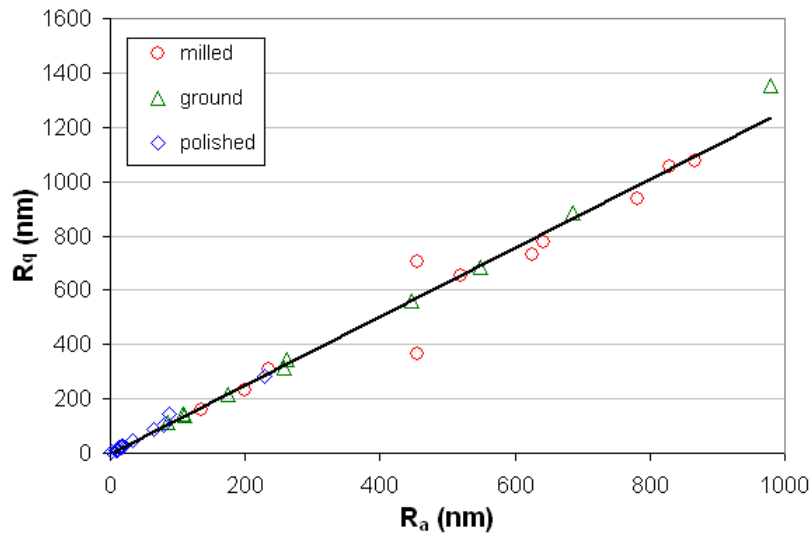


Figure 25: Relationship between R_q and R_a

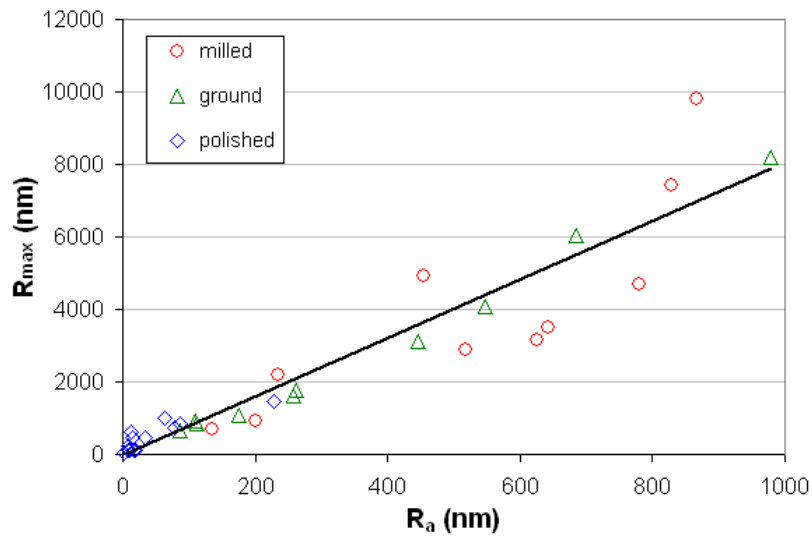


Figure 26: Relationship between R_{max} and R_a

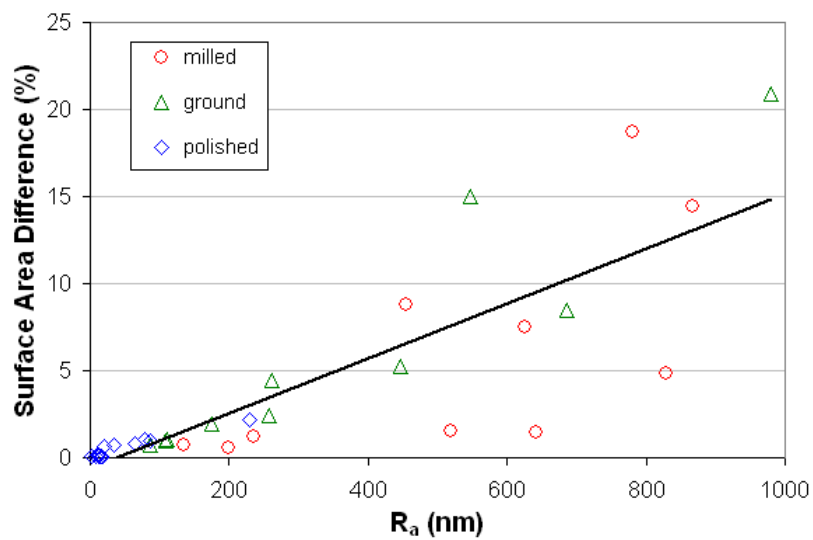


Figure 27: Relationship between Surface Area Difference and R_a

5.1.2 Commercial Capillaries

The 250 μm capillaries listed in Table 8 were examined with SEM. The glass capillary was embedded in a polymer resin and the resin and embedded capillary were slowly polished to provide a view of the inner channel wall and a channel cross-section. Cross-sections and views of the inner walls for the PTFE capillary were cut with a razor blade. A view of the inner wall of the stainless steel capillary could not be created through embedding, so it has not been examined. SEM photos of the capillaries are shown in Figure 28 through Figure 31. The leftmost picture in each figure shows the view of the inner wall. The middle picture shows a close-up of this wall. The rightmost picture shows a channel cross-section.

The surface roughness inside the capillaries could not be measured with AFM because the holder of the AFM cantilever was too wide to fit inside the channels. However, the SEM photos provide a rough impression of the condition of the inner wall. The fused silica capillary wall in Figure 28 appears very smooth; some broken fragments, probably resulting from the grinding and polishing process, can be seen on the surface. The PEEK capillary wall, Figure 29, appears to contain small striations, which perhaps occur when the capillary is extruded. The PTFE capillary wall, Figure 30, contains some longitudinal ripples in the wall. The FEP capillary wall, Figure 31, appears slightly grainy. Despite the minor unevenness seen in the capillaries, the surface roughness appears to be most comparable to that of the polished samples examined for roughness in Section 5.1.1.

The inner diameters measured from the cross-sections of the channels did not deviate significantly from the expected value of 250 μm . The errors associated with preparing the cross-sections and identifying the channel edges are likely larger than the deviations in the size of the capillary.

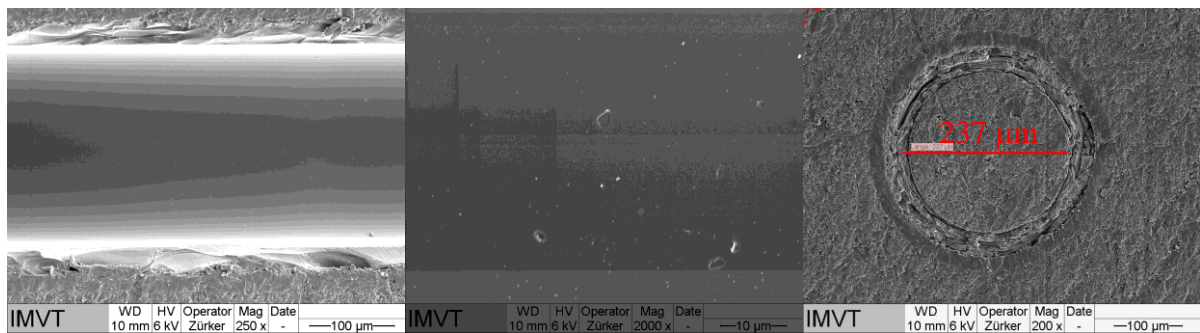


Figure 28: SEM photos of 250 μm fused silica capillary: capillary interior—resin in which the capillary was embedded and abraded walls from grinding can be seen at the top and bottom (left); magnification of the capillary wall—fragments broken off during grinding can also be seen (middle); cross-section—diameter was measured to be 237 μm (right)

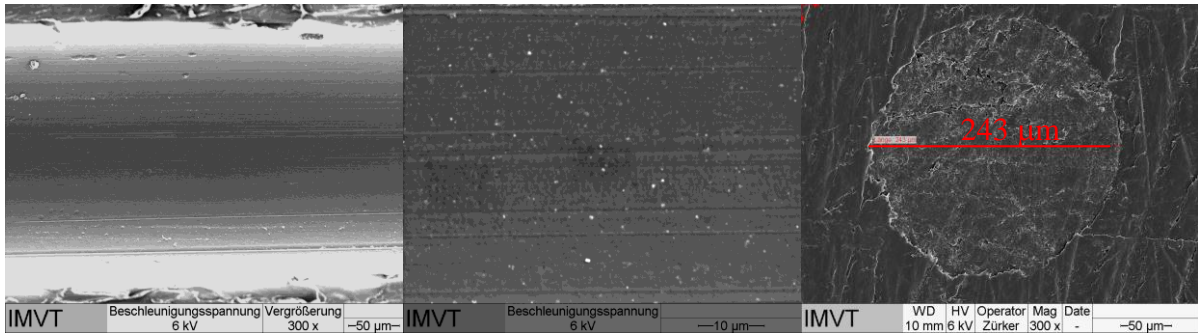


Figure 29: SEM photos of 250 μm PEEK capillary: capillary interior —abraded walls can be seen at the top and bottom (left); magnification of the capillary wall, visible striations along the length (middle); cross-section—diameter was measured to be 243 μm (right)

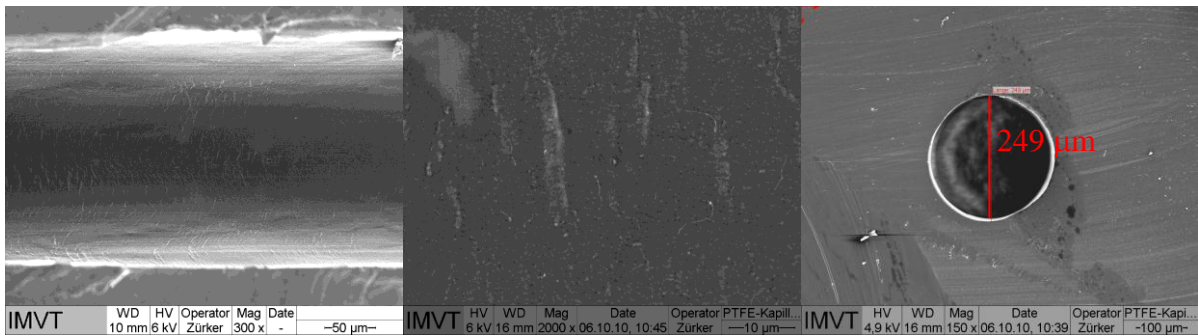


Figure 30: SEM photos of 250 μm PTFE capillary: abraded walls can be seen at the top and bottom, the entire capillary interior can be seen (left); magnification of the capillary wall—capillary wall contains ridges perpendicular to the length (middle); cross-section—diameter was measured to be 249 μm (right)

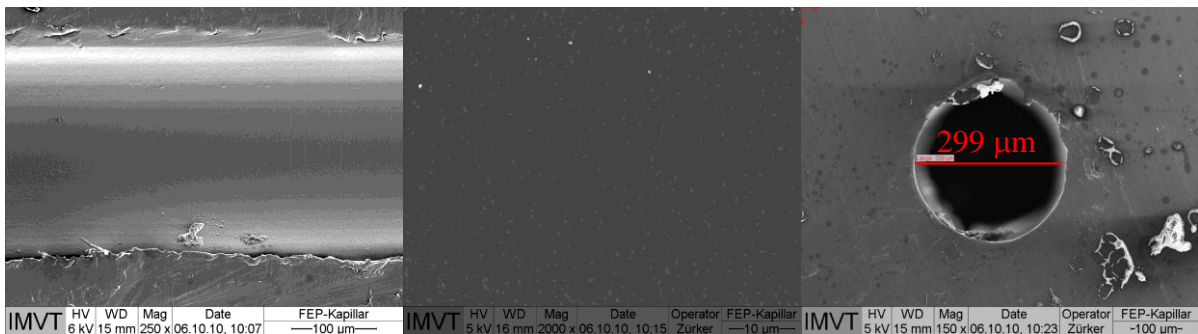


Figure 31: SEM photos of 250 μm FEP capillary: abraded walls from grinding can be seen at the top and bottom, the entire capillary interior can be seen (left); magnification of the capillary wall—capillary wall appears smooth (middle); cross-section—diameter was measured to be 299 μm (right)

5.1.3 Gas/Liquid/Solid Contact Angle

The contact angle is the angle formed between the solid/liquid and liquid/gas interfaces of a drop of liquid resting on a solid surface (see Figure 32).

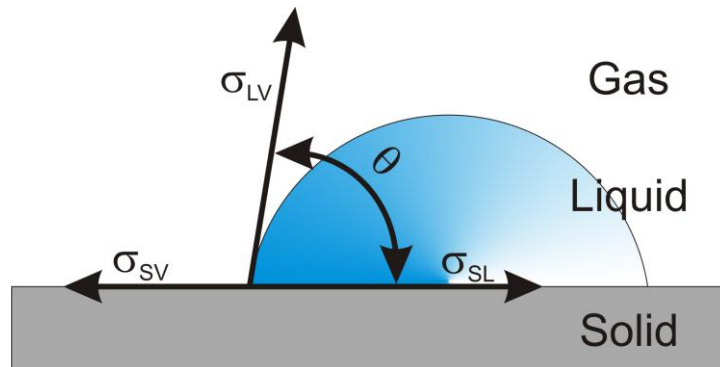


Figure 32: Contact angle formed at a gas/liquid/solid boundary

The contact angle is described according to Young's Equation:

$$\sigma_{SV} = \sigma_{SL} + \sigma_{LV} \cos \theta \quad [29]$$

where σ_{SV} is the solid/gas(vapor) interfacial tension;

σ_{SL} is the interfacial tension of the solid/liquid interface;

σ_{LV} is the liquid/gas(vapor) interfacial tension;

and θ is the contact angle.

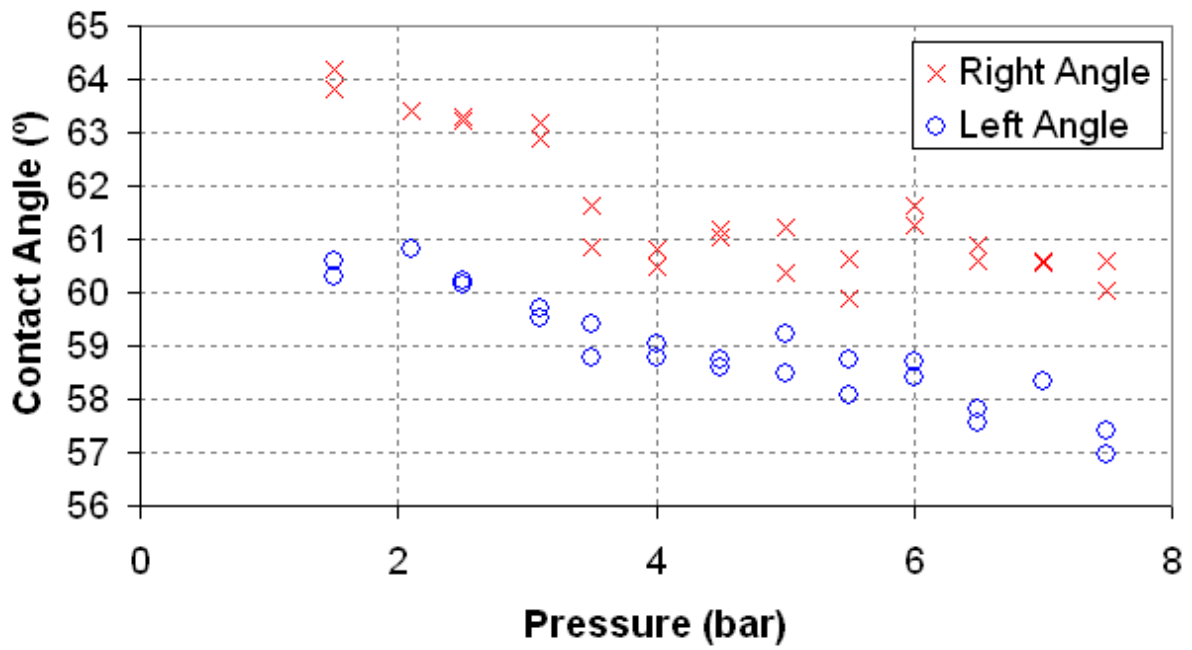
5.1.3.1 Effect of Pressure on the Contact Angle

Wesch et al. [139] found that the contact angle of water on various surfaces increased with pressure for pressures between 0 and 30 MPa. The sizes of the measured drops were not reported.

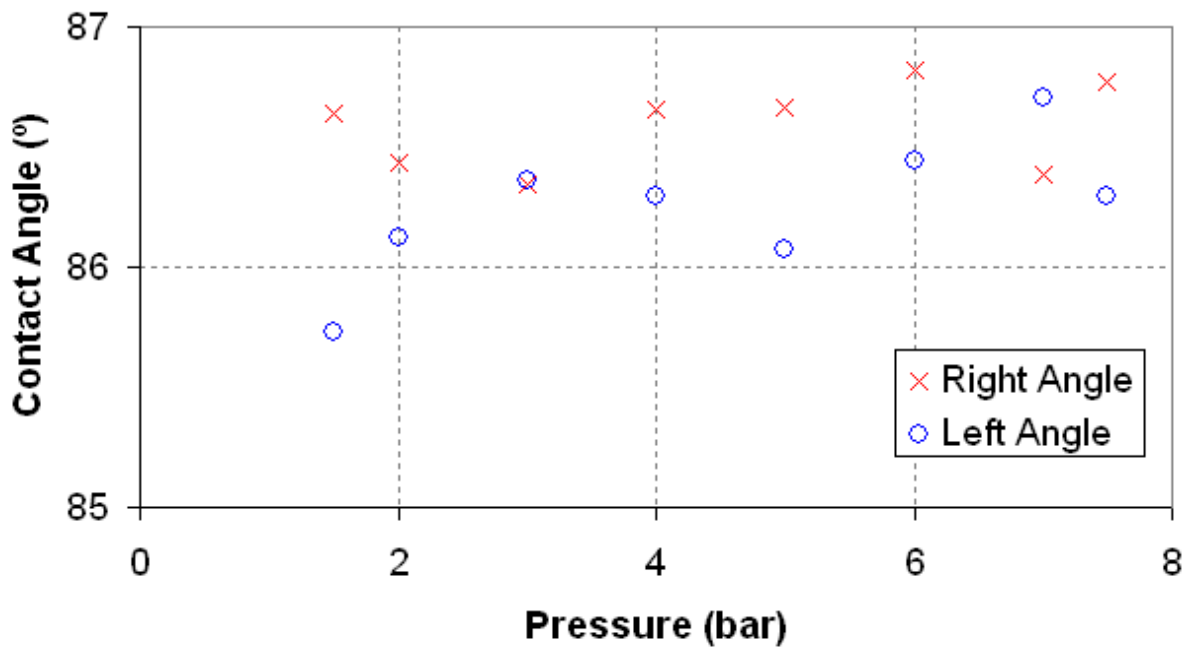
Contact angles that were collected while placing a drop on the surface and then increasing the pressure from 100 to 750 kPa for water in CO₂ on a polished stainless steel surface are shown in Figure 33 for a small (0.6 mm base diameter/0.15 μ L) and a large (2.7 mm base diameter/29 μ L) water drop. The base diameter is the diameter of the base of the drop in contact with the solid surface. The relationship between the base diameter and drop volume is explained in Appendix 8.2; it depends on the size of the drop, the contact angle, and also the deformation of the drop due to gravity. The contact angles of the small drops are influenced by changes in the pressure, but the contact angles of the large drops remain constant.

Similar measurements were repeated, but drops of various sizes, where the radius of the drop base on the solid surface ranged from 0.3 to 4.5 mm, were placed into environments where the pressure was already fixed before introduction of the drop. The results of these investigations are shown in Figure 34.

These investigations reveal no substantial contribution of pressure to the contact angles of drops formed at a fixed pressure. For pressures up to 1000 kPa, the contact angle can be regarded as being independent of the formation pressure, and changing pressures influence the contact angles of small drops but not of large drops.

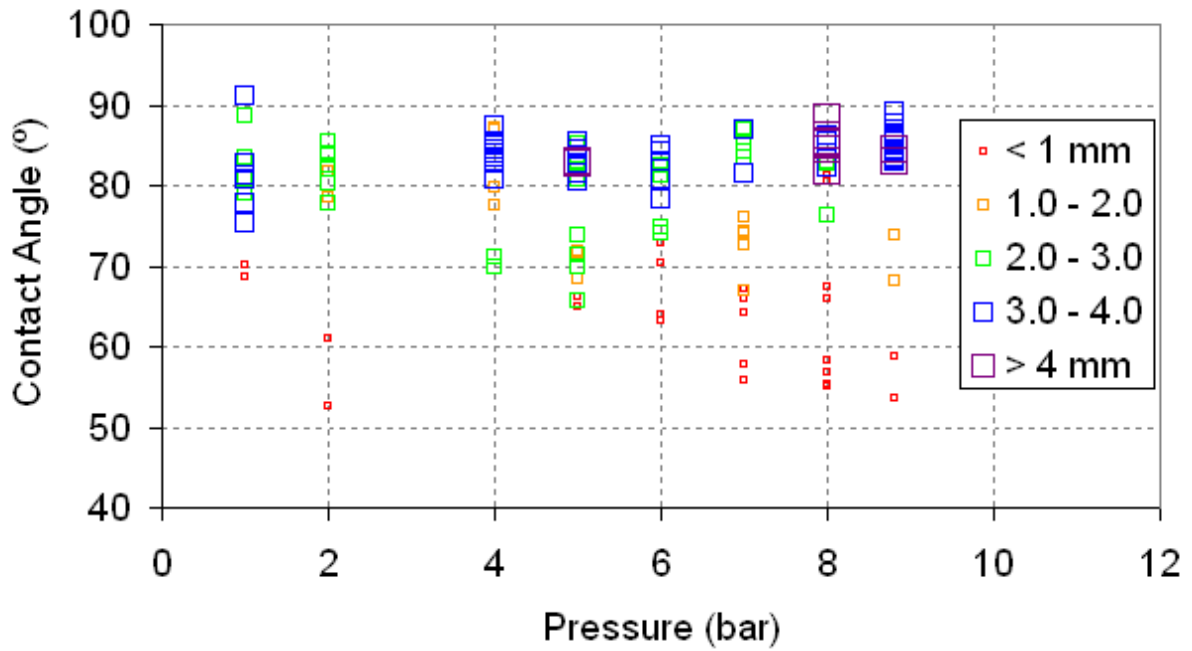


Water: Small Drop (0.6 mm base diameter/0.15 μL)

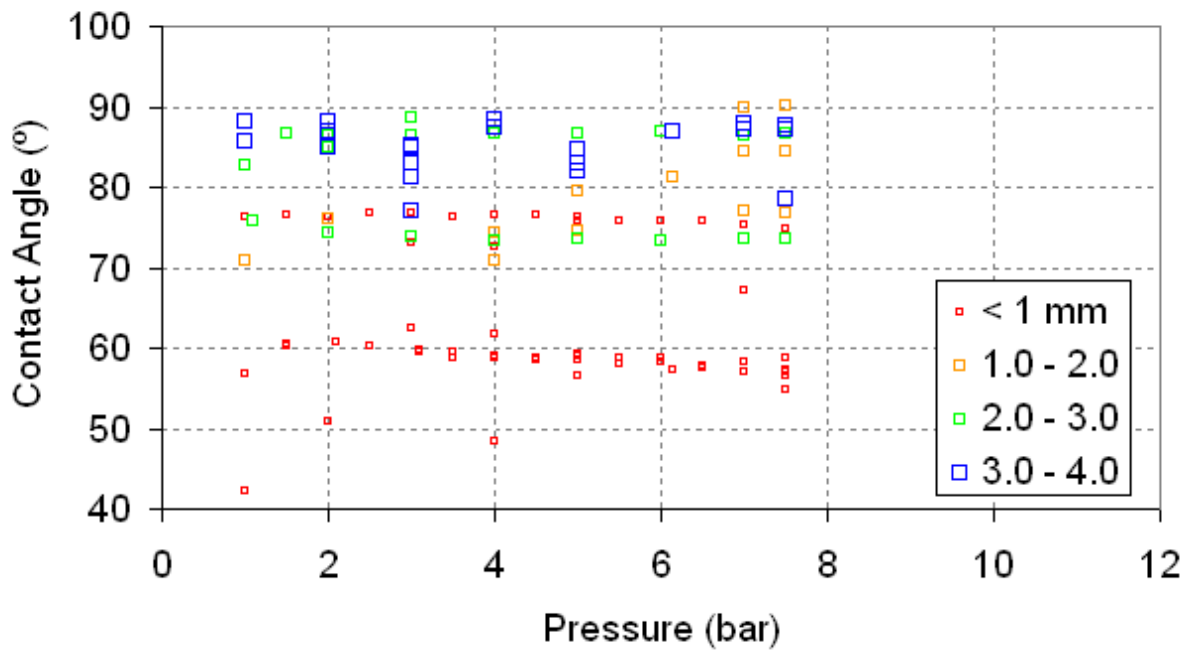


Water: Large Drop (2.7 mm base diameter/29 μL)

Figure 33: Contact angle variation with changing pressure for drops of water on polished stainless steel in CO_2



H_2O/N_2 /Stainless Steel



H_2O/CO_2 /Stainless Steel

Figure 34: Contact angle variation with pressure for drops of water on polished stainless steel, colored according to radius of drop base in mm

5.1.3.2 Effect of Drop Size on the Contact Angle

The results shown in Section 5.1.3.1 do not show an effect of pressure on the contact angle but already seem to indicate a strong influence of drop size on the measured angle.

Ponter and Yekta-Fard [149] have provided an extensive review of literature and their own work where the drop size exhibits a strong influence on the contact angle. In some systems (water/polyethylene/water-saturated air, water/poly(methyl methacrylate) (PMMA)/water-saturated nitrogen, water/PMMA/ water-saturated air, water/stainless steel/water-saturated air, water/PTFE/water-saturated nitrogen, water/FEP/water-saturated air, ethylene glycol/FEP/water-saturated air) the contact angle increased with increasing drop radius. Other systems (boiling point benzene/PTFE/benzene vapor, boiling point water/PTFE/water vapor, boiling point water/Copper/water vapor) showed the reverse trend. Most of the curves leveled-off at a drop diameter of around 1 cm.

Results measured in this work for water on stainless steel in N₂ and CO₂ environments are shown in Figure 35. The results are similar to those found in literature: they show an increase in contact angle with increasing drop size with an eventual leveling-off occurring when the drops reach a certain size, typically a drop base radius of around 2 mm.

Gravity can deform the shape of a drop and influence the contact angle when the drop is more than several millimeters large.

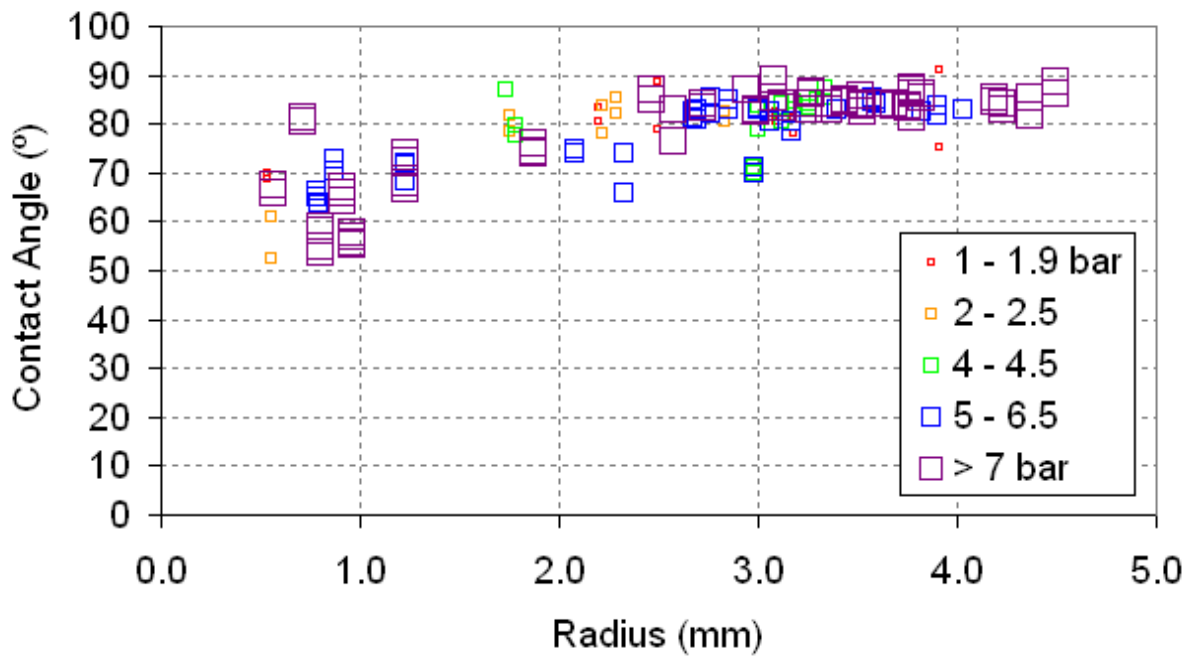
The Laplace pressure describes the pressure difference at a meniscus or phase interface:

$$\Delta P = P_{inside} - P_{outside} = \frac{2\sigma_{LV}}{r} \quad [30]$$

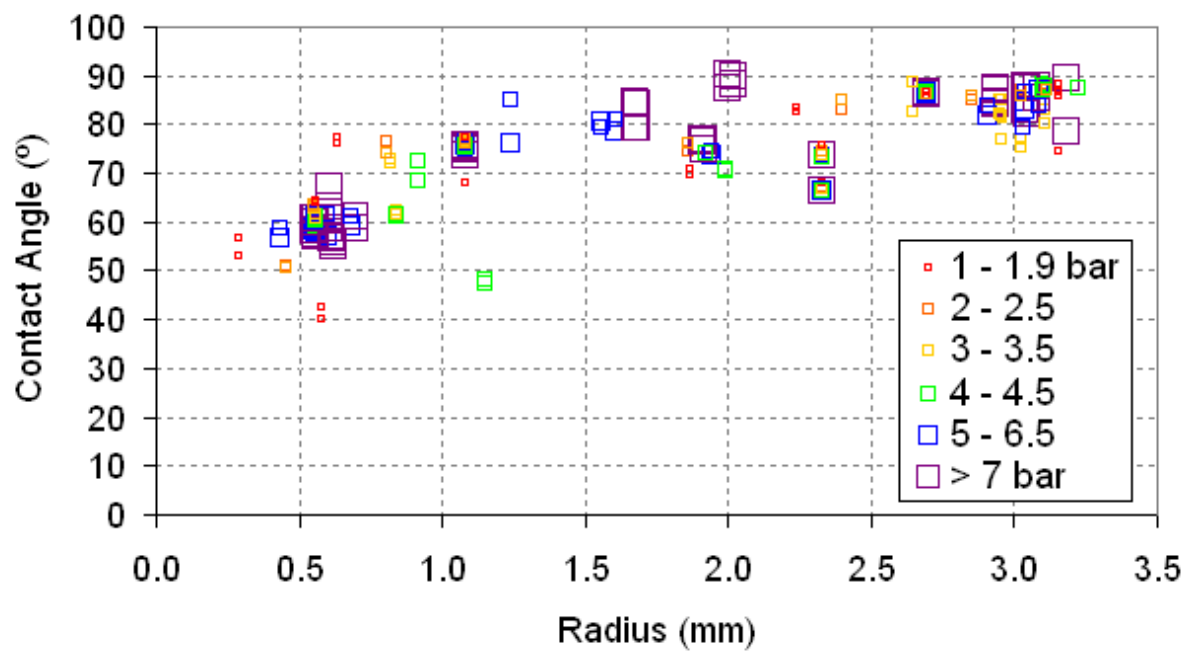
Where σ_{LV} is the interfacial tension and r denotes the drop radius. When the drop and interface are additionally deformed by gravity, the Laplace-Young equation takes the typical form:

$$\Delta P = \rho gh - \sigma_{LV} \left(\frac{1}{r_1} + \frac{1}{r_2} \right) \quad [31]$$

The application of the Laplace-Young equation requires the drop to be deformed by gravity. The Dataphysics SCA20 software can determine the contact angle either according to the Laplace-Young equation or by fitting it to a spherical profile. Small drops were typically better fit by a spherical profile; whereas, drops deformed by gravity were better fit by the profile calculated according the Laplace-Young equation. The contact angle needed for the Young equation is a balance of the various interfacial tensions as the Laplace-Young equation is a balance of the interfacial tension and gravity. The contact angle needed for the Young equation is therefore the angle that is constant for larger drop sizes.



H₂O/N₂/Stainless Steel



H₂O/CO₂/Stainless Steel

Figure 35: Contact angle variation with drop size for water in N₂ and CO₂ on polished stainless steel

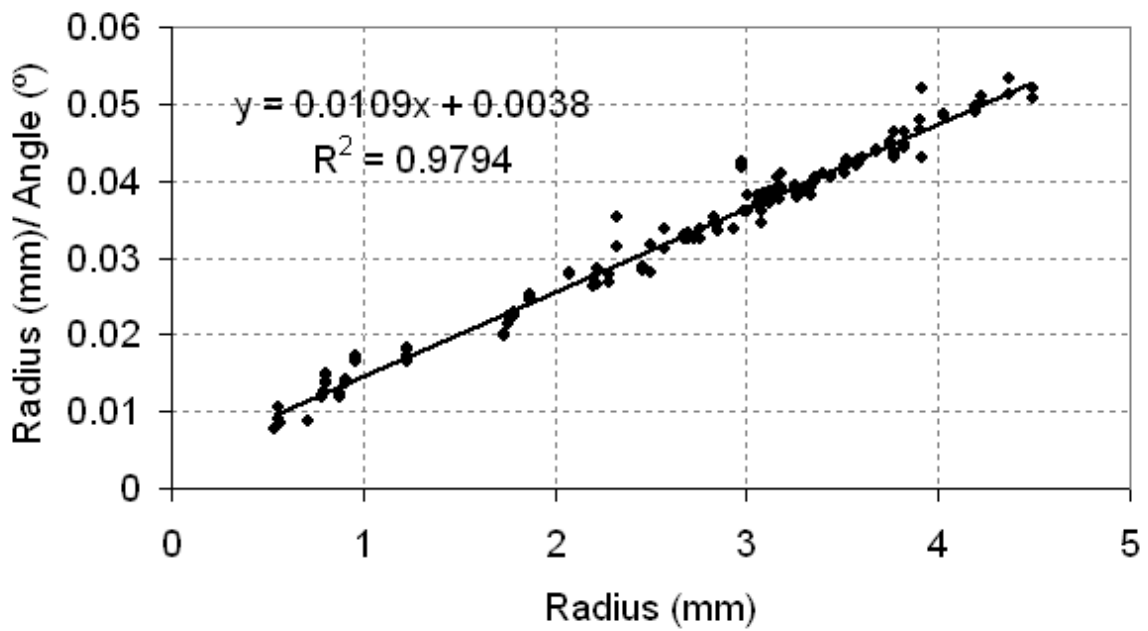
The relationship between contact angle and the radius of the drop base was fitted using a Langmuir linear regression (Equation 32). This nonlinear regression is able to describe the curves seen in Figure 35, where the contact angle approaches a constant value as the drop size increases. The equation uses only two parameters: ‘ θ_∞ ’ to describe the constant value of the contact angle for an infinitely large drop size and ‘ α ’ to describe the slope or rate at which the values approach the constant value.

$$\theta = \frac{\alpha \cdot r}{1 + \alpha \cdot r} \theta_\infty \quad [32]$$

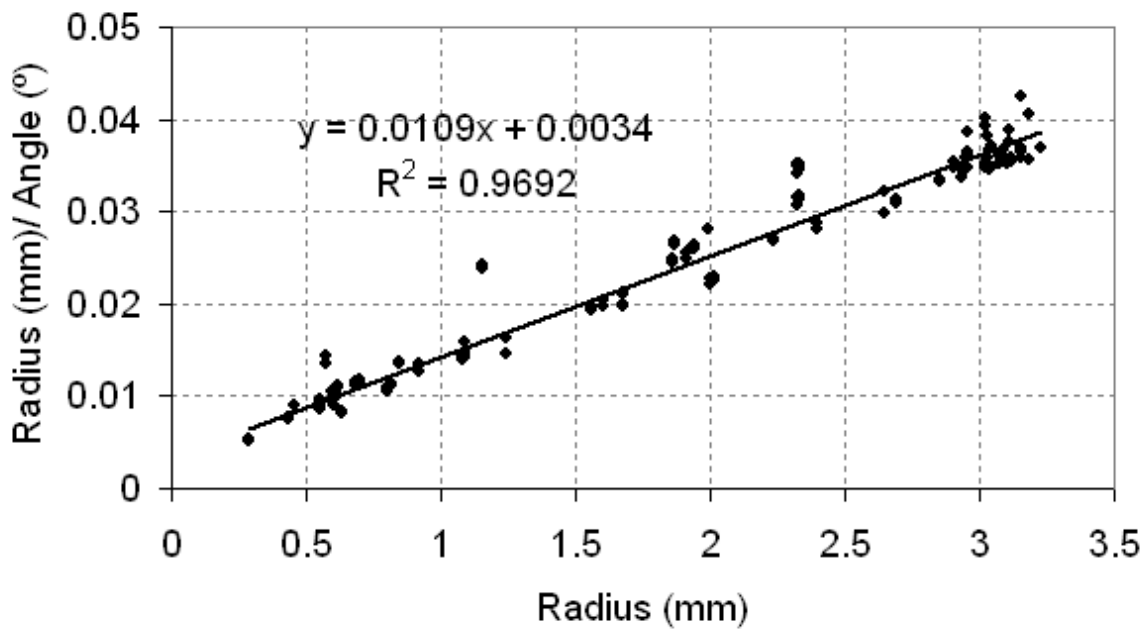
Equation 32 can be linearized such that the parameters ‘ θ_∞ ’ and ‘ α ’ can be determined from the slope ($1/\theta_\infty$) and intercept ($1/\alpha\theta_\infty$) of a linear regression of r/θ versus r .

$$\frac{r}{\theta} = \frac{1}{\theta_\infty} r + \frac{1}{\alpha \cdot \theta_\infty} \quad [33]$$

Linear regressions from plots of r/θ versus r are shown in Figure 36 for drop of water on stainless steel in nitrogen and carbon dioxide atmospheres. These regressions yield nearly identical values of θ_∞ for water on stainless steel in both nitrogen and carbon dioxide atmospheres ($\theta_\infty = 91.7^\circ$). This value is several degrees higher than the average value of drops with bases of radius 2 mm or more.



Water/N₂/Stainless Steel



Water/CO₂/Stainless Steel

Figure 36: Langmuir linear regression on the relationship between contact angle and drop size (the radius of the drop base)

5.1.3.3 Effect of Surface Tension on the Contact Angle

According to the Young Equation (Equation 29), the cosine of the contact angle should be inversely proportional to the liquid/gas surface tension. In contrast to the relationship predicted by the Young Equation, Fox and Zisman observed experimentally that the cosine of the contact angle is directly proportional to the surface tension [150]. Plots of contact angle against surface tension are commonly referred to as “Zisman plots.”

Mixtures of ethanol and deionized water were used for measuring the contact angle for a range of surface tensions. Isopropanol, glycerol, and pure water were also measured in some cases. The surface tension was measured for mixtures of 51.3 ± 0.2 wt%, 20.4 ± 0.2 wt%, and 6.0 ± 0.2 wt% ethanol. The measurements of the surface tension for these mixtures in air, nitrogen, carbon dioxide, and 10% carbon dioxide in argon are shown in Figure 37. The gas atmosphere did not affect the measured interfacial tension to any perceptible extent. The measurements of the mixtures fit well the experimental observation of Belda et al. [151]. Only the measured values of ethanol for the lowest surface tensions are consistently higher than the literature values. This difference is likely due to the error of the instrument; because it is more difficult to form large pendant drops for liquids with small surface tensions, the error of the surface tension measurements increases with decreasing surface tension. Thus, the values of surface tension used in the following analysis were taken from literature. The values of ethanol, water, and their mixtures were taken from Belda et al. [151]. Surface tension values for isopropanol (21.7 mN/m) and glycerol (63 mN/m) were also taken from literature [152].

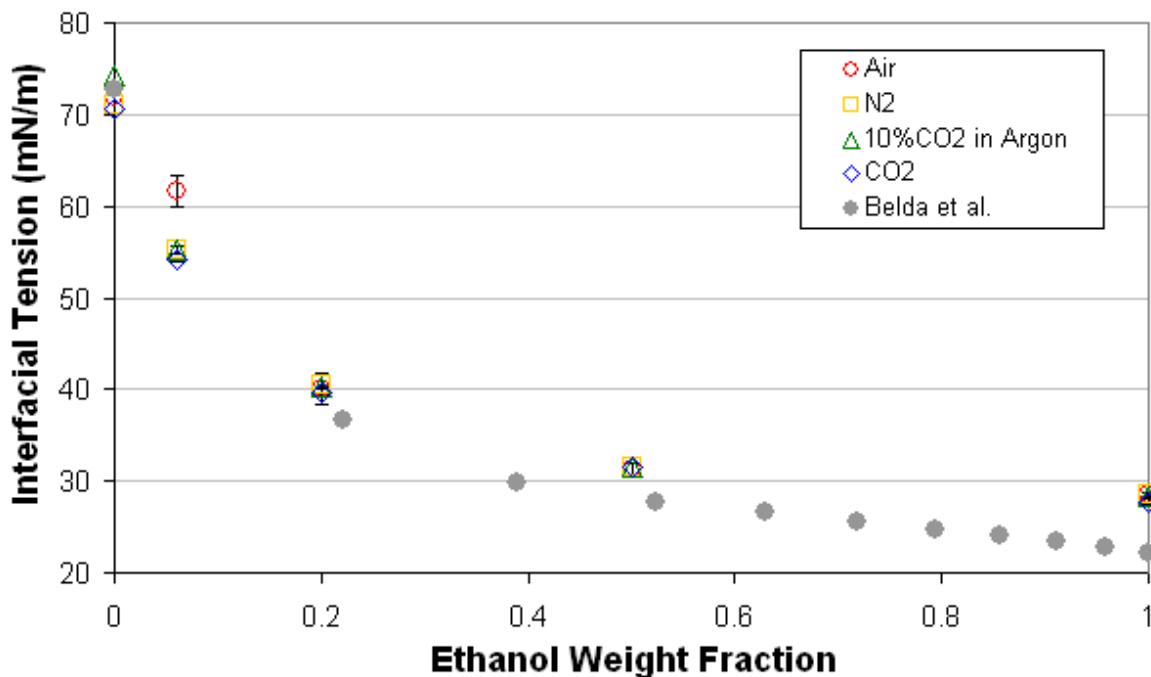


Figure 37: Values of gas/liquid surface tension (σ_{LV}) measured for mixtures of ethanol and water compared to data from Belda et al. [151]

Plots of the cosine of the contact angle against the inverse of the surface tension (Young Equation), the cosine of the contact angle against surface tension (Zisman plot), and the contact angle against surface tension are shown for the glass slide and polished stainless steel and PTFE surfaces in Figure 38 through Figure 40 for all of the measurements (water, water/ethanol mixtures, ethanol, isopropanol, and glycerol). The plots for the machined and ground surfaces as well as additional materials can be found in the Appendix 8.2. All of these representations appear to be approximately linear, but taking the cosine of the angle does seem to introduce some curvature and deviation from the linear predictions where the small contact angles lead to cosine values near unity. The cosine of the contact angle varies nearly linearly with the contact angle for angles between 45 ° and 135 ° (see Figure 43). As the contact angle approaches 0 °, i.e. complete wetting, the cosine of the contact angle approaches 1. Thus, this limit skews the relationships described by the Young equation and Zisman plot on the glass and stainless steel surfaces. Since complete wetting did not occur for any liquids on PTFE, the correlations show better linear fits on PTFE. Linear regression in each diagram has been performed using all points except those where the cosine of the contact angle is 1.

The overall variability in the measurements is quite large. The measurements with water ($\sigma_{LV} = 72 \text{ mN/m}$) show a particularly large variation. Aside from the natural variation of repeated measurements, there are a very large number of confounding variables that affect contact angle measurements. For example, this variability could be a result of drop size variation (Section 5.1.3.2); drops smaller than 8.3 μL in volume have been excluded from these graphs, but the drops still vary in size. The variability of the water measurements is not as large on the PTFE surface as it is on glass and stainless steel surfaces. Glass and stainless steel readily absorb water, which could change the state of the surface being measured. Most rigorous studies of wettability focus on hydrophobic surfaces because their measurements are much more reproducible. Although the surfaces here are not ideal, they represent real conditions that might be encountered in a microreactor.

The surface tension (σ_{LV}) parameter influences the value of the contact angle to a large extent—in Figure 38 through Figure 40 changes in the surface tension from 20 mN/m to 70 mN/m are seen to influence the contact angle by nearly 100 °. Its influence is on the same order of magnitude as the influence of the solid surface itself; the difference between the contact angle measured on glass and PTFE for liquids possessing the same surface tension is about 20 °. For the purposes of the linear regression analysis performed in Section 5.1.3.8 to determine the statistical significance of the many variables influencing the contact angle, the simple relationship between contact angle and surface tension has been used. All of the regressions were approximately linear, but the relationships based on the Young equation and Zisman plot showed poor fits for systems with good wettability where the cosine of the contact angle approaches 1; whereas the direct relationship between contact angle and surface tension was approximately linear for all surfaces and could describe the measurements with good wettability and therefore small contact angles.

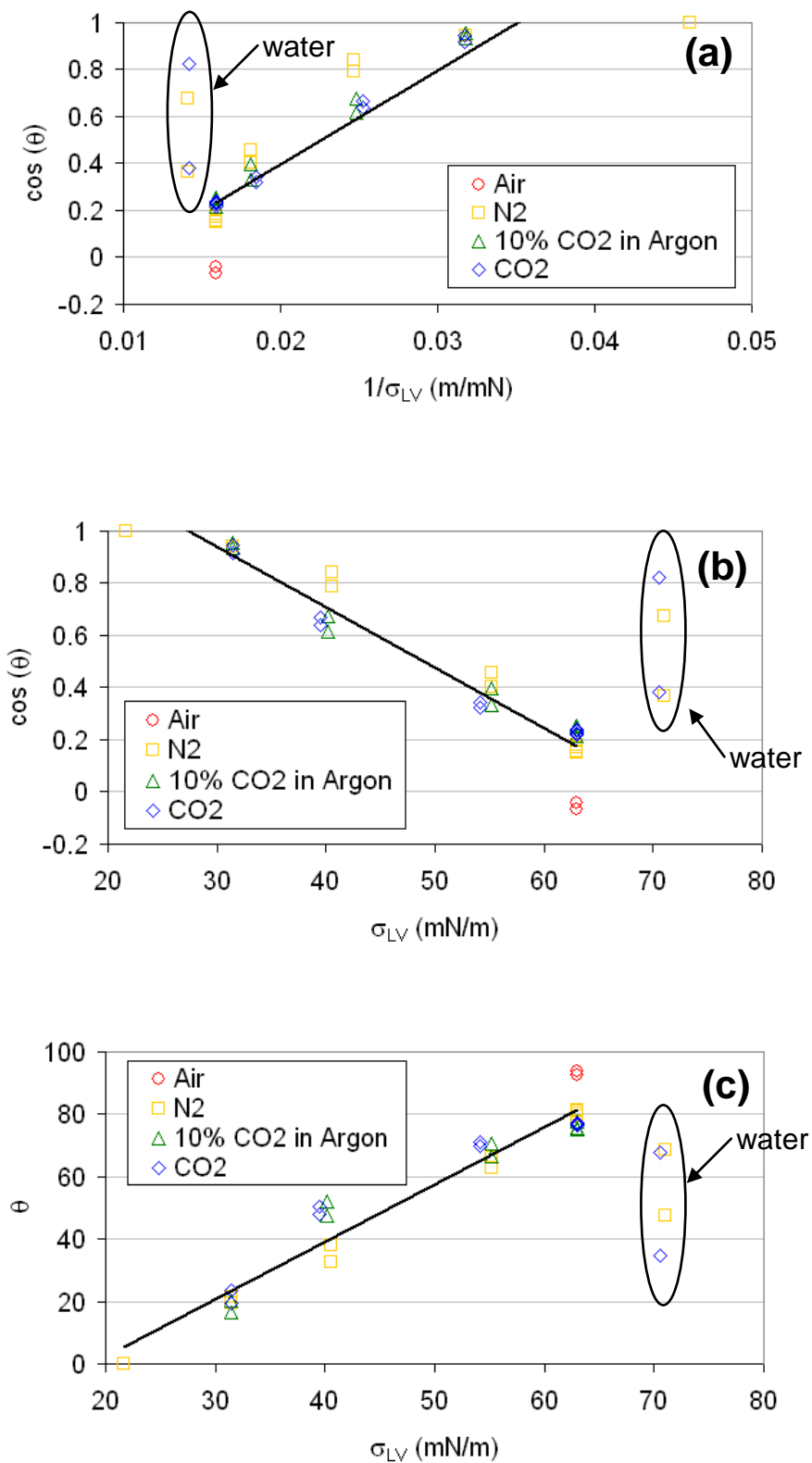


Figure 38: Relationship between the contact angle (θ) of a drop of liquid on a glass slide and the liquid/vapor surface tension (σ_{LV}) for various liquids: (a) as predicted by the Young Equation; (b) the Zisman plot; (c) simple direct relationship

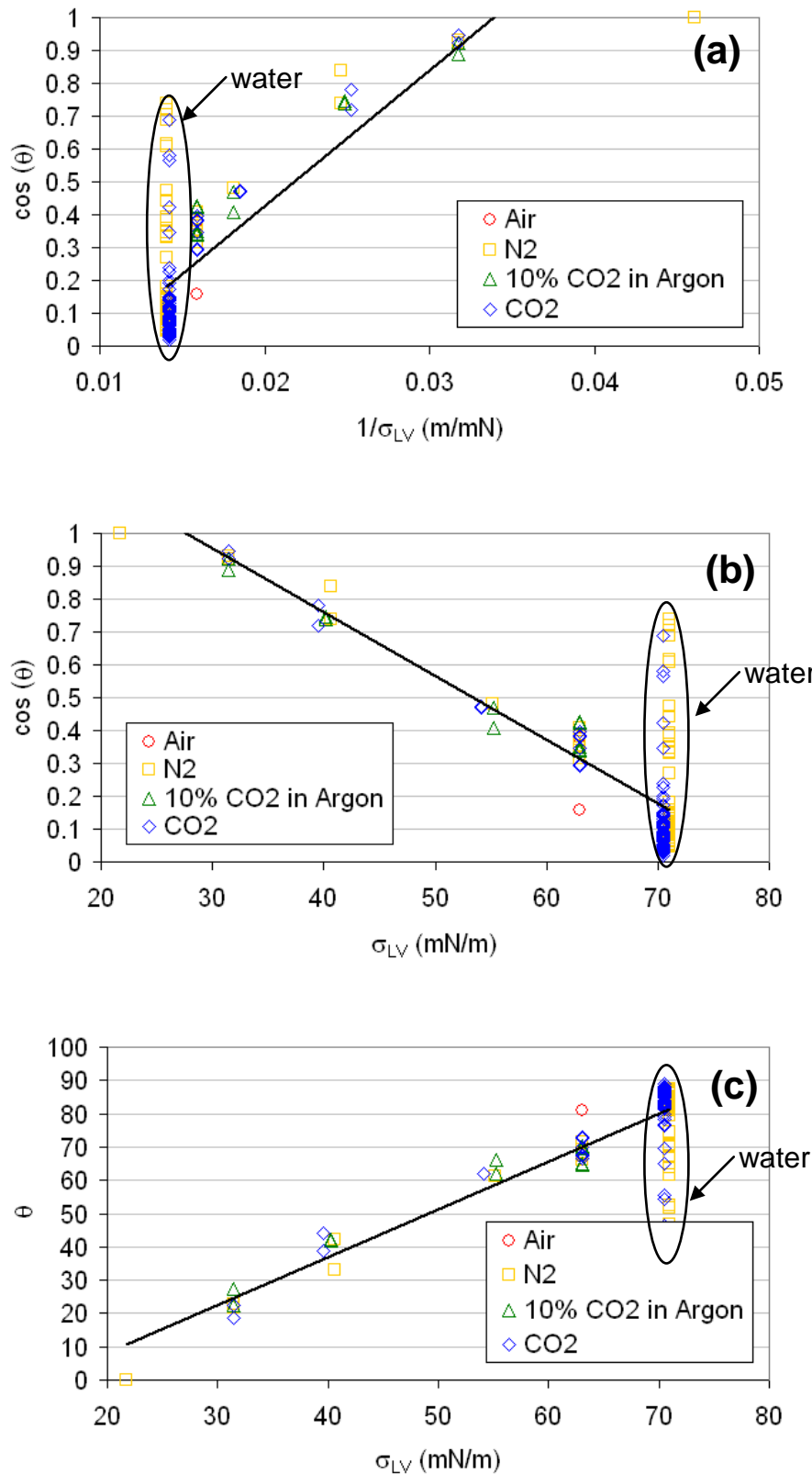


Figure 39: Relationship between the contact angle (θ) of a drop of liquid on a polished stainless steel surface and the liquid/vapor surface tension (σ_{LV}) for various liquids: (a) as predicted by the Young Equation; (b) the Zisman plot; (c) simple direct relationship

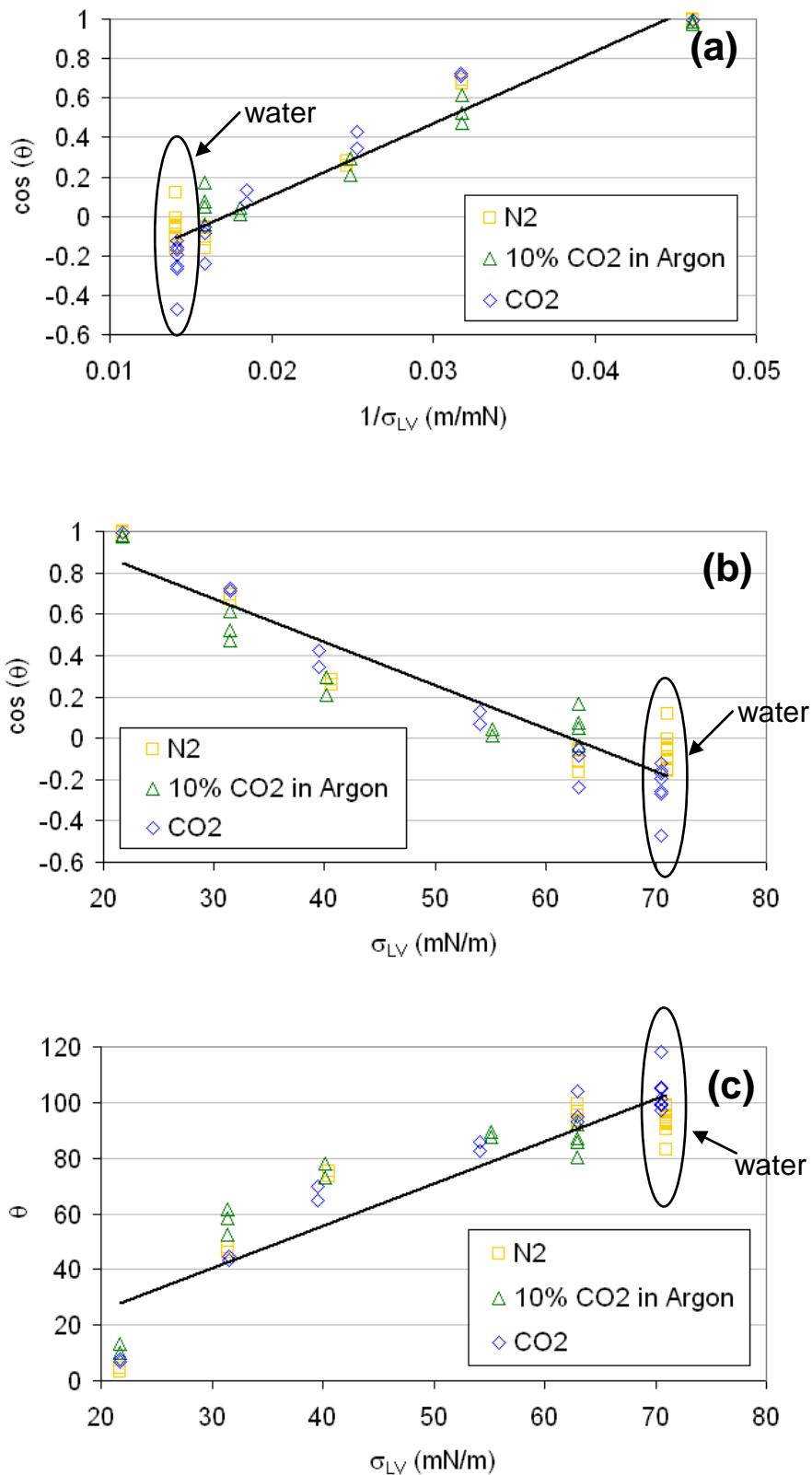


Figure 40: Relationship between the contact angle (θ) of a drop of liquid on a polished PTFE surface and liquid/vapor surface tension (σ_{LV}) for various liquids: (a) as predicted by the Young equation; (b) the Zisman plot; (c) simple direct relationship

5.1.3.4 Effect of Gas Composition on the Contact Angle

The measurements shown in Figure 38 through Figure 40 separate the measurements according to the gas phase in which the liquid was measured. According to the Young Equation, all three phases, gas, liquid, and solid, are important in the determination of the contact angle. It appears that the composition of the gas phase has only a secondary on the contact angle.

5.1.3.5 Effect of Surface Roughness on the Contact Angle

The cosine of the contact angle is plotted against the inverse of the surface tension according to their relationship in Young's equation in Figure 41 and Figure 42 for ground, milled, and polished PEEK and PTFE surfaces. Similar plots for other investigated materials can be found in Appendix 8.2. These graphs show an impact of surface roughness on the contact angle that becomes more significant for larger angles, i.e. for small $\cos(\theta)$. The effect is insignificant for small angles ($\cos(\theta) \rightarrow 1$).

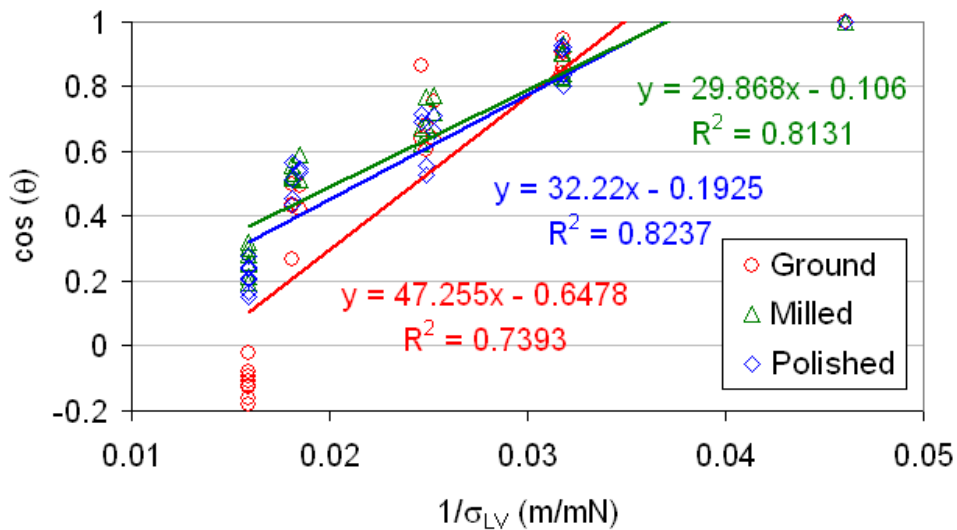


Figure 41: Effect of surface roughness for contact angles measured on PEEK

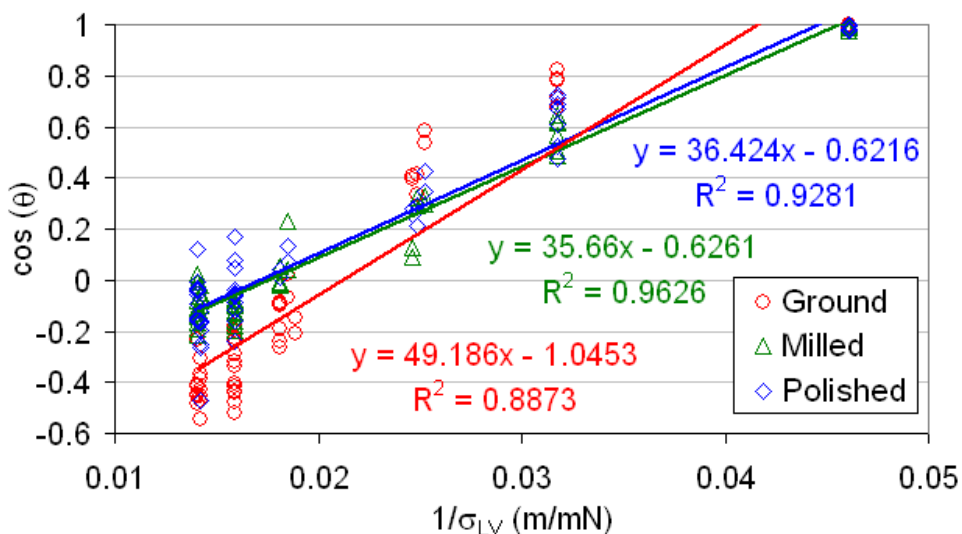


Figure 42: Effect of surface roughness for contact angles measured on PTFE

For PEEK and PTFE the contact angles measured on the polished and milled samples are nearly identical, but the contact angles on the ground samples differ from the milled and polished samples. The contact angles on the milled samples do not differ from the polished samples. This would be logical if the milled samples had very little surface roughness and the ground samples were substantially rougher. However, as the results Section 5.1.1 reveal, it is not possible to simply compare machined surfaces to each other since the processing technique impacts each material differently. For example, R_q , R_a , and R_{max} for PEEK indicate that the milled PEEK sample is rougher than the ground PEEK sample by nearly a factor of two, but the surface area difference indicates just the opposite; the surface area increase for the milled PEEK sample is 1.43 % and for the ground PEEK sample 4.47 %. The roughness trends for PTFE are similar.

The effect of surface roughness on the contact angle is typically described by either the Wenzel equation [153] or the Cassie-Baxter model [154]. The Wenzel equation describes the effect of roughness on homogeneous systems. Homogeneous means that the material and contact angle is the same over the surface in contact with the drop.

$$\cos \theta^* = r \cos \theta \quad [34]$$

Where θ^* is the apparent angle; r is the ratio of the actual surface roughness to the geometric area, similar to the surface area increase determined from the AFM measurements; θ is the intrinsic contact angle of the material.

The Cassie-Baxter model describes heterogeneous surfaces composed of multiple materials.

$$\cos \theta^* = f_1 \cos \theta_1 + f_2 \cos \theta_2 \quad [35]$$

The Cassie-Baxter model is appropriate for use with systems where air bubbles may be trapped between solid structures, and the surface is thus composed of alternating sections of air and solid material. If air is considered to have a contact angle of 180 °, the Cassie-Baxter model becomes:

$$\cos \theta^* = f_1 \cos \theta_1 - 1 + f_1 \quad [36]$$

Figure 43 demonstrates the predications of the Wenzel equation and the Cassie-Baxter model for the effect of roughness on the observed contact angle. For the Wenzel equation the roughness ratio r has been shown for a 10 % and 50 % increase in the surface area. For the Cassie-Baxter model the apparent contact angles have been calculated for a surface consisting of 10 % or 50 % air. The Wenzel Equation predicts that the roughness increases $\cos(\theta)$ for θ less than 90 ° and decreases $\cos(\theta)$ for θ greater than 90 °. The effect is nothing at 90 ° and increases as the angle becomes either larger or smaller. The Cassie-Baxter model predicts that $\cos(\theta)$ is decreased, and the effect is greater for smaller angles ($\cos(\theta) \rightarrow 1$).

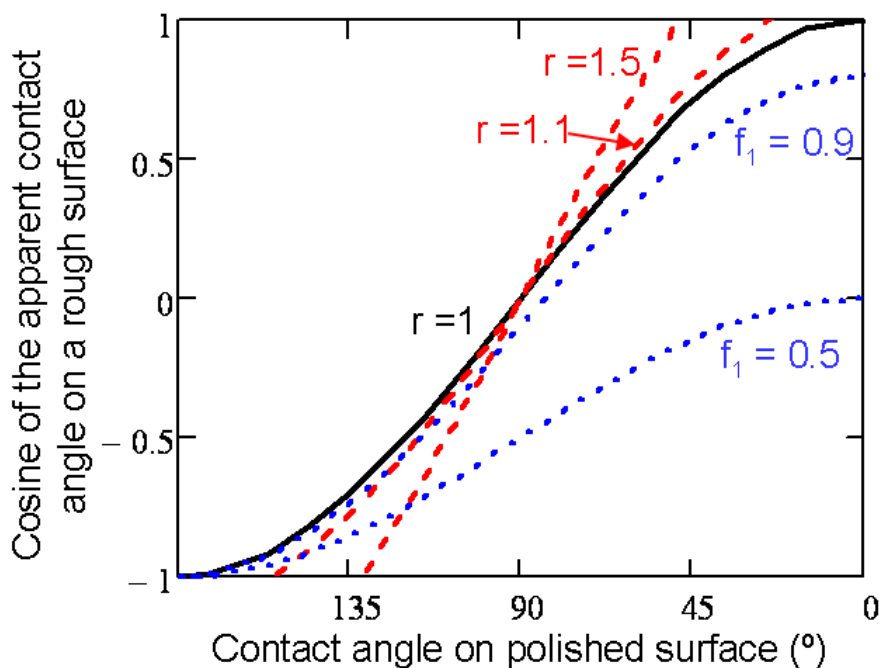


Figure 43: Effect of surface roughness on the observed contact angle according to the relations of Wenzel (red) and Cassie-Baxter (blue)

Assuming that the polished sample represents the contact angle of the intrinsic material, the explanations of these models can be compared to the measurements presented in Figure 41 and Figure 42. The Wenzel model predicts that $\cos(\theta)$ should be greater than that of the intrinsic material when $\cos(\theta)$ is greater than 0 and less when $\cos(\theta)$ is less than 0. The measurements on PTFE shown in Figure 42 could support this trend. The PEEK measurements shown in Figure 41 do not substantially differ as $\cos(\theta) \rightarrow 1$ but are less than $\cos(\theta)$ for the intrinsic material even before this value reaches 0, which is somewhat better described by the Cassie-Baxter model.

Neither model can comprehensively explain the measurements for all investigated materials. The roughness shows a larger impact on the measured angle for larger angles, but the difference can appear even before the intrinsic angle reaches 90°. It is also disconcerting that the machined sample often approximates the polished sample, despite the difference in roughness between the polished and milled samples being greater than that between the milled and ground samples. The models have been developed for ideal surfaces and geometries, typically constructed in hydrophobic materials. The influence of the roughness on the contact angles measured on the practical surfaces examined in this work is not easy to quantify and could be influenced by aspects of surface geometry that roughness values fail to quantify. Roughness is only one of many variables that influence the contact angle. However, for practical purposes, i.e. within the variation of the measurements themselves, the contact angle in milled microchannels appears to be equivalent to a polished surface.

5.1.3.6 Effect of Solid Material on the Contact Angle

Table 10 summarizes the average contact angles measured for a selection of liquid/solid systems. A complete list of all measured systems can be found in Appendix 8.2. The summary includes measurements conducted on both polished and machined surfaces and in all gas atmospheres and pressures since these parameters did not appear to substantially effect the data presented in Section 5.1.3.3. Drops are at least 8.5 μL in volume or 3.2 mm in base diameter.

Table 10: Contact angles measured for some liquid/solid systems

Liquid	Isopropanol	50 wt% Ethanol in Water	1M MEA	1M Na ₂ CO ₃	Glycerine	Water	
σ_{LV} (mN/m)	21.7 [152]	31 ± 1			57 ± 6	72 ± 2	
Contact Angle (°)	Glass	0	20 ± 2	46 ± 7	48 ± 15	80 ± 6	55 ± 16
	Stainless steel	0	26 ± 5	35 ± 3	48 ± 4	72 ± 7	79 ± 11
	PEEK	0	27 ± 5	53 ± 7	69 ± 4	77 ± 3	
	Polystyrene	0	28 ± 10	79 ± 9	82 ± 7	88 ± 9	79 ± 1
	PTFE	9 ± 4	53 ± 6	100 ± 5	98 ± 10 (0.5 M)	95 ± 6	97 ± 6

Table 10 also contains the surface tension of the investigated liquids if available. In general, the contact angles presented in this table follow the trend of Section 5.1.3.3 with the measured contact angle increasing with increasing liquid surface tension. There are, however, exceptions: for instance, the contact angle of water on glass is noticeably lower. The contact angles measured on glass and stainless steel also show greater variance than contact angles measured on other materials. Glass and stainless steel surfaces are typically hydrated by atmospheric water; therefore, the contact angles measured on these surfaces can depend on the atmospheric humidity and previous handling of the solid surface [155]. The solid surfaces in the table are generally organized from those with the lowest contact angles to those with the highest. PTFE consistently has the highest contact angle with all of the investigated liquids. It is more difficult to organize the other materials since their interactions with the liquids produce different responses. Polar, dispersive, and acid and base interactions between the solid and liquid materials must be considered in the development of the solid/liquid energy term [156]. The solid and liquid are clearly both important, but their interaction is difficult to characterize due to its complexity.

5.1.3.7 Effect of Reaction on the Contact Angle

It was not possible to measure the contact angle of solutions of NaOH directly in a CO₂ atmosphere because the reaction proceeds rapidly starting immediately when gas is introduced into the chamber. Measurements of the reactants in N₂ and of the products (Na₂CO₃) in both N₂ and CO₂ were collected. Na₂CO₃ may also react with CO₂ but much more slowly. Contact between the Na₂CO₃ solution and CO₂ was limited to the less than 2 min needed for the measurement in order to minimize the effect of this reaction. Averages of the measurements in all gases are given since the effect of the gas atmosphere is generally less than the overall standard deviation of the measurements. Figure 44 shows contact angles measured for the reactant and product solutions for the reaction of CO₂ with NaOH at several concentrations.

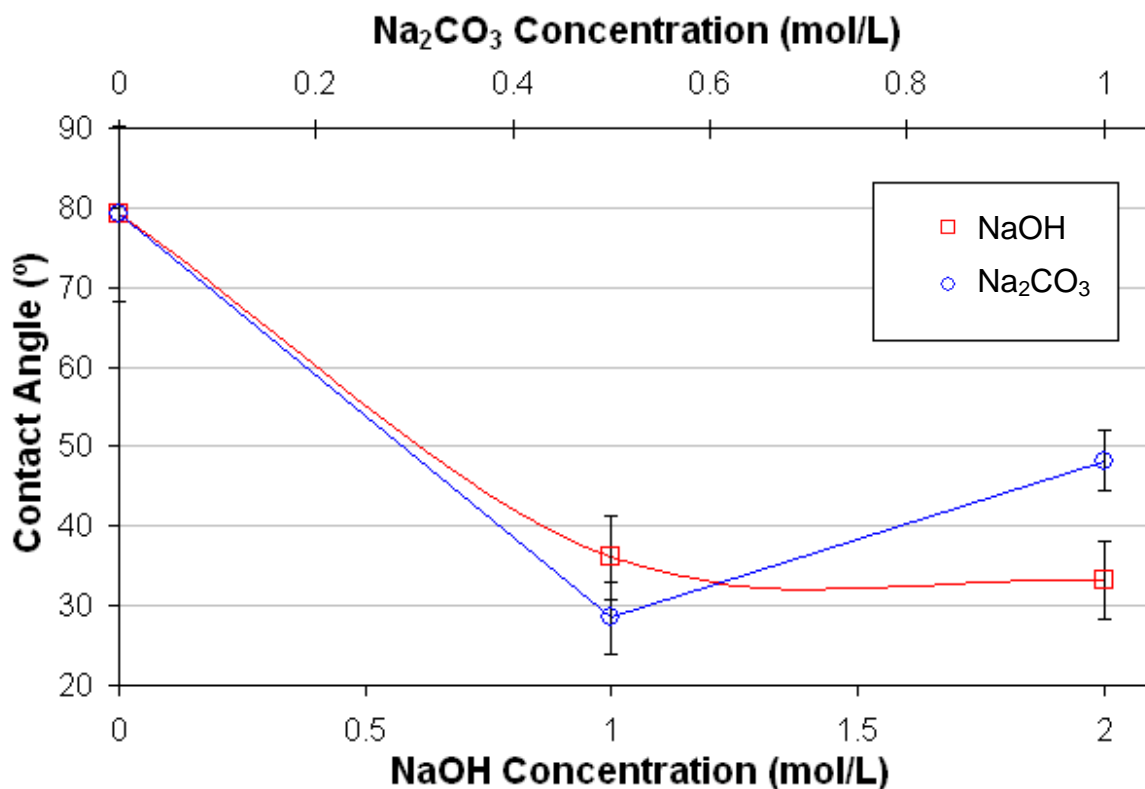


Figure 44: Difference in the contact angle of a drop of liquid on polished stainless steel between reactant (NaOH) and product (Na₂CO₃) for the reaction of CO₂ with aqueous NaOH

Figure 44 shows only small differences between the reactant and product solutions. The contact angles measured on PTFE (Appendix 8.2) were constant with a value of approximately 95 °. The scarcity of measurements and their overlapping standard deviations renders any conclusion tentative, but generally, the difference between the contact angles of the reactant solution and the product solutions do not appear to differ substantially.

5.1.3.8 Statistical Significance of the Investigated Parameters

Multiple linear regression analysis was performed for the complete set of contact angle measurements using the Data Analysis > Regression function of Microsoft Excel to determine the linear significance of gas/liquid surface tension, surface roughness, pressure, drop volume, and the fraction of CO₂ in the gas. The results are summarized in Table 11.

Table 11: Significance of investigated parameters on contact angle determined from a multiple linear regression analysis

Factor	Coefficient	p-value
σ_{LV} (mN/m)	1.229	5.8×10^{-131}
R_a (nm)	0.0223	1.9×10^{-31}
$P \times 10^{-2}$ (kPa)	-0.0123	0.97
V (μ L)	0.0661	8.8×10^{-16}
y_{CO_2}	-2.25	0.044

The p-value is a statistical measure that describes the chance of an observation occurring due to natural randomness. A very small p-value, typically less than 0.05, is considered to indicate a factor that shows a statistically significant linear relationship between the independent

variable and the response variable, in this case the measured value of the contact angle. A p-value of 0.05 represents a 5 % chance that the pattern observed can be attributed to randomness [157]. Failure to show a statistical significance does not mean that a factor is not relevant; it could also mean that the relationship between the factor and the angle is something other than linear.

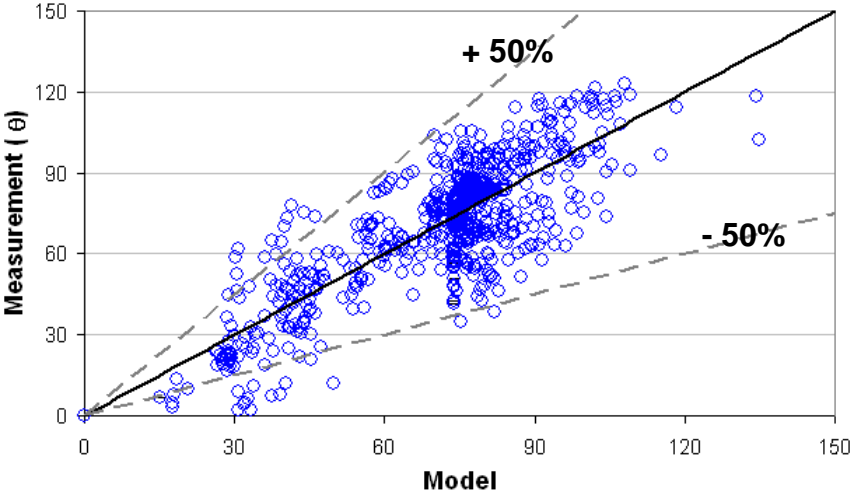


Figure 45: Experimentally measured values of contact angle shown against model

According to the linear regression analysis, the gas/liquid surface tension (σ_{LV}), the surface roughness (R_a), and the drop volume (V) are very clearly significant. The mole fraction of carbon dioxide (y_{CO_2}) in the gas phase also meets the criteria of $p < 0.05$. The pressure is the only factor that is not significant in this analysis. A parity plot showing the experimental values versus the values predicted from this regression model is shown in Figure 45. The model reflects the general trend of the data, but it should be noted that the solid material is nowhere accounted for in this analysis. Next to the gas/liquid surface tension, this factor is probably one of the most important as indicated in the Young equation.

5.2 DEPENDENCE OF GAS/LIQUID FLOW REGIMES ON MATERIAL PROPERTIES

Gas/liquid flow in horizontal glass and FEP capillaries was visualized for water and nitrogen two-phase flows with high speed videography as described in Section 4.2.1. Capillaries of 1.5–1.6 mm and 250 μm inner diameters were measured. Stills from these videos are presented in this section; however, they do not necessarily capture the transient nature of these phenomena. The videos are included as Appendix 8.4. Excerpts from this section have been published in [158].

Photos of gas/liquid flows in 1.6 mm glass capillaries are shown against a flow map of the gas and liquid superficial velocities in Figure 46. Plug flow occurs for liquid volume fractions (ϵ_L) as low as 0.1; slug and then annular flow occur with increasing relative amounts of gas. Photos of gas/liquid flows in a 1.5 mm FEP capillary are shown in Figure 47. The transition of plug flow to rivulet flow occurs at a gas superficial velocity between 1–10 m/s. Further increases in the gas superficial velocity break the larger rivulets into smaller rivulets, called “multi rivulet flow.” A comparison of the gas/liquid flows occurring under the same conditions for the 1.6 mm glass and 1.5 mm FEP capillaries is given in Table 12.

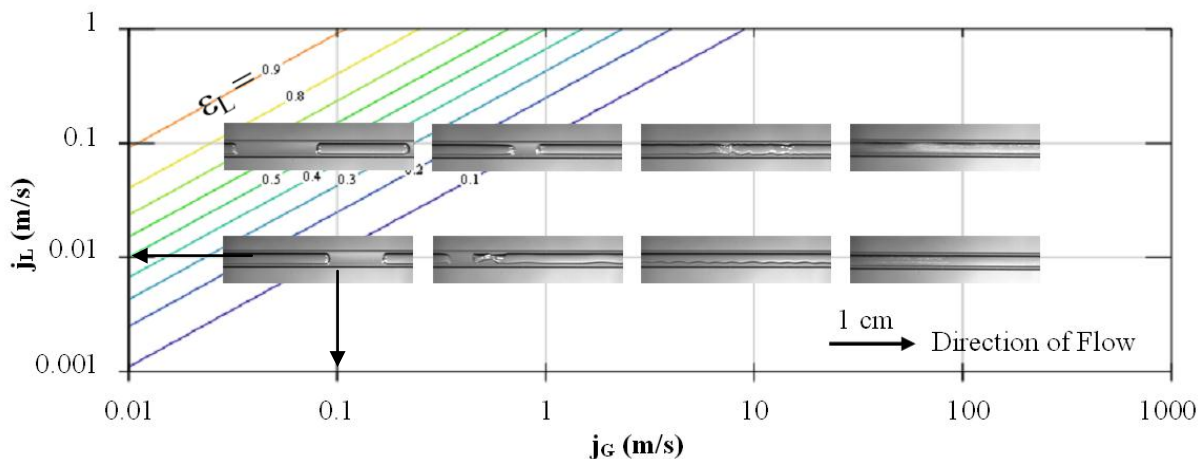


Figure 46: High speed photographs of gas/liquid flow in a 1.6 mm ID glass capillary shown against where they occur on a flow map

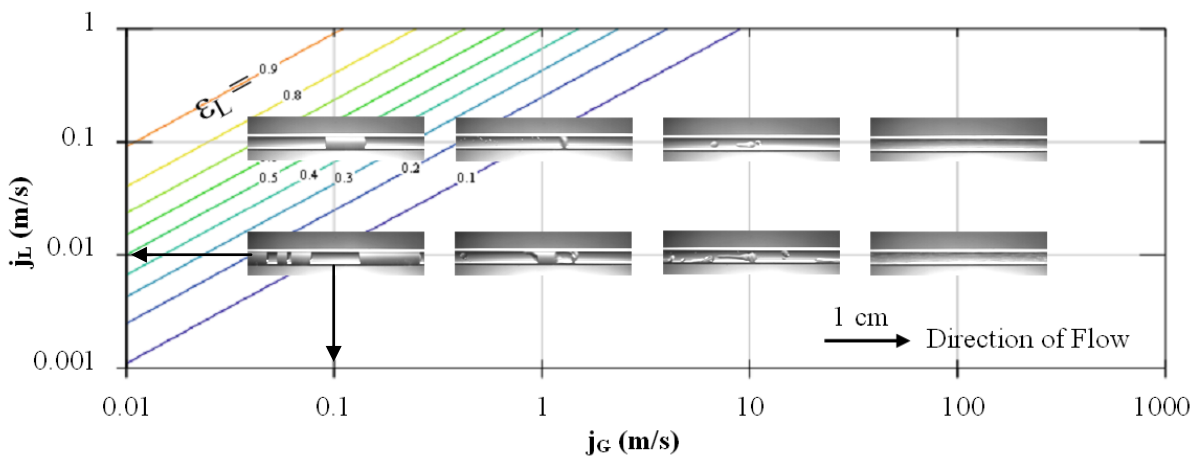
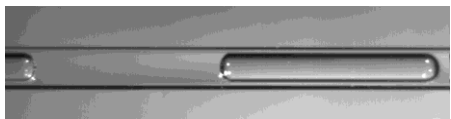

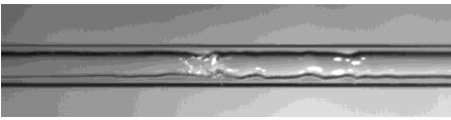
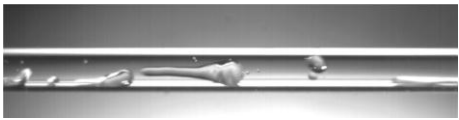
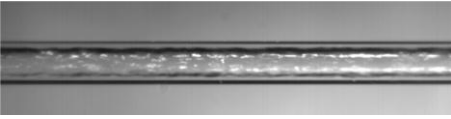



Figure 47: High speed photographs of gas/liquid flow in a 1.5mm ID FEP capillary shown against where they occur on a flow map

Table 12: Comparison of gas/liquid flows in 1.6 mm ID glass and 1.5 mm FEP capillaries at similar gas and liquid flow rates

j_L (m/s)	j_G (m/s)	Glass	FEP
0,1	0,1	 plug flow	 plug flow
0,1	10	 slug flow	 rivulet flow
0,1	50	 annular flow	 multi rivulet flow

At gas superficial velocities below 1 m/s, plug flow, also known as “Taylor flow,” predominates. As the gas flow rate increases, the gas slugs become longer for both capillaries. It is, however, possible that the plug flow in the glass capillaries differs from the plug flow in the FEP capillary, for example, with respect to the presence or absence of a liquid film between the gas bubble and the wall. It cannot be determined from the videos whether this film is present or not, but the characterization of the interfacial area through reaction could provide some insight into this question.

As the gas velocity continues to increase above the point at which the plug flow takes the form of very small liquid plugs separated by large gas plugs, the forms of the gas/liquid flows for the two capillaries diverge. In the FEP capillary the liquid plug becomes a drop or rivulet on the wall, pushed along by the gas. In the glass capillary the majority of the liquid appears to be spread as a thin film on the walls; the thickness of this film is variable, and when the liquid films on opposing walls approach each other until they block the gas flow, the liquid “slug” is rapidly accelerated along the capillary. Additional gas flow reduces the frequency of slug formation and eventually spreads the liquid on the walls thinly in “annular flow.” Annular flow does not consist of a flat liquid film; the liquid film contains obvious waves. In the FEP capillary additional gas flow serves to break up and further distribute the liquid rivulet into smaller rivulets in a flow pattern called “multi rivulet flow.”

Photos of gas/liquid flows in 250 μm glass and FEP capillaries are shown against a flow map of the gas and liquid superficial velocities in Figure 48 and Figure 49, respectively. A comparison of the flow regimes occurring under the same conditions for the 250 μm glass and FEP capillaries is given in Table 13.

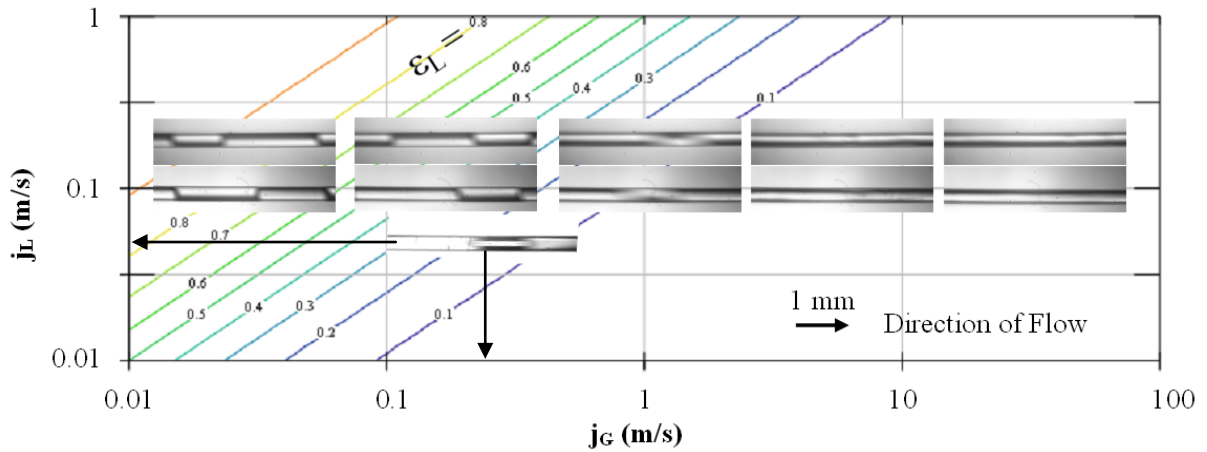


Figure 48: High speed photographs of gas/liquid flow in a 250 μm ID fused silica capillary

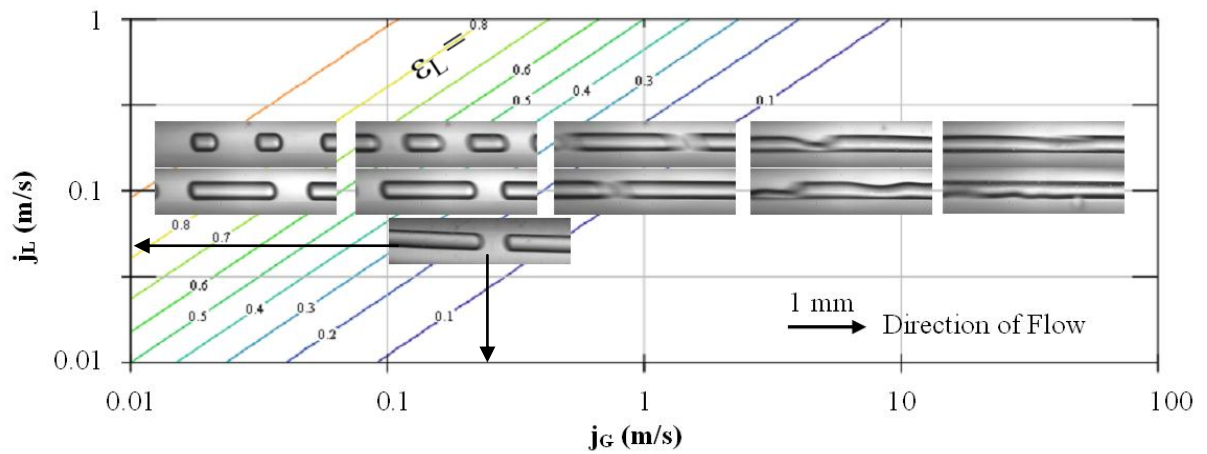
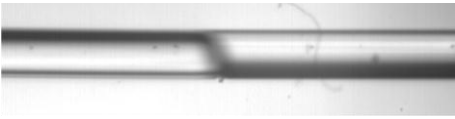
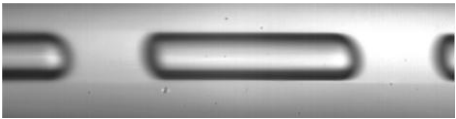
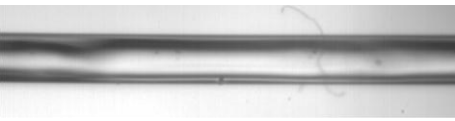
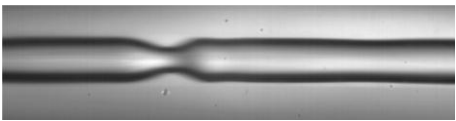
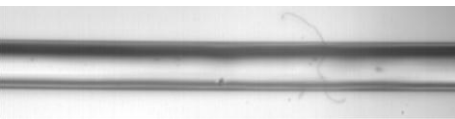
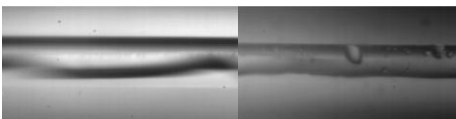


Figure 49: High speed photographs of gas/liquid flow in a 250 μm ID FEP capillary

Table 13: Comparison of gas/liquid flows in 250 μm ID glass and FEP capillaries at similar gas and liquid flow rates

j_L (m/s)	j_G (m/s)	Glass	FEP
0.124	0.04–0.05	 plug flow	 plug flow
0.124	4.35–5.03	 slug flow	 slug flow
0.124	17.86–18.08	 annular flow	 wavy flow

1 μm
Direction of flow →

The progression of flow patterns in the 250 μm capillaries looks very similar to those observed in the 1.5 mm capillaries. Plug flow occurs for small gas flow rates. The gas plugs initially grow longer with increasing gas flow rate. The glass capillary appears to demonstrate the same progression to slug flow and further to annular flow. The smaller scale seems to create more differences in the FEP capillary. Slug flow appears to form in the FEP capillary, seeming to indicate that the smaller capillary achieves a liquid film despite the hydrophobicity of the material. Further increases in the gas flow rate do not result in rivulets due to the small length scale, but the liquid flow passes along one side of the capillary and the other side remains dry. The liquid flow contains waves, occasionally switches sides, and can sometimes strand very fine droplets on the dry portions of the wall. These droplets remain until another wave bears them off.

There are a number of literature sources [13,14,19-22] that present gas/liquid flow patterns with respect to the gas and liquid superficial velocities at which they occur. The observations collected in this work are presented in a similar manner for glass/fused silica in Figure 50 and for FEP in Figure 51. For comparison, the transition boundaries between flow regimes determined in the work of Lee and Lee [9] and Triplett et al. [6] have also been shown. Triplett et al. examined air/water flows in glass capillaries of 1–1.5 mm inner diameter; Lee and Lee examined the flow of air and water or methanol in glass, “Teflon,” and polyurethane tubes of 1.46–2 mm inner diameter.

The comparisons of the results for 1.5 mm and 250 μm capillaries to each other and the literature show both similarities and differences in Figure 50 and Figure 51. For comparison, the transition boundaries between flow regimes determined in the work of Lee and Lee [9] and Triplett et al. [6] are also shown. The transition from plug flow to slug or rivulet flow occurs slightly later in FEP than in glass, and the data of Lee and Lee [9] matches the observations of this work better in this respect because they considered various materials.

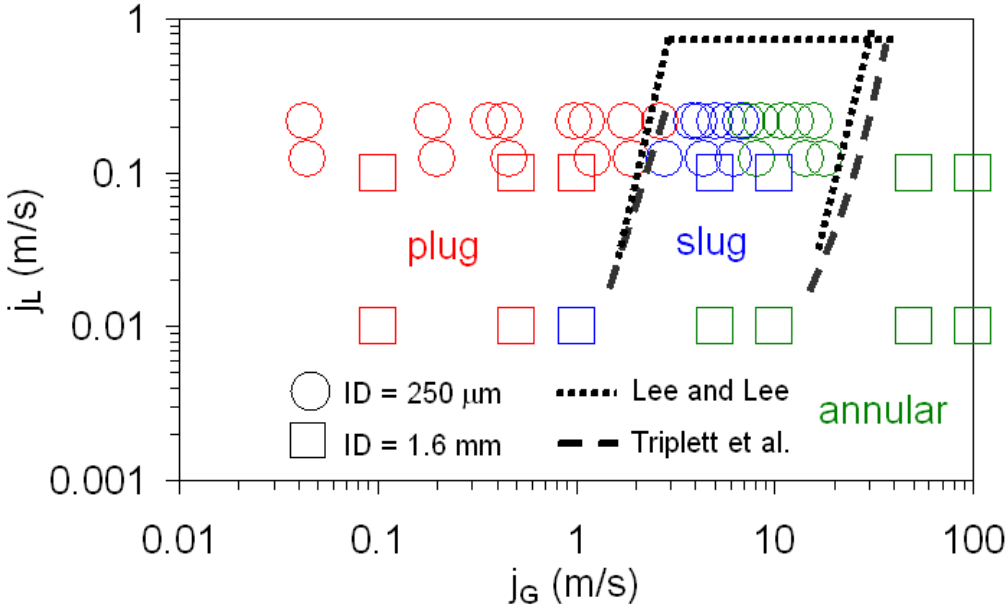


Figure 50: Gas/liquid flow patterns observed in 1.6 mm glass and 250 μm fused silica capillaries

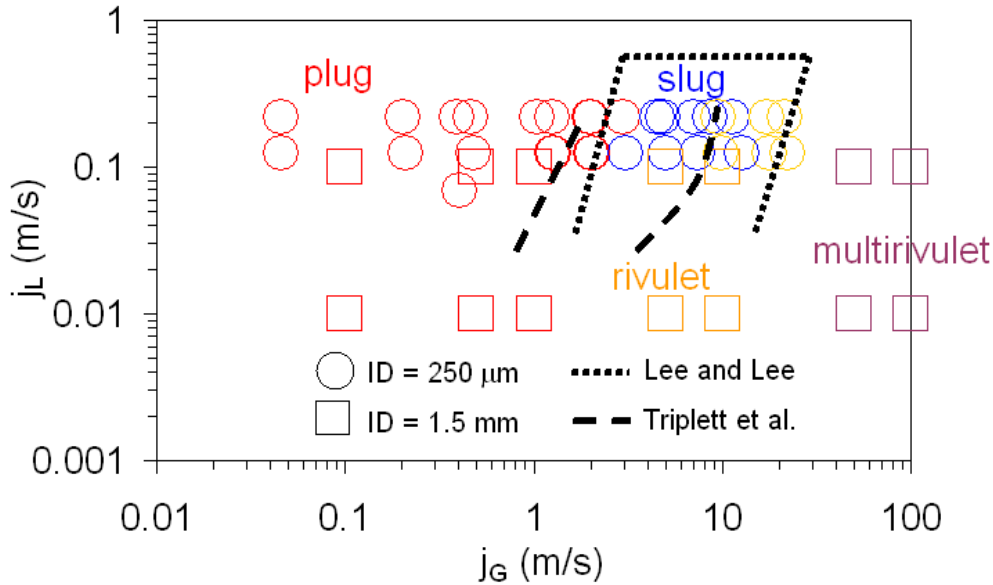


Figure 51: Gas/liquid flow patterns observed in 1.5 mm and 250 μm FEP capillaries

Figure 48 and Figure 49 show, in addition to the flow patterns, ε_L , the liquid volumetric fraction. In microchannels the residence time of the phases is the same for plug and slug flow. For annular and rivulet flow patterns the residence times of the phases may differ but are still related to each other. In the bubble column for the hydrogenation of benzene discussed in [159], the liquid residence time is on the order of hours, and the gas residence time is about two orders of magnitude smaller. Structuring bubble columns with plates or packings often serves not only to increase the interfacial area but also to lengthen the residence time of the gas phase [159]. Thus, for the adaptation of conventional gas/liquid processes to reactors using microchannels, the annular and rivulet flow regimes may be relevant at reactor inlets and for atmospheric processes, and plug flow may occur at reactor outlets if pure gas is used or at high pressures [160].

The observed flow patterns clearly depend on the capillary diameter and also on its wettability. Attempts have been made to devise flow maps that are generally applicable [9], but this task remains elusive due to the high number of compounding factors, including but not limited to: channel shape and size, material characteristics such as contact angle and surface roughness, densities and viscosities of the fluids, and interfacial tension. Indeed, the flow maps for small tubes or capillaries show little resemblance to the two-phase flow maps for pipes since the flow patterns encountered are substantially different. The flow pattern is difficult to reliably predict in practical situations due to the large number of relevant factors. What is the purpose of these flow maps? It is, of course, helpful to understand the hydrodynamics of the flow, but for the design of a reactor, it is even more important to have an idea regarding the pressure drop, interfacial area, and mass transport associated with the flow.

5.2.1 Reaction Conversion

Experiments using the absorption of CO₂ into 2 M solutions of NaOH corresponding to the flow regimes shown in Figure 48 and Figure 49 were conducted in PEEK, fused silica, and FEP capillaries of 250 μm inner diameter and 10 cm in length (see Table 8/Section 4.2.2). Conversions measured in the PEEK capillary for various molar fractions of CO₂ ($y_{\text{CO}_2,0}$) are shown in Figure 52 for a liquid superficial velocity of 0.05 to 0.07 m/s, Figure 53 for 0.11 m/s, and Figure 54 for 0.2 m/s. Increasing the gas flow rate not only affects the gas/liquid flow regime, it also changes the stoichiometry of the reactants. The maximum conversion of OH⁻ possible due to limiting gas reactant is shown as a continuous line on each graph. At low flow rates the reaction is limited by the amount of gas available.

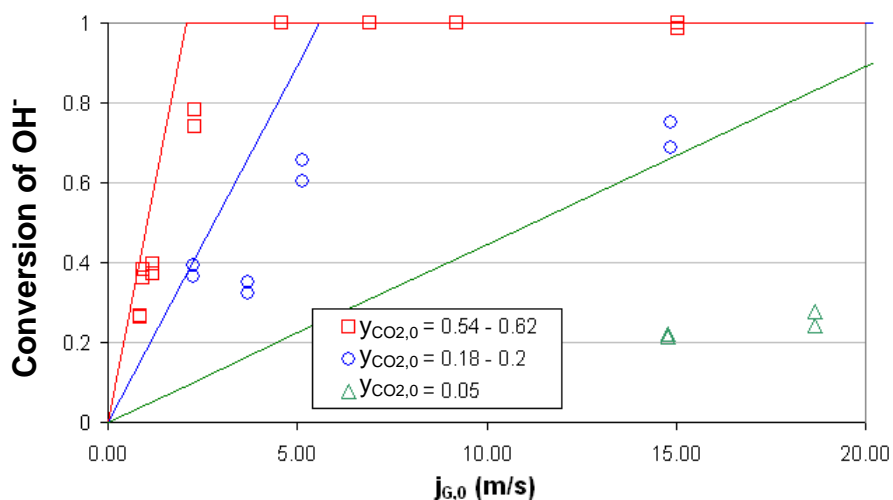


Figure 52: Conversion of OH⁻ measured for reaction of CO₂ ($y_{\text{CO}_2,0}$) with 2M NaOH in a 10 cm long, 250 μm ID PEEK capillary, $j_L = 0.05\text{--}0.07$ m/s (solid lines show maximum conversion possible due to limiting gas reactant.)

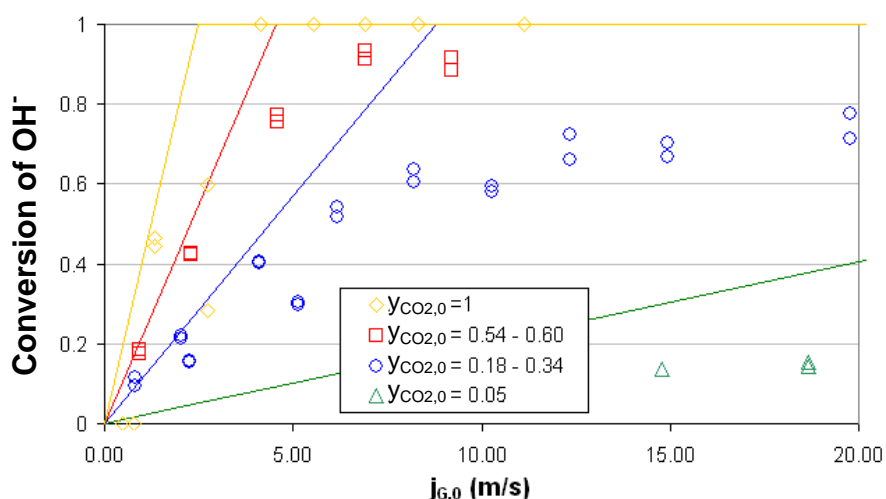


Figure 53: Conversion of OH⁻ measured for reaction of CO₂ ($y_{\text{CO}_2,0}$) with 2M NaOH in a 10 cm long, 250 μm ID PEEK capillary, $j_L = 0.11$ m/s (solid lines show maximum conversion possible due to limiting gas reactant.)

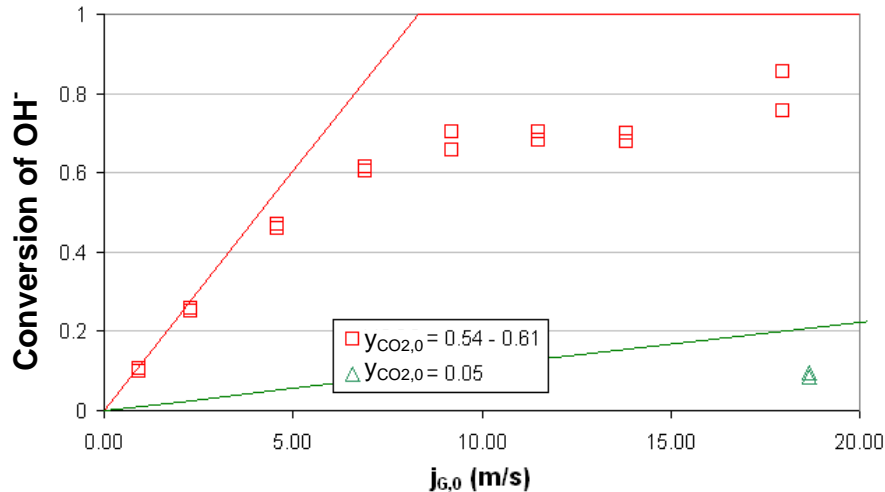


Figure 54: Conversion of OH^- measured for reaction of CO_2 ($y_{\text{CO}_2,0}$) with 2M NaOH in a 10 cm long, 250 μm ID PEEK capillary, $j_L = 0.20$ m/s (solid lines show maximum conversion possible due to limiting gas reactant.)

To maximize the amount of gas available, pure CO_2 would preferentially be used; however, a high pressure or partial pressure increases the concentration of dissolved gas at the interface, which increases the rate of gas uptake. Diluting the CO_2 and thus reducing the partial pressure reduces the rate of reaction and conversion. However, dilution can also introduce a mass transport resistance on the gas side. The necessity of using diluted CO_2 is demonstrated in Figure 53. Using pure CO_2 (diamonds), very few measurements show any difference between the maximum conversion possible and the actual conversion. With dilution and the resulting decrease in the rate of gas uptake, measurements for a wider combination of gas and liquid flow rates can be undertaken. The extent of dilution required depends strongly on the liquid flow rate and its residence time. As Figure 53 shows, higher liquid flow rates could be examined using higher gas partial pressures.

For the results to be comparable, the gas concentration must remain constant while the superficial gas velocity is varied. Experiments performed using similar mole fraction of CO_2 are compared in Figure 55, Figure 56, and Figure 57. The conversion decreases with increasing liquid flow rate but increases with the gas flow rate. With increasing flow rate, the residence time decreases, in tendency reducing the conversion reached since the reactor volume is constant. However, the pressure increases with the flow rate, resulting in a faster rate of reaction.

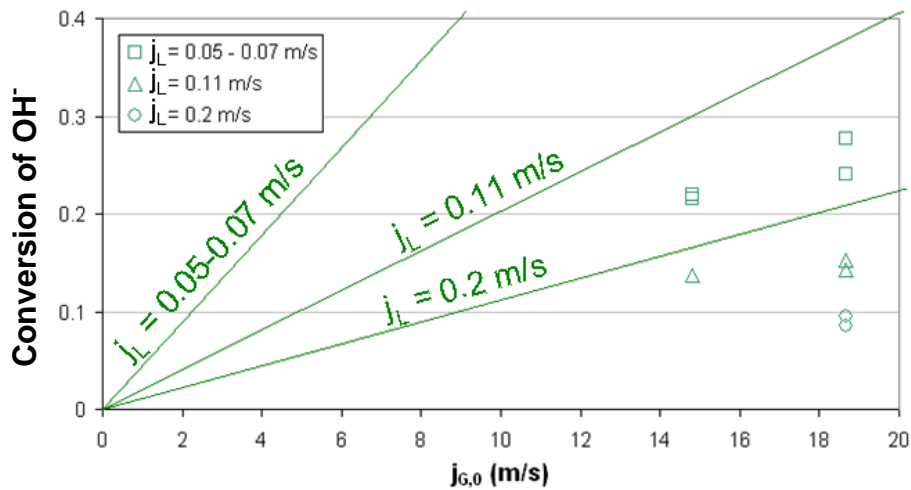


Figure 55: Conversion of 2M NaOH measured for reaction with different liquid flow rates in a 10 cm long, 250 μm ID PEEK capillary, $y_{\text{CO}_2,0} = 0.05$ (solid lines show maximum conversion possible due to limiting gas reactant.)

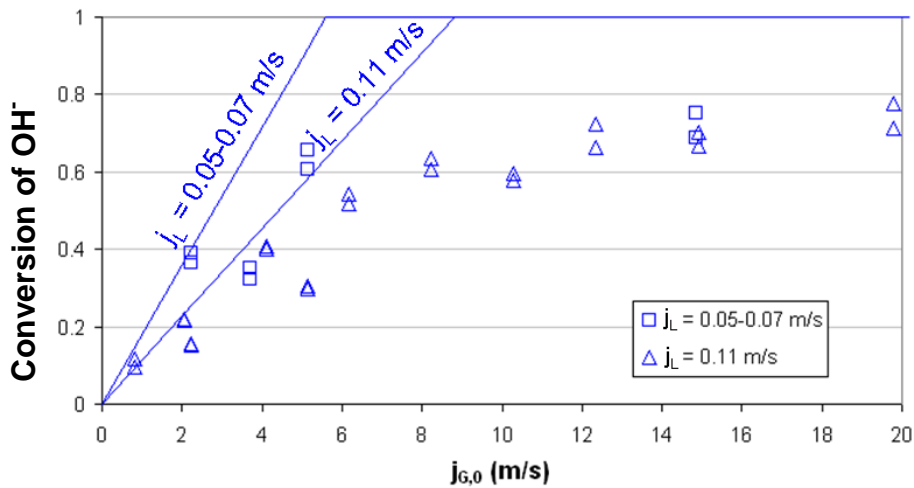


Figure 56: Conversion of 2M NaOH measured for reaction with different liquid flow rates in a 10 cm long, 250 μm ID PEEK capillary, $y_{\text{CO}_2,0} = 0.18\text{--}0.34$ (solid lines show maximum conversion possible due to limiting gas reactant.)

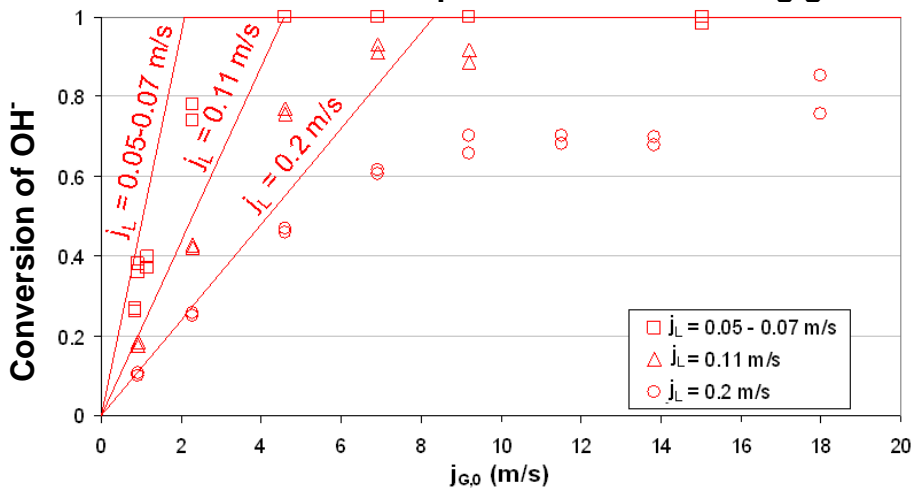


Figure 57: Conversion of 2M NaOH measured for reaction with different liquid flow rates in a 10 cm long, 250 μm ID PEEK capillary, $y_{\text{CO}_2,0} = 0.54\text{--}0.62$ (solid lines show maximum conversion possible due to limiting gas reactant.)

In the examination of flow regimes in Section 5.2, the transition from plug to slug flow occurred at a gas superficial velocity of 1–2 m/s, and the transition from slug to annular or rivulet flow occurred at around 5 m/s according to our observations and above 10 m/s in the investigations of Lee and Lee [9]. Unfortunately, the stoichiometry for the plug flow experiments is strongly gas limited and the conversion approaches the maximum for pure CO₂ as well as dilute. Therefore, no meaningful conclusions can be drawn from measurements in the plug flow regime. At the transition from slug to annular or rivulet flow between 5 and 10 m/s the conversion ceases to climb and levels out. The liquid holdup and liquid residence time are coupled to the gas flow rate for plug and slug flow since the gas and liquid plugs or slugs remain discrete and propel each other along the capillary. At the transition from slug to annular flow, the gas and liquid flows become decoupled, each occupying their own specific space. Since the two flows occupy different volumes within the channel, they may have different residence times. Thus, the observations regarding increases and leveling-off of the interfacial area for slug and annular flow can be understood through the observations of the flow patterns.

The same effects regarding the flow regime transitions, effect of gas partial pressure, and effects of gas and liquid flow rates were observed for the fused silica and FEP capillaries. The results for fused silica and FEP capillaries can be seen in Appendix 8.5. Comparisons of the conversion of OH⁻ achieved using similar gas partial pressures in the fused silica, PEEK, and FEP capillaries are shown in Figure 58 for a superficial liquid velocity of 0.11 m/s and in Figure 59 for a superficial liquid velocity of 0.2 m/s. The differences are more conspicuous for 0.2 m/s than for 0.11 m/s, but the trend is always the same: fused silica has the highest conversion; FEP has the lowest, and PEEK has a conversion in between but closer to fused silica. The conversion thus seems to be related to the wettability of the material. From Section 5.1.3, the contact angle of a drop of water on fused silica (glass) is approximately 50 °, on PEEK ~65 °, and on FEP ~95 °. The wettability influences both the flow regime as examined in Section 5.2 and the pressure drop as discussed in Section 5.2.3.

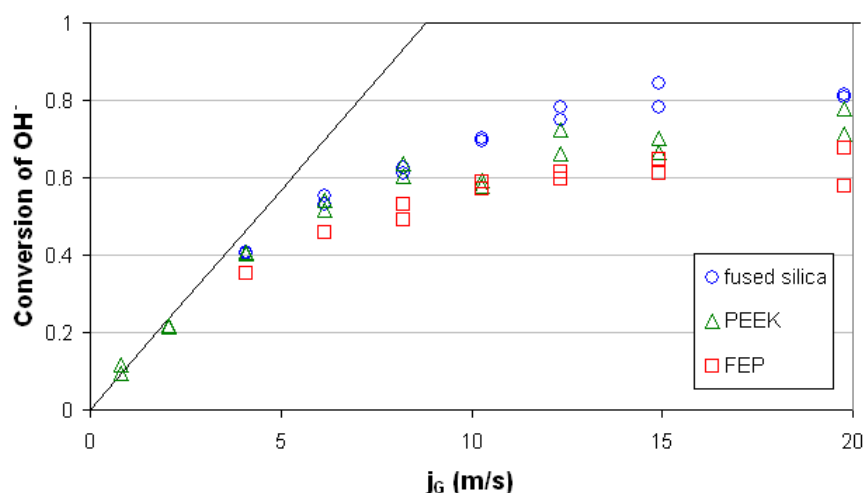


Figure 58: Conversion in fused silica, PEEK, and FEP capillaries, $j_L = 0.11$ m/s, $y_{CO_2,0} = 0.33$ – 0.34 (solid lines show maximum conversion possible due to limiting gas reactant.)

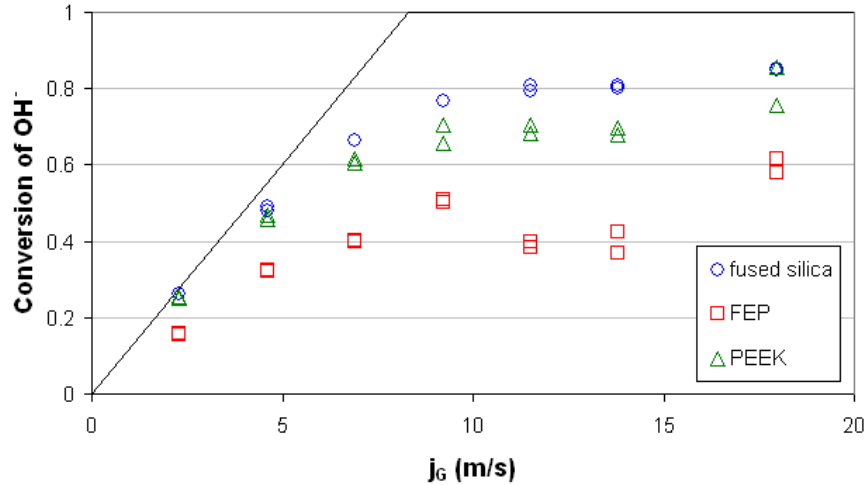


Figure 59: Conversion in fused silica, PEEK, and FEP capillaries, $j_L = 0.20$ m/s, $y_{\text{CO}_2,0} = 0.58\text{--}0.61$ (solid lines show maximum conversion possible due to limiting gas reactant.)

5.2.2 Interfacial Area

Average values of the interfacial area were derived from the measurements of reaction conversion assuming the reaction to be pseudo-1st-order with negligible gas transport resistance, i.e. the influence of a possible change in OH^- concentration across the liquid film on the reaction rate was neglected due to the high concentration of dissolved OH^- relative to the concentration of dissolved gas at the interface. The assumption of a pseudo-1st-order reaction is further discussed later in this section and also in Section 5.4.

The average rate of gas absorption (Φ) was calculated for the reactor volume. The rate of gas absorption was calculated from the conversion (Equation 28) of OH^- in the liquid collected at the reactor exit as well as the concentration of NaOH ($C_{\text{OH}^-,0}$) in the liquid feed and liquid volumetric flow rate (Q_L) divided by the reactor volume ($V_R = \pi r^2 L$):

$$\Phi = \frac{Q_L \cdot X_{\text{OH}^-} \cdot C_{\text{OH}^-,0}}{z \cdot V_R} \quad [37]$$

The rate of gas absorption was assumed to be described as a fast, pseudo-1st-order reaction with negligible gas transport resistance. A pseudo-1st-order reaction assumption is used to describe the situation where there is a large excess of liquid reactant, here dissolved OH^- , relative to the concentration of dissolved gas at the interface. For CO_2 in water the concentration of dissolved gas at the gas/liquid interface, assuming equilibrium at the interface, is 0.02 M, which is two orders of magnitude smaller than the starting concentration of NaOH. Due to the excess liquid reactant, any changes in its concentration within the liquid film can be considered to be negligible. Changes in the liquid concentration along the reactor length are not negligible, meaning that the Hatta number decreases along the length of the reactor. However, even at relatively high conversions, there is still an excess of NaOH. First at a conversion of OH^- of 0.99 the concentrations of liquid reactant and gas become equal.

The reaction of CO_2 with aqueous solutions of NaOH is a very fast reaction ($k_{\text{OH}^-} \approx 10^4$ L/mol·s [161]), which means that the Hatta number ($\text{Ha} = \sqrt{k_{\text{OH}^-} C_{\text{OH}^-} D_{\text{CO}_2} / k_L}$) is expected to be greater than 3, i.e. the rate of reaction in the liquid film is an order of magnitude larger than the rate of transport through the liquid film. Thus, the local rate of gas uptake (ϕ) can be

described by a mass balance on the liquid film, ignoring reaction/dissolved gas in the liquid bulk:

$$\phi = k_L a E \left(\frac{p_{CO_2,i}}{H_{CO_2}} - 0 \right) \quad [38]$$

Pseudo-1st-order reactions are convenient for characterizing the interfacial area because $E = Ha$ for second order reactions; thus, Equation 38 can be rewritten:

$$\phi = a \sqrt{D_{CO_2} k_{OH^-} C_{OH^-}} \left(\frac{p_{CO_2,i}}{H_{CO_2}} \right) \quad [39]$$

Figure 60 shows how well the assumption of $E = Ha$ fits the actual values of E (as calculated from the van Krevelen and Hofstijzer correlation [137]). The deviation between the assumption $E = Ha$ and the actual value of E increases with increasing Ha and is higher for lower concentrations. For a Hatta number of 10, the value of E is overestimated by 13.9% for 2 M NaOH solutions and 32.4 % for 1 M NaOH. Overestimation of E would result in artificially low values of a .

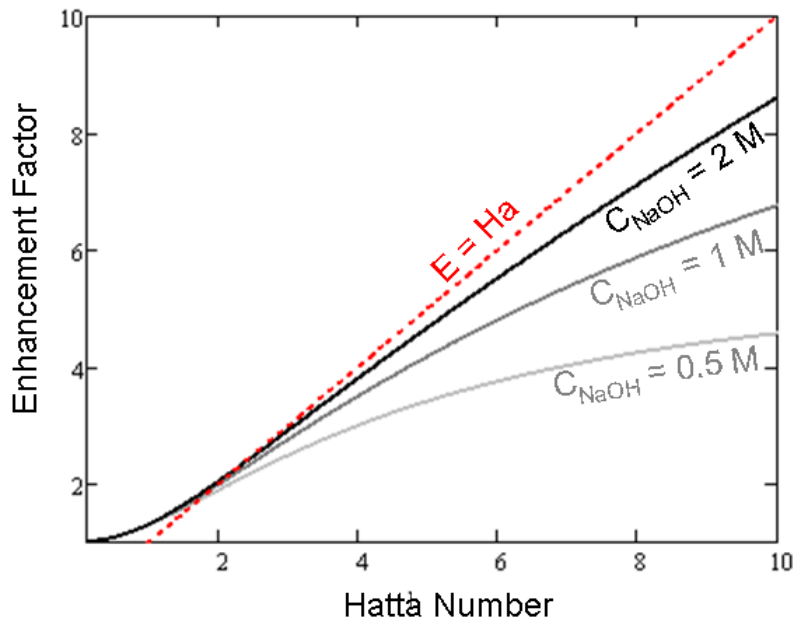


Figure 60: Enhancement factor versus Hatta number for the reaction of CO₂ with aqueous NaOH

The typical criteria for a pseudo-1st-order reaction, e.g. from [91], is $3 < Ha < E_i/2$. Figure 61 shows the value of the Hatta number for values of $k_L = 2.5 \times 10^{-4}$ m/s, $k_L = 5 \times 10^{-4}$ m/s, and $k_L = 10^{-3}$ m/s compared to the criteria $Ha = 3$ and values of E_i calculated for CO₂ pressures of 0.5 and 1 bar. For 2 M NaOH solutions, the criteria are fulfilled for k_L values larger than $k_L = 5 \times 10^{-4}$ m/s. Lowering the gas partial pressure to 0.5 bar further increases the range of validity for the pseudo-1st-order criteria. Compared to conventional gas/liquid reactors [91], these criteria would not be fulfilled for a bubble column, which has k_L values ranging from $1-4 \times 10^{-4}$ m/s, but may be fulfilled for sieve plate columns or tube reactors, which have k_L values ranging from $1-20 \times 10^{-4}$ m/s. In the literature mentioned in the introduction [65,153], k_L values between 3 and 13×10^{-4} m/s have been measured in microchannels. If the k_L value

in the capillaries studied here is equal to at least the lowest of these values, the criteria for a pseudo-1st-order reaction are fulfilled.

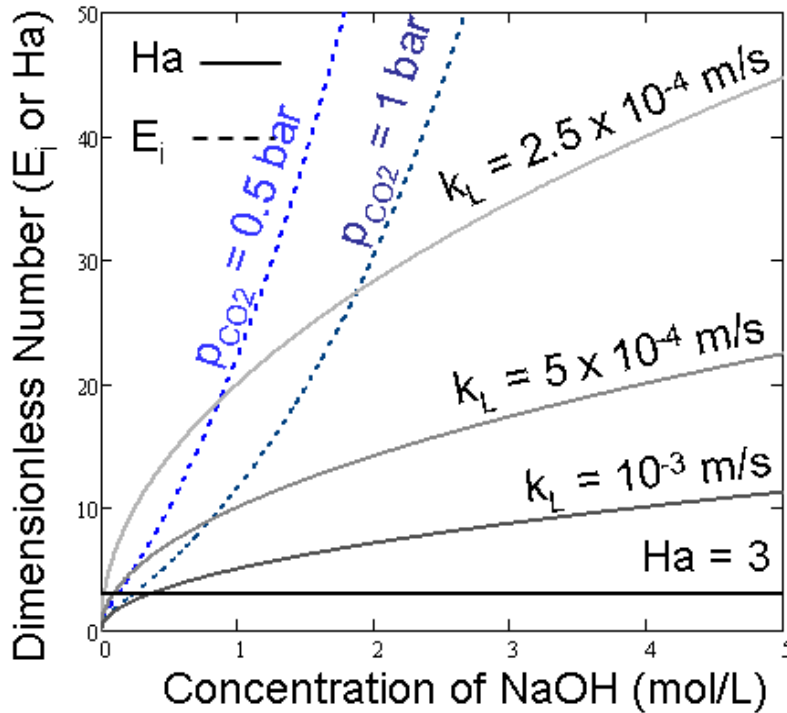


Figure 61: A Hatta number between 3 and E_i (shown for 0.5 bar and 1 bar) fulfills the criteria for a pseudo-1st-order reaction. The Hatta number depends on k_L .

Proceeding assuming that the reaction can be considered pseudo-1st-order, the average rate of gas absorption (Φ) is related to the local rates of absorption (ϕ) by integrating along the length of the capillary (L):

$$\Phi = \frac{1}{L} \int_0^L \phi dx \quad [40]$$

ut integration of Equation 39 requires knowledge of the profiles of C_{OH^-} and $p_{CO_2,i}$ along the capillary length. In this analysis the partial pressure of CO_2 has been assumed to be constant at the average value between the outlet and inlet partial pressure. The concentration change of OH^- is related stoichiometrically to the rate of gas absorption:

$$-\frac{dC_{OH^-}}{dx} = \frac{z\phi\pi r^2}{Q_L} \quad [41]$$

Substituting Equation 39 for ϕ , Equation 41 can be integrated

$$\int_{C_{OH^-,0}}^{C_{OH^-}} \frac{dC_{OH^-}}{\sqrt{C_{OH^-}}} = -\frac{z\pi r^2 p_{CO_2,i} a \sqrt{D_{CO_2} k_{OH^-}}}{Q_L H_{CO_2}} \int_0^x dx \quad [42]$$

to give C_{OH^-} as a function of the length (x):

$$2\sqrt{C_{OH^-}} - 2\sqrt{C_{OH^-,0}} = -\frac{z\pi^2 p_{CO_2,i} a \sqrt{D_{CO_2} k_{OH^-}}}{H_{CO_2} Q_L} x \quad [43]$$

$$\text{for } 0 \leq x \leq \frac{2Q_L H_{CO_2} \sqrt{C_{OH^-,0}}}{z\pi^2 a p_{CO_2,i} \sqrt{D_{CO_2} k_{OH^-}}}$$

where x is limited to a maximum value at which C_{OH^-} reaches 0.

$$C_{OH^-} = \left(\sqrt{C_{OH^-,0}} - \frac{z\pi^2 p_{CO_2,i} a \sqrt{D_{CO_2} k_{OH^-}}}{2H_{CO_2} Q_L} x \right)^2 \quad [44]$$

Note that the applicability of Equations 43 and 44 are further restricted to reaction conditions that fulfill the assumption of pseudo-1st-order reaction. The conversion of OH^- and correspondingly x are limited to conversions at which the assumption of pseudo-1st-order reaction kinetics is valid (i.e. $3 < Ha < E_i/2$).

The expression given in Equation 44 for C_{OH^-} can be substituted into Equation 39 and then integrated as specified in Equation 40.

$$\Phi = \frac{a p_{CO_2,i} \sqrt{D_{CO_2} k_{OH^-}}}{L H_{CO_2}} \int_0^L \left(\sqrt{C_{OH^-,0}} - \frac{z\pi^2 p_{CO_2,i} a \sqrt{D_{CO_2} k_{OH^-}}}{2H_{CO_2} Q_L} x \right) dx \quad [45]$$

$$0 \leq L \leq \frac{2Q_L H_{CO_2} \sqrt{C_{OH^-,0}}}{z\pi^2 a p_{CO_2,i} \sqrt{D_{CO_2} k_{OH^-}}}$$

$$\Phi = \frac{Q_L}{z\pi^2 L} \left(\left(\sqrt{C_{OH^-,0}} \right)^2 - \left(\sqrt{C_{OH^-,0}} - \frac{z\pi^2 p_{CO_2,i} a \sqrt{D_{CO_2} k_{OH^-}}}{2H_{CO_2} Q_L} L \right)^2 \right) \quad [46]$$

$$\Phi = \left(a \left(\frac{p_{CO_2,i}}{H_{CO_2}} \right) \sqrt{D_{CO_2} k_{OH^-} C_{OH^-,0}} - a^2 \left(\frac{p_{CO_2,i}}{H_{CO_2}} \right)^2 \left(\frac{z k_{OH^-} D_{CO_2} V_R}{4Q_L} \right) \right) \quad [47]$$

Equation 47 can then be solved using the quadratic equation to give a as a function of constants and measured variables:

$$a = 2 \left(\frac{H_{CO_2}}{p_{CO_2,i}} \right) \left(\frac{Q_L}{z V_R \sqrt{k_{OH^-} D_{CO_2}}} \right) \left(\sqrt{C_{OH^-,0}} - \sqrt{C_{OH^-,0} - \frac{z \Phi V_R}{Q_L}} \right) \quad [48]$$

The quadratic equation produces two roots for the solution of a ; however, the valid root is the one where a is 0 when Φ is zero, and a increases with increasing Φ .

Equation 48 can be used to determine values of a as long as the criteria for a pseudo-1st-order reaction are fulfilled and the transport resistance in the gas film can be neglected. Equation 48 is valid even for high conversions of OH^- , as long as the concentration of OH^- at the interface remains high relative to the concentration of dissolved CO_2 . Because Ha decreases with extent of reaction ($\text{Ha} = \sqrt{k_{\text{OH}^-} C_{\text{OH}^-} D_{\text{CO}_2} / k_L}$), the conditions at which the assumption of $\text{Ha} > 3$ is no longer fulfilled can be estimated by guessing a value of k_L . The condition of $\text{Ha} > 3$ is fulfilled for conversions of OH^- of up to 0.988, 0.955, and 0.820 for k_L values of 2.5×10^{-4} m/s, 5×10^{-4} m/s, and 10^{-3} m/s, respectively. In this work the application of this analysis for interfacial area has been limited to measurements where the conversion of OH^- is at most 95% of the maximum conversion possible.

The interfacial areas calculated for measurements with conversions of OH^- up to 95% are shown for PEEK, fused silica, and FEP in Figure 62 through Figure 64. The ratio between the surface area of the capillary wall and the capillary volume, $8000 \text{ m}^2/\text{m}^3$ for a $250 \mu\text{m}$ capillary, is shown on the interfacial area graphs for comparison. Table 14 summarizes the constants used in these calculations [161]. The reactor volume was $4.909 \mu\text{L}$.

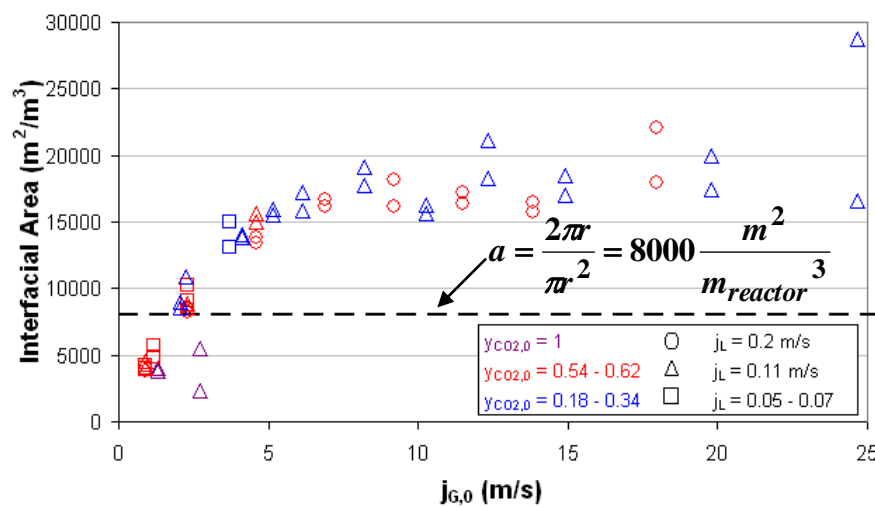


Figure 62: Interfacial areas calculated from measurements in a $250 \mu\text{m}$ ID PEEK capillary

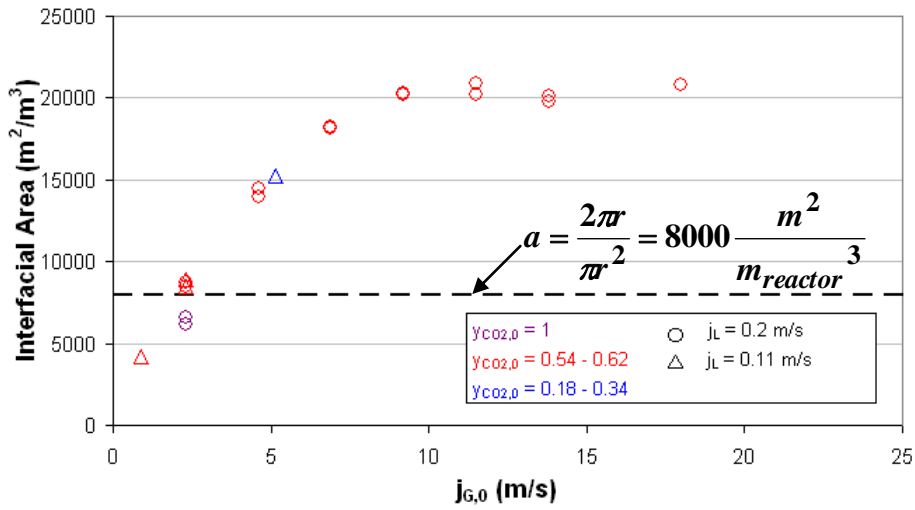


Figure 63: Interfacial areas calculated from measurements in a 250 μm ID fused silica capillary

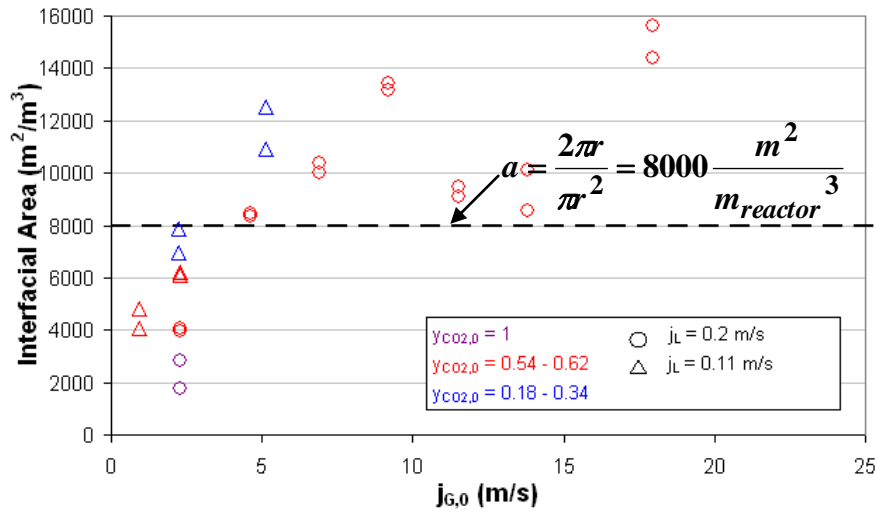


Figure 64: Interfacial areas calculated from measurements in a 250 μm ID FEP capillary

Table 14: Constants at 20 $^{\circ}\text{C}$ used for calculating interfacial area and transport coefficients (from [161])

Constant	Value
D_{CO_2}	$2.50 \times 10^{-5} \text{ cm}^2/\text{s}$
D_{OH^-}	$1.47 \times 10^{-5} \text{ cm}^2/\text{s}$
k_{OH^-}	$10^4 \text{ L/mol}\cdot\text{s}$
$C_{\text{OH}^-,0}$	2 mol/L
H_{CO_2}	$5 \times 10^3 \text{ L}\cdot\text{kPa/mol}$

For a gas superficial velocity of 2–3 m/s, the interfacial area was equal to the geometric surface area of the capillary in all materials. At superficial gas velocities above 10 m/s, a constant interfacial area approximately 50 % larger than the geometric surface area was established for PEEK and fused silica tubes. A constant surface area compares well to the observations in fused silica for the annular flow regime. The interfacial areas determined are more than double the geometric surface area of the capillaries at high superficial gas velocities; this may be attributed to ripples and waves on the interfacial surface seen with high speed videography. High speed videos of gas/liquid flow in the fused silica capillary showed that under these conditions annular flow occurred (Section 5.2).

In the hydrophobic FEP tube, the surface area above a gas superficial velocity of 5 m/s did not reach a constant value but first rose and then exhibited a local minimum at 10–15 m/s before rising again. The flow in the FEP tube under these conditions consists of rivulets or drops that are pushed along the wall. The size, position, and frequency of these rivulets could alter the interfacial area.

For gas/liquid flow in the plug and slug flow regimes, the interfacial area varies and is increasing with increasing gas velocity. In these regimes, the interfacial area may also be less than the geometric surface area of the capillary. Other authors [15,87,89] have observed that in plug flow the thin liquid film between the gas bubble and the wall can quickly become saturated. If only the caps of the bubbles contribute to the effective interfacial area, the *active* interfacial area (only this area will be assessed by characterization with chemical reaction) can be much smaller than the geometric surface area of the channel. Unfortunately, the plug flow regime is not well characterized in these experiments due to the limiting gas reactant and small differences between the observed conversion and the maximum conversion possible.

Experiments using reaction to probe the liquid film remain a promising method for exploring the existence and role of the liquid wall film and general nature of gas/liquid flows in microchannels. However, there are a number of weaknesses in the presented investigation and methodology which could be improved upon to gain further insight into gas/liquid flows:

- The gas is consumed by the reaction, meaning that the ratio of gas to liquid volume changes along the length of the reactor. This affects a number of variables. The flow regime may change. The parameter ε_L may not be constant but rather a function of reactor length. As such, the measurements presented here may be interpreted to be average estimates of the interfacial area for the conditions throughout the reactor, but they are not applicable to any exact flow regime or gas/liquid ratio.
- The residence time distributions for the gas and liquid phases also influence both conversion and ε_L . For plug and slug flow, the phases propel each other and would tend to have similar residence times. In annular flow, the gas likely has a significantly shorter residence time than the liquid.
- In these experiments the overall conversion of NaOH is high. This could be improved by increasing its concentration. However, this may affect the flow pattern (viscosity and wettability) and also has practical limits, i.e. solubility.
- In these investigations the examination of the plug flow regime was limited by too little gas. This can only be improved upon by using a different reaction (lower NaOH concentrations would not fulfill the requirements of a pseudo-1st-order reaction) or by working at a higher pressure. However, since this reaction cannot be easily quenched, working at higher pressures would require separating gas and liquid under pressure in a volume that is less than the microchannel volume itself. A technical solution to this problem is conceivable but not readily available [162]. Increasing the pressure would also increase the conversion of NaOH to the detriment of the previous point.

- There are a number of gradients along the length of the reactor that have not been considered when calculating the reaction rate over the entire reactor volume:
 - Changes in the liquid concentration (NaOH) have been included in this analysis, but only insofar as the assumption of pseudo-1st-order reaction kinetics remains valid. Since the Henry constant does not change much with changes in the concentration, this problem should not affect the results of a pseudo-1st-order reaction too much. However, changes from different reaction regimes, i.e. instantaneous reaction ($E = E_i$) or slower reaction ($E = 1$), may also occur with changes in the reactant concentration
 - The partial pressure of CO₂ used was the average of the inlet and outlet values. Depletion of CO₂ results in significant gradients in the rate of gas uptake along the reactor length.
 - A similar gradient is the overall pressure drop, which changes the flow pattern and volume occupied by the gas as well as the resulting partial pressure of CO₂.
 - This reaction is exothermic; temperature gradients along the reactor length are to be expected [63] and could alter both flow patterns and the reaction rate.

In the derivation of a , two important assumptions, namely negligible gas film transport resistance and pseudo-1st-order reaction kinetics were assumed. Based on the measurements, the assumptions can be reevaluated. When the interfacial area is known, Equation 38 can be rewritten to give k_L if E is known.

$$k_L = \frac{\Phi}{aE \left(\frac{P_{CO_2,i}}{H_{CO_2}} \right)} \quad [49]$$

E is not known but can theoretically have any value between 1 and E_i . Values of k_L were calculated for each measurement assuming $E = 1$ and $E = E_i$. Assuming $E = 1$, k_L values in a range of $5-7 \times 10^{-3}$ m/s were calculated; the values were similar among the different materials. Assuming $E = E_i$, k_L values between 2 and 2.6×10^{-4} m/s were determined for measurements using pure CO₂. Even if the lowest estimates of k_L were accurate ($E = E_i$), the measurements with pure CO₂ (assuming $E_i = 30 / Ha = 30$) would underestimate a by 37.3%, but measurements made with smaller partial pressures of CO₂ would fulfill the pseudo-1st-order criteria. Likewise, the higher estimate of k_L ($E = 1 / Ha = 1$) would overestimate a by 31%. The true value of k_L most likely lies between these two extremes, meaning that the criteria for a pseudo-1st-order reaction are fulfilled for the expected range of k_L values.

Changes in the reactant concentration or other reaction systems are necessary to determine a , k_G , and k_L . However, as this study shows, wettability can have a severe effect on both the flow and reaction in gas/liquid flow in microchannels. Thus, careful attention must be given to the effect of any changes in the reaction system on the wettability [63]. Further measurements using similar flow rates but a wider range of reactions are thus needed to develop comprehensive correlations for values of a and k_G and k_L in microchannel flows.

Transport in the gas film was also neglected. A precondition of the derivation of a is negligible gas transport resistance $\left(\frac{H_{CO_2}}{k_L E} \gg \frac{R_g T}{k_G} \right)$. Ideally, the gas film resistance would be calculated from k_G . However, the assumption of negligible transport resistance in the gas

film could be justified by the good overlap in determined values of a measured using different p_{CO_2} , including pure CO_2 , in Figure 62 through Figure 64. If the gas film transport resistance significantly influenced the rate of gas uptake, clear deviations in the values of a measured using lower partial pressures would be expected. The partial pressures examined here did not show a strong effect on the derived values of a .

The presented experiments obtain interesting information about the interfacial area, which are scarce information for the flow in microchannel reactors. These values indicate that the interfacial area for the gas/liquid reaction can be enhanced 50% over the intrinsic surface area of the microchannel by choosing materials promoting wettability or by applying coatings to modify surface properties [90]. Pseudo-1st-order reactions can be used to examine the interfacial area and thin liquid films existing in microreactors, but must be combined with other measurements to develop a complete understanding of gas/liquid flow and reaction.

5.2.3 Pressure Drop

From the inlet and outlet pressures measured during the experiments, the pressure drop across the system including the reduction to 250 μm tubing, across the T-junction, and in the 10 cm capillary length was calculated. The gas and liquid inlet pressures ranged from 1.1 bar to 2.1 bar (absolute). The liquid inlet pressure was typically slightly higher than the gas inlet pressure, by approximately 0.05 bar. Pressure drops measured for the experiments in the 250 μm ID capillaries are shown in Figure 65 and Figure 66. These graphs correspond to the same experiments as the plots of conversion shown in Figure 58 and Figure 59. The plots of conversion and pressure drop reveal similar trends. The pressure is accounted for when calculating the reaction rate, so the interfacial areas and transport coefficients determined already include this effect.

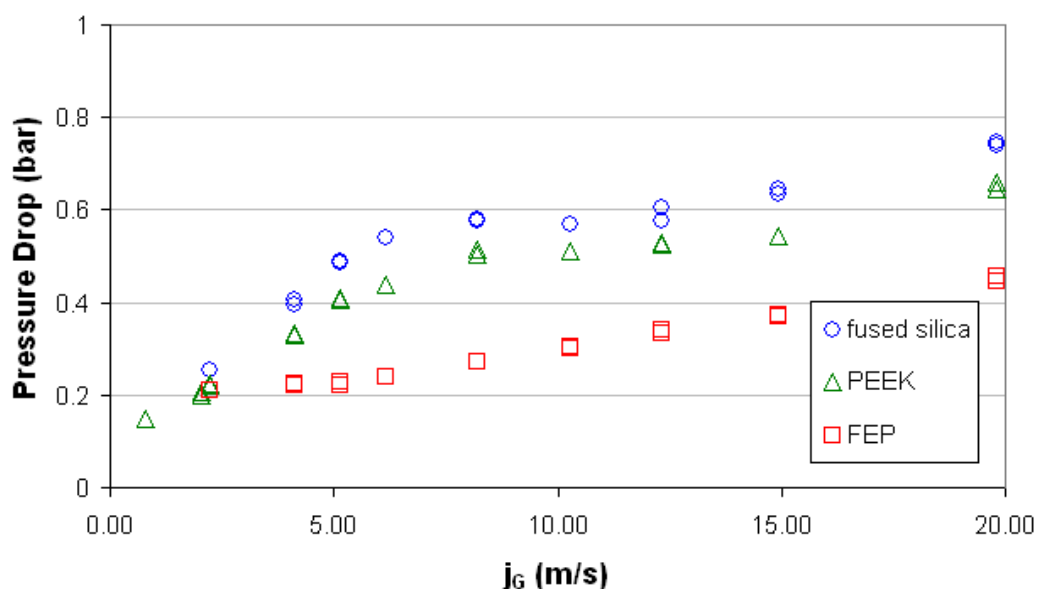


Figure 65: Pressure drop in fused silica, PEEK, and FEP capillaries for the reactive flow of 2M NaOH and CO_2 , $j_L = 0.11$ m/s, $y_{\text{CO}_2,0} = 0.18\text{--}0.34$

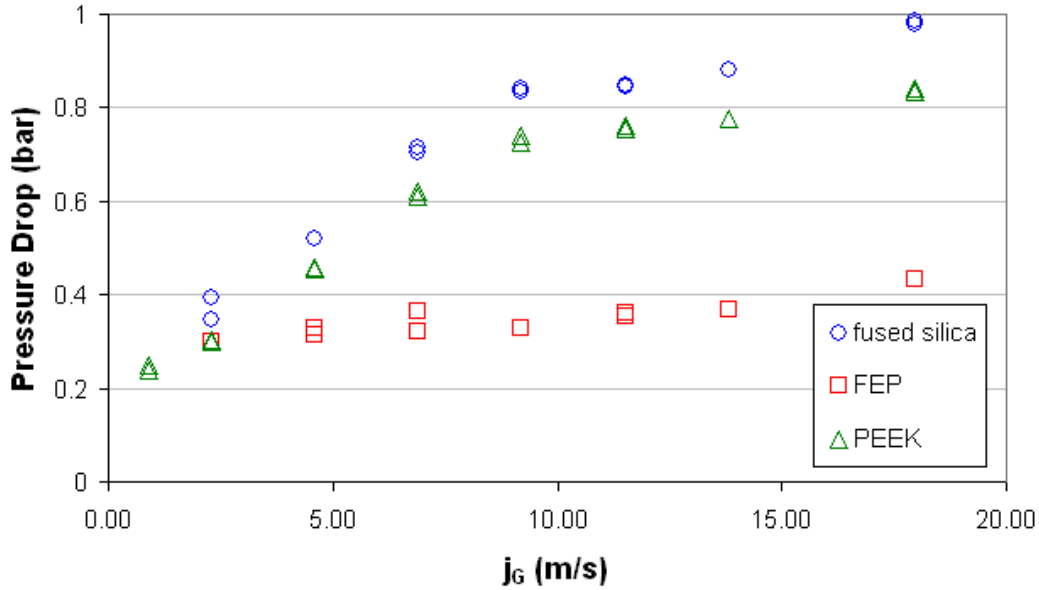


Figure 66: Pressure drop in fused silica, PEEK, and FEP capillaries for the reactive flow of 2M NaOH and CO₂, $j_L = 0.20$ m/s, $y_{CO_2,0} = 0.54-0.61$

The pressure drop of the fused silica capillary is substantially higher than that of the FEP capillary. The pressure drop of the PEEK capillary lies in between but closer to that of the fused silica capillary. Lee and Lee [163,164] observed that the pressure drop for Taylor flow (plug flow) was slightly higher in “Teflon” and polyurethane tubes than in glass for tubes ranging in inner diameter from 1.62 to 2.16 mm. They attributed the difference to increased energy dissipation at the three-phase line that exists between the gas and bubble plugs in hydrophobic materials. In hydrophilic materials, where a film of liquid surrounds the gas bubble, Lee and Lee [163,164] explained that the energy drop in glass tubes was less due to the lubricating effect of this film. For most of the measurements, the slug or annular flow pattern would be expected to occur for the high gas velocities investigated. In conventional reactors, energy dissipation is related to interfacial area and additional energy input is required to increase the interfacial area. The observations of pressure drop may be explained through the same effect since pressure drop in the flow is essentially a measure of energy dissipation.

5.2.3.1 Lockhart-Martinelli Correlation for Gas/Liquid Flows

Pressure drop in gas/liquid flows can be calculated according to the initial observations of Lockhart and Martinelli [165] and the correlations proposed by Chisholm [166]. This approach assumes that the pressure in each fluid is equal at each point along the length. The total pressure drop, ΔP , is related to the individual pressure drop of the gas flow $\left(\frac{\Delta P}{\Delta L}\right)_G$ or liquid flow $\left(\frac{\Delta P}{\Delta L}\right)_L$ alone in the pipe and a two-phase multiplication factor, ϕ_L or ϕ_G .

$$\Delta P = \left(\frac{\Delta P}{\Delta L}\right)_L \phi_L^2 = \left(\frac{\Delta P}{\Delta L}\right)_G \phi_G^2 \quad [50]$$

In these calculations, the individual pressure drops for the gas flow and liquid flow are combined into the Martinelli parameter, X:

$$X_M = \frac{\left(\frac{\Delta P}{\Delta L}\right)_L}{\left(\frac{\Delta P}{\Delta L}\right)_G} \quad [51]$$

The gas and liquid phase multiplication factors are functions of X and a constant C , which ranges from a value of 5 for laminar flow in each phase to a value of 20 for turbulent flow in each phase.

$$\phi_L^2 = 1 + \frac{C}{X_M} + \frac{1}{X_M^2} \quad [52]$$

$$\phi_G^2 = 1 + CX_M + X_M^2 \quad [53]$$

Yue et al. [167] showed that the Lockhart-Martinelli correlation significantly underpredicts the pressure drop in small channels with Reynolds numbers below 1000 and, on the basis of experimental measurements for air and water in rectangular microchannels, proposed a correlation for C :

$$C = 0.411822X_M^{-0.0305} \text{Re}^{6.00428} \quad [54]$$

In this correlation the Reynolds number is calculated for a hypothetical purely liquid flow using the properties of water for the gas and liquid flow rates combined.

The Lockhart-Martinelli correlation has been used to describe the observations of pressure drop from the experiments presented in this section by Fröhlich [168]. Fröhlich was able to fit the pressure drop in each material by adjusting the value of C and using the Hagen-Poiseuille equation to calculate the single phase pressure drops for laminar flow. He obtained values of $C = 6.5$ for fused silica, $C = 5$ for PEEK, and $C = 2.5$ for FEP.

The ground for the differences in the pressure drops observed cannot be readily explained. As shown in Section 5.1.2, the surface roughnesses of the materials are not substantially different. Since the Lockhart-Martinelli correlation is based on the pressure drops of the single phases, the descriptions and values for the single phase pressure drops were investigated.

5.2.3.2 Single Phase Pressure Drops: Liquid

Pressure drop due to frictional losses for incompressible flow in a straight pipe can be calculated according to the Darcy-Weisbach equation [169]:

$$\Delta P = f \frac{\rho j^2 L}{2D} \quad [55]$$

Where f is the Darcy friction factor used in the Moody diagram;
 ρ is fluid density;
 j is the average liquid velocity;
 L is the length of the pipe;
and D is the pipe diameter.

For laminar flow, the friction factor is a simple function of Reynolds number. Due to the Re in the denominator of the friction factor, the Darcy-Weisbach equation for laminar flow is equivalent to the Hagen-Poiseuille equation, and the pressure drop varies linearly with flow rate.

$$f = \frac{64}{Re} \quad [56]$$

The friction factor for turbulent flow can be calculated from the Moody diagram via an empirical relation:

$$f = \left(\frac{1}{-0.86 \ln \frac{Ra}{3.7D}} \right)^2 \quad [57]$$

where R_a is the roughness. A roughness of 0.0015 mm is typical for extruded tubing [169].

The pressure drops of single phase water flows were measured in various lengths of the four capillaries. The pressure drop in the capillary was determined as the difference between the pressure drops measured in two lengths of capillaries divided by the difference in length. The results are plotted in terms of flow rate and Re in Figure 67.

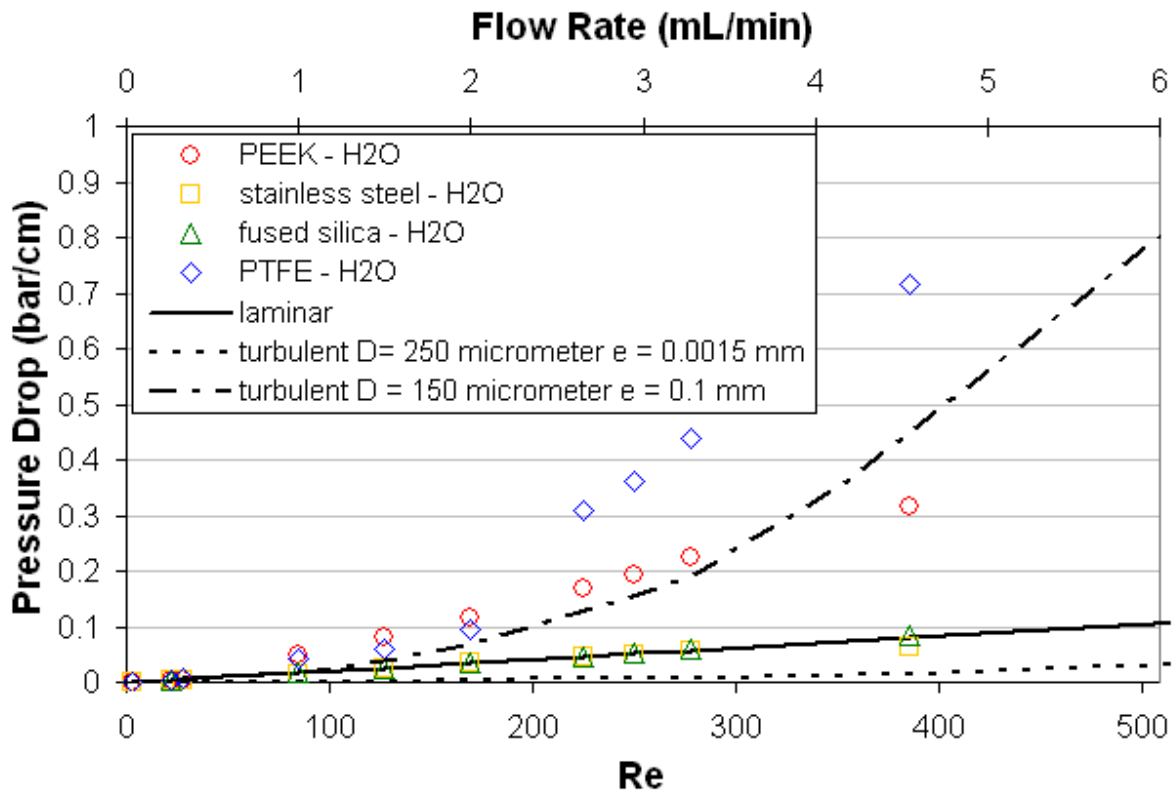


Figure 67: Pressure drops for the flow of water in PEEK, stainless steel, fused silica, and PTFE capillaries of 250 μm diameter

The pressure drops measured in the stainless steel and fused silica capillaries fit the pressure drops predicted for laminar flow from Equations 55 and 56. The pressure drops in the PEEK and PTFE capillaries are significantly higher than those predicted. The equations used to estimate the pressure drop for turbulent flow should only be used at Re greater than 4000. The transition from laminar to turbulent flow typically begins around a Re of 2000 although the transition has been reported for Re as low as 400 in microchannels [170]. Turbulent flow equations assuming a smaller diameter of 150 μm and an extreme surface roughness of 0.1 mm, nearly as large as the channel itself, still don't predict the pressure drops measured in the PTFE capillary, so these observations cannot possibly be attributed to greater surface roughness or poor tolerances resulting in capillaries of reduced diameter (see Section 5.1.2).

The pressure drops were also measured using isooctane, a nonpolar liquid. The results are shown in Figure 68. For isooctane the pressure drop in each material is similar, and the values are approximately described by the equations for laminar flow as given in Equations 55 and 56.

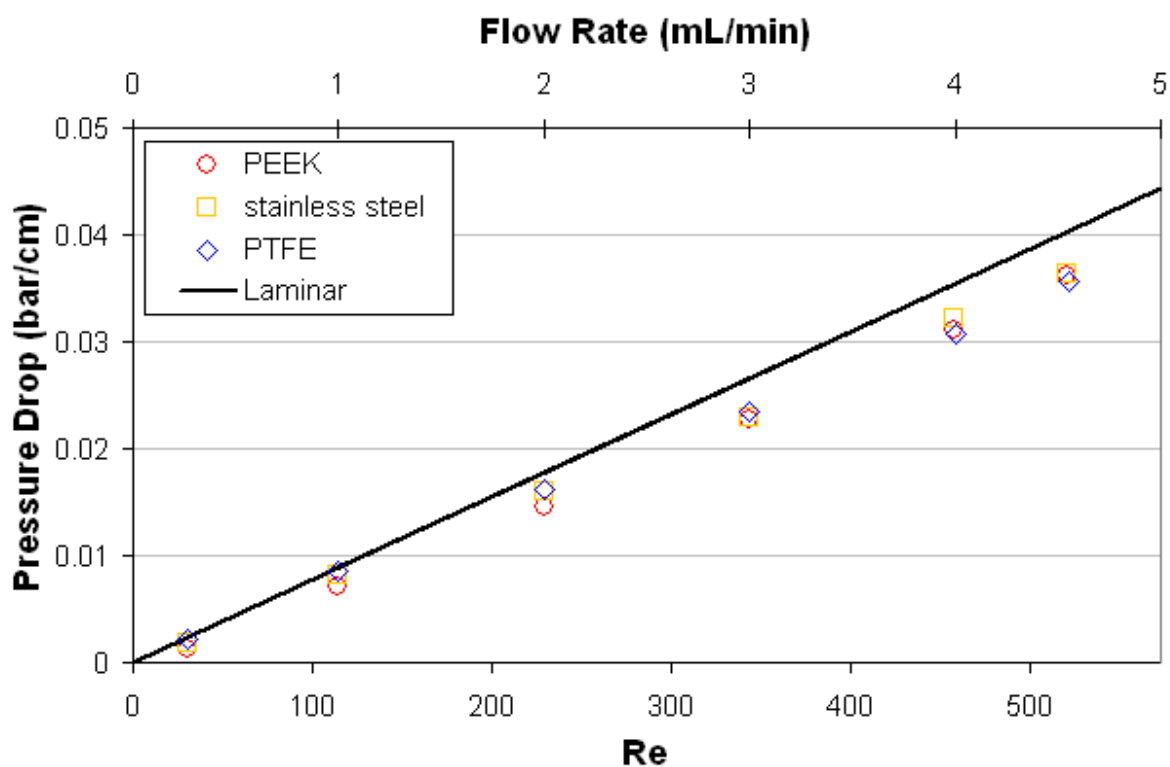


Figure 68: Pressure drops for the flow of isooctane in PEEK, stainless steel, and PTFE capillaries of 250 μm inner diameter

The pressure drop measurements were conducted by first measuring the pressure drop for a length of 10 cm and then cutting the capillary to a length of 2 cm without changing the fittings. Since the fittings were not changed, the pressure drop should only reflect the pressure drop in the 8 cm length of capillary. Because the original capillaries were destroyed during the measurements, repeat measurements were not possible. The large pressure drops observed for the flow of water in the polymer PEEK and PTFE capillaries but not in glass and stainless steel capillaries may be attributed to triboelectric charging of the capillary wall. The problem of static electricity build up is well known in the context of flammable liquids, where a static discharge can ignite the liquid; however, literature indicating an influence of this effect on the pressure drop is unknown to the author.

5.2.3.3 Single Phase Pressure Drops: Gas

For isothermal, subsonic, compressible flow in a round, rigid pipe, the mechanical energy balance/Bernoulli equation can be written [171]:

$$P_0^2 - P_L^2 = G^2 \frac{R_g T}{M_W} \left(\frac{4fL}{D} + 2 \ln \left(\frac{\rho_1}{\rho_2} \right) \right) \quad [58]$$

G is the mass flow rate divided by the cross-sectional area of the pipe. P_0 is the pressure at the pipe inlet, and P_L is the pressure at the outlet of the pipe with a length of L.

The pressure drops measured for the flow of carbon dioxide and nitrogen gas through the various capillaries are shown in Figure 69 and Figure 70. Laminar and turbulent pressure drops calculated for incompressible fluids using the properties of carbon dioxide are shown in black. The pressure drops calculated for incompressible flows of each gas are shown in blue.

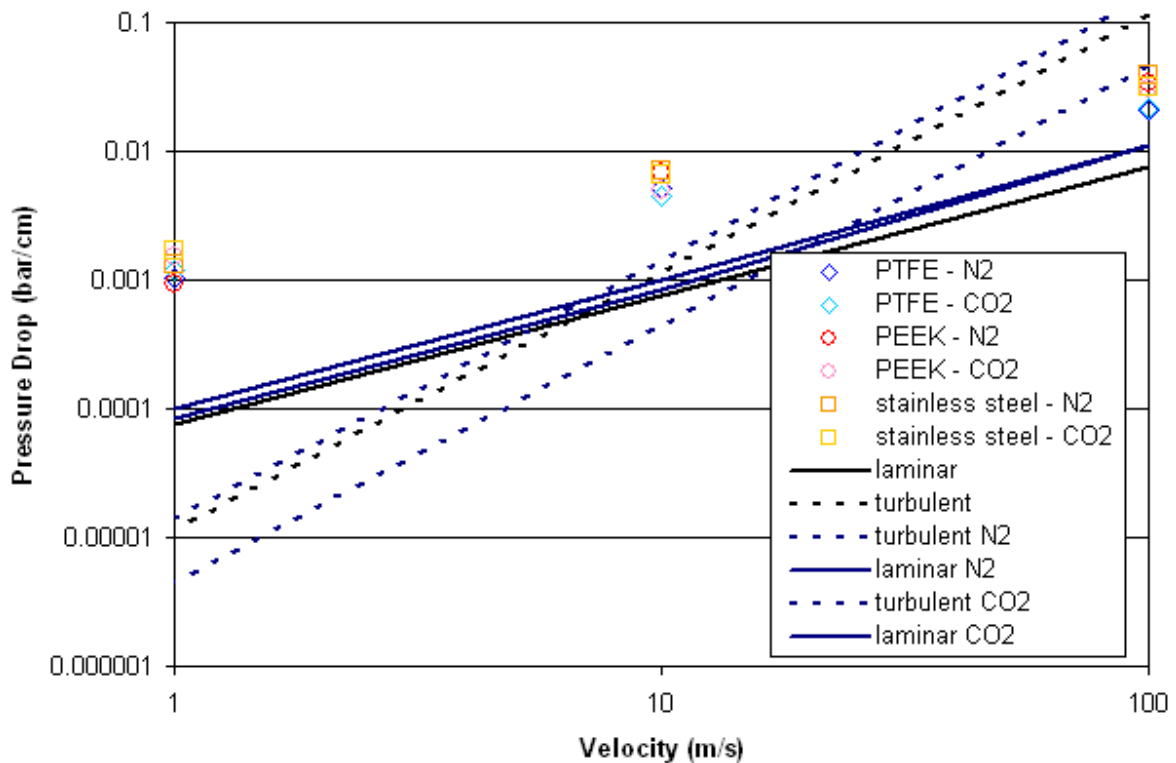


Figure 69: Pressure drop for the flow of gas in PEEK, stainless steel, and PTFE capillaries of 250 μm inner diameter

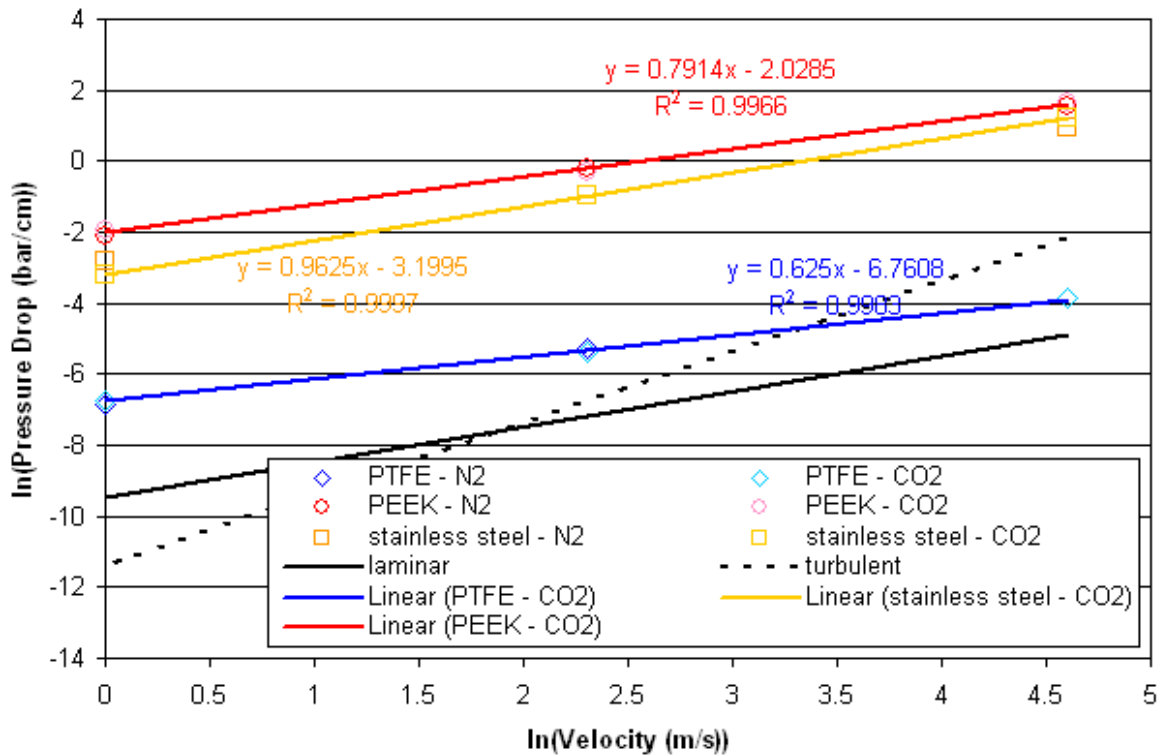


Figure 70: Correlations for pressure drop of gas in capillaries

None of the pressure drop models accurately describe the pressure drops measured in this range. The pressure drop for the flow of a gas should also scale according to the dimensionless Reynolds number; however, the densities of nitrogen and carbon dioxide differ substantially, but as can be seen in Figure 70, the pressure drops of the gases are nearly identical and can be nicely scaled through a logarithmic relationship depending only on the gas flow rate and not on any properties of the gas.

5.3 THERMOGRAPHIC INVESTIGATION OF A MICROSTRUCTURED FALLING FILM REACTOR

Experiments to determine local rates of reaction and mass transport coefficients were performed on the microstructured falling film reactor described in Section 4.2.3. These experiments have been published in [63].

Temperature profiles along the centerline of the reactor were extracted from thermographic images collected of the reactor when the reactor had reached a steady temperature profile for three experiments:

1. dry: for a high liquid flow rate of 30 mL/min using dry carbon dioxide directly from the gas bottle
2. humid: for the same liquid flow rate (30 mL/min) but prehumidifying the carbon dioxide
3. complete conversion: for a low liquid flow rate of 5.2 mL/min where the reaction reaches completion in the middle of the reactor

The temperature profiles for the three experiments are shown in Figure 71. The raw measurement data is included in Appendix 8.6. The temperature profiles were fitted with splines to smooth out small variations between the measurement points. The temperatures rise steadily along the reactor length for the first two experiments, but for the third experiment, where the reaction reaches completion before the reactor exit, the temperature peaks after about the first third of the reactor length and then decreases. The conversions for the dry and humid experiments were measured via titration to be 78 % and 76 %, respectively. The conversion for the high conversion experiment was 100 %.

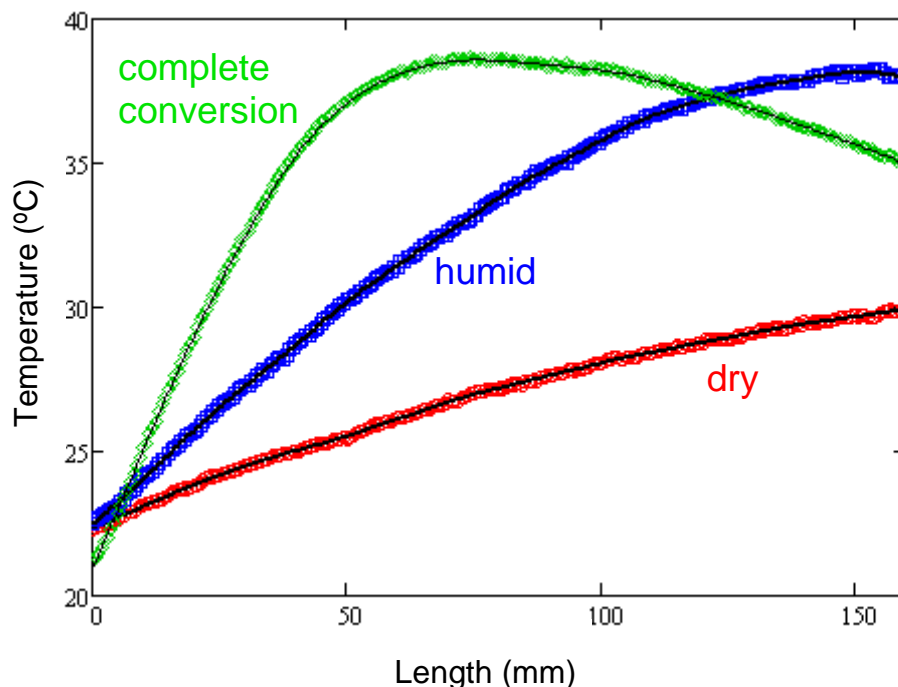


Figure 71: Temperature profiles extracted from thermographic images of falling film reactor for dry and humid experiments ($Q_L = 30$ mL/min, $X_{OH^-} = 0.78, 0.76$) and for complete conversion case ($Q_L = 5.2$ mL/min, $X_{OH^-} = 1$)

The difference between the conversion of the humid and dry experiments was negligible, but the temperature difference was substantial. The temperature in the humid experiment rose 16 °C, and the temperature in the dry experiment increased 8 °C. The adiabatic temperature rise calculated from the enthalpies of absorption and reaction from Danckwerts [161] is 12.5 °C. The temperature rise in the humid experiments exceeds the value given by Danckwerts. Danckwerts likely used dry carbon dioxide in his experiments, and as seen in the experiments here, a large fraction of the energy released from the reaction could be transferred to vaporizing the water solvent resulting in artificially low temperatures. An 8 °C temperature difference is equivalent to evaporating 1.5 % of the water in the liquid stream. When calculating the adiabatic temperature rise from thermodynamic properties [172], an even higher value of 51.7 °C is obtained.

These observations have several important implications. The first implication regarding the temperature profile in microreactors is that microreactors are not necessarily isothermal despite their excellent heat transfer characteristics. Also, the energy involved in phase change must be accounted for in both assessing the isothermality or heat transfer efficiency of such a system [173] or when conducting thermodynamic measurements. The second implication regarding the characterization of the interfacial area and mass transport within the gas and liquid film is that water does evaporate into the gas phase, but it doesn't seem to occur to an extent that influences the analysis. Even when using dry carbon dioxide, there is certainly some partial pressure of water vapor present, and exactly at the gas/liquid interface there is necessarily either more water vapor due to evaporation or a higher temperature, meaning that although the effects do not seem to effect the analysis of the mass transport according to the two film theory, the theory is at best an imperfect description of the true nature of interfacial phenomena.

5.3.1 Interfacial Area

Some authors who have studied similar reactors (Section 2.3.1) have assumed that the interfacial area is simply equal to the area of the liquid channels [61]. Zhang et al. [90] proposed that the liquid profile in the channels is a function of the contact angle (Equation 2). According to Equation 2, the surface area differs less than 20 % from the geometric area of the microchannels for contact angles between 30 ° and 150 °. Claudel et al. [61] measured interfacial areas between 180 and 200 m²/m³ for a falling film reactor with round-bottomed microchannels. If only the height of the gas chamber is considered (5.8 mm), an approximate geometric surface area between the channel faces and the gas is 1/5.8 mm = 172 m²/m³. However, since only a fraction of the entire reactor volume contains channels, it can be concluded that the values of interfacial area measured by Claudel et al. [61] are somewhat higher than the pure geometric surface area. Other aspects of the liquid flow such as the unequal distribution of the liquid among the channels and incompletely filled channels [90] could likely have a larger impact on the actual interfacial area.

For the reactor investigated (Section 4.2.3), the geometrical area of the interface of the liquid channels divided by the entire reactor volume was 30.9 m²/m³. It is difficult to determine an accurate contact angle value for the system. Because the reaction proceeds so quickly, the product could be measured in a carbon dioxide atmosphere, but the contact angle of the reactant solution could only be measured in an inert atmosphere (Section 5.1.3.7). If a contact angle of 50 ° is assumed to represent the stainless steel/2 M NaOH/carbon dioxide system, then the interfacial area predicted by Equation 2 is 33.5 m²/m³. If a pseudo-1st-order reaction is assumed and the interfacial area is calculated according to Equation 39 (assuming a constant reaction rate along the reactor, i.e. $\Phi = \phi$), a value of 25.2 m²/m³ results. These values are similar although the value derived from measurement is lower than either of the

predictions. An interfacial area of $33.5 \text{ m}^2/\text{m}^3$ has been used in the calculations presented here.

5.3.2 Conversion and Concentration Profiles

The temperature rise in a reactor segment i was assumed to be proportional to the rate of reaction in that segment. This approach implicitly assumes constant heat losses along all segments. The temperature gradient from one channel to another was minimal along the centerline of the reactor. The contribution of a segment to the overall conversion was thus defined as the temperature rise in the segment divided by the total temperature rise. Temperature decreases were assigned values of 0.

$$\text{contribution}_i = \frac{\Delta T_i}{\sum_i \Delta T_i} \quad [59]$$

The contribution factor was multiplied by the overall conversion determined by titration to obtain the conversion in the segment. N was the total number of temperature measurement points along the reactor length and $N-1$ was the number of segments into which the reactor was divided.

$$X_{OH^-,i} = \sum_{i=0}^{N-1} \text{contribution}_i \cdot X_{OH^-} \quad [60]$$

Concentration profiles were determined based on conversion and reaction stoichiometry:

$$C_{OH^-} = (1 - X_{OH^-}) \cdot C_{OH^-,0} \quad [61]$$

$$C_{CO_3^{2-}} = \frac{X_{OH^-} \cdot C_{OH^-,0}}{2} \quad [62]$$

The conversions and concentration profiles along the reactor length derived for the dry and humid experiments are shown in Figure 72, and the profiles derived for the complete conversion experiment are shown in Figure 73. The profiles derived for the dry and humid experiments look very similar and increase throughout the reactor. The profiles in the high conversion experiment rapidly reach their final values and remain constant throughout the second two-thirds of the reactor.

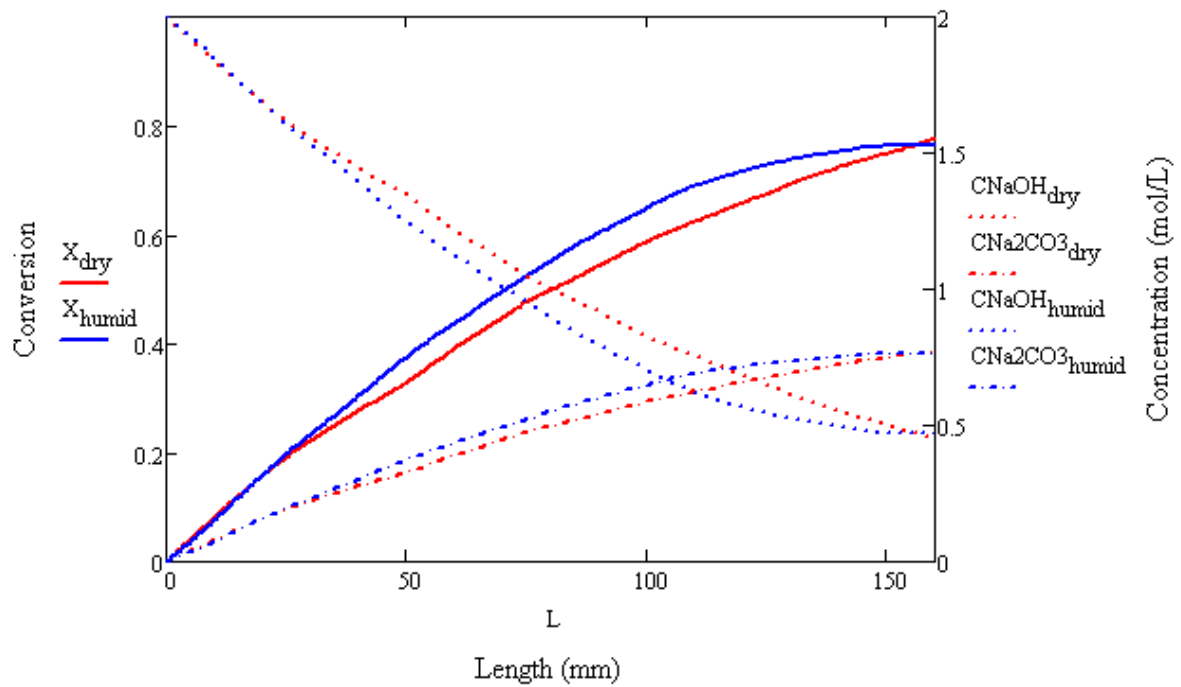


Figure 72: Profiles of conversion and concentration derived from falling film reactor temperature profiles for dry and humid experiments

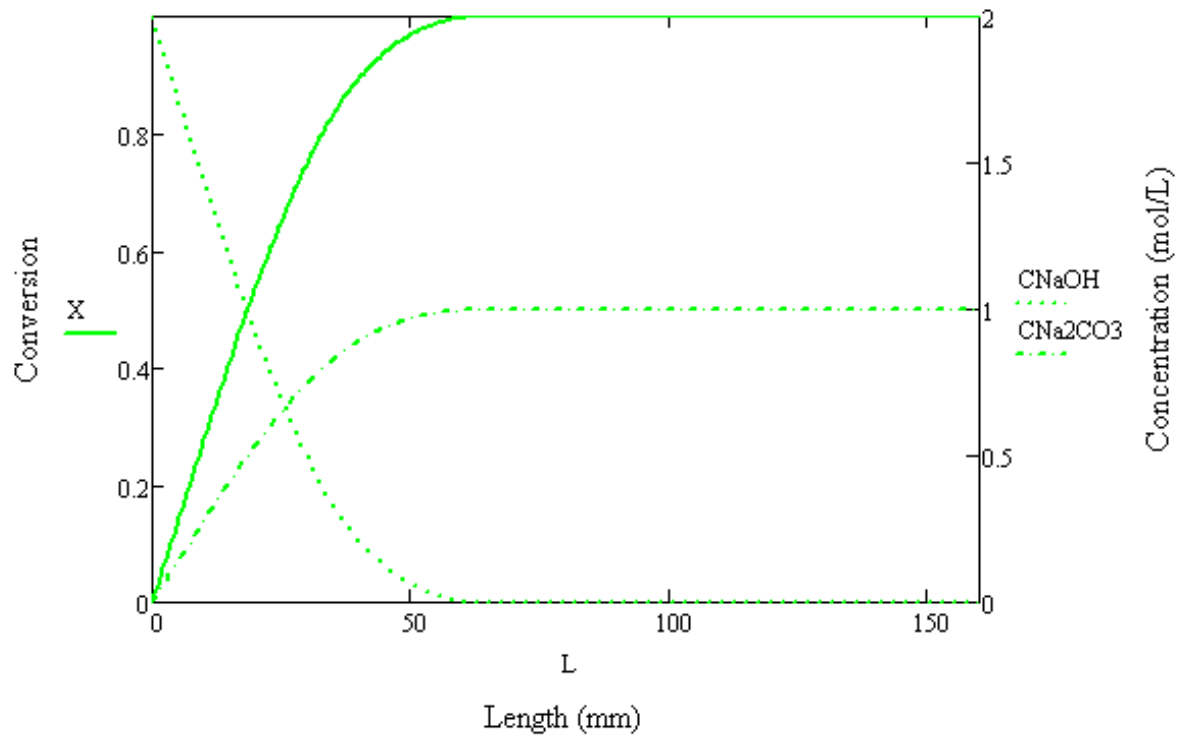


Figure 73: Profiles of conversion and concentration derived from falling film reactor temperature profiles for complete conversion experiment

5.3.3 Reaction Rate

The reaction rate in a reactor segment was calculated from the difference between the concentration of NaOH in the previous segment and the concentration in the segment itself:

$$\phi_i = \frac{\left(C_{OH^-_{i-1}} - C_{OH^-_i} \right) \cdot Q_L}{2 \left(\frac{V_R}{N-1} \right)} \quad [63]$$

The reaction rates calculated along the reactor length for all three experiments are shown in Figure 74.

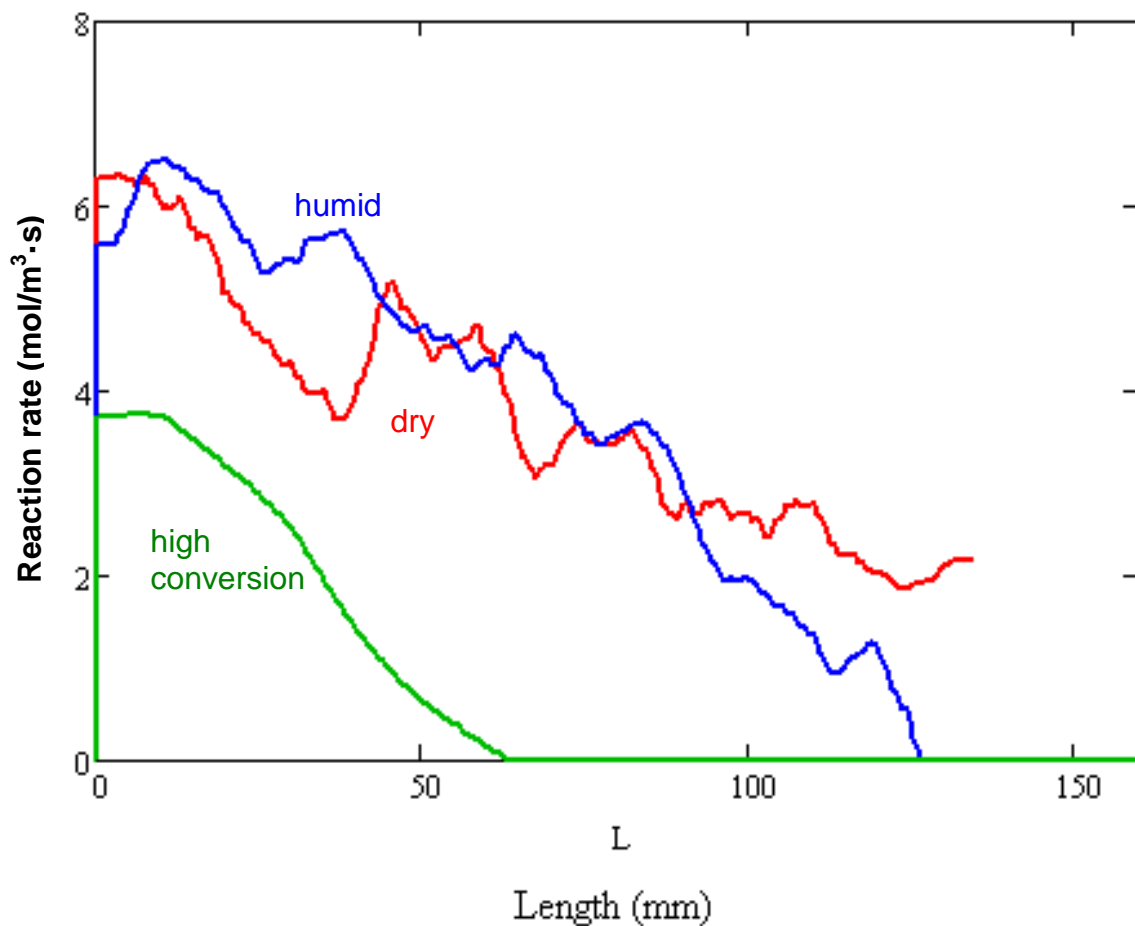


Figure 74: Reaction rate calculated along the reactor length from thermographic temperature measurements of the reaction of 2M NaOH with dry CO₂, prehumidified CO₂, and at a low flow rate where complete conversion is achieved in the middle of the reactor

5.3.4 Liquid Mass Transport Coefficient, Enhancement Factor, and Hatta Number

Values of the liquid mass transport coefficient were obtained through a similar analysis to that used in Section 5.2, but no simplifying assumptions such as a pseudo-1st-order reaction are necessary. Transport in the gas phase could be neglected since pure CO₂ was used. Because the interfacial area was already known, k_L could be calculated directly from the reaction measurements. Henry's law (Equation 6) was used to relate the pressure to the dissolved concentration of CO₂ at the interface. The pressure was considered to be constant throughout the reactor at the average value of the reactor inlet and outlet. The pressure drop in the reactor was less than 10 kPa, and the overall pressure was nearly atmospheric.

The Henry constant was calculated for each segment using the concentrations determined for that segment according to Danckwerts's method for solutions of electrolytes [161]:

$$H_{CO_2} = H_{CO_2}^{\infty} \cdot 10^{hI} \quad [64]$$

H_{CO_2} is the Henry constant for CO₂ in the liquid. $H_{CO_2}^{\infty}$ is the Henry constant for CO₂ in pure water and has a value of L·atm/0.039 mol [161]. I is the ionic strength of the solution, and h is the sum of the contributions for the positive ionic species, negative ionic species, and dissolved gas. The contributions have been summarized by Danckwerts and are shown for the relevant species in Table 15.

Table 15: Ion contributions for the calculation of the Henry constant for CO₂ in solutions of electrolytes

Species	Contribution
Na ⁺	0.091
OH ⁻	0.066
CO ₃ ²⁻	0.021
CO ₂ (20°C)	-0.015

The Henry constant for carbon dioxide in a 20 °C solution containing NaOH and Na₂CO₃ can therefore be calculated:

$$H_{CO_2} = \frac{L \cdot atm}{0.039 mol} \cdot 10^{(0.091 + 0.021 - 0.015) \cdot \frac{1}{2} C_{Na_2CO_3} (2 \cdot 1^2 + 2^2) + (0.091 + 0.066 - 0.015) \cdot \frac{1}{2} C_{NaOH} (1^2 + 1^2)} \quad [65]$$

Since the reaction is inherently fast, the concentration of gas in the liquid bulk phase was assumed to be zero and the transport through the liquid film could be described given in Equation 38. Thus, k_L could be obtained:

$$k_{Li} = \frac{\phi_i}{a \cdot E \cdot C_{CO_2,i}} \quad [66]$$

E can be obtained from an approximate expression such as that of van Krevelen and Hoftijzer [137]:

$$E = \frac{Ha \sqrt{\frac{E_i - E}{E_i - 1}}}{\tanh\left(Ha \sqrt{\frac{E_i - E}{E_i - 1}}\right)} \quad [67]$$

In the original paper [63] the definition of E (here Equation 67) mistakenly included \sqrt{Ha} instead of Ha. The calculations of the original paper are consistent with the mistaken definition of E given. The change in the definition for E changes the derived values by a factor of 2. The original paper also did not assume that $C_{CO_2,L} = 0$ but rather calculated the average value for C_{CO_2} over the entire liquid volume that would provide the same value of ϕ (by setting Equation 9 equal to Equation 8 and ignoring the volume of the liquid film). Since the values of $C_{CO_2,L}$ calculated in the original paper were very small, assuming $C_{CO_2,L} = 0$ simplifies the calculation without changing the results (Table 16). The applicability of the assumption $C_{CO_2,L} = 0$ is further discussed in Section 5.4.4.2.

The enhancement factor for an instantaneous reaction, E_i , can be calculated at each point as a function of the Henry constant and NaOH concentration.

$$E_{i_i} = 1 + \frac{D_{OH^-} \cdot C_{NaOH_i}}{2 \cdot D_{CO_2} \frac{P}{H_{CO_2_i}}} \quad [68]$$

The Hatta number is a function of k_L and constants or known parameters.

$$Ha = \frac{\sqrt{D_{CO_2} \cdot k_{OH^-} \cdot C_{NaOH}}}{k_L} \quad [69]$$

The diffusivities and reaction rate constant were given previously in Table 14. Substituting Equations 68 and 69 into Equation 67 allows Equations 66 and 67 to be solved for k_L and E.

Derived values of k_L , E, and the Hatta number for the dry and humid experiments are shown in Figure 75. Values derived for the maximum conversion experiment are shown in Figure 76. Values were also calculated with the same mathematical strategy using the conventional approach of considering the reactor volume as a single element with the reaction rate assumed to be constant throughout the volume; results are given in Table 16.

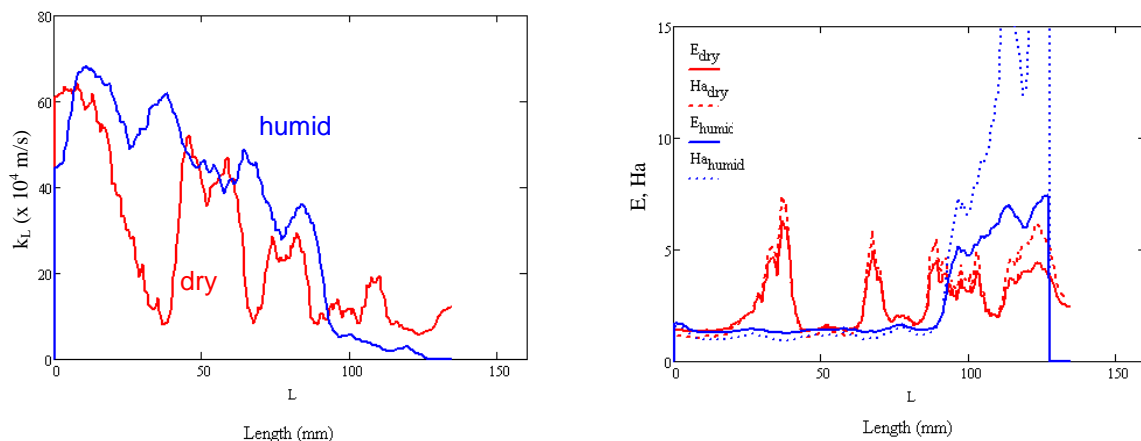


Figure 75: Liquid transport coefficient (k_L), enhancement factor (E), and Hatta number (Ha) derived along reactor profile for dry and humid experiments

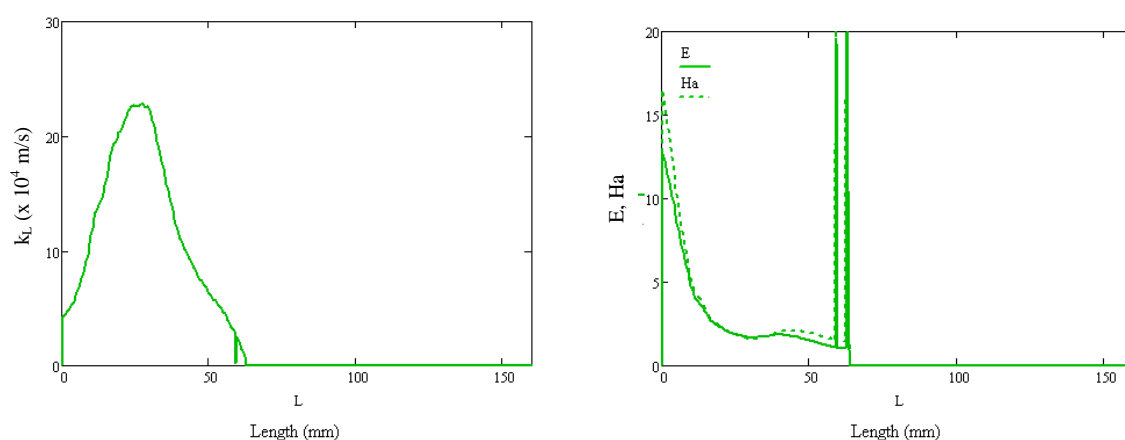


Figure 76: Liquid transport coefficient (k_L), enhancement factor (E), and Hatta number (Ha) derived along reactor profile for high conversion experiment

Table 16: Average values for the Enhancement factor for an instantaneous reaction, actual calculated enhancement factor, liquid transport coefficient, and Hatta number calculated by assuming a constant reaction rate for the entire reactor volume

Measurement	E_i	E	$k_L \times 10^4$ (m/s)	Ha
dry CO ₂	17.96	2.65	20	2.76
humidified CO ₂	17.88	3.50	15	3.79
maximum conversion	15.37	14.49	0.85	58.7

For both the dry and humidified experiments, the values of E and Ha along the reactor length are approximately equal, signifying a pseudo-1st-order reaction. These values increase as the reaction rate goes to zero, but this is only an artifact since k_L goes to zero with reaction rate and E and Ha number are inversely proportional to k_L . The values calculated for the integral analysis of the entire reactor volume match the average values of k_L , E, and Ha in the profiles for the dry and humid experiments, but the values calculated for the high conversion experiment differ substantially and do not represent the reaction conditions within the reactor. The calculations based on the entire reactor volume for the case where conversion is complete before the end of the reactor suggest that the reaction proceeds nearly instantaneously ($E \approx E_i$); however, the profiles show that, at least where the reaction occurs, the reaction falls in the

pseudo-1st-order regime as in the other two cases. The k_L values determined here are higher than the values measured by Claudel et al.[61] and Zhang et al.[90]

In all experiments the k_L values fall along the reactor length. The k_L value follows the reaction rate, which also decreases along the reactor length. However, the analysis of each slice already takes into account the differences in the rate of absorption due to the changes in the concentrations. Further modeling, or better models, is needed to reconcile these observations. Danckwerts[161] observed the same effect in wetted wall columns and attributed the effect to entrance effects, buildup of a rigid film at the surface, and departure from stagnant, semi-infinite behavior.

5.4 MEASUREMENTS OF SLUG FLOW IN 1.6 MM GLASS CAPILLARIES OF DIFFERENT LENGTHS

The absorption of pure carbon dioxide into aqueous solutions of NaOH was measured for different concentrations in different lengths of 1.6 mm ID glass capillary for one single flow pattern (see Section 4.2.2: 1.2 L/min CO₂ and 12.06 mL/min liquid; $j_G = 10$ m/s, $j_L = 0.1$ m/s). These superficial velocities place the flow pattern in the slug flow regime, where the gas and flow rates remain coupled with each other, but the gas phase is not segregated into individual plugs.

For the high relative volume of gas, the gas flow is expected to be relatively unaffected by the fraction of gas consumed in the reaction. A maximum of up to 50% of the gas is consumed in these measurements. More gas is consumed in longer capillaries and at higher NaOH concentrations. Even if the amount of gas is reduced by one-half, the hydrodynamic flow pattern remains in the slug flow regime (compare Figure 50). In this capillary the pressure drop along the capillary was essentially negligible (maximally 0.16 bar). Thus, these experiments examine a single flow pattern ($j_G = 10$ m/s, $j_L = 0.1$ m/s) that prevails along the entire length of the capillary, and the conversion measured at a given capillary length also represents the conversion at that length within the longer capillary—meaning that the results can be interpreted as measurements within segments of a single reactor.

The results of the experiments are shown in Figure 77 for initial NaOH concentrations of 2 M and higher ($z = 2$) and in Figure 78 for concentrations of 1 M and lower ($z = 1$). A table containing the exact values of conversion, length, inlet and outlet temperatures, and pressures can be found in Appendix 8.7. Two important observations can be made immediately from these figures. The first is that the conversion increases linearly with the length of the capillary. The second is that the intercept, meaning the conversion at a length of 0, is greater than zero.

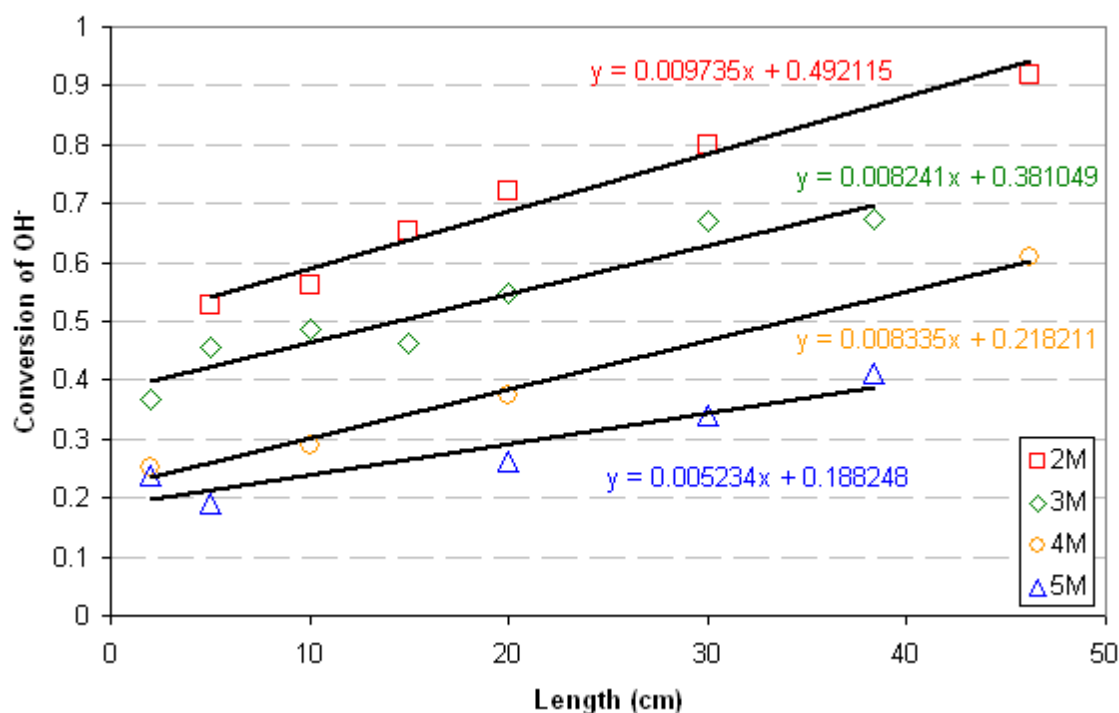


Figure 77: Conversion of OH⁻ as a function of capillary length for the reaction of pure CO₂ with NaOH ($j_G = 10$ m/s, $j_L = 0.1$ m/s) in a 1.6 mm ID glass capillary: $C_{OH^-,0}$ from 2 M to 5 M ($z = 2$)

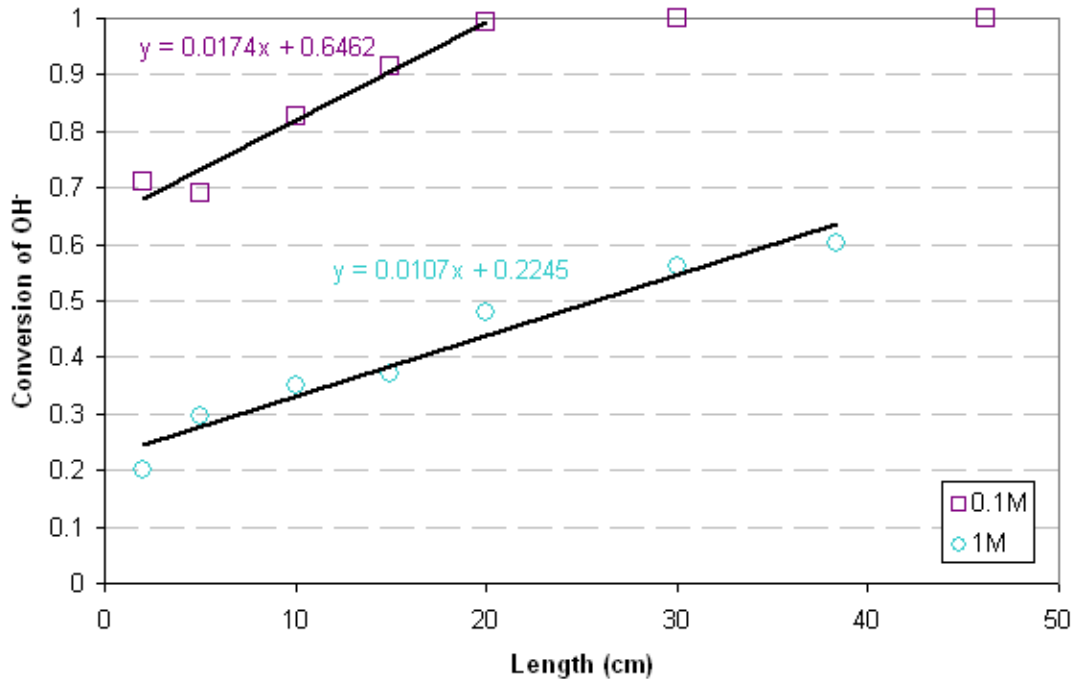


Figure 78: Conversion of OH⁻ as a function of capillary length for the reaction of pure CO₂ with NaOH ($j_G = 10$ m/s, $j_L = 0.1$ m/s) in a 1.6 mm ID glass capillary: $C_{OH^-,0}$ from 0.1 M to 1 M ($z = 1$)

The first observation, that conversion increases linearly along the length of the capillary, means that the reaction rate throughout the capillary is constant. This is true even if the overall conversion is very high. Thus, a constant reaction rate throughout the reactor can be used in deriving values of a and k_L according to method of the Danckwerts plot in Section 5.4.2. However, due to the changes in the concentration of NaOH along the capillary, changes in the reaction rate along the capillary length are expected to be present. The linear relationship between conversion and length may result if the changes in the reaction rate along the length are small (since mass transport limits the rate of reaction and concentration changes have only a secondary effect on E for pseudo-1st-order reactions). Section 5.4.3 applies the analytical solution accounting for concentration gradients derived in Section 5.2.2 to determine interfacial areas for measurements in the pseudo-1st-order regime. Section 5.4.4 applies a discretized model based on film theory to the same measurements to provide a more complete description of the reaction in the capillary. These models can show to what extent changes in the concentration affect the rate of reaction along the capillary length and be used to evaluate the validity of the approach based on the average reaction rate used in the Danckwerts plot.

5.4.1 Description of T-Junction

As previously mentioned, an important observation from Figure 77 and Figure 78 is that a substantial conversion occurs prior to the capillary entrance. The initial contacting of gas and liquid phases took place in a 3 mm Swagelok tee union to which the 1.6 mm ID capillary was attached. A diagram of the T-junction is shown in Figure 79. The diameter of the channel within the tee union is 2.4 mm and the length from the point where the gas and liquid phases collide until the gas/liquid flow enters the capillary is at least 9.4 mm. At the capillary entrance, a reduction of the inner diameter occurs abruptly. The T-junction has a volume of ~ 43 μ L, equivalent to the volume of approximately the first 2 cm of capillary. Despite the small contribution to the volume, the contribution to the conversion is nearly half of the conversion

occurring in the entire system. The conversion occurring in the T-junction for each concentration is shown in Figure 80.

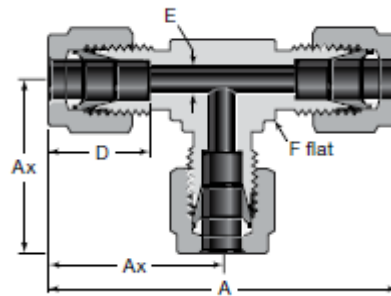


Figure 79: Diagram of T-junction where gas and liquid phases are combined (Swagelok tee union)

Swagelok Catalog: Gaugeable Tube Fittings and Adapter Fittings, p. 35

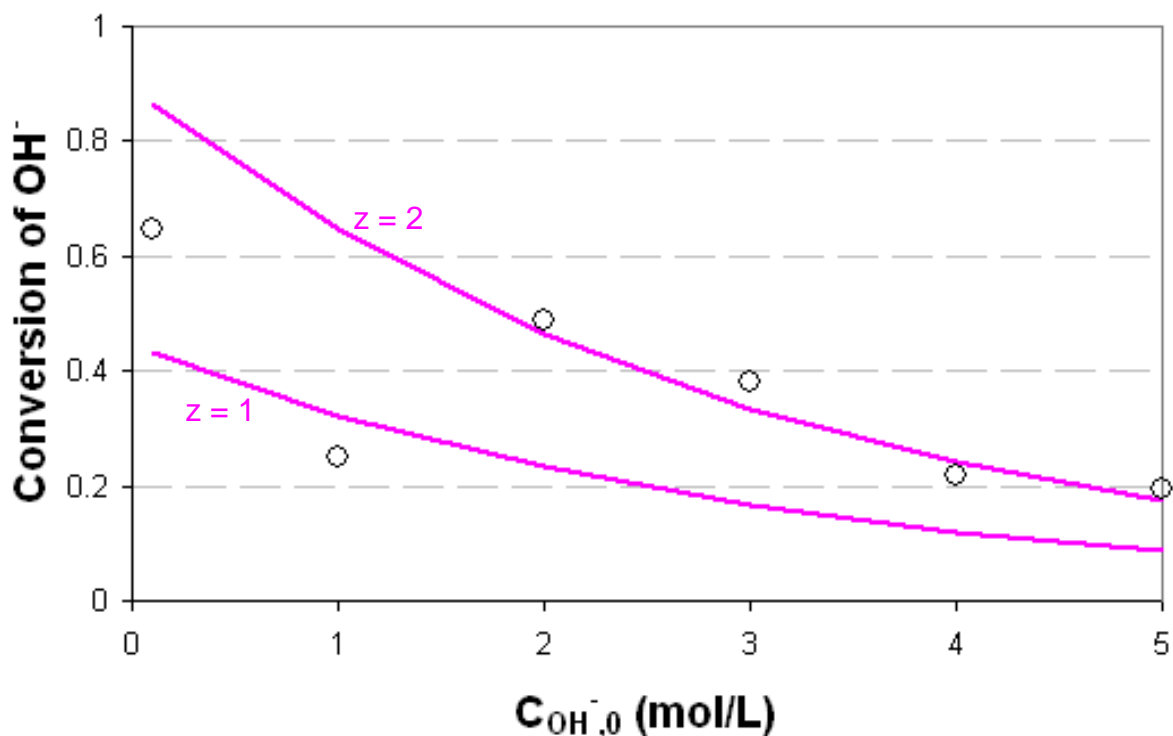


Figure 80: Reaction conversion occurring in T-junction

The relationship between $(\Phi/C_{\text{CO}_2,i})^2$ and $\Phi/C_{\text{CO}_2,i}$ to $D_{\text{CO}_2}k_{\text{OH}^-}C_{\text{OH}^-,0}$ is shown in Figure 81. The rate of reaction in the T-junction divided by the interfacial concentration $C_{\text{CO}_2,i}$ did not show a linear relationship between $(\Phi/C_{\text{CO}_2,i})^2$ and $D_{\text{CO}_2}k_{\text{OH}^-}C_{\text{OH}^-,0}$ as used in analysis with a Danckwerts plot (compare Equation 74, Figure 84). However, a linear fit between $\Phi/C_{\text{CO}_2,i}$ and $D_{\text{CO}_2}k_{\text{OH}^-}C_{\text{OH}^-,0}$ was observed. It may also be noted that the relationship between $\Phi/C_{\text{CO}_2,i}$ and $D_{\text{CO}_2}k_{\text{OH}^-}C_{\text{OH}^-,0}$ for the measurements in the capillary was also linear.

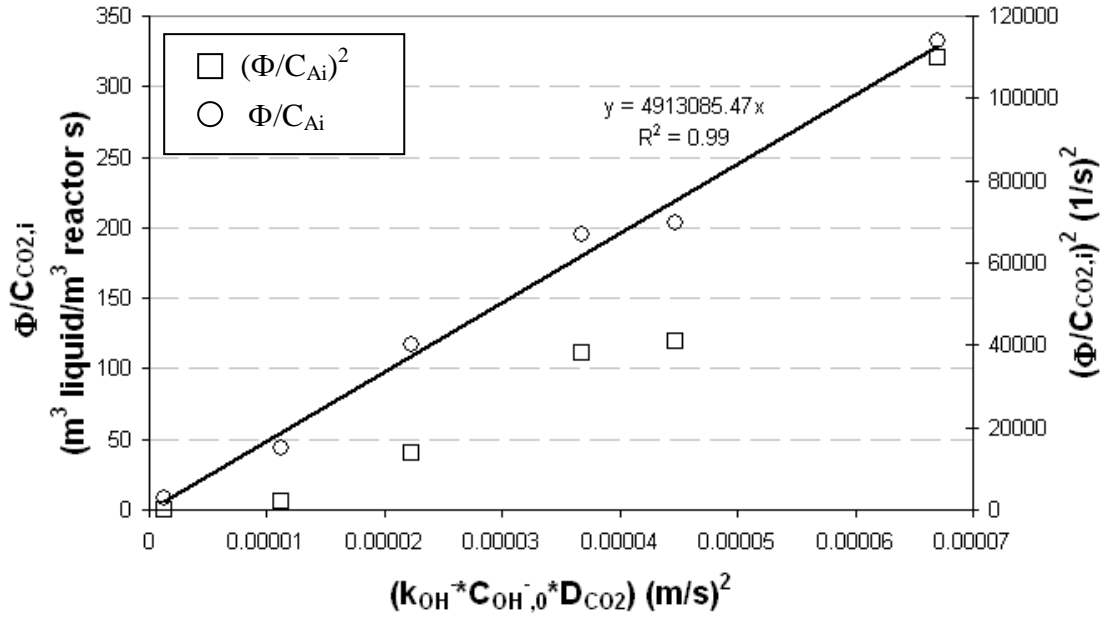


Figure 81: Empirical relation of $\Phi/C_{CO_2,i}$ and $D_{CO_2}k_{OH^-,0}$ describing T-junction

The relationship between $\Phi/C_{CO_2,i}$ to $D_{CO_2}k_{OH^-,0}$ was fitted through linear regression ($m = 4913085 \text{ s/m}^2$), and the conversion occurring in the T-junction was described:

$$\Phi = m \cdot C_{CO_2,i} D_{CO_2} k_{OH^-,0} C_{OH^-,0} \quad [70]$$

$$X_{OH^-} = \frac{z\Phi V_{mixer} \varepsilon L}{Q_L C_{OH^-,0}} \quad [71]$$

The results of the model describing the conversion in the T-junction are shown as lines in Figure 80. The empirical model fit the measurements well and could describe the T-junction as a single element in the reactor model.

5.4.2 Determination of Interfacial Area and Mass Transport Coefficient with Danckwerts Plot

In this section the reaction rate is assumed to be constant throughout the capillary and average properties are assumed to derive values of a and k_L . This analysis neglects changes in the concentration along the length of the capillary. This rudimentary analysis has been widely used to determine values of a and k_L for conventional gas/liquid reactors. A model approach accounting for concentration gradients along the length is discussed in Section 5.4.4. A comparison of the methods employed to determine a and k_L values from these measurements is given in Section 5.4.5.

The values of $\Delta X_{OH^-}/\Delta L$ and concentrations at the beginning of the capillary have been determined from the slope and intercepts in Figure 77 and Figure 78 and are summarized in Table 17.

Table 17: Values of concentration, temperature, and pressure from the presented measurements and values of the physical properties corresponding to these conditions

Values from measurements							Values of properties calculated from [145]						
$C_{OH^-,0}$ (mol/L)	$C_{OH^-,L=0}$ (mol/L)	$C_{OH^-,L}$ (mol/L)	$C_{OH^-,avg}$ (mol/L)	T_0 (°C)	T_L (°C)	ΔP (bar)	$\Delta X_{OH^-}/\Delta L$ (1/cm)	$D_{CO_2,0}$ $\times 10^9$ (m ² /s)	$D_{CO_2,L}$ $\times 10^9$ (m ² /s)	$k_{OH^-,L=0}$ (L/mol·s)	$k_{OH^-,L}$ (L/mol·s)	$H_{CO_2,L=0}$ (m ³ ·bar/mol)	$H_{CO_2,L}$ (m ³ ·bar/mol)
0.1	0.035	0	0.018	22	24	0.1	0.0174	1.83	1.94	6676	7566	0.028	0.030
1	0.78	0.4	0.588	21	28	0.09	0.0107	1.78	2.15	6267	9668	0.037	0.045
2	1.02	0.16	0.588	21	35	0.11	0.0097	1.78	2.55	6267	14622	0.051	0.075
3	1.86	0.9	1.38	22	34	0.14	0.0082	1.83	2.49	6676	13798	0.073	0.101
4	3.13	1.56	2.34	21	38	0.13	0.0083	1.78	2.74	6267	17359	0.098	0.155
5	4.08	3	3.53	23	33	0.16	0.0052	1.88	2.44	7109	13017	0.145	0.190

When the rate of gas absorption within the reactor is constant, the rate can be determined from changes in the concentration of OH⁻ between the inlet and outlet:

$$\Phi = \frac{(C_{OH^-,L} - C_{OH^-,0}) \cdot Q_L}{z \cdot V_R} = \frac{C_{OH^-,0} \cdot (X_{OH^-,0} - X_{OH^-,L}) \cdot Q_L}{z \cdot \pi \cdot r^2 \cdot L} \quad [72]$$

$$= \frac{C_{OH^-,0} \cdot Q_L}{z \cdot \pi \cdot r^2} \cdot \frac{\Delta X_{OH^-}}{\Delta L}$$

The constants used in this work have been calculated from the correlations given in [145] (see Equations 92-94). The applicable constants have been calculated for the capillary entrance conditions (temperature and concentration) as well as for the reactor outlet conditions and are listed in Table 17 to give some idea of the amount of variation that can be expected within the reactor.

Because the reaction is fast, the reaction occurs completely within the liquid film and the concentration of dissolved gas in the liquid bulk is zero. The reaction rate can be described according to a balance on the liquid film:

$$\Phi = k_L \cdot a \cdot E \cdot (C_{CO_2,i} - C_{CO_2,bulk}^0) \quad [73]$$

In Equation 73, Φ is measured in the experiments, $C_{CO_2,i}$ is determined from the Henry constant and the pressure, and k_L and a are the constants to be determined, which characterize the hydrodynamics of the gas/liquid flow. The value of E must also be determined.

Figure 82 shows a diagram relating the enhancement factor (E) to the dimensionless Hatta number (Ha) for a second order reaction from the numerical solution derived by van Krevelen and Hoftijzer [137]. In Figure 82 the approximations $E = Ha$ and $E = \sqrt{1 + Ha^2}$ are shown in red and blue. The exact solution ($E = Ha/\tanh(Ha)$), as long as $E \ll E_i$, is also shown in green. $E = \sqrt{1 + Ha^2}$ is a valid approximation with no apparent lower limit and a higher limit at the point where the value of E_i causes the curve to diverge from $E_i \rightarrow \infty$ as seen for $C_{NaOH} = 0.1$ M. However, low concentrations will also result in low Hatta numbers. Thus, for $C_{NaOH} = 0.1$ M the Hatta number will be less than one and for higher concentrations and resulting higher Hatta numbers, the approximation of $E = \sqrt{1 + Ha^2}$ can be applied to all measurements presented in this work with relatively little error. Substituting $E = \sqrt{1 + Ha^2}$ into Equation 73:

$$\Phi = k_L \cdot a \cdot \sqrt{1 + Ha^2} \cdot C_{CO_2,i} \quad [74]$$

This equation can be rewritten using the definition of Ha :

$$\underbrace{\Phi^2}_y = \underbrace{C_{CO_2,i}^2 a^2 D_{CO_2} k_{OH^-}}_m \underbrace{C_{OH^-}}_x + \underbrace{k_L^2 a^2 C_{CO_2,i}^2}_b \quad [75]$$

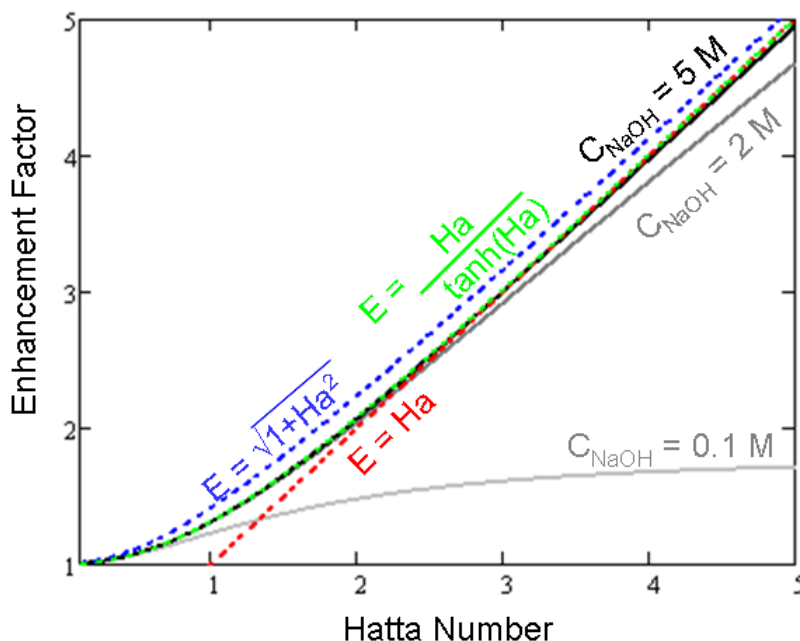


Figure 82: Enhancement factor as a function of Hatta number for 0.1 M NaOH, 2 M NaOH, and 5 M NaOH compared to the approximations $E = Ha$ and $E = \sqrt{1 + Ha^2}$ and the exact solution $E = Ha/\tanh(Ha)$

The plot of Φ^2 versus $k_{OH}^- C_{OH}^-$ is called a Danckwerts plot. Values of a can be determined from the slope and values of k_L from the intercept. The Danckwerts plot is generally specified to be applicable for pseudo-1st-order reactions (the region in Figure 82 where $E = Ha$ is also valid) [95,165]. The criteria of $Ha \ll E_i$ and $Ha > 3$ are often given to describe this requirement. The requirement that $Ha \ll E_i$ is necessary due to the inaccuracy of $E = \sqrt{1 + Ha^2}$ for instantaneous reactions. Ha^2 is the ratio of the maximum rate of reaction in the film to the rate of transport through the film. If the rate of reaction is an order of magnitude larger than the rate of transport, the requirement $Ha > \sqrt{10} \approx 3$ is obtained. However, the application of the approximation $E = \sqrt{1 + Ha^2}$ has no lower limit. The assumption that $C_{A,bulk}$ is zero is also valid at even lower values of Ha since even for $0.3 < Ha < 1$, where the transport through the liquid film is an order of magnitude higher or equal with the maximum rate of reaction in the film, $E > 1$, the moderate rate of reaction coupled with the presumably large volume of the liquid bulk should reduce the concentration of dissolved (unreacted) gas in the liquid bulk to nearly zero [91].

Figure 83 shows the Danckwerts plot as it is typically prepared. One linear regression shown in black has been fitted to the concentrations 2 M and above, where Ha is expected to be at least greater than 1. A second regression shown in gray also includes the lower concentrations of 1 M and 0.1 M. Values of a and k_L have been determined from these regressions using average values of $D_{CO_2} = 2.14 \times 10^{-9} \text{ m}^2/\text{s}$ and $C_{CO_2,i} = 13.48 \text{ mol}/\text{m}^3$ as well as the highest and lowest values expected for each of these constants. The results are given in Table 18. The average values of a are less than half of the capillary surface area, $2500 \text{ m}^2/\text{m}^3$. The average values of k_L vary between 60 and $90 \times 10^{-4} \text{ m}/\text{s}$ and are among the highest values of k_L ever reported. The value of D_{CO_2} has the least impact on the calculations; changes in the values of a and k_L on the order of 10 % occur for the range of expected D_{CO_2} values. Changes in $C_{CO_2,i}$ have a drastic effect on a , up to a factor of 3, but have no influence on k_L . Changes in the concentrations used for C_{OH}^- effect a by less than 10% and k_L by up to 23 %. Changes in k_{OH}^- effect a and k_L by about 10 %.

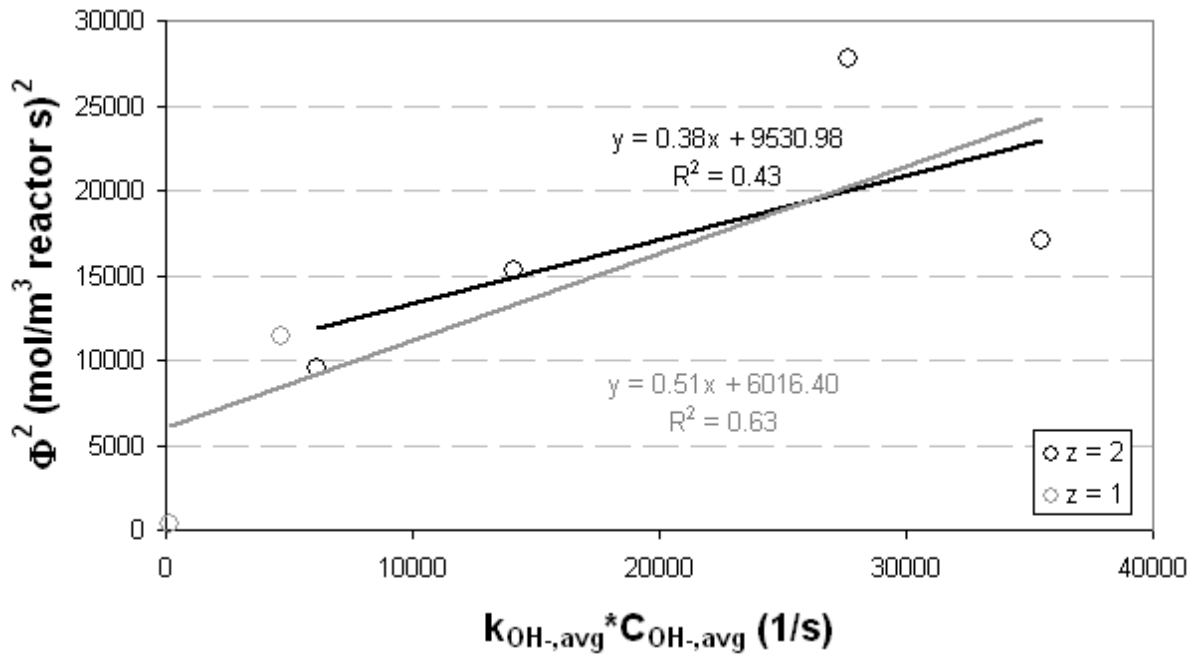


Figure 83: Danckwerts plot (Equation 75) used to determine a and k_L

Table 18: Values of a and k_L determined with Danckwerts plot (Equation 75)

m (mol ² /m ⁶ reactor·s)	b (mol/m ³ reactor·s) ²	C_{OH^-} (mol/L)	k_{OH^-} (L/mol·s)	D_{CO_2} (m ² /s)	$C_{CO_2,i}$ (mol/L)	a (m ² /m ³ reactor)	$k_L \times 10^4$ (m/s)
0.38	9531	$C_{OH^-,avg}$	$k_{OH^-,avg}$	2.14×10^{-9}	13.48	988	73
0.38	9531	$C_{OH^-,avg}$	$k_{OH^-,avg}$	1.8×10^{-9}	13.48	1078	67
0.38	9531	$C_{OH^-,avg}$	$k_{OH^-,avg}$	2.70×10^{-9}	13.48	880	82
0.38	9531	$C_{OH^-,avg}$	$k_{OH^-,avg}$	2.14×10^{-9}	36	370	73
0.38	9531	$C_{OH^-,avg}$	$k_{OH^-,avg}$	2.14×10^{-9}	5	2663	73
0.40	6798	$C_{OH^-,L=0}$	$k_{OH^-,avg}$	2.14×10^{-9}	13.48	1013	60
0.33	12513	$C_{OH^-,L}$	$k_{OH^-,avg}$	2.14×10^{-9}	13.48	920	90
0.38	12354	$C_{OH^-,avg}$	$k_{OH^-,L=0}$	2.14×10^{-9}	13.48	988	83
0.32	8299	$C_{OH^-,avg}$	$k_{OH^-,L}$	2.14×10^{-9}	13.48	906	75
0.32	11061	$C_{OH^-,avg}$	10000	2.14×10^{-9}	13.48	906	86
0.46	11061	$C_{OH^-,avg}$	7000	2.14×10^{-9}	13.48	1087	72

The variation caused by treating $C_{CO_2,i}$ as a constant could be removed by including the concentration-dependent value of the constant in the y-variable of the plot:

$$\underbrace{\left(\frac{\Phi}{C_{CO_2,i}}\right)^2}_y = \underbrace{a^2}_{m} \underbrace{D_{CO_2} k_{OH^-} C_{OH^-}}_x + \underbrace{k_L^2 a^2}_b \quad [76]$$

The results plotted in this form are shown in Figure 84. Including $C_{CO_2,i}$ dramatically evens out the curves and increases the determined values of a ; for the average values shown in Figure 84, the resulting value of a is 2687 m²/m³, close to the value of the capillary surface

area (2500 m²/m³). Including C_{CO₂,i} also results in a negative value of the intercept, making a determination of the k_L value impossible.

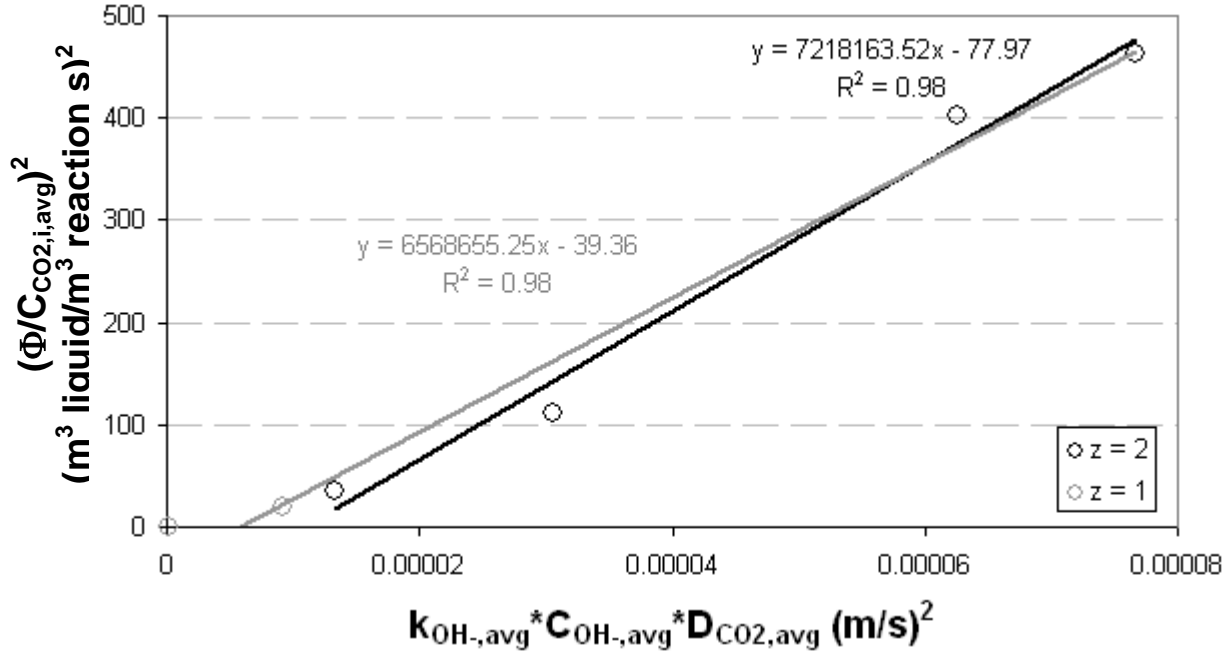


Figure 84: Danckwerts plot modified with C_{CO₂,i} (Equation 76)

It may, however, still be possible to determine a value of k_L from these measurements. The overall curve of the results in Figure 84 is interesting due to its reflection of the relationship between E and Ha. If Φ/C_{CO₂,i} is plotted on the y-axis, the y-axis can be considered to represent E multiplied by constants (compare Equation 73).

$$\frac{\Phi}{C_{CO_2,i}} = (k_L \cdot a) \cdot E \quad [77]$$

Likewise if $\sqrt{D_{CO_2}k_{OH^-}C_{OH^-}}$ is plotted on the x-axis, the x-axis can be considered to represent Ha multiplied by constants.

$$\sqrt{D_{CO_2}k_{OH^-}C_{OH^-}} = k_L \cdot Ha \quad [78]$$

Realizing that Φ/C_{CO₂,i} and $\sqrt{D_{CO_2}k_{OH^-}C_{OH^-}}$ are analogous to E and Ha multiplied by constants, Figure 85 can be constructed from the measurements analogously to Figure 82. Average values of D_{CO₂}, C_{OH⁻}, and k_{OH⁻} have been used to calculate $\sqrt{D_{CO_2}k_{OH^-}C_{OH^-}}$ in Figure 85. A linear regression has been used to fit the measurements from 2 M to 5 M. These measurements appear to fall in the pseudo-1st-order regime, where E = Ha.

$$\frac{\Phi}{C_{CO_2,i}} = k_L \cdot a \cdot \frac{\sqrt{D_{CO_2}k_{OH^-}C_{OH^-}}}{k_L} = a \cdot \sqrt{D_{CO_2}k_{OH^-}C_{OH^-}} \quad [79]$$

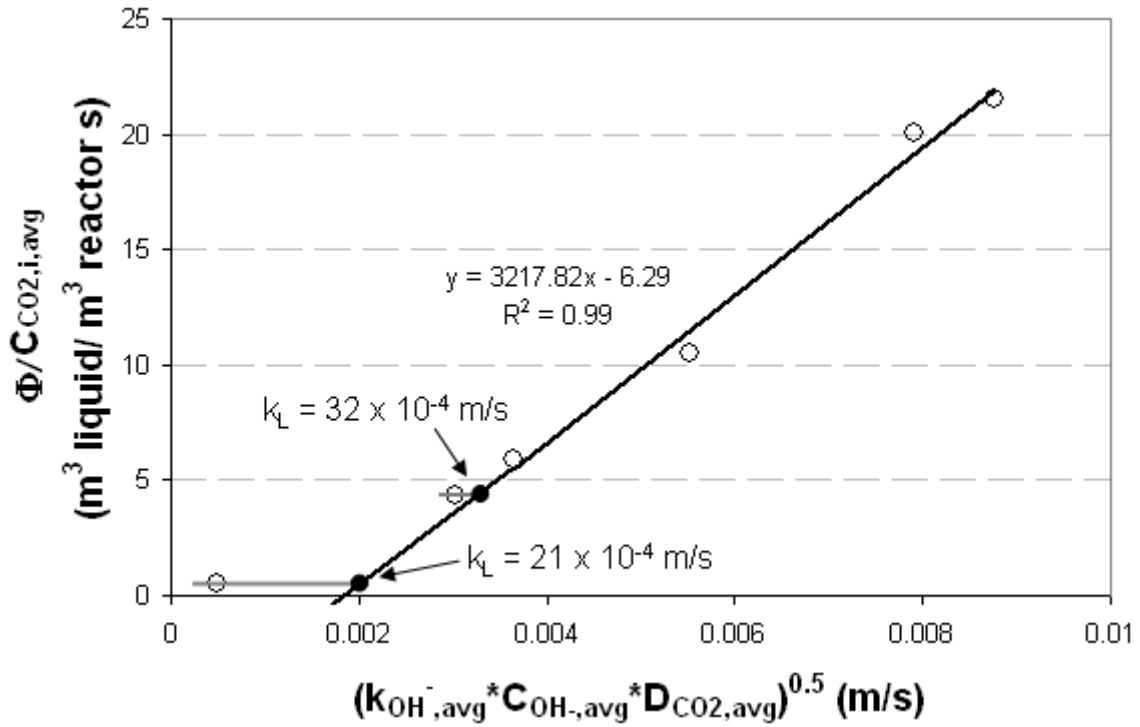


Figure 85: E/Ha-style graph (Equation 79)

From the slope an interfacial area of 3218 m^2/m^3 reactor was determined. This value is larger than the values of $\sim 1000 \text{ m}^2/\text{m}^3$ determined from Figure 83. The slope/interfacial area has been calculated for the expected range of values of D_{CO_2} , k_{OH^-} , and C_{OH^-} in Table 19. The values of D_{CO_2} , k_{OH^-} , and C_{OH^-} used in calculating that Hatta number are each associated with maximally a change in 15% in the value of interfacial area.

Table 19: Values of a and k_L determined from pseudo-1st-order measurements (Equation 79)

C_{OH^-} (mol/L)	D_{CO_2} (m^2/s)	$C_{\text{CO}_2,i}$ (mol/L)	k_{OH^-} (L/mol·s)	$m = a$ (m^2/m^3 reactor)	b (m^3 liquid/ m^3 reactor·s)	$k_L \times 10^4$ (m/s)	$k_L \times 10^4$ (m/s)
average	1.8×10^{-9}	$C_{\text{CO}_2,i,0}$	average	3073	-5.66	20	31
$C_{\text{OH}^-,L=0}$	$D_{\text{CO}_2,0}$	$C_{\text{CO}_2,i,0}$	$k_{\text{OH}^-,0}$	3697	-7.47	22	31
$C_{\text{OH}^-,L}$	$D_{\text{CO}_2,L}$	$C_{\text{CO}_2,i,0}$	$k_{\text{OH}^-,L}$	1945	-0.49	5	23
$C_{\text{OH}^-,L}$	$D_{\text{CO}_2,L}$	$C_{\text{CO}_2,i,L}$	$k_{\text{OH}^-,L}$	2713	-0.25	2	15
average	$D_{\text{CO}_2,0}$	$C_{\text{CO}_2,i,0}$	average	2983	-5.27	19	31
average	$D_{\text{CO}_2,L}$	$C_{\text{CO}_2,i,0}$	average	2580	-5.66	24	37
$C_{\text{OH}^-,L=0}$	1.8×10^{-9}	$C_{\text{CO}_2,i,0}$	average	3241	-9.5	31	41
$C_{\text{OH}^-,L}$	1.8×10^{-9}	$C_{\text{CO}_2,i,0}$	average	2622	-0.08	22	15
$C_{\text{OH}^-,0}$	1.8×10^{-9}	$C_{\text{CO}_2,i,0}$	average	4028	-20.2	51	60
average	1.8×10^{-9}	$C_{\text{CO}_2,i,0}$	$k_{\text{OH}^-,0}$	3576	-4.21	13	23
average	1.8×10^{-9}	$C_{\text{CO}_2,i,0}$	$k_{\text{OH}^-,L}$	2660	-5.91	24	37
average	1.8×10^{-9}	$C_{\text{CO}_2,i,0}$ to $C_{\text{CO}_2,i,0}/2$	average	950	0.32	2	32

Although Ha can be much smaller than 1, the smallest value of E is 1. Comparing Figure 85 to Figure 82, a basis for the estimation of k_L from the measurements can be found. According to Figure 82 measurements would be expected to follow the pseudo-1st-order line as Hatta number (and concentration) decreases until leveling off at a level where $E = 1$. Differences should become apparent around $Ha = 2$. A value of k_L can be determined at the intersection of $E = 1$ with $E = Ha$. A lower limit for k_L can thus be found at the x-axis intercept of the line $E = Ha$, i.e. assuming $E \cdot k_L \cdot a = 0$ represents $E = 1$. As seen in Figure 85, the value of $Ha \cdot k_L$ (i.e. k_L since $Ha = 1$) at this intersection is 20×10^{-4} m/s, and the actual k_L value must be higher. The 1M measurement doesn't deviate from $E = Ha$ and should therefore be associated with an E value of 2 or greater. A maximum value of $k_L = 32 \times 10^{-4}$ m/s can thus be derived by assuming $E = 1$ at the $\Phi/(C_{CO_2,i})$ value of 4.3 associated with this measurement point. The true value of E at this point is unknown, but it must be greater than 1. The 0.1 M measurement lies in a region where $E = 1$ might be fulfilled. However, deviations in $C_{CO_2,bulk}$ from 0 would cause values of $\Phi/(C_{CO_2,i} - C_{CO_2,bulk})$ in this region to be smaller than if the concentration difference was properly accounted for. If the intercept of a horizontal line through 0.1 M measurement is used to calculate the associated k_L value, a value of 21×10^{-4} m/s is obtained. This value can also be used as a lower limit, meaning that k_L may be equal to but not lower than this value, since the value would increase if $\Phi/(C_{CO_2,i} - C_{CO_2,bulk})$ accounted for $C_{CO_2,bulk}$.

Lower and upper limit estimates using the 0.1 M and 1 M measurements are given in Table 19. These values are among the lower of the values calculated in the analysis of the Danckwerts plots in Table 18. The effect on these values due to variations in k_{OH^-} , C_{OH^-} , and D_{CO_2} are also shown in Table 19. Variations in D_{CO_2} and k_{OH^-} create variations on the value of k_L on the order of 20%. Variations in C_{OH^-} have a much more drastic effect on k_L , up to a factor of 10.

The estimations of a and k_L obtained with Figure 85 are expected to be more accurate than those resulting from the Danckwerts plot since they account for changes in gas solubility and offer a much better linear fit. In video observations of this flow regime, ripples and slugs of liquid could be seen. An interfacial area greater than the surface area to volume ratio of the capillary itself is thus in agreement with visual observations of the flow.

5.4.3 Determination of Interfacial Area with Analytical Solution

An analytical solution for the interfacial area taking into account changes in the concentration of NaOH along the capillary length was derived for measurements falling in the pseudo-1st-order regime in Section 5.2.2 (Equation 48). Equation 48 can be rewritten:

$$a = 2 \left(\frac{1}{C_{CO_2,i}} \right) \left(\frac{Q_L}{zV_R} \right) \left(\frac{\sqrt{C_{OH^-,L=0}} - \sqrt{C_{OH^-,L}}}{\sqrt{k_{OH^-} D_{CO_2}}} \right) \quad [80]$$

This solution has been applied to the measurements in the 1.6 mm ID glass capillary. The results are shown in Table 20. Average values of D_{CO_2} , $C_{CO_2,i}$, and k_{OH^-} over the expected range of variation (see Table 17) were used.

Table 20: Values of interfacial area determined from analytical solution for a pseudo-1st-order reaction (Equation 48)

$C_{OH-,0}$ (mol/L)	D_{CO_2} (m ² /s)	$C_{CO_2,i}$ (mol/L)	k_{OH^-} (L/mol·s)	a (m ² /m ³ reactor)
0.1	1.89×10^{-9}	34.6	7121	1273
1	1.97×10^{-9}	24.8	7968	1353
2	2.17×10^{-9}	16.5	10445	1680
3	2.16×10^{-9}	11.8	10237	1746
4	2.26×10^{-9}	8.3	11813	2622
5	2.16×10^{-9}	6.1	10063	2737

The analytical solution is only valid for measurements that meet the requirements of a pseudo-1st-order reaction. In Section 5.4.2 measurements for concentrations of at least 2 M and above appeared to fall in this range. However, in this analysis, the calculated value of a increases with increasing concentration and is not constant for concentrations above 2 M, which are expected to meet the pseudo-1st-order criteria. The highest concentrations yield values approximately equal to the surface area of the capillary (2500 m²/m³) and also the value obtained from the modified analysis of the Danckwerts plot in Section 5.4.2.

5.4.4 Model Description of Capillary: A Simplified Film Model

The capillary was modeled as a cascade of N stirred tanks, implicitly assuming that all CO_2 reacts within the segment where it is absorbed and $C_{CO_2,bulk,i} = 0$. The liquid volumetric flow rate is assumed to be constant, but the volumetric flow rate or partial pressure of the gas phase may vary. A balance was written for each reactor segment as illustrated in Figure 86.

$$CO_2 \text{ lost by gas} = 1/z * OH^- \text{ lost by liquid} = -r_{CO_2} * dV_R \quad [81]$$

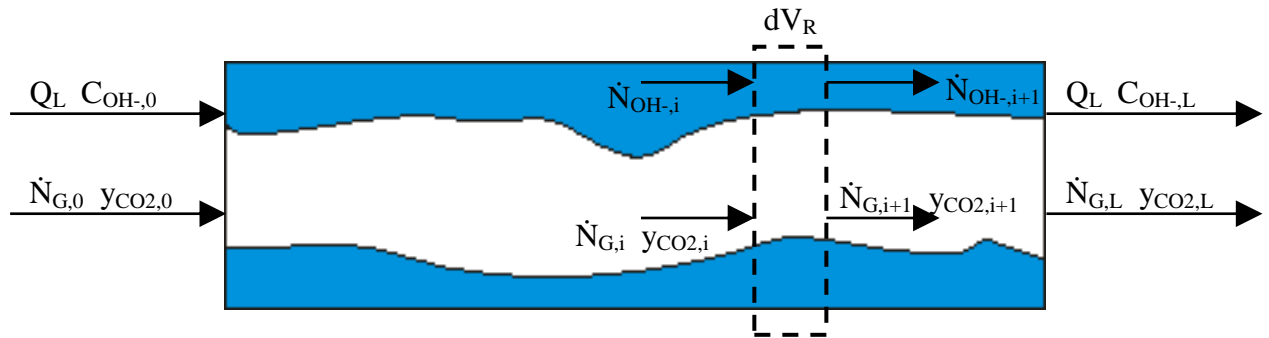


Figure 86: Reactor segment of a gas/liquid capillary

$$\dot{N}_{G,i+1} \cdot y_{CO_2,i+1} - \dot{N}_{G,i} \cdot y_{CO_2,i} = \frac{1}{z} (\dot{N}_{OH-,i+1} - \dot{N}_{OH-,i}) = r_{CO_2}(i) \cdot dV_R \quad [82]$$

Assuming the number of moles of inert gas in the gas phase remains constant:

$$\dot{N}_{inert} = \text{constant} = \dot{N}_{G,0} (1 + y_{CO_2,0}) \quad [83]$$

$$\dot{N}_{CO_2} = \dot{N}_G y_{CO_2} \quad [84]$$

$$\dot{N}_G = \dot{N}_{CO_2} + \dot{N}_{inert} \quad [85]$$

$$\dot{N}_{G,i} = \frac{\dot{N}_{G,0}(1 - y_{CO_2,0})}{(1 - y_{CO_2,i})} \quad [86]$$

Combining Equation 86 with Equation 82 and assuming the liquid volumetric flow rate to be constant:

$$\begin{aligned} \dot{N}_{G,0} \frac{(1 - y_{CO_2,0})}{(1 - y_{CO_2,i+1})} \cdot y_{CO_2,i+1} - \dot{N}_{G,i} \cdot y_{CO_2,i} \\ = \frac{Q_L}{z} (C_{OH^-,i+1} - C_{OH^-,i}) = r_{CO_2}(i) \cdot dV_R \end{aligned} \quad [87]$$

This equation can be simplified:

$$\frac{\dot{N}_{G,0}}{1 - y_{CO_2}} \cdot \frac{dy_{CO_2}}{-r_{CO_2}} = \frac{Q_L}{z} \cdot \frac{dC_{OH^-}}{-r_{CO_2}} = dV_R \quad [88]$$

A discretized model was thus implemented:

The reaction rate was defined as the rate at which gas was absorbed through the liquid film, always assuming $C_{CO_2,bulk} = 0$ and assuming k_L and a to be constant throughout the reactor.

$$r_{CO_2}(i) = k_L a E(i) \left(\frac{P_i y_{CO_2,i}}{H_{CO_2,i}} - 0 \frac{mol}{L} \right) \quad [89]$$

The units of r_{CO_2} depend on those of a . In this work a has units of m^2/m^3 reactor, and r_{CO_2} has units of $mol(CO_2)/m^3$ reactor*s. The enhancement factor was calculated (see Figure 82):

$$E(i) = \frac{Ha(i)}{\tanh(Ha(i))} \quad [90]$$

Since this model is being applied to the measurements already presented, E can safely be assumed to be much less than E_i . Replacing the expression for E with an exact solution, for example the van Krevelen-Hoftijzer correlation would be necessary to extend the model to higher Hatta numbers. The Hatta number was calculated:

$$Ha(i) = \frac{\sqrt{D_{CO_2,i} k_{OH^-,i} C_{OH^-,i}}}{k_L} \quad [91]$$

Temperature-dependent values of D_{CO_2} , k_{OH^-} , and H_{CO_2} were calculated according to the correlations given in Pohorecki and Moniuk [145].

$$D_{CO_2,i} = 10^{-8.1764 + \frac{712.5K}{T_i} - \frac{2.591 \cdot 10^5 K^2}{T_i^2}} \frac{m^2}{s} \quad [92]$$

$$k_{OH^-,i} = 10^{11.895 - \frac{2382K}{T_i}} \frac{L}{mol \cdot s} \quad [93]$$

$$H_{CO_2,i} = \frac{10^{(0.091+0.021-0.015) \cdot 3 \cdot C_{CO_3,i} \frac{L}{mol} + (0.091+0.066-0.015) \cdot C_{OH^-,i} \frac{L}{mol}}}{10^{9.1229 - 5.9044 \cdot 10^{-2} \cdot \frac{T_i}{K} + 7.8857 \cdot 10^{-5} \cdot \frac{T_i^2}{K^2}}} \frac{L \cdot bar}{mol} \quad [94]$$

The initial reaction rate ($i = 0$) in Equation 89 could thus be calculated from the initial concentrations and conditions. The concentration of OH^- was calculated as the initial concentration or concentration of the previous cell minus the amount of OH^- consumed in reaction.

$$C_{OH^-,i+1} = C_{OH^-,i} - z \cdot r_{CO_2}(i) \cdot \frac{V_R}{N} \cdot \frac{1}{Q_L} \quad [95]$$

The resulting concentrations of carbonate (C_{CO_3}) and CO_2 were calculated from their simple stoichiometric relationships to OH^- :

$$C_{CO_3,i} = C_{CO_3,0} + \frac{C_{OH^-,0} - C_{OH^-,i}}{z} \quad [96]$$

For gas mixtures, $y_{CO_2,0} < 1$, y_{CO_2} was calculated:

$$y_{CO_2,i} = \frac{\dot{N}_{G,0} \cdot y_{CO_2,0} + \frac{Q_L}{z} (C_{OH^-,i} - C_{OH^-,0})}{\dot{N}_{G,0} + \frac{Q_L}{z} (C_{OH^-,i} - C_{OH^-,0})} \quad [97]$$

For experiments using pure CO_2 , $y_{CO_2,0} = 1$, the mole fraction of CO_2 was specified to be 1 ($y_{CO_2,i} = 1$) as long as the moles of gas consumed in reaction were less than those fed to the reactor

$$0 < \dot{N}_{G,0} + \frac{Q_L}{z} \cdot (C_{OH^-,i} - C_{OH^-,0}) \quad [98]$$

and zero ($y_{CO_2,i} = 0$) if the total amount of gas had already been consumed.

5.4.4.1 Simplified Film Model Results

The discretized model was implemented using both the a and k_L values determined from the Danckwerts plot ($a = 1000 \text{ m}^2/\text{m}^3$, $k_L = 70 \times 10^{-4} \text{ m/s}$) and from an analysis of the E/Ha-style plot ($a = 3000 \text{ m}^2/\text{m}^3$, $k_L = 20 \times 10^{-4} \text{ m/s}$). The results are shown in Figure 87 and Figure 88, respectively. For these calculations the temperature and pressure were assigned constant

values of 21 °C and 1 bar, and the experimentally determined intercepts ($C_{OH^-,L=0}$) were used for the initial concentrations. Neither model can be considered to offer a good fit of all of the experimental measurements. The combination of lower interfacial area and higher mass transport coefficient describes the conversion at higher concentrations better, and the combination of higher interfacial area and lower mass transport coefficient describes the conversion at lower concentrations better. Essentially, each concentration set requires unique values of a and k_L to achieve a good fit.

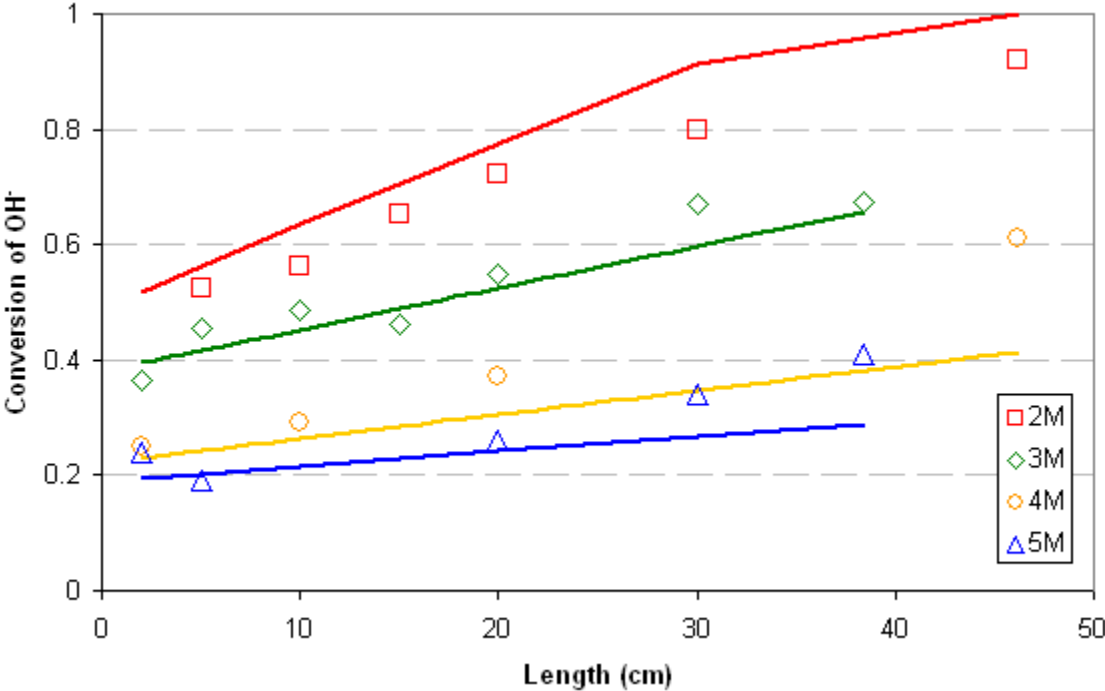


Figure 87: Comparison of model using $a = 1000 \text{ m}^2/\text{m}^3$, $k_L = 70 \times 10^{-4} \text{ m/s}$ to experimental measurements

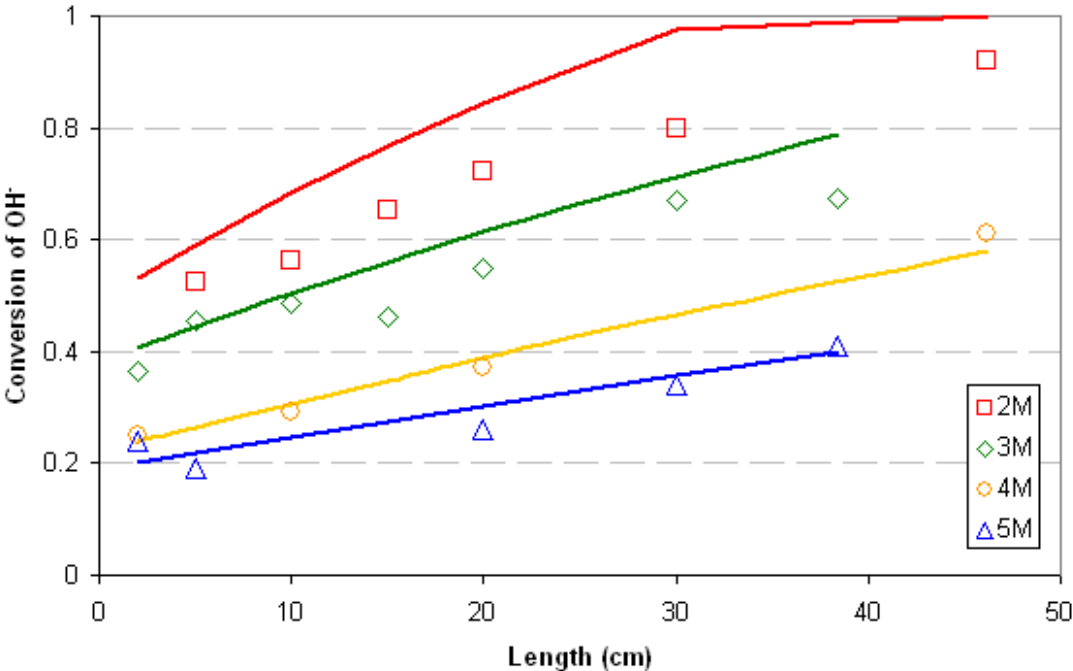


Figure 88: Comparison of model using $a = 3000 \text{ m}^2/\text{m}^3$, $k_L = 20 \times 10^{-4} \text{ m/s}$ to experimental measurements

The results of the model using different sets of a and k_L values were compared on the basis of the average reaction rate in Figure 89. As mentioned in the description of the T-junction, the relationship between $\Phi/C_{CO_2,i}$ and $D_{CO_2}k_{OH^-}C_{OH^-}$ was apparently linear. A comparison on this basis shows that the higher interfacial area ($a = 3000 \text{ m}^2/\text{m}^3$ reactor) more accurately described the reaction rates. The effect of k_L on the results is secondary to that of a , but lower values ($2 \times 10^{-4} \text{ m/s}$) fit the experiments at lower concentrations much better and had no effect on the reaction rates predicted for higher concentrations.

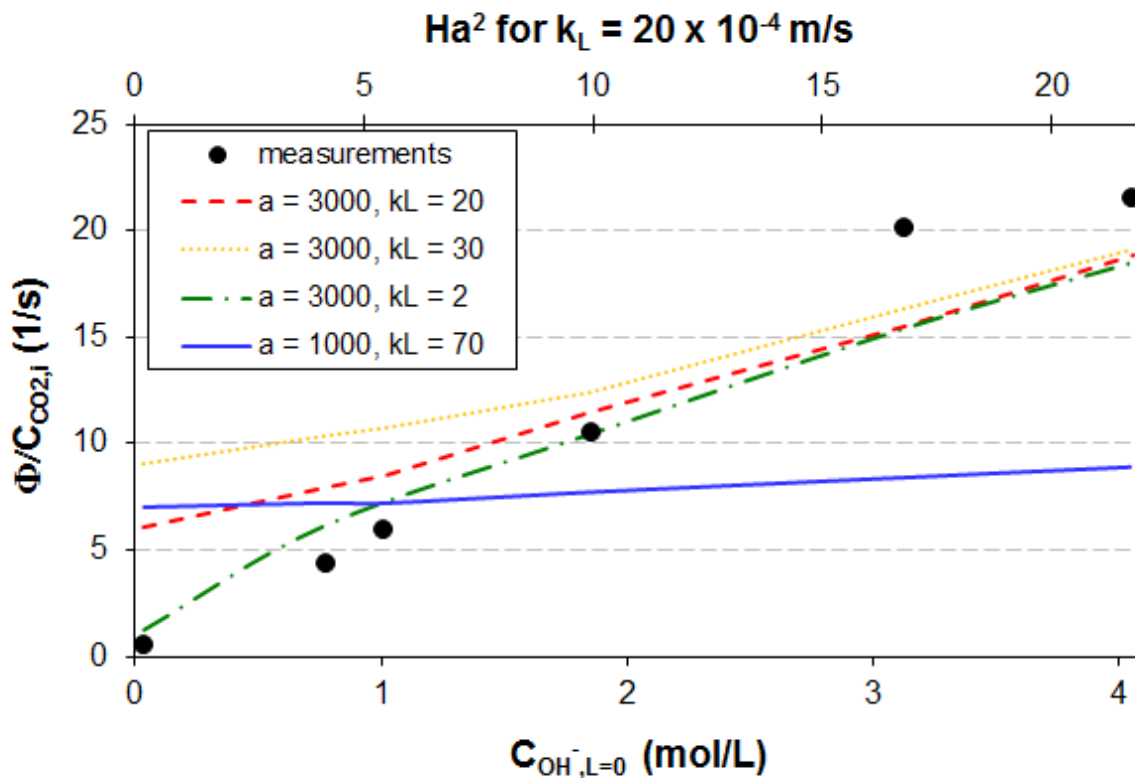


Figure 89: Reaction rate compared between measurements and model

The model is not explicitly limited to fast reactions. (The definition of E used is also accurate for $Ha < 1$.) Deviations between the model and measurements at lower concentrations may however result from deviations of $C_{CO_2,bulk}$ from 0.

On the basis of the experimental observation that the conversion rose linearly with the capillary length, a constant reaction rate throughout the capillary was justified for using average properties to derive values of a and k_L in Section 5.4.2. However, the simplified model presented in this section reveals that the reaction rate is not constant but rather decreases along the reactor length due to the decreases in the concentration of OH^- resulting in lower values of Ha and thus lower values of E . Profiles along the capillary length for concentrations of $NaOH$ and Na_2CO_3 , reaction rate, and dimensionless parameters E and Ha are shown in Figure 90 and Figure 91 for 2 M and 3 M, respectively. As long as the profiles of each of these values is nearly linear, there is little error incurred in basing calculations on the average values, assuming that they are appropriately ascertained (i.e. the average concentration must be used and not $C_{OH^-,0}$).

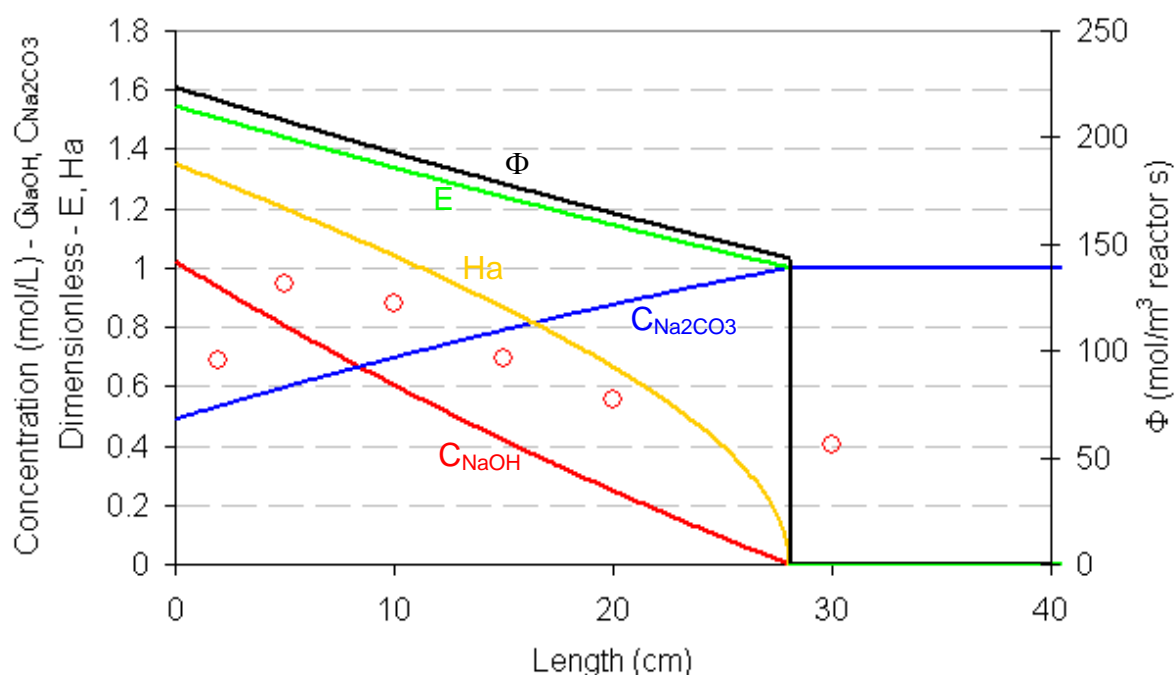


Figure 90: Profiles of C_{NaOH} , C_{Na2CO3} , Φ , E, and Ha calculated with simplified film model along capillary length for 2 M ($a = 3000 \text{ m}^2/\text{m}^3$, $k_L = 20 \times 10^{-4} \text{ m/s}$)

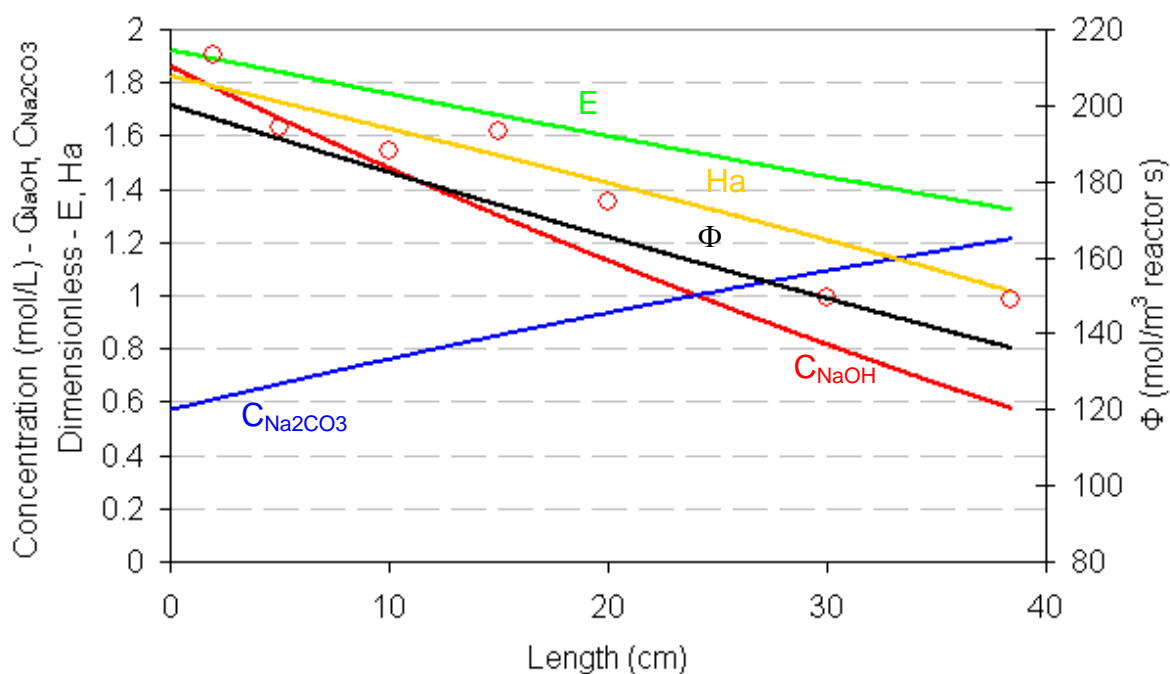


Figure 91: Profiles of C_{NaOH} , C_{Na2CO3} , Φ , E, and Ha calculated with simplified film model along capillary length for 3 M ($a = 3000 \text{ m}^2/\text{m}^3$, $k_L = 20 \times 10^{-4} \text{ m/s}$)

The error between the model and experimental points in Figure 89 increases with decreasing concentration and is off by more than a factor of 2 for concentrations less than 2 M. Possible sources of error include the assumptions of constant temperature and pressure, experimental error, and $C_{CO_2,bulk}$ values higher than 0. The effects of these assumptions have been judged for their effect on $\Phi/C_{CO_2,i}$ calculated for the 3 M reaction using $a = 3000 \text{ m}^2/\text{m}^3$ reactor and $k_L = 20 \times 10^{-4} \text{ m/s}$. The results are shown in Table 21. The temperature and pressure profiles were imposed on the capillary as linear relationships between the starting and end points. The effects of concentration, temperature, and pressure were calculated for k_{OH^-} , D_{CO_2} , $C_{CO_2,i}$, thus, the variation of these variables in the expected range given in Table 17 is already incorporated into the analysis of temperature and pressure. The variations in the average value of Φ associated with variations in temperature and pressure and their effect on $C_{CO_2,i}$, k_{OH^-} , and D_{CO_2} are less than 5 %.

Table 21: Effect of temperature and pressure profiles on Φ calculated with simplified film model for $C_{OH^-,0} = 3 \text{ M}$ ($a = 3000 \text{ m}^2/\text{m}^3$, $k_L = 20 \times 10^{-4} \text{ m/s}$)

T_0	T_L	P_0	P_L	$C_{CO_2,i}$	$\left(\frac{\Phi}{C_{CO_2,i}}\right)_0$	$\left(\frac{\Phi}{C_{CO_2,i}}\right)_{avg}$	$\left(\frac{\Phi}{C_{CO_2,i}}\right)_L$
(°C)	(°C)	(bar)	(bar)	(mol/L)	(1/s)		
21	21	1	1	Eqn. 94	14.0	11.5	9.2
21	35	1	1	Eqn. 94	14.0	11.6	9.1
21	21	1.14	1	Eqn. 94	14.0	11.1	8.3
21	35	1.14	1	Eqn. 94	14.0	11.1	8.1
22	34	1.14	1			9.0 (experimental)	

Optimal values of a and k_L were determined by minimizing the sum of the square errors between the average value of $\Phi/C_{CO_2,i}$ resulting from the model and the experimentally determined value for all concentrations points as shown in Figure 89. The sum of the square errors between the model and experimental values were determined for values of a between 1000 and 5000 m^2/m^3 reactor and k_L values between 2 and $70 \times 10^{-4} \text{ m/s}$. A plot showing the sum of the square errors between the model and experimental values with respect to the values of a and k_L entered in the model are shown in Figure 92. The optimal values determined through this analysis were a : $3500 \text{ m}^2/\text{m}^3$ reactor (evaluated to the nearest 100) and an optimal k_L value of $2 \times 10^{-4} \text{ m/s}$ (the range minimum). Smaller values of k_L were then calculated using $a = 3500 \text{ m}^2/\text{m}^3$ reactor. The error continued to decrease with decreasing k_L . Since the value of k_L had a large impact on the values calculated for concentrations less than 1 M and only a minor effect on the values calculated for higher concentrations, it may not be appropriate to determine k_L by optimizing this model since the assumption of $C_{CO_2,bulk} = 0$ may not be fulfilled at low concentrations of NaOH.

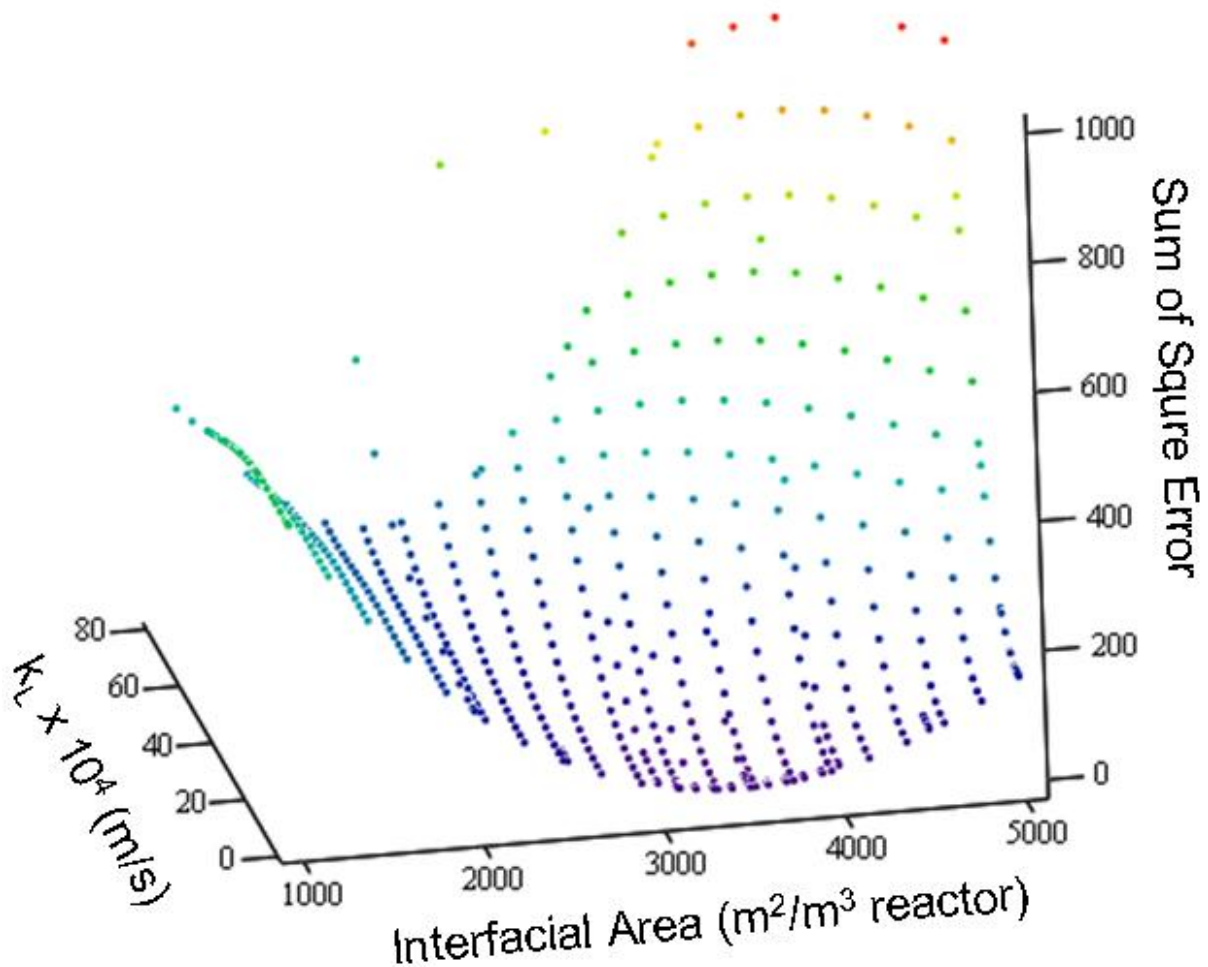


Figure 92: Sum of square errors between experiments and predictions of simplified film model

5.4.4.2 Validity of Simplified Film Model

The validity of the simplified film model, which uses the film theory to determine the rate of gas absorption, depends upon the accuracy of the underlying assumptions. The influence of the “constants” used in the model has already been discussed in Section 5.4.4.1. The simplified model condenses the complicated flow patterns observed in the capillaries to single values of a and k_L and does not consider local variations in the hydrodynamics and in these parameters. However, the linear rise in conversion along the capillary observed in Section 5.4.2 and modeled in Section 5.4.4.1 seem to support the use of the simplified model. The main assumptions which must be discussed are thus the validity of the film model itself and the validity of the assumption of a negligible concentration of dissolved gas in the liquid bulk.

To examine these assumptions, a second discretized model using a direct calculation of mass transport and reaction in the liquid film was compared to the model of Section 5.4.4. To distinguish the two models, the first model is called the simplified film model and the second model is called the 2D film model. The models are essentially the same except that Equation 89 is replaced by a mass balance on the liquid film, and the concentration of A in the liquid bulk is calculated rather than assumed to be zero.

A steady-state mass balance was written for the liquid film (see Figure 7), or on each element thereof, which balances the transport of species (through diffusion) with reaction:

$$D_{CO_2} \frac{d^2 C_{CO_2}}{dx^2} = k_{OH^-} \cdot C_{CO_2} \cdot C_{OH^-} \quad [99]$$

$$D_{OH^-} \frac{d^2 C_{OH^-}}{dx^2} = z \cdot k_{OH^-} \cdot C_{CO_2} \cdot C_{OH^-} \quad [100]$$

The boundary conditions at the gas/liquid interface ($x = 0$) are:

$$C_{CO_2,i} = \frac{P_{CO_2,i}}{H_{CO_2}} \quad [101]$$

$$\frac{dC_{OH^-}}{dx} = 0 \quad [102]$$

The boundary conditions at the boundary of the liquid film and liquid bulk ($x = \delta_L$) are determined from a mass balance constructed on the liquid bulk. Since the interfacial area and film thickness (i.e. $k_L = D_{CO_2}/\delta_L$) are required inputs of the model, the volume of the liquid film in the reactor segment can be calculated:

$$V_{film} = a \delta_L \frac{V_R}{N} \quad [103]$$

The volume of the liquid bulk is the total liquid volume ($\varepsilon_L \cdot V_R$) minus the volume of the film:

$$V_{bulk} = \varepsilon_{L,i} \frac{V_R}{N} - a \delta_L \frac{V_R}{N} \quad [104]$$

A material balance on species A in the liquid bulk can be constructed as a balance of the amount of A entering and leaving the bulk with the flow plus the amount of A entering from the liquid film through diffusion minus the amount of A consumed by reaction in the liquid bulk:

$$0 = Q_L C_{CO_2,bulk_{i-1}} - Q_L C_{CO_2,bulk_i} - a \frac{V_R}{N} D_{CO_2} \left. \frac{dC_{CO_2}}{dx} \right|_{x=\delta_L} - V_{bulk} k_{OH^-} C_{CO_2,bulk_i} C_{OH^-,bulk_i} \quad [105]$$

In this balance all liquid flow occurs through the bulk and the film is assumed to be stagnant. This assumption is consistent with the classical description of the film theory but may not accurately reflect flow in a capillary, especially if the volume of the liquid film is large relative to the total liquid volume. An analogous balance can be constructed on species B:

$$0 = Q_L C_{OH^-,bulk,i-1} - Q_L C_{OH^-,bulk,i} - a \frac{V_R}{N} D_{OH^-} \left. \frac{dC_{OH^-}}{dx} \right|_{x=\delta_L} - z V_{bulk} k_{OH^-} C_{CO_2,bulk,i} C_{OH^-,bulk,i} \quad [106]$$

Equations 105 and 106 can be rearranged to express the concentrations $C_{CO_2,bulk,i}$ and $C_{OH^-,bulk,i}$ in the liquid bulk as functions of their initial values (i-1), the gradient at the edge of the liquid film ($x = \delta_L$), and each other. Since the volume of the liquid bulk is contained in this mass balance, the 2D model is limited to film thicknesses and k_L values where the volume of the liquid bulk is > 0 . Thus, for an interfacial area of $3000 \text{ m}^2/\text{m}^3$ reactor, the lowest value of k_L that can be used with this model is $8 \times 10^{-4} \text{ m/s}$, and for an interfacial area of $3500 \text{ m}^2/\text{m}^3$ reactor, the lowest value of k_L that can be used is $9 \times 10^{-4} \text{ m/s}$.

$$C_{CO_2,bulk,i} = \frac{Q_L C_{CO_2,bulk,i-1} - a D_{CO_2} \left. \frac{dC_{CO_2}}{dx} \right|_{x=\delta_L} \frac{V_R}{N}}{Q_L + k_{OH^-} C_{OH^-,bulk,i} \left(\varepsilon_{Li} \frac{V_R}{N} - a \delta_L \frac{V_R}{N} \right)} \quad [107]$$

$$C_{OH^-,bulk,i} = \frac{Q_L C_{OH^-,bulk,i-1} - a D_{OH^-} \left. \frac{dC_{OH^-}}{dx} \right|_{x=\delta_L} \frac{V_R}{N}}{Q_L + z k_{OH^-} C_{CO_2,bulk,i} \left(\varepsilon_{Li} \frac{V_R}{N} - a \delta_L \frac{V_R}{N} \right)} \quad [108]$$

The balance on the liquid film (Equations 99 and 100) are solved with the four boundary conditions (Equations 101-102 and 107-108) using a finite difference method implemented in Mathcad 14 to solve the equations for a liquid film divided into 100 cells of equal volume. The Mathcad program is included in Appendix 8.7. The reactor was divided into 500 cells along its length as in the previous section, and a constant pressure of 1 bar and temperature of $21 \text{ }^\circ\text{C}$ were assumed. The concentrations of CO_2 and OH^- in the liquid bulk were thus directly calculated from the film model. The loss of gas was calculated (for pure gas; compare Equation 97) from the flux at the gas/liquid interface ($x = 0$):

$$N_{G,i} = N_{G,i-1} - a \frac{V_R}{N} D_{CO_2} \left. \frac{dC_{CO_2}}{dx} \right|_{x=0} \quad [109]$$

The rate of gas absorption is not directly calculated as a part of this model, but can be derived from the rate of gas consumption (i.e. from the results of Equation 109):

$$\Phi_i = \frac{N_{G,i-1} - N_{G,i}}{\frac{V_R}{N}} \quad [110]$$

The profiles of dissolved OH^- and CO_2 in the liquid bulk along the reactor length are shown in Figure 93 and Figure 95 for NaOH concentrations of 3 M and 1 M, respectively. The profiles within the liquid film at the capillary entrance and exit are shown in Figure 94 and Figure 96.

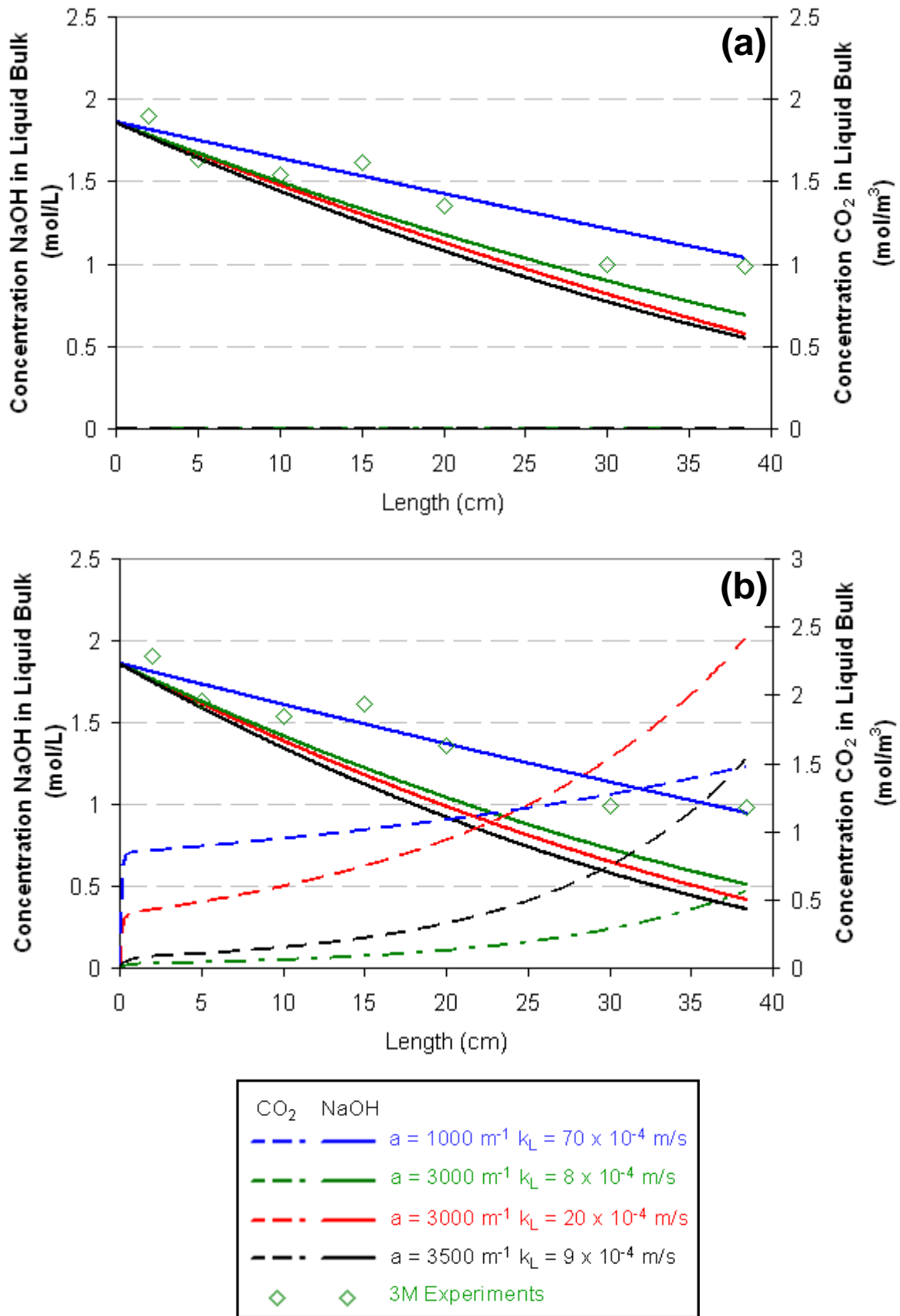


Figure 93: Comparison of liquid bulk concentrations C_{NaOH} and C_{CO_2} along the capillary length calculated with the (a) simplified film model and (b) 2D film model for conditions of the experiments of the reaction of CO_2 with 3 M NaOH ($T = 21 \text{ }^\circ\text{C}$, $P = 1 \text{ bar}$)

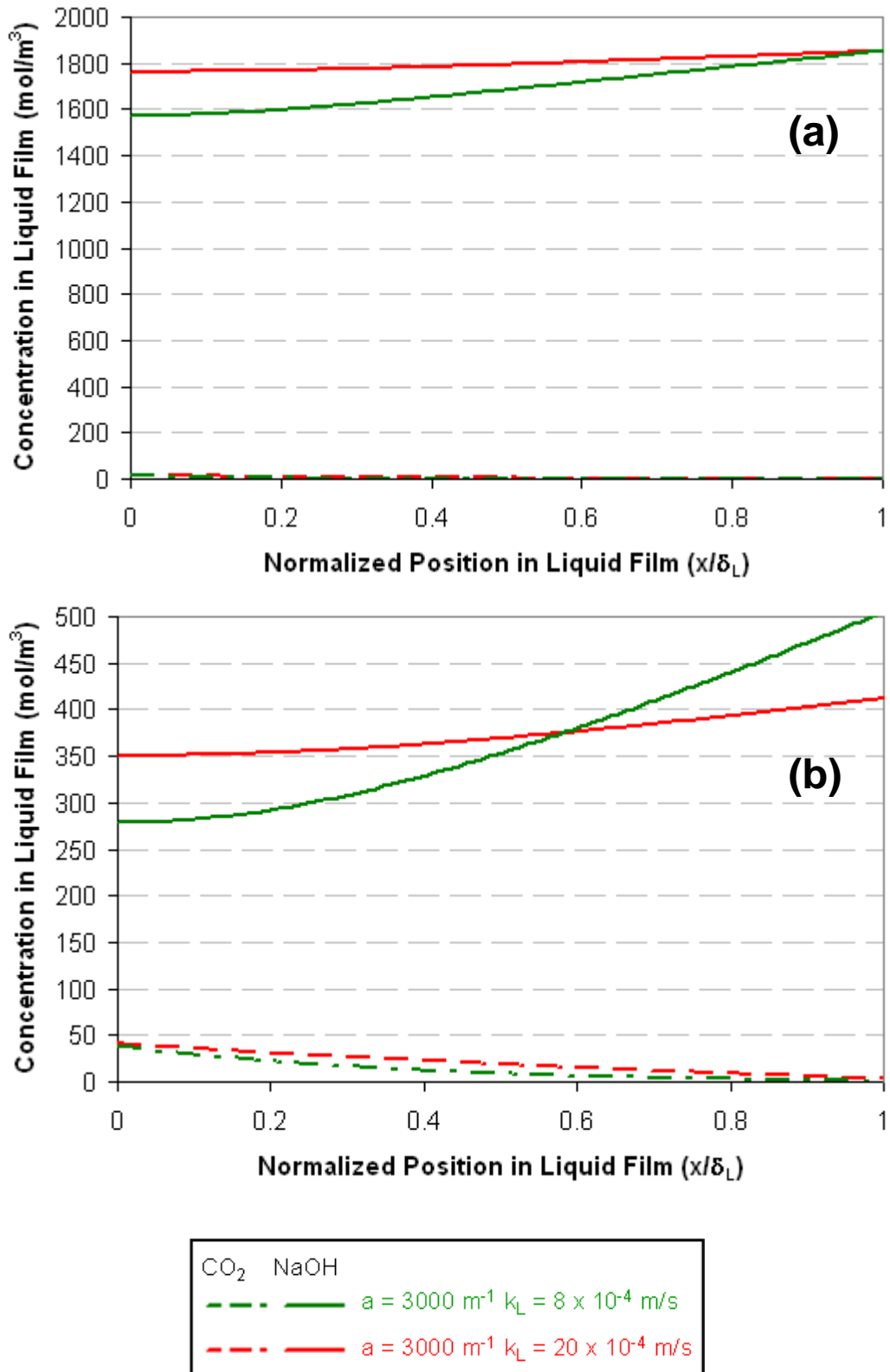


Figure 94: Comparison of profiles of C_{NaOH} and C_{CO_2} within the liquid film calculated with the 2D film model for the (a) capillary entrance (b) capillary exit using the starting conditions of the experiments of the reaction of CO₂ with 3 M NaOH (T = 21 °C, P = 1 bar)

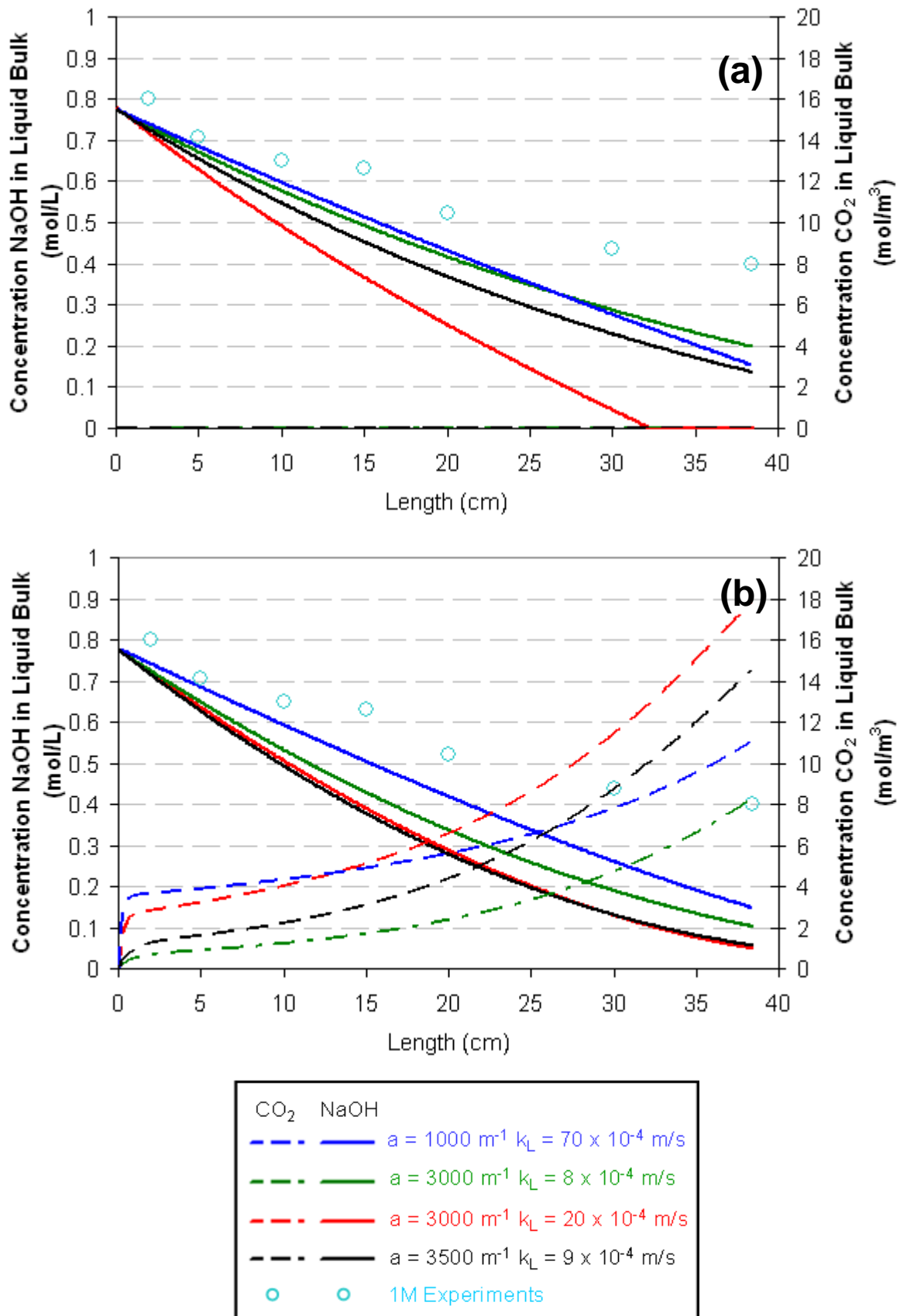


Figure 95: Comparison of liquid bulk concentrations C_{NaOH} and C_{CO_2} along the capillary length (a) simplified film model and (b) 2D film model for conditions of the experiments of the reaction of CO₂ with 1 M NaOH (T = 21 °C, P = 1 bar)

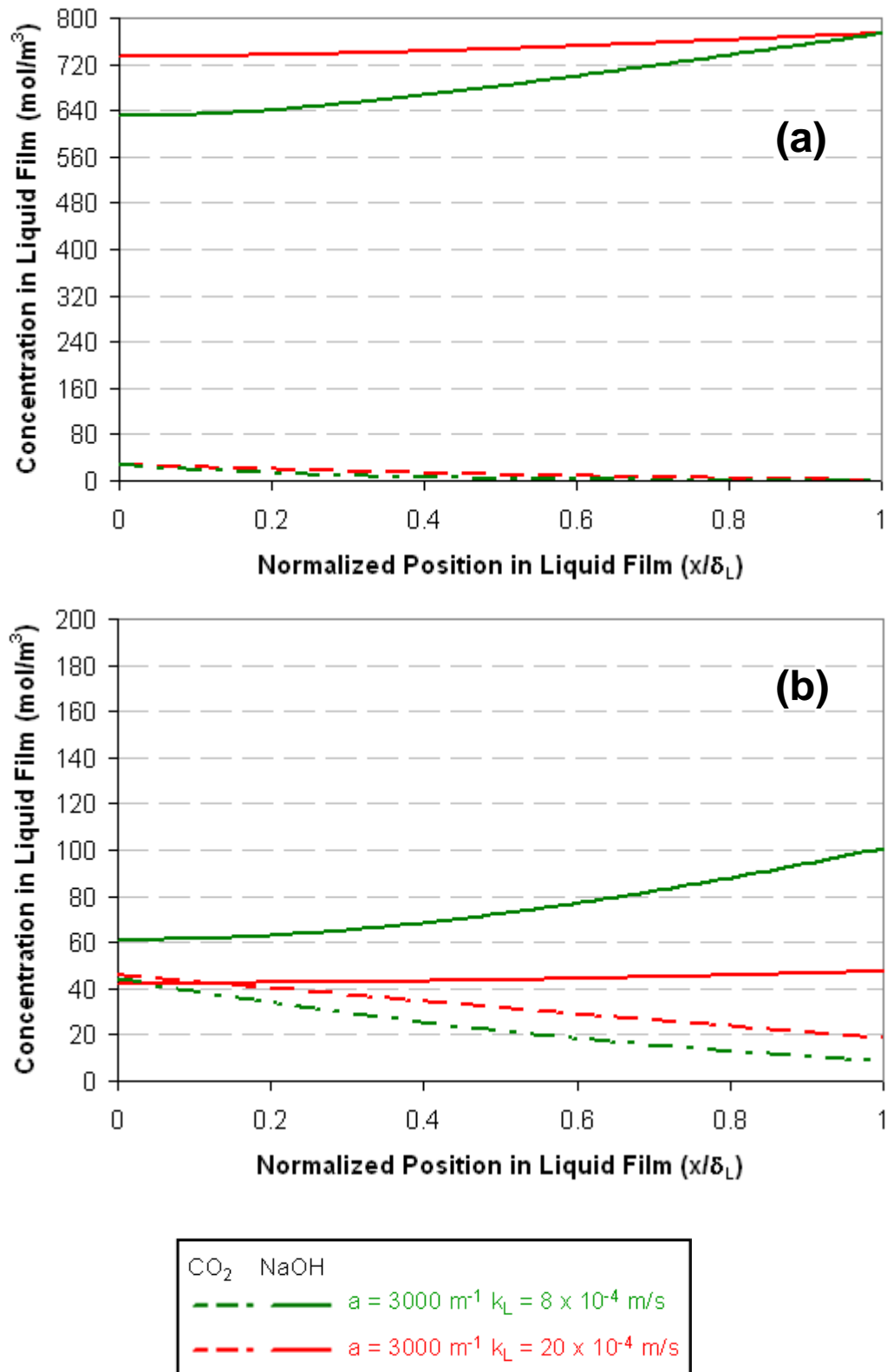


Figure 96: Comparison of profiles of C_{NaOH} and C_{CO_2} within the liquid film calculated with the 2D film model for the (a) capillary entrance (b) capillary exit using the starting conditions of the experiments of the reaction of CO₂ with 1 M NaOH (T = 21 °C, P = 1 bar)

The results of the simplified film model as well as the experimental measurements are shown in Figure 93 and Figure 95 for comparison. The purpose of this comparison is not to evaluate which model or set of parameters better fits the data (which is done in the previous section) but rather to evaluate the validity of the simplified model. The differences between the models are complicated and reveal why both a and k_L rather than just $k_L a$ must be known to accurately model fast reactions. Differences between the models seem to be related to the volume of the liquid film with respect to the liquid bulk. The film theory separates the film into a perfectly mixed bulk and a film where mass transport occurs through diffusion. The film model is not a perfect representation of reality, but the rate of mass transport must lie between the two limits of an instantaneously perfectly mixed environment and purely diffusional transport. However, since the liquid bulk is used as a boundary condition in the film theory, its volume is implicitly assumed to be much larger than that of the liquid film. The 2D film model partially accounts for the exact size of each phase through the boundary conditions applied, whereas the simplified film model also assumes a quasi-infinite liquid bulk in the definition of its concentrations. The 2D film model generally predicts slightly higher rates of decrease in the concentration of NaOH although including the concentration of CO₂ in the liquid bulk ought to reduce the rate of absorption. This may be because the 2D film model includes reaction in the liquid bulk. The 2D film model includes the concentration of dissolved CO₂ in the liquid bulk, but even for the 1 M experiments, the concentration of dissolved CO₂ in the liquid bulk remains more than an order of magnitude smaller than the concentration of NaOH. Therefore, the assumption of negligible dissolved CO₂ in the liquid bulk is not expected to reduce the gradient driving the transport of CO₂ through the liquid film to a significant extent, and the simplified model should be valid with respect to this assumption. The comparison shows that the assumption of negligible dissolved gas in the liquid bulk is valid and does not introduce large errors, even at high conversions.

5.4.5 Comparison of Methods Used to Obtain Values of Interfacial Area and Mass Transport Coefficient

The approximate values of interfacial area and mass transport coefficient determined for slug flow ($j_G = 10$ m/s, $j_L = 0.1$ m/s) in a 1.6 mm ID glass capillary from the Danckwerts plot (Section 5.4.2), modified analysis of the Danckwerts plot (Section 5.4.2), analytical solution for a pseudo-1st-order reaction (Section 5.4.3), and through optimization of a simplified film model (Section 5.4.4) are summarized in Table 22.

Table 22: Values of interfacial area and mass transport coefficient determined using various methods

Method	a (m ² /m ³ reactor)	k_L (m/s)
Danckwerts Plot	1000	70
E/Ha Analysis of Danckwerts Plot	3000	20
Analytical Solution for Pseudo-1 st -Order Reaction	2700	-
Optimization of Simplified Film Model	3500	< 2

The traditional Danckwerts plot did not provide good estimates of values of interfacial area and mass transport coefficients since the interfacial concentration of carbon dioxide was treated as a constant for all measured concentrations but in fact the concentration decreases with increasing salt concentration. Accounting for this effect, the modified analysis of the Danckwerts plot seemed to provide reasonable estimates of a as well as k_L . The values of a determined with the analytical solution for a pseudo-1st-order reaction depended on the concentration; the highest concentrations gave values of a similar to those obtained with the modified Danckwerts analysis. No values of k_L could be obtained with the analytical solution.

Optimizing a model of the capillary based on a simplified film theory yielded a higher value of a and lower value of k_L than those derived in the E/Ha analysis of the Danckwerts plot. Based on visual observations of the flow, the interfacial area was expected to be larger than the surface area of the capillary ($a = 2500 \text{ m}^{-1}$). The best estimate of the actual interfacial area for slug flow is thus a value of 3000-3500 m^2/m^3 reactor, an increase of 20 – 40 % above the surface area of the capillary.

The value of k_L for slug flow determined for slug flow in the capillary is much more uncertain. Although the value of $20 \times 10^{-4} \text{ m/s}$ derived from the E/Ha analysis of the Danckwerts plot seems reasonable, this analysis treats the complete capillary essentially as a stirred tank despite large gradients in the concentrations along the reactor length. The value of $2 \times 10^{-4} \text{ m/s}$ obtained through optimizing a discretized model accounts for concentration gradients along the reactor. However, this model showed only minimal differences between results for measurements at concentrations above 2 M, so the optimized values depend heavily on measurements at low concentrations, where the assumptions of the model may be violated. Additionally, if the lower value obtained through the model optimization is the “real” value, the model would be anyway invalid since the liquid film volume would exceed the total liquid volume.

The discussion of the relative volumes of the liquid film and bulk are directly related to the general applicability of film theory to microreactors. Assuming that the liquid flows ($j_L = 0.1 \text{ m/s}$) as an annulus on the wall of the capillary ($D = 1.6 \text{ mm}$) with the gas ($j_L = 10 \text{ m/s}$) in the middle and that they have the same residence times, the thickness of the liquid layer would be $4 \text{ }\mu\text{m}$. The k_L values of $40 \times 10^{-4} \text{ m/s}$, $20 \times 10^{-4} \text{ m/s}$, and $10 \times 10^{-4} \text{ m/s}$ correspond to liquid film thicknesses of $0.625 \text{ }\mu\text{m}$, $1.25 \text{ }\mu\text{m}$, and $2.5 \text{ }\mu\text{m}$, respectively. Thus, the film theory seems to still be applicable if a high value of k_L is applicable. However, optimization of the simplified film model in Section 5.4.4.1 suggested much lower values of k_L , where the thickness of the liquid film would exceed the total thickness of the liquid layer. Thus, the results of each method are only valid insofar as the assumptions of each method are fulfilled, and further information regarding the exact interfacial area and the residence times of the respective phases is needed to definitively determine the respective sizes of the liquid film and bulk.

6 SUMMARY AND CONCLUSIONS

Although not a complete description of gas/liquid reaction in microstructured devices, this work establishes a framework for characterizing gas/liquid reactors and is the first work to systematically study the surfaces of microfabricated structures and their effect on not only gas/liquid flow but also on transport and reaction. Ideally, values for the interfacial area (a) and liquid transport coefficient (k_L) would be available in the engineering handbooks for microchannels of certain sizes, shapes, and material, but a correlation describing all these parameters requires first characterizing the performance of a wide range of microstructured devices. Despite repeated demonstrations of the advantages of microreactors and their increasing ubiquity on the chemist's workbench, engineers are lacking critical information that is necessary for the expected expansion of microreactors in chemical production.

1. The effect of surface roughness on the contact angle in microchannels is negligible.

Various materials were structured through polishing, grinding, or machining. The surface roughnesses of these surfaces were measured with AFM. The contact angle of a sessile drop of liquid on the surface was measured for liquids with different surface tensions and in different gas atmosphere. The surface tension, surface roughness, and drop size were found to strongly affect measured values of the contact angle. A correlation using surface tension, surface roughness, drop volume, and gas atmosphere was able to roughly predict the contact angle on any surface within $\pm 50\%$ even though the most important component of the contact angle, the solid surface, was not included in the correlation. Although the roughnesses of the machined surfaces were higher, the differences between the contact angles measured on the polished and machined surfaces were small. Thus, the contact angle in a microchannel can be assumed to have the same value as the contact angle on a polished surface.

2. More wettable materials produce higher interfacial areas for gas/liquid flows.

Nonreacting gas/liquid flows were observed with high speed videography in wettable glass and fused silica capillaries and in hydrophobic FEP capillaries. For the same gas and liquid flow rates, differences in the flow hydrodynamics could be visually observed. Assuming pseudo-1st-order reaction ($E = Ha$) for the absorption of CO₂ into aqueous 2.0 M NaOH, interfacial areas could be derived from measurements of reaction for fused silica ($\theta \approx 50^\circ$), PEEK ($\theta \approx 65^\circ$), and FEP ($\theta \approx 95^\circ$) capillaries. Better wettability corresponded to higher interfacial area. Interfacial areas up to 50 % larger than the surface area of the channel wall were obtained.

3. Average values derived from measurements of reaction using the complete reactor are comparable to local values within the reactor as long as the reaction rate along the reactor length is constant.

Thermographic measurements of the backside of the liquid plate in a microstructured falling film reactor were used to estimate the local rate of reaction using the exothermic absorption of CO₂ into aqueous 2.0 M NaOH. The local values of the liquid mass transport coefficient (assuming a geometric value of a), Ha , and E were derived from the local rates of reaction. These values were compared to values of k_L , Ha , and E calculated only from the inlet and outlet concentrations of the reactor. In the case of moderate conversion ($X_{OH^-} = 0.76$), the average reactor values were comparable to the average local values. In the case of complete conversion ($X_{OH^-} = 1$), the average value of k_L underestimated the values of k_L because the reaction rate was assumed to be constant but in reality changed from a high initial rate of reaction to a rate of zero after completion was reached.

4. The gas/liquid mixer contributes strongly to the overall conversion.

Measurements conducted with various lengths of capillaries revealed that although the reaction rate was constant along the length of the capillary (The pressure drop and gas shrinkage were negligible at the conditions of the study, and the reaction was mass transport limited, i.e. pseudo-1st-order), half of the conversion occurred in the T-junction where the gas and liquid phases were initially contacted.

5. Values of a and k_L can be derived from measurements where a pseudo-1st-order reaction assumption is valid using a modified Danckwerts plot.

This statement is true but requires qualification. The absorption of CO₂ into aqueous solutions of different concentrations of NaOH was conducted for different lengths of 1.5 mm glass capillaries. The pressure drop in the system was negligible, and the gas ($j_G = 10$ m/s) and liquid flow rates ($j_L = 0.1$ m/s) were such that the volume of gas was not substantially reduced with reaction. Thus, the flow pattern and pressure along the reactor could reasonably be assumed to be constant. If the flow regime remains constant, the rate of gas uptake for of a pseudo-1st-order reaction (mass transport limited) remains constant even for very high conversions (short of 100%). The value of a can be derived from the slope of a line interpolated through the concentrations where the pseudo-1st-order assumption is appropriate. By conducting measurements at lower concentrations where $E = 1$, values of k_L can be estimated. In any case, the value of k_L must at least be larger than the x-axis intercept of the interpolated pseudo-1st-order line.

6. In wettable materials ripples in the liquid surface occurring for the slug and annular flow patterns may increase the interfacial area above the geometric surface to volume ratio of the channel. For plug flow the interfacial area may be smaller.

In both literature studies and the measurements conducted in this work, the size of the gas/liquid interfacial area may as a first approximation be assumed to be equal to the surface to volume ratio of the microchannel. For slug and annular flow patterns, ripples observed in the surface of the liquid corresponded to higher values of a derived from measurements with chemical reaction. Conflicting information has been found for plug flow. The thin liquid film at the side of the bubble may too quickly become saturated and not contribute to the interfacial area but in other studies good agreement between optical measurements and measurements with chemical reaction have been found. This work offers no new insight into this question. The role of the film likely depends on the reaction rate and solubility of the gas and should be evaluated on a case by case basis. Characterization of the plug flow regime with chemical reaction is difficult since the gas bubble shrinkage occurs very rapidly at atmospheric pressure for fast reactions.

8. The best approach for determining values of a and k_L from gas/liquid reaction in microchannels and capillaries remains unclear.

A simplified film model based only on a balance of the liquid film was used to model the experimentally measured conversions. The simplified model used a balance on the liquid film using a and k_L values derived from the measurements and assuming a negligible concentration of dissolved gas in the liquid bulk due to the fast reaction. It was not possible to model all measured concentrations using a single parameter set of a and k_L with the model. An optimization based on the residual errors of the rate of gas absorption gave more weight to the lower concentrations, where the assumptions of the model may not be fulfilled, and produced an optimal k_L of the range minimum, which if true would violate the assumptions of the model. A 2D film model using direct calculation of mass transport and reaction in the liquid film was implemented to calculate the concentration of dissolved gas in the liquid bulk and evaluate its effect on the accuracy of the simplified model. The second model was able to

accurately model the physical absorption of gas occurring after reaction reached completion which the simplified model could not, but even for the high conversions obtained experimentally, the gas concentration dissolved in the bulk liquid phase did not seem to affect the rate of absorption. Without a better idea of the “real” values, the diverging values of k_L from the modified analysis of the Danckwerts plot and that of the discretized model cannot be discriminated.

Much work remains to be done in order to provide correlations for a and k_L for all possible reactions and materials. What is clear from this work is that not only the properties of the liquid and gas must be accounted for in such correlations but that the effect of material wettability on interfacial area may not be neglected. Alternatively, better wettability, e.g. through wettable coatings, could be used to increase the interfacial area. Analysis of gas/liquid reactions using pseudo-1st-order reactions can be used to characterize gas/liquid microreactors, but the system properties must be accurately known to obtain useful results. Future work must also consider the role of the initial contacting of the gas and liquid phases and not just the flow in the microchannel. In conclusion the advantages of microstructured reactors would seem to offer attractive benefits for industrial processes, especially the high interfacial areas and surface area for heat transfer, but the design of the reactors themselves will be more complicated than anticipated since it requires a better understanding of material and interfacial effects.

7 REFERENCES

1. Chambers, R.D., M.A. Fox, D. Holling, T. Nakano, T. Okazoe, and G. Sandford, *Elemental Fluorine. Part 16. Versatile Thin-Film Gas-Liquid Multi-Channel Microreactors for Effective Scale-Out*. Lab on a Chip, 2005. 5: 191-198. DOI: 10.1039/b416400h
2. Losey, M.W., M.A. Schmidt, and K.F. Jensen, *Microfabricated Multiphase Packed-Bed Reactors: Characterization of Mass Transfer and Reactions*. Industrial and Engineering Chemistry Research, 2001. 40(12): 2555-2562. DOI: 10.1021/ie000523f
3. Mendorf, M., H. Nachtrodt, A. Mescher, A. Ghaini, and D.W. Agar, *Design and Control Techniques for the Numbering-up of Capillary Microreactors with Uniform Multiphase Flow Distribution*. Industrial & Engineering Chemistry Research, 2010. 49(21): 10908-10916. DOI: 10.1021/ie100473d
4. Serizawa, A., Z. Feng, and Z. Kawara, *Two-Phase Flow in Microchannels*. Experimental Thermal and Fluid Science, 2002. 26(6-7): 703-714. DOI: 10.1016/S0894-1777(02)00175-9
5. Taitel, Y., B. Dvora, and A.E. Dukler, *Modelling Flow Pattern Transitions for Steady Upward Gas-Liquid Flow in Vertical Tubes*. AIChE Journal, 1980. 26(3): 345-354. DOI: 10.1002/aic.690260304
6. Triplett, K.A., S.M. Ghiaasiaan, S.I. Abdel-Khalik, and D.L. Sadowski, *Gas-Liquid Two-Phase Flow in Microchannels Part I: Two-Phase Flow Patterns*. International Journal of Multiphase Flow, 1999. 25(3): 377-394. DOI: 10.1016/S0301-9322(98)00054-8
7. Yue, J., R. Boichot, L. Luo, Y. Gonthier, G. Chen, and Q. Yuan, *Flow Distribution and Mass Transfer in a Parallel Microchannel Contactor Integrated with Constructal Distributors*. AIChE Journal, 2010. 56(2): 298-317. DOI: 10.1002/aic.11991
8. Barajas, A.M. and R.L. Panton, *The Effects of Contact Angle on Two-Phase Flow in Capillary Tubes*. International Journal of Multiphase Flow, 1993. 19(2): 337-346. DOI: 10.1016/0301-9322(93)90007-H
9. Lee, C.Y. and S.Y. Lee, *Influence of Surface Wettability on Transition of Two-Phase Flow Pattern in Round Mini-Channels*. International Journal of Multiphase Flow, 2008. 34(7): 706-711. DOI: 10.1016/j.ijmultiphaseflow.2008.01.002
10. Yue, J., L. Luo, Y. Gonthier, G. Chen, and Q. Yuan, *An Experimental Investigation of Gas-Liquid Two-Phase Flow in Single Microchannel Contactors*. Chemical Engineering Science, 2008. 63(16): 4189-4202. DOI: 10.1016/j.ces.2008.05.032
11. Zhao, T.S. and Q.C. Bi, *Co-Current Air-Water Two-Phase Flow Patterns in Vertical Triangular Microchannels*. International Journal of Multiphase Flow, 2001. 27(5): 765-782. DOI: 10.1016/S0301-9322(00)00051-3
12. Taitel, Y. and A.E. Dukler, *A Model for Predicting Flow Regime Transitions in Horizontal and near Horizontal Gas-Liquid Flow*. AIChE Journal, 1976. 22(1): 47-55.
13. Suo, M. and P. Griffith, *Two-Phase Flow in Capillary Tubes*. Journal of Basic Engineering, 1964. 86: 576-582.
14. Barnea, D., Y. Luninski, and Y. Taitel, *Flow Pattern in Horizontal and Vertical Two Phase Flow in Small Diameter Pipes*. The Canadian Journal of Chemical Engineering, 1983. 61(5): 617-620.
15. Kreutzer, M.T., F. Kapteijn, J.A. Moulijn, and J.J. Heiszwolf, *Multiphase Monolith Reactors: Chemical Reaction Engineering of Segmented Flow in Microchannels*. Chemical Engineering Science, 2005. 60(22): 5895-5916. DOI: 10.1016/j.ces.2005.03.022

16. Taylor, G.I., *Deposition of a Viscous Fluid on the Wall of a Tube*. Journal of Fluid Mechanics, 1961. 10(2): 161-165. DOI: 10.1017/S0022112061000159
17. Bretherton, F.P., *The Motion of Long Bubbles in Tubes*. Journal of Fluid Mechanics, 1961. 10(02): 166-188. DOI: 10.1017/S0022112061000160
18. Vankayala, B.K., P. Löb, V. Hessel, G. Menges, C. Hofmann, D. Metzke, U. Krtschil, and H.-J. Kost, *Scale-up of Process Intensifying Falling Film Microreactors to Pilot Production Scale*. International Journal of Chemical Reactor Engineering, 2007. 5: A91.
19. Löb, P., H. Löwe, and V. Hessel, *Fluorinations, Chlorinations and Brominations of Organic Compounds in Micro Reactors*. Journal of Fluorine Chemistry, 2004. 125(11): 1677-1694. DOI: 10.1016/j.jfluchem.2004.09.006
20. Mason, B.P., K.E. Price, J.L. Steinbacher, A.R. Bogdan, and D.T. McQuade, *Greener Approaches to Organic Synthesis Using Microreactor Technology*. Chemical Reviews, 2007. 107(6): 2300-2318. DOI: 10.1021/cr050944c
21. McPake, C.B. and G. Sandford, *Selective Continuous Flow Processes Using Fluorine Gas*. Organic Process Research and Development, 2012. 16(5): 844-851. DOI: 10.1021/op200331s
22. Löwe, H., W. Ehrfeld, K. Gebauer, K. Golbig, O. Hausner, V. Haverkamp, V. Hessel, and T. Richter, *Microreactor Concepts for Heterogeneous Gas Phase Reactions*, in *IMRET 2 Proceedings*. New Orleans, Louisiana. 63-74. 1998.
23. Hessel, V., W. Ehrfeld, K. Golbig, V. Haverkamp, H. Löwe, M. Storz, C. Wille, A.E. Guber, K. Jähnisch, and M. Baerns, *Gas/Liquid Microreactors for Direct Fluorination of Aromatic Compounds Using Elemental Fluorine*, in *Microreaction Technology: IMRET 3: Proceedings of the Third International Conference on Microreaction Technology*. Frankfurt, Germany: Springer. 526-540. 1999.
24. Jähnisch, K., M. Baerns, V. Hessel, W. Ehrfeld, V. Haverkamp, H. Löwe, C. Wille, and A.E. Guber, *Direct Fluorination of Toluene Using Elemental Fluorine in Gas/Liquid Microreactors*. Journal of Fluorine Chemistry, 2000. 105(1): 117-128. DOI: 10.1016/S0022-1139(00)00300-6
25. de Mas, N., R.J. Jackman, M.A. Schmidt, and K.F. Jensen, *Microchemical Systems for Direct Fluorination of Aromatics*, in *Microreaction Technology: IMRET 5: Proceedings of the Fifth International Conference on Microreaction Technology*. Strasbourg, France: Springer. 60-67. 2001.
26. de Mas, N., *Heat Effects in a Microreactor for Direct Fluorination of Aromatics*, in *IMRET 6 Proceedings*. New Orleans, Louisiana. 184-185. 2002.
27. de Mas, N., A. Günther, M.A. Schmidt, and K.F. Jensen, *Microfabricated Multiphase Reactors for the Selective Direct Fluorination of Aromatics*. Industrial and Engineering Chemistry Research, 2003. 42(4): 698-710. DOI: 10.1021/ie020717q
28. de Mas, N. *Scalable Multiphase Microchemical Systems for Direct Fluorination*, Ph.D. thesis. Massachusetts Institute of Technology. 2004.
29. de Mas, N., A. Günther, M.A. Schmidt, and K.F. Jensen, *Increasing Productivity of Microreactors for Fast Gas-Liquid Reactions: The Case of Direct Fluorination of Toluene*. Industrial and Engineering Chemistry Research, 2009. 48(3): 1428-1434. DOI: 10.1021/ie801232d
30. Chambers, R.D. and R.C.H. Spink, *Microreactors for Elemental Fluorine*. Chemical Communications, 1999(10): 883-884. DOI: 10.1039/a901473j
31. Chambers, R.D., D. Holling, R.C.H. Spink, and G. Sandford, *Elemental Fluorine. Part 13. Gas-Liquid Thin Film Microreactors for Selective Direct Fluorination*. Lab on a Chip, 2001. 1(2): 132-137. DOI: 10.1039/b108841f

32. Chambers, R.D., D. Holling, A.J. Rees, and G. Sandford, *Microreactors for Oxidations Using Fluorine*. Journal of Fluorine Chemistry, 2003. 119(1): 81-82. DOI: 10.1016/S0022-1139(02)00244-0
33. Chambers, R.D. and G. Sandford, *Durham Microreactors for Direct Fluorination*. Chimica Oggi, 2004.
34. Chambers, R.D., M.A. Fox, and G. Sandford, *Elemental Fluorine. Part 18. Selective Direct Fluorination of 1,3-Ketoesters and 1,3-Diketones Using Gas/Liquid Microreactor Technology*. Lab on a Chip, 2005. 5(10): 1132-1139. DOI: 10.1039/b504675k
35. Lang, P., M. Hill, I. Krossing, and P. Woias, *Multiphase Minireactor System for Direct Fluorination of Ethylene Carbonate*. Chemical Engineering Journal, 2012. 179: 330-337. DOI: 10.1016/j.cej.2011.11.015
36. Chambers, R.D., M.A. Fox, D. Holling, T. Nakano, T. Okazoe, and G. Sandford, *Versatile Gas/Liquid Microreactors for Industry*. Chemical Engineering & Technology, 2005. 28(3): 344-352. DOI: 10.1002/ceat.200407123
37. Chambers, R.D., M.A. Fox, G. Sandford, J. Trmcic, and A. Goeta, *Elemental Fluorine: Part 20. Direct Fluorination of Deactivated Aromatic Systems Using Microreactor Techniques*. Journal of Fluorine Chemistry, 2007. 128(1): 29-33. DOI: 10.1016/j.jfluchem.2006.09.010
38. Ehrich, H., D. Linke, K. Morgenschweis, M. Baerns, and K. Jähnisch, *Application of Microstructured Reactor Technology for the Photochemical Chlorination of Alkylaromatics*. Chimia International Journal for Chemistry, 2002. 56(11): 647-653. DOI: 10.2533/000942902777680063
39. Morgenschweis, K., R. Kraus, E. Ströfer, M. Fiene, M. Ochse, K. Thiele, K. Jähnisch, M. Baerns, and H. Ehrich, BASF AG. DE10246626. Selective Halogenation of Alkyl Aromatic Compounds, Useful as Intermediates for the Production of Plant Protection Agents, Comprises Insertion of Halogenating Agents in a Micro-Reactor under Photochemical Induction. 2004.
40. Matsubara, H., Y. Hino, M. Tokizane, and I. Ryu, *Microflow Photo-Radical Chlorination of Cycloalkanes*. Chemical Engineering Journal, 2011. 167(2-3): 567-571. DOI: 10.1016/j.cej.2010.08.086
41. Wehle, D., M. Dejmek, J. Rosenthal, H. Ernst, D. Kampmann, S. Trautschold, and R. Pechatschek, Clariant GmbH. WO0210094, DE10036603. Method for Selective Chlorination in Microreactors. 2002.
42. TeGrotenhuis, W.E., R.J. Cameron, V.V. Viswanathan, and R.S. Wegeng, *Solvent Extraction and Gas Absorption Using Microchannel Contractors*, in *Microreaction Technology: IMRET 3: Proceedings of the Third International Conference on Microreaction Technology*. Frankfurt, Germany: Springer. 541-549. 1999.
43. Koos, P., U. Gross, A. Polyzos, M. O'Brien, I. Baxendale, and S.V. Ley, *Teflon Af-2400 Mediated Gas-Liquid Contact in Continuous Flow Methoxycarbonylations and in-Line Ftir Measurement of Co Concentration*. Organic & Biomolecular Chemistry, 2011. 9(20): 6903-6908. DOI: 10.1039/c1ob06017a
44. de Bellefon, C., N. Tanchoux, S. Caravielhes, P. Grenouillet, and V. Hessel, *Microreactors for Dynamic, High Throughput Screening of Fluid/Liquid Molecular Catalysis*. Angewandte Chemie International Edition, 2000. 39(19): 3442-3445. DOI: 10.1002/1521-3773(20001002)39:19<3442::AID-ANIE3442>3.0.CO;2-Q
45. de Bellefon, C., S. Caravielhes, and P. Grenouillet, *Application of a Micromixer for the High Throughput Screening of Fluid-Liquid Molecular Catalysis*, in *Microreaction Technology: IMRET 5: Proceedings of the Fifth International Conference on Microreaction Technology*. Strasbourg, France: Springer. 408-413. 2001.

46. de Bellefon, C., N. Pestre, T. Lamouille, P. Grenouillet, and V. Hessel, *High Throughput Kinetic Investigations of Asymmetric Hydrogenations with Microdevices*. *Advanced Synthesis & Catalysis*, 2003. 345(1-2): 190-193. DOI: 10.1002/adsc.200390010
47. Abdallah, R., V. Meille, J. Shaw, D. Wenn, and C. de Bellefon, *Gas-Liquid and Gas-Liquid-Solid Catalysis in a Mesh Microreactor*. *Chemical Communications*, 2004. 4: 372-373. DOI: 10.1039/b312290e
48. de Bellefon, C., T. Lamouille, N. Pestre, F. Bornette, H. Pennemann, F. Neumann, and V. Hessel, *Asymmetric Catalytic Hydrogenations at Micro-Litre Scale in a Helicoidal Single Channel Falling Film Micro-Reactor*. *Catalysis Today*, 2005. 110(1-2): 179-187. DOI: 10.1016/j.cattod.2005.09.002
49. Leclerc, A., M. Alame, D. Schweich, P. Pouteau, C. Delattre, and C.d. Bellefon, *Gas-Liquid Selective Oxidations with Oxygen under Explosive Conditions in a Micro-Structured Reactor*. *Lab on a Chip*, 2008. 8(5): 814-817. DOI: 10.1039/b717985e
50. O'Brien, M., N. Taylor, A. Polyzos, I.R. Baxendale, and S.V. Ley, *Hydrogenation in Flow: Homogeneous and Heterogeneous Catalysis Using Teflon Af-2400 to Effect Gas-Liquid Contact at Elevated Pressure*. *Chemical Science*, 2011. 2(7): 1250-1257. DOI: 10.1039/c1sc00055a
51. Mercadante, M.A., C.B. Kelly, C. Lee, and N.E. Leadbeater, *Continuous Flow Hydrogenation Using an on-Demand Gas Delivery Reactor*. *Organic Process Research and Development*, 2012. 16(5): 1064-1068. DOI: 10.1021/op300019w
52. Mhiri, N., H. Monnier, and L. Falk, *Intensification of the G/L Absorption in Microstructured Falling Film Application to the Treatment of Chlorinated VOC's. Part III: Influence of Gas Thickness Channel on Mass Transfer*. *Chemical Engineering Science*, 2011. 66(23): 5989-6001. DOI: 10.1016/j.ces.2011.08.021
53. Müller, A., V. Cominos, V. Hessel, B. Horn, J. Schürer, A. Ziogas, K. Jähnisch, V. Hillmann, V. Großer, K.A. Jam, A. Bazzanella, G. Rinke, and M. Kraut, *Fluidisches Bussystem Für Die Chemische Verfahrenstechnik Und Für Die Produktion Von Feinchemikalien*. *Chemie Ingenieur Technik*, 2004. 76(5): 641-651. DOI: 10.1002/cite.200406166
54. Müller, A., V. Cominos, V. Hessel, B. Horn, J. Schürer, A. Ziogas, K. Jähnisch, V. Hillmann, V. Großer, K.A. Jam, A. Bazzanella, G. Rinke, and M. Kraut, *Fluidic Bus System for Chemical Process Engineering in the Laboratory and for Small-Scale Production*. *Chemical Engineering Journal*, 2005. 107(1-3): 205-214. DOI: 10.1016/j.cej.2004.12.030
55. Jähnisch, K., N. Steinfeldt, U. Dingerdissen, A. Müller, B. Horn, V. Cominos, V. Hessel, A. Bazzanella, V. Großer, V. Hillmann, G. Rinke, and M. Kraut, *Application of a Microplant for the Sulfonation of Toluene with Gaseous Sulfur Trioxide*, in *Proceedings of the 2000 AIChE Spring Meeting*. Atlanta, Georgia: Omnipress. 2005.
56. Commenge, J.-M., X. Framboisier, S. Rode, V. Schanen, P. Pitiot, and M. Matlosz, *Gas-Phase Mass-Transfer Measurements in a Falling-Film Microreactor*, in *IMRET 7 Proceedings*. Lausanne, Switzerland. 2003.
57. Shaw, J., C. Turner, B. Miller, and M. Harper, *Reaction and Transport Coupling for Liquid and Liquid/Gas Micro-Reactor Systems*, in *IMRET 2 Proceedings*. New Orleans, Louisiana. 176-180. 1998.
58. Su, H., S. Wang, H. Niu, L. Pan, A. Wang, and Y. Hu, *Mass Transfer Characteristics of H₂S Absorption from Gaseous Mixture into Methyl-diethanolamine Solution in a T-Junction Microchannel*. *Separation and Purification Technology*, 2010. 72(3): 326-334. DOI: 10.1016/j.seppur.2010.02.024

59. Wille, C. *Entwicklung Und Charakterisierung Eines Mikrofallfilm-Reaktors Für Stofftransportlimitierte Hochexotherme Gas/Flüssig-Reaktionen*, Ph.D. thesis. University Clausthal-Zellerfeld. 2002.
60. Hessel, V., W. Ehrfeld, T. Herweck, V. Haverkamp, H. Löwe, J. Schiewe, C. Wille, T. Kern, and N. Lutz, *Gas/Liquid Microreactors: Hydrodynamics and Mass Transfer*, in *Proceedings of the 2000 AIChE Spring Meeting*. Atlanta, Georgia: AIChE. 2000.
61. Claudel, S., C. Nikitine, C. Boyer, and P. Font. *Gas-Liquid Mass Transfer in a Microstructured Falling Film Reactor*. in *2005 AIChE Spring Meeting*. 2005. Atlanta, Georgia: Omnipress.
62. Zafir, M., A. Gavrilidis, C. Wille, and V. Hessel, *Carbon Dioxide Absorption in a Falling Film Microstructured Reactor: Experiments and Modeling*. Industrial and Engineering Chemistry Research, 2005. 44(6): 1742-1751. DOI: 10.1021/ie049726kS0888-5885(04)09726-X
63. Hecht, K. and M. Kraut, *Thermographic Investigations of a Microstructured Thin Film Reactor for Gas/Liquid Contacting*. Industrial & Engineering Chemistry Research, 2010. 49(21): 10889-10896. DOI: 10.1021/ie100431r
64. Sobieszuk, P., R. Pohorecki, P. Cygański, M. Kraut, and F. Olschewski, *Marangoni Effect in a Falling Film Microreactor*. Chemical Engineering Journal, 2010. 164(1): 10-15. DOI: 10.1016/j.cej.2010.07.053
65. Ziegenbalg, D., P. Löb, M.m. Al-Rawashdeh, D. Kralisch, V. Hessel, and F. Schönfeld, *Use of 'Smart Interfaces' to Improve the Liquid-Sided Mass Transport in a Falling Film Microreactor*. Chemical Engineering Science, 2010. 65(11): 3557-3566. DOI: 10.1016/j.ces.2010.02.039
66. Yue, J., G. Chen, Q. Yuan, L. Luo, and Y. Gonthier, *Hydrodynamics and Mass Transfer Characteristics in Gas-Liquid Flow through a Rectangular Microchannel*. Chemical Engineering Science, 2007. 62(7): 2096-2108. DOI: 10.1016/j.ces.2006.12.057
67. Hou, J., G. Qian, and X. Zhou, *Gas-Liquid Mixing in a Multi-Scale Micromixer with Arborescence Structure*. Chemical Engineering Journal, 2011. 167(2-3): 475-482. DOI: 10.1016/j.cej.2010.10.054
68. Sobieszuk, P., R. Pohorecki, P. Cygański, and J. Grzelka, *Determination of the Interfacial Area and Mass Transfer Coefficients in the Taylor Gas-Liquid Flow in a Microchannel*. Chemical Engineering Science, 2011. 66(23): 6048-6056. DOI: 10.1016/j.ces.2011.08.029
69. Li, W., K. Liu, R. Simms, J. Greener, D. Jagadeesan, S. Pinto, A. Günther, and E. Kumacheva, *Microfluidic Study of Fast Gas-Liquid Reactions*. Journal of the American Chemical Society, 2011. 134(6): 3127-3132. DOI: 10.1021/ja2101278
70. Polyzos, A., M. O'Brien, T.P. Petersen, I.R. Baxendale, and S.V. Ley, *The Continuous-Flow Synthesis of Carboxylic Acids Using CO₂ in a Tube-in-Tube Gas Permeable Membrane Reactor*. Angewandte Chemie International Edition, 2011. 50(5): 1190-1193. DOI: 10.1002/anie.201006618
71. Haverkamp, V., W. Ehrfeld, G. Emig, V. Hessel, M.A. Liauw, and H. Löwe, *Characterization of a Gas/Liquid Microreactor, the Micro Bubble Column: Determination of Specific Interfacial Area*, in *Microreaction Technology: IMRET 5: Proceedings of the Fifth International Conference on Microreaction Technology*. Strasbourg, France: Springer. 202-214. 2001.
72. Haverkamp, V. *Charakterisierung Einer Mikroblasensäule Zur Durchführung Stofftransportlimitierter Und/Oder Hoch-Exothermer Gas/Flüssig-Reaktionen*, Ph.D. thesis. University of Erlangen-Nürnberg. 2002.
73. Fischer, J., T. Lange, R. Boehling, A. Rehfinger, and E. Klemm, *Uncatalyzed Selective Oxidation of Liquid Cyclohexane with Air in a Microcapillary Reactor*.

- Chemical Engineering Science, 2010. 65(16): 4866-4872. DOI: 10.1016/j.ces.2010.05.028
74. Rebrov, E.V., T. Duisters, P. Löb, J. Meuldijk, and V. Hessel, *Enhancement of the Liquid-Side Mass Transfer in a Falling Film Catalytic Microreactor by in-Channel Mixing Structures*. Industrial & Engineering Chemistry Research, 2012. 51(26): 8719-8725. DOI: 10.1021/ie301058h
 75. Woerz, O., *Microreactors as Tools in Chemical Research*, in *Microreaction Technology: IMRET 5: Proceedings of the Fifth International Conference on Microreaction Technology*. Strasbourg, France: Springer. 377-386. 2001.
 76. Wootton, R.C.R., R. Fortt, and A.J. de Mello, *A Microfabricated Nanoreactor for Safe, Continuous Generation and Use of Singlet Oxygen*. Organic Process Research & Development, 2002. 6(2): 187-189. DOI: 10.1021/op0155155
 77. Jähnisch, K. and M. Baerns, Institut für Angewandte Chemie Berlin-Adlershof e.V. DE10257239. Continuous Partial Photooxidation of Liquid or Dissolved Olefin, Used for Preparing Organic Intermediate or Fine Chemical, E.G. Allyl Hydroperoxides, 1,2-Dioxetanes or Endo-Peroxides, Uses Falling Film Microreactor Then Immediate Reduction. 2004.
 78. Lévesque, F. and P.H. Seeberger, *Highly Efficient Continuous Flow Reactions Using Singlet Oxygen as a "Green" Reagent*. Organic Letters, 2011. 13(19): 5008-5011. DOI: 10.1021/ol2017643
 79. Wada, Y., M.A. Schmidt, and K.F. Jensen, *Multi-Phase Oxidation Reaction and Ozonolysis in the Limit of Explosion with Multi-Channel Microreactors*, in *IMRET 7 Proceedings*. Lausanne, Switzerland. 346-348. 2003.
 80. Wada, Y., M.A. Schmidt, and K.F. Jensen, *Flow Distribution and Ozonolysis in Gas-Liquid Multichannel Microreactors*. Industrial and Engineering Chemistry Research, 2006. 45(24): 8036-8042 DOI: 10.1021/ie060893p
 81. Steinfeldt, N., U. Bentrup, and K. Jähnisch, *Reaction Mechanism and in Situ ATR Spectroscopic Studies of the 1-Decene Ozonolysis in Micro- and Semibatch Reactors*. Industrial & Engineering Chemistry Research, 2010. 49(1): 72-80. DOI: 10.1021/ie900726s
 82. Roydhouse, M.D., A. Ghaini, A. Constantinou, A. Cantu-Perez, W.B. Motherwell, and A. Gavriilidis, *Ozonolysis in Flow Using Capillary Reactors*. Organic Process Research and Development, 2011. 15(5): 989-996. DOI: 10.1021/op200036d
 83. Steinfeldt, N., R. Abdallah, U. Dingerdissen, and K. Jähnisch, *Ozonolysis of Acetic Acid 1-Vinyl-Hexyl Ester in a Falling Film Microreactor*. Organic Process Research & Development, 2007. 11(6): 1025-1031. DOI: 10.1021/op7000673
 84. Irfan, M., T.N. Glasnov, and C.O. Kappe, *Continuous Flow Ozonolysis in a Laboratory Scale Reactor*. Organic Letters, 2011. 13(5): 984-987. DOI: 10.1021/ol102984h
 85. Battilocchio, C., I.R. Baxendale, M. Biava, M.O. Kitching, and S.V. Ley, *A Flow-Based Synthesis of 2-Aminoadamantane-2-Carboxylic Acid*. Organic Process Research and Development, 2012. 16(5): 798-810. DOI: 10.1021/op300084z
 86. Sobieszuk, P., P. Cyganski, and R. Pohorecki, *Volumetric Liquid Side Mass Transfer Coefficient in a Gas-Liquid Microreactor*. Inzynieria Chemiczna i Procesowa, 2008. 29(3): 651-661.
 87. Bercic, G. and A. Pintar, *The Role of Gas Bubbles and Liquid Slug Lengths on Mass Transport in the Taylor Flow through Capillaries*. Chemical Engineering Science, 1997. 52(21-22): 3709-3719. DOI: 10.1016/S0009-2509(97)00217-0
 88. Vandu, C.O., H. Liu, and R. Krishna, *Mass Transfer from Taylor Bubbles Rising in Single Capillaries*. Chemical Engineering Science, 2005. 60(22): 6430-6437. DOI: 10.1016/j.ces.2005.01.037

89. van Baten, J.M. and R. Krishna, *CFD Simulations of Mass Transfer from Taylor Bubbles Rising in Circular Capillaries*. Chemical Engineering Science, 2004. 59(12): 2535-2545. DOI: 10.1016/j.ces.2004.03.010
90. Zhang, H., G. Chen, J. Yue, and Q. Yuan, *Hydrodynamics and Mass Transfer of Gas-Liquid Flow in a Falling Film Microreactor*. AIChE Journal, 2009. 55(5): 1110-1120. DOI: 10.1002/aic.11743
91. Charpentier, J.-C., *Mass-Transfer Rates in Gas-Liquid Absorbers and Reactors*, in *Advances in Chemical Engineering*. New York: Academic Press, Inc. 1-133. 1981. ISBN: 9780120085118
92. Roudet, M., K. Loubiere, C. Gourdon, and M. Cabassud, *Hydrodynamic and Mass Transfer in Inertial Gas-Liquid Flow Regimes through Straight and Meandering Millimetric Square Channels*. Chemical Engineering Science, 2011. 66(13): 2974-2990. DOI: 10.1016/j.ces.2011.03.045
93. Irandoust, S., S. Ertle, and B. Andersson, *Gas-Liquid Mass Transfer in Taylor Flow through a Capillary*. The Canadian Journal of Chemical Engineering, 1992. 70: 115-119.
94. Luo, D. and S.M. Ghiaasiaan, *Liquid-Side Interphase Mass Transfer in Cocurrent Vertical Two-Phase Channel Flows*. International Journal of Heat and Mass Transfer, 1997. 40(3): 641-655. DOI: 10.1016/0017-9310(96)00104-4
95. Scott, D.S. and W. Hayduk, *Gas Absorption in Horizontal Cocurrent Bubble Flow*. The Canadian Journal of Chemical Engineering, 1966. 44(3): 130-136. DOI: 10.1002/cjce.5450440302
96. Shilimkan, R.V. and J.B. Stepanek, *Effect of Tube Size on Liquid Side Mass Transfer in Co-Current Gas-Liquid Upward Flow*. Chemical Engineering Science, 1977. 32(11): 1397-1400. DOI: 10.1016/0009-2509(77)85036-7
97. Robinson, C.W. and C.R. Wilke, *Simultaneous Measurement of Interfacial Area and Mass Transfer Coefficients for a Well-Mixed Gas Dispersion in Aqueous Electrolyte Solutions*. AIChE Journal, 1974. 20(2): 285-294. DOI: 10.1002/aic.690200212
98. Sahay, B.N. and M.M. Sharma, *Effective Interfacial Area and Liquid and Gas Side Mass Transfer Coefficients in a Packed Column*. Chemical Engineering Science, 1973. 28(1): 41-47.
99. Linek, V., V. Stoy, V. Machon, and Z. Krivský, *Increasing the Effective Interfacial Area in Plastic Packed Absorption Columns*. Chemical Engineering Science, 1974. 29(9): 1955-1960. DOI: 10.1016/0009-2509(74)85014-1
100. Yoshida, F. and K. Akita, *Performance of Gas Bubble Columns: Volumetric Liquid-Phase Mass Transfer Coefficient and Gas Holdup*. AIChE Journal, 1965. 11(1): 9-13. DOI: 10.1002/aic.690110106
101. Dillon, G.B. and I.J. Harris, *The Determination of Mass Transfer Coefficients and Interfacial Areas in Gas-Liquid Contacting Systems*. The Canadian Journal of Chemical Engineering, 1966. 44(6): 307-312. DOI: 10.1002/cjce.5450440602
102. Mashelkar, R.A. and M.M. Sharma, *Mass Transfer in Bubble and Packed Bubble Columns*. Transactions of the Institution of Chemical Engineers, 1970. 48: T162-T172.
103. Akita, K. and F. Yoshida, *Gas Holdup and Volumetric Mass Transfer Coefficient in Bubble Columns. Effects of Liquid Properties*. Industrial & Engineering Chemistry Process Design and Development, 1973. 12(1): 76-80. DOI: 10.1021/i260045a015
104. Akita, K. and F. Yoshida, *Bubble Size, Interfacial Area, and Liquid-Phase Mass Transfer Coefficient in Bubble Columns*. Ind. Eng. Chem. Proc. Des. Dev., 1974. 13(1): 84-91. DOI: 10.1021/i260049a016

105. Shah, Y.T., B.G. Kelkar, S.P. Godbole, and W.D. Deckwer, *Design Parameters Estimations for Bubble Column Reactors*. AIChE Journal, 1982. 28(3): 353–379. DOI: 10.1002/aic.690280302
106. Chaumat, H., A.M. Billet-Duquenne, F. Augier, C. Mathieu, and H. Delmas, *Mass Transfer in Bubble Column for Industrial Conditions—Effects of Organic Medium, Gas and Liquid Flow Rates and Column Design*. Chemical Engineering Science, 2005. 60(22): 5930-5936. DOI: 10.1016/j.ces.2005.04.026
107. Onda, K., E. Sada, and Y. Murase, *Liquid-Side Mass Transfer Coefficients in Packed Towers*. AIChE Journal, 1959. 5(2): 235-239. DOI: 10.1002/aic.690050220
108. Yoshida, F. and Y. Miura, *Effective Interfacial Area in Packed Columns for Absorption with Chemical Reaction*. AIChE Journal, 1963. 9(3): 331-337. DOI: 10.1002/aic.690090311
109. Richards, G.M., G.A. Ratcliff, and P.V. Danckwerts, *Kinetics of CO₂ Absorption--III : First-Order Reaction in a Packed Column*. Chemical Engineering Science, 1964. 19(5): 325-328. DOI: 16/0009-2509(64)80001-4
110. Danckwerts, P.V. and A.J. Gillham, *The Design of Gas Absorbers. I-Methods for Predicting Rates of Absorption with Chemical Reaction in Packed Columns, and Tests With 1 1/2 In. Raschig Rings*. Transactions of the Institution of Chemical Engineers, 1966. 44: T42-T54.
111. Danckwerts, P.V. and M.M. Sharma, *The Absorption of Carbon Dioxide into Solutions of Alkalis and Amines (with Some Notes on Hydrogen Sulphide and Carbonyl Sulphide)*. The Chemical Engineer, 1966: CE244-CE280.
112. de Waal, K.J.A. and W.J. Beek, *A Comparison between Chemical Absorption with Rapid First-Order Reactions and Physical Absorption in One Packed Column*. Chemical Engineering Science, 1967. 22(4): 585-593. DOI: 10.1016/0009-2509(67)80041-1
113. Carleton, A.J., R.J. Flain, J. Rennie, and F.H.H. Valentin, *Some Properties of a Packed Bubble Column*. Chemical Engineering Science, 1967. 22(12): 1839-1845. DOI: 16/0009-2509(67)80214-8
114. Chen, B.H. and R. Vallabh, *Holdup and Mass Transfer in Bubble Columns Containing Screen Cylinders*. Ind. Eng. Chem. Proc. Des. Dev., 1970. 9(1): 121-126. DOI: 10.1021/i260033a022
115. Danckwerts, P.V. and S.F. Rizvi, *The Design of Gas Absorbers Part II: Effective Interfacial Areas for Several Types of Packing*. Transactions of the Institution of Chemical Engineers, 1971. 49: 124-127.
116. Reiss, L.P., *Cocurrent Gas-Liquid Contacting in Packed Columns*. Industrial & Engineering Chemistry Process Design and Development, 1967. 6(4): 486-499. DOI: 10.1021/i260024a017
117. Voyer, R.D. and A.I. Miller, *Improved Gas-Liquid Contacting in Co-Current Flow*. The Canadian Journal of Chemical Engineering, 1968. 46(5): 335-341. DOI: 10.1002/cjce.5450460510
118. Gianetto, A., V. Specchia, and G. Baldi, *Absorption in Packed Towers with Concurrent Downward High-Velocity Flows—II: Mass Transfer*. AIChE Journal, 1973. 19(5): 916-922. DOI: 10.1002/aic.690190505
119. Shende, B.W. and M.M. Sharma, *Mass Transfer in Packed Columns: Co-Current Operation*. Chemical Engineering Science, 1974. 29(8): 1763-1772. DOI: 16/0009-2509(74)87035-1
120. Snider, J.W. and J.J. Perona, *Mass Transfer in a Fixed-Bed Gas-Liquid Catalytic Reactor with Concurrent Upflow*. AIChE Journal, 1974. 20(6): 1172-1177. DOI: 10.1002/aic.690200617

121. Sharma, M.M., R.A. Mashelkar, and V.D. Mehta, *Mass Transfer in Plate Columns*. British Chemical Engineering, 1969. 14(1): 70-76.
122. Calderbank, P.H., *Physical Rate Processes in Industrial Fermentation. Part II.--Mass Transfer Coefficients in Gas-Liquid Contacting with and without Mechanical Agitation*. Transactions of the Institution of Chemical Engineers, 1959. 37: 173-185.
123. Calderbank, P.H. and M.B. Moo-Young, *The Mass-Transfer Efficiency of Distillation and Gas-Absorption Plate Columns Part I: Techniques for Measuring Gas-Liquid Interfacial Areas and Foam Densities in Plate Columns*, in *Proceedings of the International Symposium on Distillation*. Brighton, U.K.: The Institution of Chemical Engineers. 59-72. 1960.
124. Barrett, P.V.L. *Gas Absorption on a Sieve Plate, Ph.D. dissertation. Cambridge. 1966.*
125. Pohorecki, R., *The Absorption of CO₂ in Carbonate--Bicarbonate Buffer Solutions Containing Hypochlorite Catalyst on a Sieve Plate*. Chemical Engineering Science, 1968. 23(12): 1447-1451. DOI: 16/0009-2509(68)89054-2
126. Hatta, S., *On the Absorption Velocity of Gases by Liquids. I. Absorption of Carbon Dioxide by Potassium Hydroxide Solution*. The Technology reports of the Tohoku University. Tohoku-daigaku-kogyo-hokoku, 1928/1929: 1-25.
127. Westerterp, K.R., L.L. van Dierendonck, and J.A. de Kraa, *Interfacial Areas in Agitated Gas-Liquid Contactors*. Chemical Engineering Science, 1963. 18(3): 157-176. DOI: 10.1016/0009-2509(63)85002-2
128. Mehta, V.D. and M.M. Sharma, *Mass Transfer in Mechanically Agitated Gas--Liquid Contactors*. Chemical Engineering Science, 1971. 26(3): 461-479. DOI: 10.1016/0009-2509(71)83019-1
129. Joshi, J.B. and M.M. Sharma, *Mass Transfer and Hydrodynamic Characteristics of Gas Inducing Type of Agitated Contactors*. The Canadian Journal of Chemical Engineering, 1977. 55(6): 683-695. DOI: 10.1002/cjce.5450550609
130. Hassan, I.T.M. and C.W. Robinson, *Stirred-Tank Mechanical Power Requirement and Gas Holdup in Aerated Aqueous Phases*. AIChE Journal, 1977. 23(1): 48-56. DOI: 10.1002/aic.690230109
131. Farritor, R.E. and G.A. Hughmark, *Interfacial Area and Mass Transfer with Gas-Liquid Systems in Turbine-Agitated Vessels*. Chemical Engineering Communications, 1980. 4(1-3): 143-147. DOI: 10.1080/00986448008935898
132. Nernst, W., *Theorie Der Reaktionsgeschwindigkeit in Heterogenen Systemen*. Zeitschrift für Physikalische Chemie, 1904. 47: 52-55.
133. Whitman, W.G., *A Preliminary Experimental Confirmation of the Two-Film Theory of Gas Absorption*. Chemical and Metallurgical Engineering, 1923. 29(4): 146-148.
134. Henry, W., *Experiments on the Quantity of Gases Absorbed by Water, at Different Temperatures, and under Different Pressures*. Philosophical Transactions of the Royal Society of London, 1803. 93: 29 -274. DOI: 10.1098/rstl.1803.0004
135. *Coulson and Richardson's Chemical Engineering: Chemical and Biochemical Reactors and Process Control*, 2 ed. J.F. Richardson and D.G. Peacock, Editors. Vol. 3. Oxford: Pergamon Press. 1979.
136. de Santiago, M. and I.H. Farina, *Mass Transfer with Second Order Reaction. Numerical Solution*. Chemical Engineering Science, 1970. 25(4): 744-747. DOI: 10.1016/0009-2509(70)85106-5
137. van Krevelen, D.W. and P.J. Hoftijzer, *Kinetics of Gas-Liquid Reactions-Part I. General Theory*. Recueil des Travaux Chimiques des Pays-Bas, 1948. 67: 563-586.
138. Lietz, C. *Aufbau Einer Apparatur Zur Kontaktwinkelbestimmung Am Liegenden Tropfen Unter Erhöhten Drücken, Studienarbeit. Forschungszentrum Karlsruhe. 2000.*

139. Wesch, A., N. Dahmen, K. Ebert, and J. Schön, *Grenzflächenspannungen, Tropfengrößen Und Kontaktwinkel Im Zweiphasensystem H₂O/CO₂ Bei Temperaturen Von 298 Bis 333 K Und Drücken Bis 30 Mpa*. Chemie Ingenieur Technik, 1997. 69: 942-946. DOI: 10.1002/cite.330690709
140. Adamson, A.W. and A.P. Gast, *Physical Chemistry of Surfaces*. New York: John Wiley & Sons, Inc. 1997.
141. Commenge, J.M., L. Falk, J.P. Corriou, and M. Matlosz, *Optimal Design for Flow Uniformity in Microchannel Reactors*. AIChE Journal, 2002. 48(2): 345-358
142. Rasband, W.S. *Image J* National Institutes of Health, Bethesda, Maryland, USA. 1997. [accessed 9 Dec 2010]; Available from: <http://rsbweb.nih.gov/ij>.
143. Stalder, A.F. *Big>Drop Analysis*. [accessed 27 January 2011]; Available from: <http://bigwww.epfl.ch/demo/dropanalysis>.
144. Stalder, A.F., G. Kulik, D. Sage, L. Barbieri, and P. Hoffmann, *A Snake-Based Approach to Accurate Determination of Both Contact Points and Contact Angles*. Colloids and Surfaces A, 2006. 286(1-3): 92-103. DOI: 10.1016/j.colsurfa.2006.03.008
145. Pohorecki, R. and W. Moniuk, *Kinetics of Reaction between Carbon Dioxide and Hydroxyl Ions in Aqueous Electrolyte Solutions*. Chemical Engineering Science, 1988. 43(7): 1677-1684. DOI: 10.1016/0009-2509(88)85159-5
146. Fleischer, C., S. Becker, and G. Eigenberger, *Transient Hydrodynamics, Mass Transfer, and Reaction in Bubble Columns: CO₂ Absorption into Naoh Solutions*. Chemical Engineering Research & Design, 1995. 73: 649-653.
147. Fleischer, C., S. Becker, and G. Eigenberger, *Detailed Modeling of the Chemisorption of CO₂ into Naoh in a Bubble Column*. Chemical Engineering Science, 1996. 51(10): 1715-1724. DOI: 10.1016/0009-2509(96)00030-9
148. Hecht, K., F. Messerschmidt, P. Pfeifer, R. Dittmeyer, B. Kraushaar-Czarnetzki, and S. Hecht, *Surface Roughness of Machined Microchannels and Its Effect on Multiphase Boundary Conditions*. Chemical Engineering Journal. DOI: 10.1016/j.cej.2012.11.127
149. Ponter, A.B. and M. Yekta-Fard, *The Influence of Environment on the Drop Size - Contact Angle Relationship*. Colloid & Polymer Science, 1985. 263(8): 673-681. DOI: 10.1007/BF01419892
150. Fox, H.W. and W.A. Zisman, *The Spreading of Liquids on Low Energy Surfaces. I. Polytetrafluoroethylene*. Journal of Colloid and Interface Science, 1950. 5(6): 514-531. DOI: 10.1016/0095-8522(50)90044-4
151. Belda, R., J.V. Herraiez, and O. Diez, *A Study of the Refractive Index and Surface Tension Synergy of the Binary Water/Ethanol: Influence of Concentration*. Physics and Chemistry of Liquids, 2005. 43(1): 91-101. DOI: 10.1080/00319100512331327342
152. *Lange's Handbook of Chemistry*, 13 ed. J.A. Dean, Editor. New York: McGraw-Hill, Inc. 1985.
153. Wenzel, R.N., *Resistance of Solid Surfaces to Wetting by Water*. Industrial & Engineering Chemistry, 1936. 28(8): 988-994. DOI: 10.1021/ie50320a024
154. Cassie, A.B.D. and S. Baxter, *Wettability of Porous Surfaces*. Transactions of the Faraday Society, 1944. 40: 546. DOI: 10.1039/tf9444000546
155. Engländer, T., D. Wiegel, L. Naji, and K. Arnold, *Dehydration of Glass Surfaces Studied by Contact Angle Measurements*. Journal of Colloid and Interface Science, 1996. 179(2): 635 - 636. DOI: DOI: 10.1006/jcis.1996.0260
156. van Oss, C.J., *Interfacial Forces in Aqueous Media*. Boca Raton, USA: CRC Press. 2006.
157. Montgomery, D.C., G.C. Runger, and N.F. Hubele, *Engineering Statistics*. New York: John Wiley & Sons, Inc. 1998.

158. Hecht, K., G. Fröhlich, P. Pfeifer, R. Dittmeyer, and B. Kraushaar-Czarnetzki, *The Influence of Surface Properties on Chemical Reaction in Multiphase Flow in Capillaries*. Chemical Engineering Journal. DOI: 10.1016/j.cej.2012.11.092
159. Zehner, P. and M. Kraume, *Bubble Columns*, in *Ullmann's Encyclopedia of Industrial Chemistry*. Wiley-VCH Verlag GmbH & Co. KGaA. 1-32. 2000. ISBN: 9783527306732
160. Doraiswamy, L.K. and M.M. Sharma, *Heterogeneous Reactions: Analysis, Examples, and Reactor Design, Volume 2: Fluid-Fluid-Solid Reactions*. New York: John Wiley & Sons. 1984.
161. Danckwerts, P.V., *Gas-Liquid Reactions*. New York: McGraw-Hill Book Company. 1970.
162. Kraus, M. and U. Krewer, *Experimental Analysis of the Separation Efficiency of an Orientation Independent Gas/Liquid Membrane Separator*. Separation and Purification Technology, 2011. 81(3): 347-356. DOI: 10.1016/j.seppur.2011.08.001
163. Lee, C.Y. and S.Y. Lee, *Pressure Drop of Two-Phase Plug Flow in Round Mini-Channels: Influence of Surface Wettability*. Experimental Thermal and Fluid Science, 2008. 32(8): 1716-1722 DOI: 10.1016/j.expthermflusci.2008.06.007
164. Lee, C.Y. and S.Y. Lee, *Pressure Drop of Two-Phase Dry-Plug Flow in Round Mini-Channels: Effect of Moving Contact Line*. Experimental Thermal and Fluid Science, 2010. 34: 1-9. DOI: 10.1016/j.expthermflusci.2009.08.005
165. Lockhart, R.W. and R.C. Martinelli, *Proposed Correlation of Data for Isothermal Two-Phase, Two-Component Flow in Pipes*. Chemical Engineering Progress, 1949. 45(1): 39-48.
166. Chisholm, D., *A Theoretical Basis for the Lockhart-Martinelli Correlation for Two-Phase Flow*. International Journal of Heat and Mass Transfer, 1967. 10(12): 1767-1778. DOI: 10.1016/0017-9310(67)90047-6
167. Yue, J., G. Chen, and Q. Yuan, *Pressure Drops of Single and Two-Phase Flows through T-Type Microchannel Mixers*. Chemical Engineering Journal, 2004. 102(1): 11-24. DOI: 10.1016/j.cej.2004.02.001
168. Fröhlich, G. *Einfluss Von Oberflächeneigenschaften Auf Mehrphasenreaktionen in Mikroreaktoren, masters thesis. Karlsruher Institut für Technologie. 2010.*
169. Potter, M.C. and D.C. Wiggert, *Mechanics of Fluids*, 3 ed. Pacific Grove, USA: Brooks/Cole. 2002.
170. Peiyi, W. and W.A. Little, *Measurement of Friction Factors for the Flow of Gases in Very Fine Channels Used for Microminiature Joule-Thomson Refrigerators*. Cryogenics, 1983. 23(5): 273-277. DOI: 10.1016/0011-2275(83)90150-9
171. Tilton, J.N., *Section 6: Fluid and Particle Dynamics*, in *Perry's Chemical Engineers' Handbook*, 7 ed, R.H. Perry and D.W. Green, Editors. New York: McGraw-Hill. 39-50 1997.
172. Liley, P.E., G.H. Thomson, D.G. Friend, T.E. Daubert, and E. Buck, *Section 2: Physical and Chemical Data*, in *Perry's Chemical Engineers' Handbook*, 7 ed, R.H. Perry and D.W. Green, Editors. New York: McGraw-Hill. 1997. ISBN: 0-07-049841-5
173. Wille, C., W. Ehrfeld, V. Haverkamp, T. Herweck, V. Hessel, H. Löwe, N. Lutz, K.P. Möllmann, and F. Pinno, *Dynamic Monitoring of Fluid Equipartition and Heat Release in a Falling Film Microreactor Using Real-Time Thermography*, in *Proceedings of the Micro.tec 2000*. Hannover, Germany. 349-354. 2000.

8 SUPPLEMENTARY MATERIAL

The supplementary material is included as a DVD affixed to the following page.

8.1 ANALYTICAL METHODS

Titration, acidic evolution of absorbed gas, density measurement, pH measurement, electrical conductivity measurement, and gas chromatography were evaluated for use in the determining the conversion of the reaction of CO₂ with MEA and NaOH. This appendix contains details regarding each method and calibration curves.

8.2 CONTACT ANGLE AND SURFACE TENSION MEASUREMENTS

This appendix contains a list of each individual contact angle and interfacial tension measurement completed in the course of this work. It also contains information regarding the testing of the measurement apparatus; the system cannot be calibrated per se, but an overall test of the system accuracy with a known standard was made each time a new solid sample was placed in the device. The relationship between the interfacial tension and the contact angle was shown for polished surfaces in Section 5.1.3.3. The same information for ground and machined surfaces are included in this appendix.

8.3 AFM MEASUREMENTS

The results of AFM characterization for stainless steel and PTFE surfaces were described in Section 4.1. The results for all surfaces prepared for contact angle measurements are included in this appendix.

8.4 VIDEOS OF TWO-PHASE FLOW IN CAPILLARIES

The photos shown in Section 5.2 do not completely capture the nature of a moving gas/liquid flow. The high speed videos associated with the pictures shown in Table 12 and Table 13 are contained in this appendix. If suitable software is needed for viewing, Virtualdub can be downloaded from www.virtualdub.org.

8.5 CALCULATIONS OF CONVERSION, INTERFACIAL AREA, AND LIQUID MASS TRANSPORT COEFFICIENTS FROM CAPILLARY MEASUREMENTS

The influence of gas partial pressure on the conversions measured for the absorption of CO₂ was only shown for PEEK capillaries. The trends remain the same, but the same data for fused silica and stainless steel capillaries are included in this appendix. This Appendix also contains the calculations of a and k_L as they were applied to the experiments.

8.6 CALCULATION OF LIQUID MASS TRANSPORT COEFFICIENT FOR FALLING FILM REACTOR INVESTIGATIONS

This appendix contains the temperature profiles measured in the thermographic investigations of the microstructured falling film reactor described in Section 5.3. The calculations performed to derive a and k_L along the reactor length as well as the calculations of the average a and k_L values for the integral reactor volume are also included.

8.7 MEASUREMENTS OF DIFFERENT LENGTHS OF GLASS CAPILLARY AND DISCRETIZED REACTOR MODELS (SIMPLIFIED FILM MODEL & FILM MODEL)

This appendix contains the experimental data obtained from the measurements of different length of glass capillary and their analysis as described in Section 5.4. The models presented in Section 5.4, the simplified film model and the film model, were implemented in Mathcad

14. Mathcad files for each model as well as a short version of the film model that only calculates the film profiles in a single segment are included.